University of Nevada, Reno

Dynamic State Estimation of Microgrid with Imperfect Data Communication

A thesis submitted in partial fulfillment of the
requirements for the degree of Master of Science in
Electrical Engineering

by

Meh Fuzur Rahaman

Dr. M. Sami Fadali/Thesis Advisor

August, 2017

THE GRADUATE SCHOOL

We recommend that the thesis
prepared under our supervision by

MEH FUZUR RAHAMAN

Entitled

Dynamic State Estimation of Microgrid with Imperfect Data Communication

be accepted in partial fulfillment of the
Requirements for the degree of

MASTER OF SCIENCE

M. Sami Fadali, Ph.D., Advisor

Hanif Livani, Ph.D., Committee Member

Mehmet Hadi Gunes, Ph.D., Graduate School Representative

David W. Zeh, Ph.D., Dean, Graduate School

August, 2017

Abstract

Dynamic state estimation of power systems is essential for wide area control purposes. In this thesis, we present the results of dynamic state estimation for a grid-connected microgrid including two synchronous generators and three loads. The Unscented Kalman filter and the Extended Kalman filter are implemented using a classical generator model connected to a Thevenin equivalent of the remainder of the microgrid. The model is used to estimate the six states variables of the generator; namely, rotor angle, speed variant, d- and q- axis transient voltages, d-axis damper flux, and q-axis second damper flux. Both real power and reactive power are used as measurements in our state estimation algorithm. The estimation results are compared with the true values to demonstrate the accuracy of the state estimator. In addition to data loss or delay, sensor measurements may include outliers that distort state estimation. We utilized the Generalized Maximum Likelihood-extended Kalman filter (GM-EKF), as a robust estimator, which exhibits good tracking capabilities suppressing the effects of bad data. We also used two methods of state estimation on UKF to deal with bad data. Simulation results obtained from the UKFs are compared with those of GM-EKF. We present simulation results at a high frequency of 1 kHz of state estimation for different scenarios that include normal operation, fault at Point of Common Coupling, loss of generator, and loss of load. We also developed a scheme to use delayed data in Kalman filter estimation and used it to simulate the effect of data loss and/or delay in the communication system of the microgrid. For the same scenarios, we also present simulation results at 50 Hz, which is compatible with Phasor Measurement Units, including bad data as well as data loss or delay.

Acknowledgements

First and foremost, I would like to thank my research advisor Dr. M. Sami Fadali for guiding me in my research. He set a great example and provided hard-to-find insights that aided me in my academic career. I would also like to my committee members, specially, Dr. Hanif Livani for his valuable feedback, and Dr. Mehmet Hadi Gunes.

I would like to thank my parents, my brother Ashikur Rahman, my friend Hamid Khodabandehlou for moral support and my beloved wife, Kuhinur Jahan for her patience while I was writing this thesis.

Finally, I would like to thank Marcos Netto, Junbo Zhao for providing me with a MATLAB program that calculates the projection statistics for the generalized maximum-likelihood extended Kalman filter.

This work was supported by the National Science Foundation under Grant No. IIA-1301726.

Table of Contents

LIST OF TABLES

LIST OF FIGURES

CHAPTER 1 INTRODUCTION

1.1 BACKGROUND

Conventional power systems are facing the problems of gradual depletion of fossil fuel resources, poor energy efficiency and environmental pollution. The current trend is moving to distributed power generation using non-conventional energy sources such as natural gas, bio gas, wind power, solar photovoltaic cells, fuel cells, combined heat and power systems, microturbines, and Stirling engines and their integration into the utility distribution network. The resources used in this distributed generation (DG) are called distributed energy resources.

A microgrid is a single, controllable, independent power system comprising DG, load, energy storage, and control devices, in which DG and ES are directly connected to the user side. A microgrid can be considered as a controlled cell that provides many advantages, such as reduced feeder loss and higher local reliability. Being capable of autonomous control, protection, and management, a microgrid can operate either in parallel with the main grid or in an intentional islanded mode.A microgrid is a small electric power system that incorporates generation, transmission, and distribution, and can achieve power balance and optimal energy allocation over a given area, or as a virtual power source or load in the distribution network. Compared with traditional transmission and distribution networks, a microgrid has a much more flexible structure.

It can consist of one or more virtual power plants to meet the demand of a load center, which can be offices, factories, or remote residences where the traditional electricity supply is expensive.

1.2.1 LITERATURE REVIEW ON STATE ESTIMATION

State estimation has been a fundamental function in power system operation. It is a driving force in some key operations such as contingency analysis, optimal power flow, and economic dispatch. Static state estimation using measurements from supervisory control and data acquisition(SCADA) is important for power system monitoring and provides input data for applications such as automatic generation control. However, state estimation may not be sufficient for good system monitoring as power systems becomes more dynamic. Therefore, dynamic state estimates obtained through real-time dynamic state estimation have become essential. The use of these models together with Kalman filters has been widely studied in the literature. In addition, the introduction of high speed phasor measurement units (PMUs) has made the use of dynamic models with a Kalman filter more effective in dynamic state estimation.

Peng et al. investigated the feasibility of applying the Extended Kalman Filter (EKF) to a 9 bus-3-generator system using a second order model of a synchronous generator [1]. They obtained estimates of the dynamic states of a power system e.g. generator rotor angle and generator speed, instead of the static states of voltage magnitudes and phase angles. For problem formulation, they presented a simple system with one machine feeding an infinite bus through two parallel lines. Measurements of bus voltage and phase angle were taken at the generator terminal. A classical model composed of a voltage source in series with an impedance was used for the generator. They showed that

the Kalman filter converges quickly and accurately estimates the dynamic states during the system transients. They also presented dynamic state estimation using the EKF in the presence of a small disturbance and a large disturbance for a multi-machine test system. They showed that the performance of the EKF is affected by measurement characteristics such as sampling rate and measurement noise level. They also investigated the EKF performance against sampling rate and found a lower rate limit below which DSE performance deteriorates. In addition, the EKF was successful in dealing with measurement noise having SNR level even up to 40%. All the results confirmed successful implementation of communication and control are tightly coupled in NCS and cannot be considered independently. EKF in dynamic state estimation is feasible.

Qi et al. studied an unscented Kalman filter(UKF) with enhanced numerical stability [2]. In order to enhance numerical stability of the UKF for dynamic state estimation, a new UKF with guaranteed positive semi-definite estimation error covariance (UKF-GPS) was proposed. The proposed method was compared with five published methods including UKF-schol, UKF-κ, UKF-modified, UKF-ΔQ and the square root unscented Kalman filter. Both the EKF and the UKF can suffer from the curse of dimensionality which can adversely affect performance. Although the classic UKF has good performance for small systems, its performance deteriorates for large systems, such as large power systems. Reference [2] observed that numerical stability is the main limitation of the UKF. The UKF algorithm requires the calculation of the square root of the error covariance matrix. When the error covariance matrix was propagated, it might lose its positive definiteness and its square root matrix cannot be calculated. A Western System Coordinating Council (WSCC) 3-machine 9-bus system and a Northeast Power

Coordinating Council (NPCC) 48-machine 140-bus system were used as the test bed for performance analysis of the proposed UKF-GPS method along with the extended Kalman filter. For the WSCC system, no numerical stability problem was encountered and all methods performed well. However, for the NPCC system the EKF failed to converge and encountered numerical stability problems. In addition, UKF-schol, UKF-κ, UKF-ΔQ had large estimation errors. UKF with a guaranteed positive definite error covariance matrix was found to perform well in almost all estimation cases.

E. Ghahremani and I. Kamwa utilized a single machine infinite bus (SMIB) test bed to evaluate an EKF based estimator with missing input information [3]. Two different approaches were presented for dynamic state estimation of a power system including a synchronous generator. The first approach was a traditional EKF using PMU data. Simulation results showed appropriate estimation accuracy for a saturated fourth-order generator connected to infinite bus, with process and measurement noise. Traditional EKF requires that all input data be available. However, this may not always be the case in practice. For example with brushless exciters, the field voltage cannot be easily measured from the power plant control room. To address this problem, the extended Kalman filter with unknown input was proposed for identifying and estimating the states and the unknown inputs of the synchronous machine simultaneously. The robustness and effectiveness of the proposed method ware checked using various kinds of field voltages and torque inputs ranging from step to ramp signals. In addition, the proposed method was found to perform successfully under network fault condition with additive process and measurement noise.

E. Ghahremani and I. Kamwa used UKF for online state estimation of synchronous generator in SMIB configuration using PMU measurements [4]. In classic state estimation, such as in the extended Kalman filter, linear approximation of the system may introduce errors in estimation results. To overcome the drawbacks of the EKF, the UKF was used to estimate and predict states of a synchronous machine using PMU quantities. The UKF algorithm propagates the probability density function of a random variable which is accurate up to the second order statistics. The UKF based scheme provided high quality results in comparison with EKF in terms of robustness, speed of convergence with different noise levels. Furthermore, good estimation results were obtained under grid fault conditions.

Linawati et al. proposed a hybrid observer scheme for power system [5]. To estimate the state variables, linear observers based on linearized power system model were designed. However, this introduces steady-state estimation error when applied to nonlinear power system models that can make the estimation results useless.

Although the design of a nonlinear observer can be a possible solution of this problem, the derivation of nonlinear observer is tedious and the observer can be ineffective for very high-order system. For power system synchronous machine can be of 6^{th} order or more. Reference [5] presented a hybrid estimation scheme for a 6^{th} order synchronous generator. The 6^{th} order model was first decoupled into a 3^{rd} order non-linear subsystem and a 3^{rd} order linear subsystem. A low-order nonlinear observer and a low order linear observer were designed. The resulting hybrid observer was found to perform well both under steady-state condition and transient conditions. Their approach provided nonlinear state estimation for very high order systems.

1.2.2 LITERATURE REVIEW ON NETWORKED CONTROL SYSTEM

Networked control systems (NCSs) have been a major research focus in academia as well as in industry for many decades. In NCS, both wired and wireless networks can be used. Wireless networks play an important role in distributed control applications. They allow fully mobile operation, fast deployment and flexible installation. However, there are some problems associated with NCS that require careful consideration. Communication and control are tightly coupled in NCS and cannot be considered independently. Data must arrive at their destination in time to be used for control. Packet losses and delays of the sensor data are very common because of collision and transmission errors. This loss of data can complicate state estimation using a Kalman filter.

Kalman filtering in the presence of packet losses and time delay has been studied in several papers. Sinopoli et al. investigated the statistical convergence properties of the error covariance matrix with intermittent observations [6]. They modeled the arrival of an observation as a random Bernoulli process whose parameters are related to the characteristics of the communication channel. The main contribution of [6] was to show that the mean error covariance is always finite if the probability of arrival of an observation exceeds a critical Bernoulli parameter value that depends on the eigenvalues of the state matrix and on the output matrix. The authors derived an upper and a lower bound on the critical value and showed that they are tight in some special cases.

M. Micheli and M. I. Jordan proposed a Kalman filter based state estimation algorithm [7]. Noisy measurements occurred at discrete times with Poisson arrivals.

Such a system can be an ideal example for a network with a large number of sensors that are not synchronized and the waiting time between two consecutive measurements is an exponential random variable.

The sequence of estimation error covariance matrices is not deterministic, but stochastic process itself. The stochastic process is homogeneous Markov process. The authors described the computation of the statistical properties, which depend on the Poisson sampling rate and system dynamics. They determined a lower bound on the sampling rate which keeps the estimation error covariance below a threshold value.

Liu and Goldsmith studied Kalman filtering with random partial observation losses [8]. They proposed Kalman filter update equations with partial observation measurements. The error covariance matrix of the Kalman filter is stochastic in nature with partial measurements; the filter depended on the random packet arrivals of the sensor measurements, which can be lost or delayed over communication channel. The communication channel must guarantee a sufficient amount of sensor measurements in order to ensure the stability of the Kalman filter. Reference [8] investigated the statistical convergence properties of the error covariance matrix iteration as a function of sensor measurements. A throughput region of measurements was found for which error covariance matrix converges. In addition, a region of sensor measurements was obtained where state estimation error becomes unbounded. The expected error covariance matrix must be bounded both from above and from below for the Kalman filter to work.

L. Shi and L. Qiu investigated discrete time state estimation over a network [9]. Two cases were analyzed. In the first case, the sensor sends its measurement packets

over a packet dropping network. Later they derived the minimum packet arrival rate for which certain performance is guaranteed at the remote estimator. In the second case, the network does not drop any packets but the sensor has the freedom in sending or not sending the data packet so as to reduce cost. Sending less measurement data at the estimator requires less bandwidth of channel and less power is consumed. Therefore, there is a tradeoff between cost and estimator performance. The authors obtained a unique packet sending rate that provides the optimal tradeoff between the cost of the sensor and the estimation error of the estimator.

1.2.3 LITERATURE REVIEW ON ROBUST STATE ESTIMATION

In power systems, sudden load changes may lead to sudden changes of states. Sudden load changes along with network topology errors may result in outliers in measurements or *bad data*. The outliers can degrade the performance of state estimators, resulting in estimation errors. Observation redundancy is necessary for an estimator to suppress the effects of outliers in a system. In practice, more sensors are required to achieve this observation redundancy. Therefore, it is required to detect the outliers or bad data for reliable state estimation.

Numerous papers have addressed bad data detection in last few decades. Mili et al. provided a comparative assessment of the "post-estimation" identification methods, concentrating on evaluating the techniques able to identify bad data [10]. The techniques were divided into three classes: (a) identification by elimination, (b) non-quadratic criteria, and (c) hypothesis testing identification. The three classes were explored and compared both theoretically and practically. Experimental results were acquired through simulations performed on four different power systems. Three types

of bad data were considered: non-interacting, interacting and unidentifiable. The main weakness of all of these approaches resulted from the fact that they used detection tests which was based on least squares residuals prone to the masking effects of multiple bad data.

We summarize their review next:

a) Identification by elimination is a continuation of the traditional bad data detection technique based on the residual vector. A list of candidate bad data is selected first on the basis of a normalized residual vector, then successive cycles of elimination-estimation-detection are performed until the bad data is eliminated. The main drawback of this approach is its high computational load which is not suitable for online implementation.

b) Non-quadratic criteria for bad data detection are part of the state estimation algorithm. Suspected measurements are rejected based on the magnitude of their residuals; the larger the magnitude, the larger was the degree of rejection. The method is simple but exhibits slow convergence or even divergence.

c) Hypothesis Testing Identification (HTI) comprises three steps. First a standard detection test is utilized to detect bad data, then the detected bad data are arranged in decreasing values of normalized residuals. A list of suspected measurements is drawn up and an estimate of the measurements error vector is computed. A threshold is computed on the basis of the variance of the estimated measurements error vector and on a fixed risk factor. The estimated measurements error vector is compared with the threshold value for bad data detection. HTI can detect all bad data in a single step and can even detect

strongly interacting bad data. However, HTI has a higher computation al load that both non-quadratic criteria and identification by elimination.

E. Handschin et al. addressed the problem of detection and identification of bad data and structure error [11]. The solutions of bad data and structure error problems were provided on the basis of residual analysis and a non-quadratic estimation criterion. The tradeoffs between these methods were compared and presented. The comparison helps a designer to decide which combination will fit their particular needs. New bad data analysis techniques were also provided which enables (1) evaluation of bad data spreading effect leading to the concepts of "interacting- non-interacting" bad data and "local redundancy" and (2) calculation of the probability of detecting bad data and false alarm. "Ordered residual search" was presented as an approach for dealing with non-interacting bad data. The weighted residuals were arranged in descending order of magnitude and the measurement with largest residual was removed first. The results of Weighted Least Squares (WLS) estimation with updated measurement vector were passed through the detection schemes. If bad data was still detected, the measurement with the second largest residual was removed, and this process goes on. For dealing with multiple interacting bad data, the method of non-quadratic error criteria was suggested. However, the large number of interacting bad data limited the use of non-quadratic error criteria.

Because of the drawbacks of standard bad data detection techniques and the masking effects of multiple bad data, several researchers have proposed methods for using the existing bad data after rectifying them. Netto et al. developed a robust extended Kalman filter in order to estimate rotor angle and rotor speed of synchronous

generators of a power system [12]. The EKF is able to process the predicted state vector and PMU measurements to track system dynamics faster when batch mode regression form is used. A new Generalized Maximum Likelihood extended Kalman filter (GM-EKF) was developed and was found exhibiting good statistical efficiency under Gaussian process and measurement noises. The use of Huber cost function facilitated in achieving good statistical efficiency of GM-EKF. GM-EKF estimator is capable of bounding the influence of vertical outliers and bad leverage point, which are identified by projection statistics [13]. The state estimation error covariance matrix was derived from covariance matrix of total influence function of GM estimator [14].As a case study, the IEEE 39 bus was used and robust GM-EKF estimator and was found to exhibit good tracking capabilities under Gaussian process and observation noise while suppressing observation outliers.

Gandhi and Mili proposed a new robust Kalman filter, generalized maximum likelihood Kalman filter (GM-KF), that bounds the influence of outliers [16]. A new *structural outlier* was also considered along with outliers in process and observation noises. As a first step of GM-KF, the classical approach of Kalman filter was converted into a batch mode regression form. In this formulation, both observation and innovation outliers are seen as vertical outliers and structural outliers as bad leverage points [15]. Since an M estimator is not robust to bad leverage points, a GM- estimator, which is robust, was used [15-18]. Later, a prewhitening procedure utilizing a robust estimator of location and covariance, such as projection statistics, was considered. Projection statistics uncorrelate the noise when outliers are there in predictions and observations. An iteratively re-weighted least squares algorithm, in which residuals are

standardized utilizing robust weights and scale estimates, was implemented to solve unconstrained optimization in the GM-estimator which yields robust estimates of states suppressing all types of outliers. Finally, the error covariance matrix for GM-KF was derived from an influence function.

Zhao et al. proposed a robust dynamic state estimator that combines historical measurements obtained from SCADA system with PMU and improves the estimation accuracy [19]. A fusion method called fusion measurements based time-variant state transition matrix updating was proposed to incorporate present and historical measurements from SCADA and PMU into the estimation. Results from the method with a new state accuracy based weighting function were incorporated in a new scheme which increases the robustness when the system encounters a sudden and unexpected load change. Three IEEE test systems under normal and dynamic operating conditions were considered to demonstrate the effectiveness of the method.

Shih and Huang proposed a computation algorithm that incorporates an exponential function to increase robustness of dynamic state estimator [20]. An exponential weight function consisting of the absolute residual vector was formulated such that anomaly condition can be taken into account. When any measurement with significant deviation is encountered, the absolute residual vector is increased. The inversion of this vector leads to a small value that helps to suppress the influence of outlier in measurement. On the other hand, if the residual vector is small, the value of the weight function approaches unity and the weight function does not diverge. This method is simple, and easy to implement but enhances the sensitivity and reliability of the state estimation.

1.3 THESIS CONTRIBUTION AND ORGANIZATION

In this thesis, we examine dynamic state estimation for a grid-connected microgrid including two synchronous generators and three loads. We considered state estimation using the EKF, the UKF, the GM-EKF and two robust UKF implementations. The Kalman filters were designed using a sixth order model of the synchronous generator together with a Thevenin equivalent of the remainder of the microgrid. The microgid was simulated using the MATLAB SimPower Toolbox.

For the EKF and UKF, we first present state estimation results for the following scenarios with a sampling frequency of 1 kHz: (1) normal microgrid operation, (2) a three-phase-to-ground fault at the point of common coupling (PCC) (3) loss of generator, (4) loss of load, (5) packet loss or delay, and (6) bad data in the measurements. We then present results for a robust UKF and the GM-EKF for the first four scenarios, with bad data and packet loss or delay, at the phasor measurement unit (PMU) frequency of 50 Hz.

To deal with packet drop and time delay, we propose an approach that utilizes the delayed measurements in state estimation. To deal with bad data, we use the GM-EKF and two robust UKFs. The first robust UKF replaces the bad data with the last uncorrupted measurement while the second replaces the bad data with the predicted measurement. To allow simulation using the lower sampling frequency of 50 Hz, we use a second order Runge-Kutta approximation, whereas the simpler Euler approximation was sufficient at the higher 1 kHz frequency. It was also necessary to use several iterations of the KF predictor between sampling points in scenarios other than normal operation.

We compare the performance of the EKF and the UKF to the performance of robust state estimators. We also compare the GM-EKF to the robust UKFs. As expected, robust filters perform better than the standard EKF and UKF in the presence of bad data. More significantly, both robust UKF estimators perform better that the GM-EKF.

The thesis is organized as follows. Chapter 2 describes the microgrid model under study. Chapter 3 reviews the synchronous generator model. Chapter 4 contains a description of the unscented KalmanFilter (UKF) and the extended Kalman filter (EKF). A brief overview of networked control systems (NCS) is provided in Chapter 5. Chapter 6 discusses robust state estimation using the GM-EKF and the robust UKFs. Simulation results for the microgrid under normal operating conditions and for a variety of abnormal conditions are shown in Chapter 7. Conclusions and future work are presented in Chapter 8.

CHAPTER 2 MICROGRID

2.1 BACKGROUND

In recent years, environmental pollution, air quality and other issues have become increasingly prominent, which have a great relationship with the extensive use of fossil fuels. Coal, oil are non-renewable resources and will be used up by mankind one day. Therefore, to develop and use renewable new clean energy, and convert these clean energy into electrical energy, which can not only increase the diversity of energy use, but is also an inevitable choice to solve the problems of increasing depletion of fossil energy, serious environmental pollution and other issues. The important feature of traditional conventional power grid is that the grids are connected together which is called interconnected grid system. The main advantage of this centralized grid system is enhanced efficiency of energy use. There are some significant drawbacks of a conventional microgrid. These are high costs, operational difficulties, difficulty in meeting user's increasing requirements for safety and reliability [22].

Microgrids are small-scale, LV CHP supply networks designed to supply electrical and heat loads for a small community. Microgrid is essentially an active distribution network because it is the conglomerate of DG systems and different loads at distribution voltage level. The generators or microsources employed in a Microgrid are usually renewable/non-conventional DERs integrated together to generate power at distribution voltage. The microsources must be equipped with power electronic interfaces (PEIs) and controls to maintain the specified power quality and energy output. The control facility allows Microgrid to present itself to the main utility power

system as a single controlled unit that meets local energy needs for reliability and security [23].

The most important differences between a microgrid and a traditional power grid are as follows:

(a) The traditional power grids have much more capacity than that of microgrids.

(b) Power generated at distribution voltage can be directly fed to utility distribution network.

(c) Microgrids are usually installed closed to the customer premises. Therefore, it can reduce line losses significantly.

2.2 HISTORY

The concept of microgrid can be traced back to 2001. In 2001, Professor R.H. Lasseter of the University of Wisconsin-Madison proposed the concept of the "microgrid." Later, the Consortium for Electric Reliability Technology Solutions (CERTS) and the European Commission Project Micro-Grid gave definition of microgrid.

In 2002, the National Technical University of Athens (NTUA) built a microgrid for tests on the control of distributed resources and load with multiagent technology. In 2003, the University of Wisconsin established a small laboratory microgrid (NREL Laboratory Microgrid) with a capacity of 80 kVA, for tests on the control of various types of distributed resources. Multiple demonstration projects were built across the world, including the 7.2 kV microgrid in Mad River Park, Vermont, USA; the 400 V microgrid in Kythnos Islands, Greece; as well as the Aichi, Kyotango, and Hachinohe projects in Japan.In 2004, the CESI RICERCA test facility was built in Milan, Italy for steady-state and transient operation tests and power quality analysis. The Imperial

College London control and power research center was set up in London, UK for distribution network prototype tests in 2005.

In 2006, Tsinghua University began studies on the microgrid and established a laboratory microgrid encompassing DG, ES, and loads utilizing the facilities in the National Key Laboratory on Power System and Generating Equipment Safety Control and Simulation under the Department of Electrical Engineering. In 2008, Tianjin University and Hefei University of Technology conducted tests and studies on the microgrid. Tianjin University studied on the scientific dispatch of energy resources for improving energy efficiency and reliability. Hefei University of Technology focused on operation, control and energy management. In 2010, the State Grid Corporation of China (SGCC) built a demonstration project in Zhengzhou for study on operation control of a microgrid combining distributed PV (photovoltaic) generation and energy storage and engineering application [24]. Several other projects are going on for microgrid around the world.

2.3 BASIC STRUCTURE OF MICROGRID

A basic structure of microgrid is shown in Figure 2.1 [25]. It shows several distributed energy sources such as bio-energy, wind power, photovoltaic (PV), fuel cell, energy storage devices and microturbine are connected together in a microgrid. The microgrid is connected to the power grid. The point of connection is called point of common coupling (PCC). Also, several loads are connected to the microgrid. The microgrid is operated in two modes: (1) grid connected and (2) stand alone. In grid-connected mode, the microgrid remains connected to the main grid either totally or partially, and imports and exports power from or to the main grid. In case of any disturbance in the

main grid, the microgrid switches over to stand alone mode while still feeding power to priority loads.

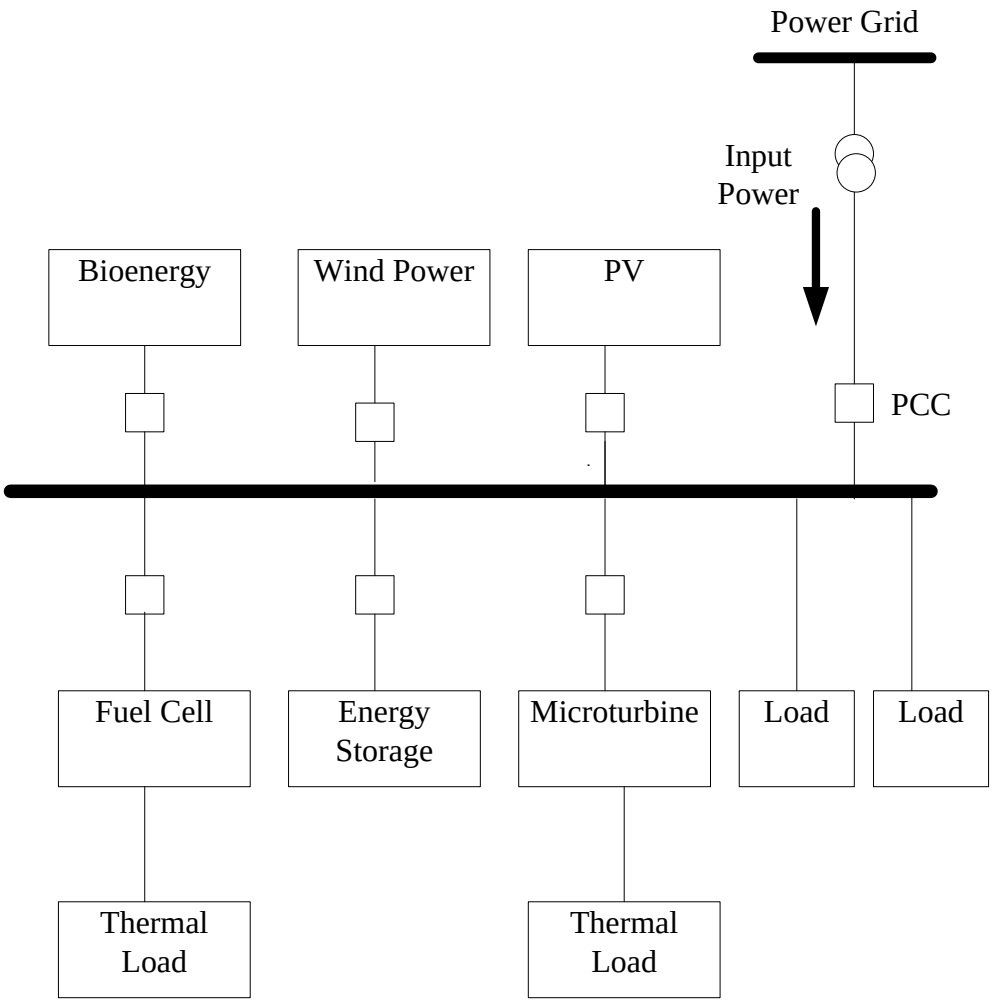

Figure 2.1 Basic structure of microgrid.

2.4 OPERATION AND MANAGEMENT OF MICROGRID

Different modes of operation of microgrid are controlled and coordinated through local microsource controllers (MCs) and central controllers (CCs). Functions of these controllers are described as follows:

(1) Microsource Controller (MC): Microsource controller controls the power flow and voltage profile of microsources independently. It can perform independently from the central controller in case of any disturbance or load changes. It also performs load tracking, economic generation scheduling, demand side management. The prominent function of MC is to respond rapidly to locally monitored voltages and currents without having data from neighboring MCs. This feature leads to the ability of microgrid to perform as play and plug device. This facilitates the addition of other microsources without any disturbance of existing microsource [23].

(2) Central Controller (CC): Central controller performs the task of overall control and protection of microgrid through coordination of MCs. Two important tasks are (i) to maintain specified voltage and frequency at the load end and (ii) to ensure optimization of power for microgrid. It sets the optimal power dispatch and voltage profile for MCs. Energy Management Module (EMM) and Protection Coordination Module (PCM) are among the crucial functional modules of CC. EMM works for the optimization of power in microgrid. PCM responds to microgrid and main grid faults and loss of grids in such a way so that it can ensure protection coordination of microgrid. It can adapt to changing fault currents from grid connected to stand alone mode of operation. Proper communication between PCM and MCs are required for performing this task. In case of any major faults, the PCM switches the microgrid to stand-alone mode of operation. However for minor faults, PCM may allow the microgrid to stay connected to the main grid for a short time. PCM will disconnect microgrid if it feels that the fault in main grid will endanger microgrid. In one word we can say that central controller ensures

synchronized operation with the main grid maintaining the power exchange at priory contract points [23].

2.5 TECHNICAL AND ECONOMICAL ADVANTAGES AND DISADVANTAGES OF MICROGRID

(1) Environmental Issues: Microgrids would have much less environmental impact than the large conventional power stations. Close control of combustion process results in reduced gaseous and particulate emissions.

(2) Investment Issues: The reduction of physical and electrical distance between microsource and loads contributes enhanced voltage profile. The feeder congestion and line losses are also reduced.

(3) Power Quality: Power quality and reliability are improved due to decentralization of supply, matched supply and demand, and reduced transmission and distribution outages.

(4) Cost Saving: A prominent amount of cost saving comes from utilization of heat coming from the CHP mode of operation in microgrid. Savings of costs come from reduced transmission and distribution of the power system.

(5) Vast use of plug and play microsources may contribute to reduced price of energy in power market.

2.6 CHALLENGES FACED BY MICROGRID

In spite of several prominent advantages of microgrid, there are a number of challenges a microgrid faces. These challenges can be seen from the technical and economical point of view. Some of the salient challenges are described as follows.

(1) The installation cost of a microgrid is very high.

(2) Implementing microgrid in reality requires a lot of technical expertise. Lots of research are going on for proper management and control of microsources.

(3) As a power system, microgrid is comparatively very new idea. Therefore, it suffers from absence of standardizations.

(4) There is a lack of synchronization for price of energy between microgrid and main power grid.

Several challenges will be always there with a new technology. However, lots of research are going on for solving the problems faced by microgrid.

2.7 PROFILE OF MICROGRID UNDER STUDY

We simulate a microgrid model which includes two generators, loads, lines and feeders, and connection to the power grid. We model the microgrid using the MATLAB SimPower toolbox. The model is composed of a 13.8 kV distribution subsystem which is connected to the power grid through a 69 kV radial line. The power grid is represented as a 69 kV, 1000 MVA capacity bus. DG1 is a synchronous generator having rating of 5 MVA 13.8 kV. DG2 is also a synchronous generator having rating of 1.5 MVA 13.8 kV [62].

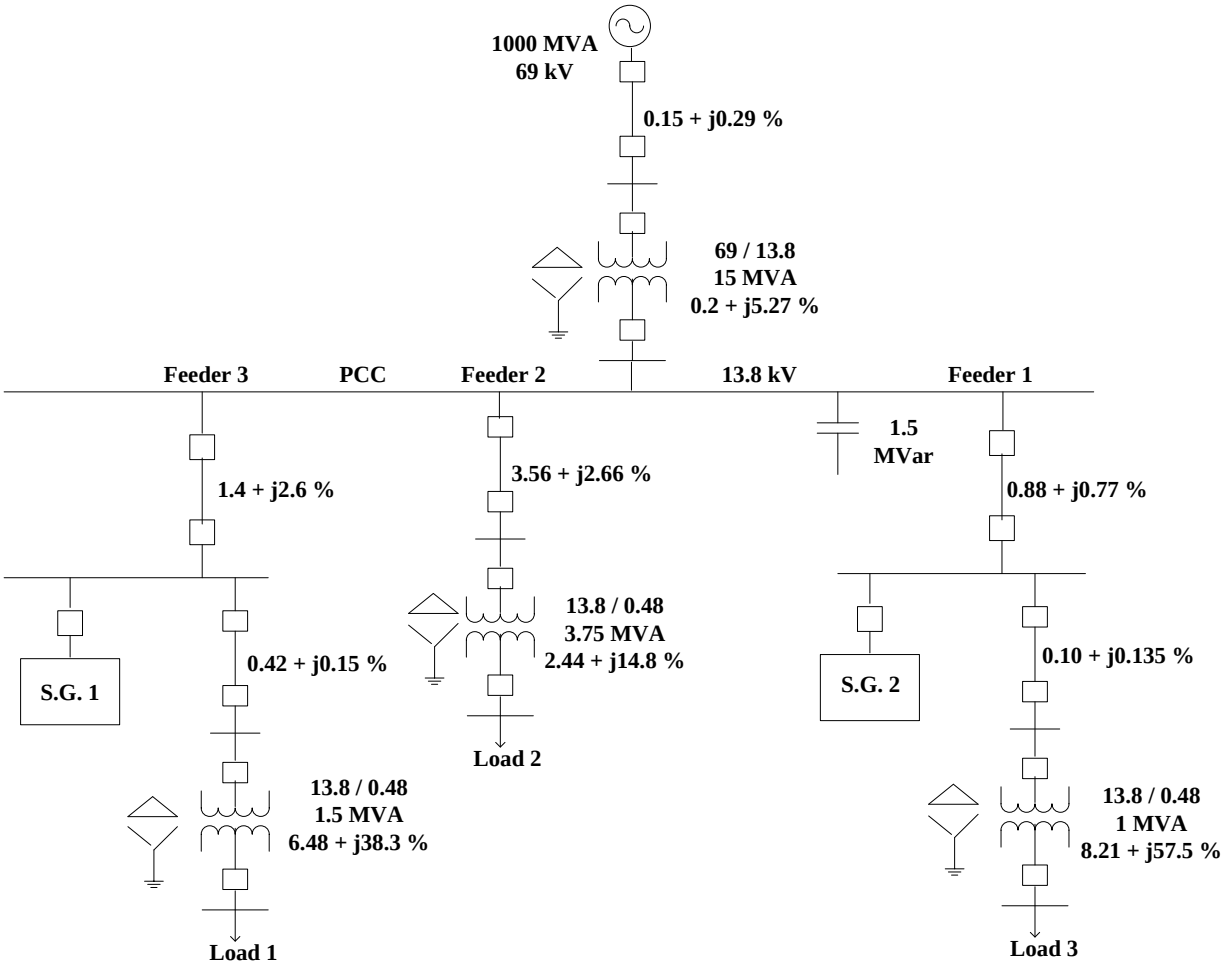

Figure 2.2 Single-line diagram of microgrid under study.

Profile of microgrid shown in Figure 2.2:

S.G.1: 5 MVA/ 13.8 kV

S.G.2: 1.5 MVA/ 13.8 kV

Load 1: 1.8 MW/1.82 MVAR

Load 2: 2.31 MW/1.49 MVAR

Load 3: 0.6 MW/0.3 MVAR

CHAPTER 3 SYNCHRONOUS MACHINE

3.1 SYNCHRONOUS GENERATOR BASICS

A synchronous generator is an electrical machine used to convert mechanical energy to electrical energy. The key principle in the operation of the synchronous generator is magnetic induction which is described by Faraday's Law. Faraday's Law states that a changing (or rotating) magnetic field will induce current to flow in a nearby conductor [26].

The main components of a generator are the stator (stationary) and the rotor (rotating) as shown in Figure 3.1. The rotor contains an electromagnet or field winding which produces the main magnetic field of the machine. The rotor rotates within the stator and induces current in the stator windings. The stator is a stationary part that contains the stator or armature windings and encases the rotor. Stator windings consists of three output phases of the machine and are embedded in the inner stator wall in slots. For a three-phase machine, the stator consists of three identical windings. The windings are separated by 120^{o}apart and are assumed to be sinusoidally distributed around the stator perimeter. This arrangement ensures that the induced voltages on the phase outputs produce a balanced, three-phase voltage set [26].

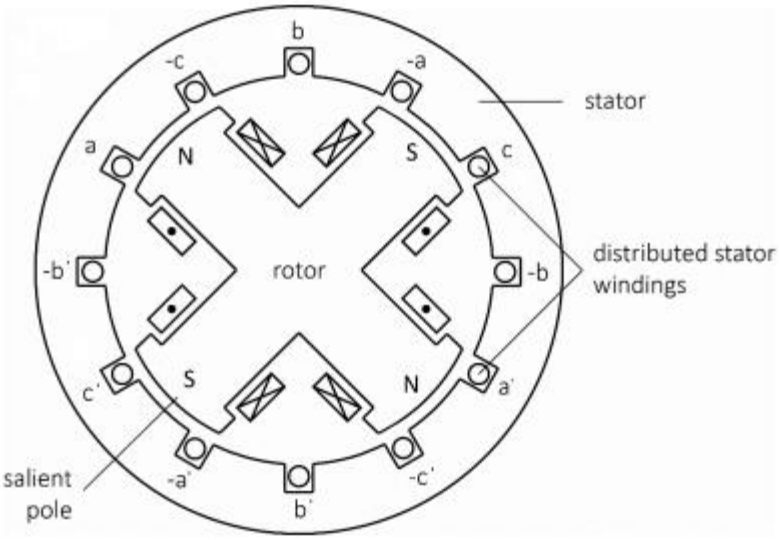

Figure 3.1 4 pole 3 phase synchronous generator.

The rotor consists of electromagnetic coils which are energized by a voltage to generate the main magnetic field of the machine. The synchronous machine studied herein is a four pole salient-rotor design. This means that there are four windings corresponding to the opposing poles of two electromagnets and are evenly spaced around the rotor perimeter. Such a design consists of a rotor shape which resembles a cross where each pole is wrapped on a core extending from the center. The ends of the poles have curved “shoes” which are for allowing a suitable air gap at the poles. Damper windings are shorted windings in the rotor. They serve to improve the response and stability of the machine by creating induced currents providing machine synchronization. While machine operates at steady state, the damper windings have no induced current [27].

For many synchronous machines, excitation voltage comes from another, usually small, generator. When the main generator rotates, an AC voltage is induced which is

converted by a rotating rectifier into a DC voltage. This DC voltage is used for field excitation, which is known as brushless exciter [27].

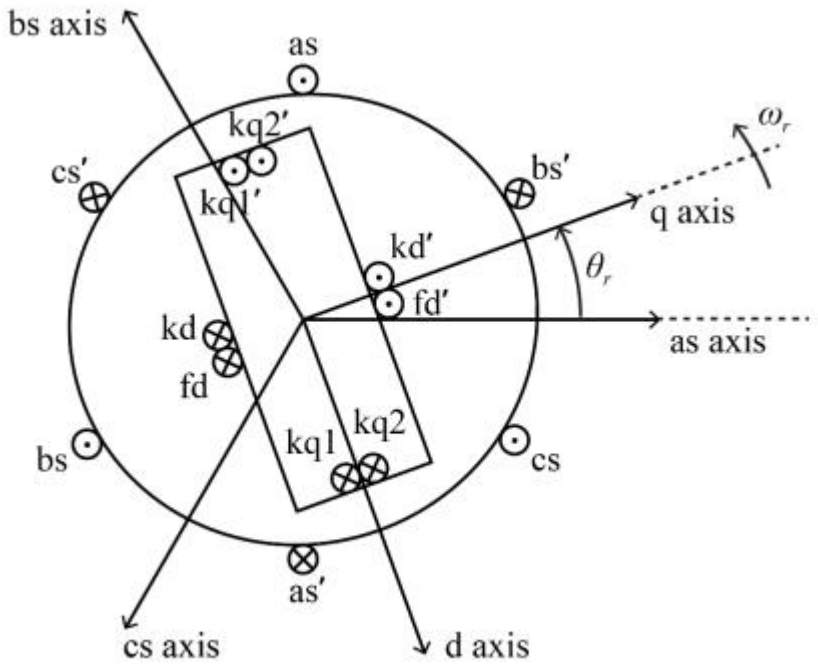

Figure 3.2 Two pole synchronous generator winding and construction.

3.2.1 SYNCHRONOUS GENERATOR MODELLING

The synchronous machine considered in this thesis is shown in Figure 3.3. The structure contains three stator windings and four rotor windings including a field winding$f$. Three damper coils are shown in Figure 3.3. Damper coil h is along the d axis, while g and k are along the q axis. The number of damper coils may vary from zero to five or seven but usually three damper coils are used [28].

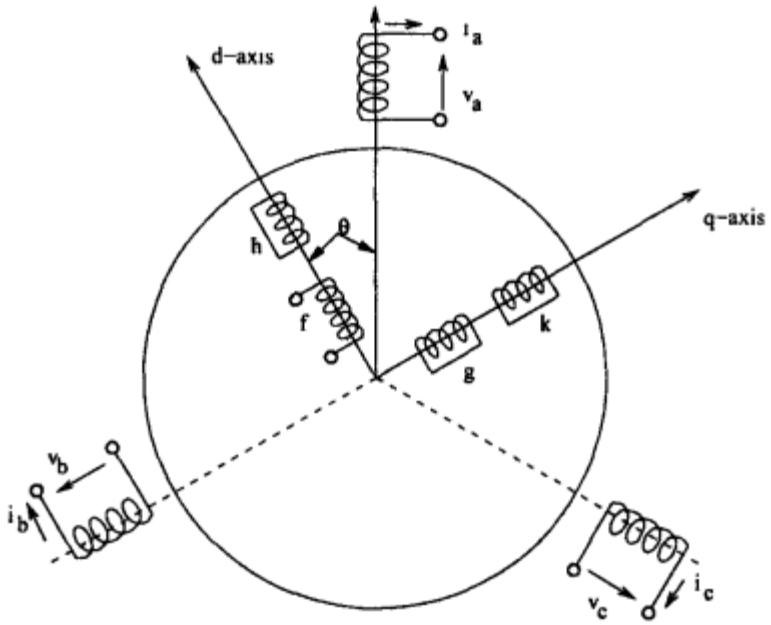

Figure 3.3 Synchronous machine.

3.2.2 FLUX LINKAGE EQUATIONS

The derivation of the synchronous generator model is described as follows [28]. The stator and rotor flux linkages are given by

$$\psi_s = L_{ss} i_s + L_{sr} i_r \tag{3.1}$$

$$\psi_r = L_{rs} i_s + L_{rr} i_r \tag{3.2}$$

where

$i_s = [i_a i_b i_c]^T$

$\psi_s = [\psi_a \psi_b \psi_c]^T$

$i_r = \left[i_f i_h i_g i_k\right]^T$

$\psi_r = \left[\psi_f \psi_h \psi_g \psi_k\right]^T$

Matrices L_{ss} and L_{rr} are symmetric and $L_{sr} = L_{rs}^T$.

From two reaction theory, the inductance coefficients are

$$L_{ss} = \begin{bmatrix} L_{aao} & L_{abo} & L_{abo} \\ L_{abo} & L_{aao} & L_{abo} \\ L_{abo} & L_{abo} & L_{aao} \end{bmatrix} + L_{aa2} \begin{bmatrix} \cos 2\theta & \cos\left(2\theta - \frac{2\pi}{3}\right) & \cos\left(2\theta + \frac{2\pi}{3}\right) \\ \cos\left(2\theta - \frac{2\pi}{3}\right) & \cos\left(2\theta + \frac{2\pi}{3}\right) & \cos 2\theta \\ \cos\left(2\theta + \frac{2\pi}{3}\right) & \cos 2\theta & \cos\left(2\theta - \frac{2\pi}{3}\right) \end{bmatrix}$$

(3.3)

$$L_{rr} = \begin{bmatrix} L_f & L_{fh} & 0 & 0 \\ L_{fh} & L_h & 0 & 0 \\ 0 & 0 & L_g & L_{gk} \\ 0 & 0 & L_{gk} & L_k \end{bmatrix} \tag{3.4}$$

$$L_{sr} = \begin{bmatrix} M_{af}cos\theta & M_{ah}cos\theta & M_{ag}sin\theta & M_{ak}sin\theta \\ M_{af}\cos\left(\theta - \frac{2\pi}{3}\right) & M_{ah}\cos\left(\theta - \frac{2\pi}{3}\right) & M_{ag}\sin\left(\theta - \frac{2\pi}{3}\right) & M_{ak}\sin\left(\theta - \frac{2\pi}{3}\right) \\ M_{af}\cos\left(\theta + \frac{2\pi}{3}\right) & M_{ah}\cos\left(\theta + \frac{2\pi}{3}\right) & M_{ag}\sin\left(\theta + \frac{2\pi}{3}\right) & M_{ak}\sin\left(\theta + \frac{2\pi}{3}\right) \end{bmatrix}$$

(3.5)

3.2.3 VOLTAGE EQUATIONS

The stator and rotor voltages and currents equations can be written in terms of the flux as [28].

$$-\frac{d\psi_s}{dt} - R_s i_s = v_s \tag{3.6}$$

$$-\frac{d\psi_r}{dt} - R_r i_r = v_r \tag{3.7}$$

where

$v_s = [v_a v_b v_c]^T$

$v_r = \left[-v_f\ 0\ 0\ 0\right]^T$

$$R_s = \begin{bmatrix} R_a & 0 & 0 \\ 0 & R_a & 0 \\ 0 & 0 & R_a \end{bmatrix}$$

$$R_r = \begin{bmatrix} R_f & 0 & 0 & 0 \\ 0 & R_h & 0 & 0 \\ 0 & 0 & R_g & 0 \\ 0 & 0 & 0 & R_k \end{bmatrix}$$

Combining the voltage equations gives

$$\frac{d\psi}{dt} = -RL^{-1}\psi - v \tag{3.8}$$

$$i = L^{-1}\psi \tag{3.9}$$

where

$$L = \begin{bmatrix} L_{ss} & L_{sr} \\ L_{rs} & L_{rr} \end{bmatrix}$$

$$R = \begin{bmatrix} R_s & 0 \\ 0 & R_r \end{bmatrix}$$

$$\psi^T = [\psi_s^T \psi_r^T] i^T = [i_s^T i_r^T]$$

$$v^T = [v_s^T v_r^T]$$

Similarly, the current equations can be expressed as

$$\frac{di}{dt} = L^{-1}\left[-Ri - \frac{d\theta}{dt}\left[\frac{\partial L}{\partial \theta}\right] i - v\right] \tag{3.10}$$

$$\psi = Li \tag{3.11}$$

3.2.4 PARK TRANSFORMATION

The equations that describe the variables and inductances of a synchronous machine are quite complex and include time-varying quantities. Several formulations have been developed in order to simplify these equations. The rotor reference frame transformation is one of them. It is a transformation that changes the variables from the stator components of a synchronous machine to components of virtual windings rotating within the rotor. This transformation eliminates all time-varying inductances from the voltage equations of the machine. Both stator and rotor windings rotate;

therefore, there is no dependence on the rotor angular displacement in the machine inductances.

The rotor reference frame theory was developed in the 1920's by R.H. Park [29]. The theory provided a very strong tool that revolutionized electric machine analysis. Later, other researchers developed new variations on reference frame theory. Park's transformation is in fact a specific case of a general transformation. It refers machine variables to a reference frame rotating at an arbitrary angular velocity [27]. The general transformation is described by

$$f_{dq0s} = C_p^{-1} f_{abcs} \tag{3.12}$$

$$C_p^{-1} = \frac{2}{3}\begin{bmatrix} \cos(\theta) & \cos\left(\theta - \frac{2\pi}{3}\right) & \cos\left(\theta + \frac{2\pi}{3}\right) \\ \sin(\theta) & \sin\left(\theta - \frac{2\pi}{3}\right) & \sin\left(\theta + \frac{2\pi}{3}\right) \\ \frac{1}{2} & \frac{1}{2} & \frac{1}{2} \end{bmatrix} \tag{3.13}$$

$$f_{dq0s} = \left[f_{ds} f_{qs} f_{0s}\right]^T \tag{3.14}$$

$$f_{abcs} = [f_{as} f_{bs} f_{cs}]^T \tag{3.15}$$

$$\omega = \frac{d\theta}{dt} \tag{3.16}$$

For this transformation, f stands for either voltage, current, flux linkage, or electric charge. The angular position $\theta$is continuously differentiable. It can take any value including zero.

Although the transformed variables with *q*, *d*, and 0 subscripts are not physical variables, the variables and their interrelation can be visualized as in Figure 3.4.

The variables f_{as}, $f_{bs}$and f_{cs} are displaced by 120^o apart and therefore form a balanced set. In addition, the variablesf_{qs} and f_{ds} are orthogonal and rotates at an

angular velocity of ω. The variables, *a*, *b*, and *c* can be interpreted as the direction of the magnetic axes of the stator windings while the transformed *q* and *d* components can be interpreted as the transformed or rotor-referred magnetic axes.

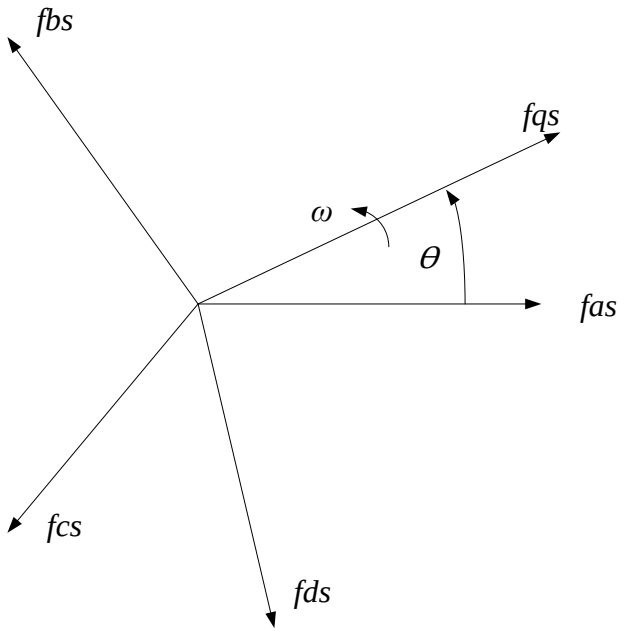

Figure 3.4 General reference frame representation.

3.2.5 TRANSFORMATION OF FLUX LINKAGES

Consider the transformation of flux linkage in the form [28].

$$\begin{bmatrix}\psi_s\\ \psi_r\end{bmatrix} = \begin{bmatrix}C_p & \mathbf{0}\\ \mathbf{0} & U_4\end{bmatrix}\begin{bmatrix}\psi_{dq0}\\ \psi_r\end{bmatrix} \tag{3.17}$$

where

$U_4$is a unit matrix of order 4, and $\psi_{dq0} = \left[\psi_d \psi_q \psi_0\right]^T$

Again, we have

$$\begin{bmatrix}\psi_s\\ \psi_r\end{bmatrix} = \begin{bmatrix}L_{ss} & L_{sr}\\ L_{rs} & L_{rr}\end{bmatrix}\begin{bmatrix}C_p & \mathbf{0}\\ \mathbf{0} & U_4\end{bmatrix}\begin{bmatrix}i_{dq0}\\ i_r\end{bmatrix} \tag{3.18}$$

where

$$i_{dq0} = \left[i_d i_q i_0\right]^T$$

Substituting Equation (3.18) into Equation (3.17) we obtain

$$\begin{bmatrix}\psi_{dq0}\\ \psi_r\end{bmatrix} = \begin{bmatrix}C_p^{-1} & \mathbf{0}\\ \mathbf{0} & U_4\end{bmatrix}\begin{bmatrix}L_{ss} & L_{sr}\\ L_{rs} & L_{rr}\end{bmatrix}\begin{bmatrix}C_p & \mathbf{0}\\ \mathbf{0} & U_4\end{bmatrix}\begin{bmatrix}i_{dq0}\\ i_r\end{bmatrix}$$

$$= \begin{bmatrix}C_p^{-1}L_{ss}C_p & C_p^{-1}L_{sr}\\ L_{rs}C_p & L_{rr}\end{bmatrix}\begin{bmatrix}i_{dq0}\\ i_r\end{bmatrix}$$

$$= \begin{bmatrix}L'_{ss} & L'_{sr}\\ L'_{rs} & L'_{rr}\end{bmatrix}\begin{bmatrix}i_{dq0}\\ i_r\end{bmatrix}$$

where

$$L'_{ss} = \begin{bmatrix}L_d & 0 & 0\\ 0 & L_q & 0\\ 0 & 0 & L_0\end{bmatrix}$$

$$L_d = L_{aa0} - L_{ab0} + \frac{3}{2}L_{aa2}$$

$$L_d = L_{aa0} - L_{ab0} - \frac{3}{2}L_{aa2}$$

$$L_0 = L_{aa0} + 2L_{ab0}$$

$$L'_{rs} = \begin{bmatrix}\frac{3}{2}M_{af}K_d & 0 & 0\\ \frac{3}{2}M_{af}K_d & 0 & 0\\ 0 & \frac{3}{2}M_{af}K_q & 0\\ 0 & \frac{3}{2}M_{ak}K_q & 0\end{bmatrix}$$

3.2.6 TRANSFORMATION OF VOLTAGES

Applying Park's transformation Equation (3.6) can be written as [28].

$$-\frac{d}{dt}\left[C_p\psi_{dq0}\right] - R_s C_p i_{dq0} = C_p v_{dq0} \tag{3.19}$$

Again we have

$$-\frac{d}{dt}\left[C_p\psi_{dq0}\right] = -\frac{\dot{\theta}dC_p}{d\theta}\psi_{dq0} - C_p\frac{d}{dt}\psi_{dq0} \tag{3.20}$$

where

$$\frac{dC_p}{d\theta} = C_p P_1$$

and $P_1 = \begin{bmatrix} 0 & \frac{k_q}{k_d} & 0 \\ -\frac{k_d}{k_q} & 0 & 0 \\ 0 & 0 & 0 \end{bmatrix}$

Substituting Equation (3.20) into Equation (3.19) we obtain

$$-C_p\frac{d\psi_{dq0}}{dt} - \dot{\theta}C_pP_1\psi_{dq0} - R_sC_pi_{dq0} = C_pv_{dq0} \tag{3.21}$$

$$-\frac{d\psi_{dq0}}{dt} - \dot{\theta}P_1\psi_{dq0} - C_p^{-1}R_sC_pi_{dq0} = v_{dq0}$$

$$-\frac{d\psi_{dq0}}{dt} - \dot{\theta}P_1\psi_{dq0} - R_ai_{dq0} = v_{dq0} \tag{3.22}$$

Eq. (3.22) can be rewritten in the form

$$-\frac{d\psi_d}{dt} - \dot{\theta}\frac{k_q}{k_d}\psi_q - R_ai_d = v_d \tag{3.23}$$

$$-\frac{d\psi_q}{dt} - \dot{\theta}\frac{k_d}{k_q}\psi_d - R_ai_q = v_q \tag{3.24}$$

$$-\frac{d\psi_0}{dt} - R_ai_0 = v_0 \tag{3.25}$$

Similarly rotor voltage equations can be rewritten as

$$\frac{d\psi_f}{dt} + R_fi_f = v_f \tag{3.26}$$

$$\frac{d\psi_h}{dt} + R_hi_h = 0 \tag{3.27}$$

$$\frac{d\psi_g}{dt} + R_gi_g = 0 \tag{3.28}$$

$$\frac{d\psi_k}{dt} + R_ki_k = 0 \tag{3.29}$$

The synchronous generator model is represented by Equations (3.23-3.29).

3.3 MATLAB SIMULINK SYNCHRONOUS GENERATOR

The fundamental components of a synchronous machine is shown in Figure 3.5 [30].The synchronous machine operates either in generator or motor mode. The operating mode is determined by the sign of the mechanical power, which is positive for generator mode and negative for motor mode. The electrical part of the machine is represented by a sixth-order state-space model. The model considers the dynamics of the stator, field, and damper windings. The equivalent circuit of the model is represented in the rotor reference frame (d-q frame). All rotor parameters and electrical quantities are viewed from the stator and are identified by primed variables as in Figure 3.6. The subscripts are defined as follows:

d, q: d and q axis variable

R,s: rotor and stator variable

l,m: leakage and magnetizing inductance

f,k: field and damper winding quantity

The electrical model is presented in Figure 3.6 [30]. The associated mathematical model is in the form

$$V_d = R_s i_d + \frac{d}{dt}\varphi_d - \omega_R \varphi_q \tag{3.30}$$

$$V_q = R_s i_q + \frac{d}{dt}\varphi_q + \omega_R \varphi_d \tag{3.31}$$

$$V'_{fd} = R'_{fd} i'_{fd} + \frac{d}{dt}\varphi'_{fd} \tag{3.32}$$

$$V'_{kd} = R'_{kd} i'_{kd} + \frac{d}{dt}\varphi'_{kd} \tag{3.33}$$

$$V'_{kq1} = R'_{kq1} i'_{kq1} + \frac{d}{dt}\varphi'_{kq1} \tag{3.34}$$

$$V'_{kq2} = R'_{kq2} i'_{kq2} + \frac{d}{dt}\varphi'_{kq2} \tag{3.35}$$

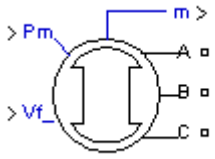

Figure3.5. Fundamental block of synchronous machine.

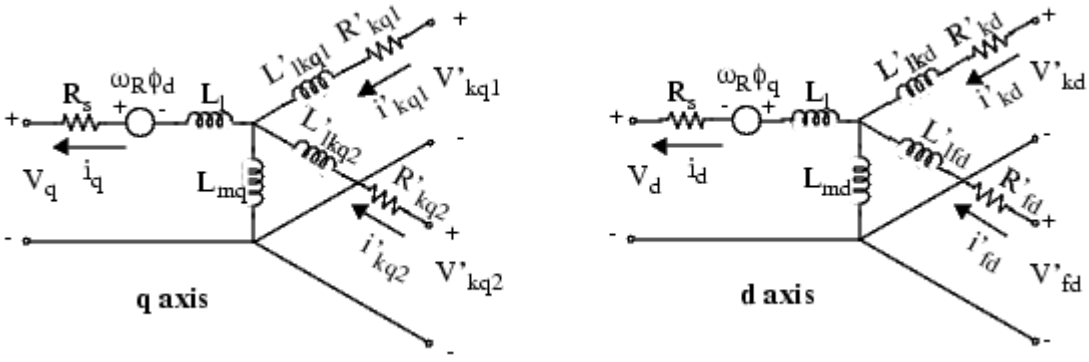

Figure 3.6 Electrical model of synchronous generator.

The sixth order state space model is presented by Equations (3.30-3.35). The popular mathematical model of synchronous generator is derived from the flux model, and is described in Section 3.2 and Section 3.3 in [31]. We have the model as follows:

$$\dot{x}_1 = \omega_o x_2$$

$$\dot{x}_2 = \frac{1}{J}[u_1 - T_e - Dx_2]$$

$$\dot{x}_3 = \frac{1}{T'_{do}}\left[u_2 - x_3 - (x_d - x'_d)\left\{i_d - \frac{x'_d - x''_d}{(x'_d - x_{ls})^2}(x_5 + (x'_d - x_{ls})i_d - x_3)\right\}\right]$$

$$\dot{x}_4 = \frac{1}{T'_{qo}}\left[-x_4 + (x_q - x'_q)\left\{i_q - \frac{x'_q - x''_q}{(x'_q - x_{ls})^2}(x_6 + (x'_q - x_{ls})i_q + x_4)\right\}\right]$$

$$\dot{x}_5 = \frac{1}{T''_{do}}[-x_5 + x_3 - (x'_d - x_{ls})i_d]$$

$$\dot{x}_6 = \frac{1}{T''_{qo}}[-x_6 - x_4 - (x'_q - x_{ls})i_q]$$

where the state variables are defined as:

x_1 = Rotor angle, x_2 = Rotor speed deviant, x_3 = q-axis transient voltage, x_4 = d-axis transient voltage, x_5 = d-axis damper flux, x_6 = q-axis second damper flux. The inputs are defined as $[u_1 u_2]^T = \left[T_m E_{fd}\right]^T$, where, T_m = mechanical torque, and E_{fd} = field voltage.

For the case of generator connected to infinite bus through an electrical network, as discussed in Section 6.3, in [28], in Section II in [32], we obtain that d-axis and q-axis currents of synchronous generator can be written as

$$i_d = \frac{e'_q - v_b \cos\delta}{x_{td}}, i_q = \frac{v_b \sin\delta}{x_{tq}}$$

where, $e'_q = x_3, \delta = x_1, x_{td} = x'_d + x_e, x_{tq} = x'_q + x_e$

x_e = Thevenin's equivalent reactance of the network from generator to infinite bus.

Substituting the values of i_d, i_q in sixth order state space model, we have

$$\dot{x}_1 = \omega_o x_2$$

$$\dot{x}_2 = \frac{1}{J}\left[u_1 - \left(\frac{v_b}{x_{td}} x_3 \sin x_1 + \frac{v_b^2}{2}\left(\frac{1}{x_{tq}} - \frac{1}{x_{td}}\right)\sin 2x_1\right) - D x_2\right]$$

$$\dot{x}_3 = \frac{1}{T'_{do}}\left[u_2 - x_3 - (x_d - x'_d)\left\{\frac{x_3 - v_b \cos x_1}{x_{td}} - \frac{x'_d - x''_d}{(x'_d - x_{ls})^2}\left(x_5 + (x'_d - x_{ls})\frac{x_3 - v_b \cos x_1}{x_{td}} - x_3\right)\right\}\right]$$

$$\dot{x}_4 = \frac{1}{T'_{qo}}\left[-x_4 + (x_q - x'_q)\left\{\frac{v_b}{x_{tq}} sin\, x_1 - \frac{x'_q - x''_q}{\left(x'_q - x_{ls}\right)^2}\left(x_6 + \left(x'_q - x_{ls}\right)\frac{v_b}{x_{tq}} sin\, x_1 + x_4\right)\right\}\right]$$

$$\dot{x}_5 = \frac{1}{T''_{do}}\left[-x_5 + x_3 - (x'_d - x_{ls})\frac{x_3 - v_b\, cos\, x_1}{x_{td}}\right]$$

$$\dot{x}_6 = \frac{1}{T''_{qo}}\left[-x_6 - x_4 - \left(x'_q - x_{ls}\right)\frac{v_b}{x_{tq}} sin\, x_1\right]$$

3.4 STATE SPACE MODEL OF THE SYSTEM

The sixth order state space model of the system is given below.

$$\boldsymbol{x} = \left[\delta\ \Delta\omega\ e'_q e'_d \psi_{1d} \psi_{2q}\right]^T = [x_1 x_2 x_3 x_4 x_5 x_6]^T$$

$$\boldsymbol{u} = \left[T_m E_{fd}\right]^T$$

where, $\omega_o = 2\pi f_o$is the nominal synchronous speed (elec. rad/s), $\omega$is the rotor speed (pu), $T_m$the mechanical input torque (pu), T_e the air-gap torque or electrical output torque (pu), $E_{fd}$is the exciter output voltage or the field voltage as seen from the armature (pu) and $\delta$is the rotor angle in (electrical radian), $\Delta\omega$, rotor speed deviation, e'_q, the q-axis component of the transient voltage, e'_d, the d-axis component of the transient voltage, ψ_{1d}, d axis damper winding flux, ψ_{2q}, q axis second damper winding flux.

The sixth-order nonlinear synchronous machine state space model is rewritten below in a form suitable for state estimation:

$$\dot{x}_1 = \omega_o x_2$$

$$\dot{x}_2 = \frac{1}{J}\left[u_1 - \left(\frac{v_b}{x_{td}} x_3\, sin\, x_1 + \frac{v_b^2}{2}\left(\frac{1}{x_{tq}} - \frac{1}{x_{td}}\right) sin\, 2x_1\ \right) - D x_2\right]$$

$$\dot{x}_3 = \frac{1}{T'_{do}}\left[u_2 - x_3 - (x_d - x'_d)\left\{\frac{x_3 - v_b \cos x_1}{x_{td}} - \frac{x'_d - x''_d}{(x'_d - x_{ls})^2}\left(x_5 + (x'_d - x_{ls})\frac{x_3 - v_b \cos x_1}{x_{td}} - x_3\right)\right\}\right]$$

$$\dot{x}_4 = \frac{1}{T'_{qo}}\left[-x_4 + (x_q - x'_q)\left\{\frac{v_b}{x_{tq}} sin\, x_1 - \frac{x'_q - x''_q}{\left(x'_q - x_{ls}\right)^2}\left(x_6 + \left(x'_q - x_{ls}\right)\frac{v_b}{x_{tq}} sin\, x_1 + x_4\right)\right\}\right]$$

$$\dot{x}_5 = \frac{1}{T''_{do}}\left[-x_5 + x_3 - (x'_d - x_{ls})\frac{1}{x_{td}}(x_3 - v_b cos x_1)\right]$$

$$\dot{x}_6 = \frac{1}{T''_{qo}}\left[-x_6 - x_4 - \left(x'_q - x_{ls}\right)\frac{1}{x_{tq}} v_b sin\, x_1\right]$$

$$y_1 = \frac{v_b}{x_{td}} x_3\, sin\, x_1 + \frac{v_b^2}{2}\left(\frac{1}{x_{tq}} - \frac{1}{x_{td}}\right) sin\, 2x_1$$

$$y_2 = \frac{v_b}{x_{td}} x_3 \cos x_1 - v_b^2\left(\frac{\sin^2 x_1}{x_{tq}} + \frac{\cos^2 x_1}{x_{td}}\right) - 2x_e I_t^2$$

The active and reactive power $y_1 = P_t$and $y_2 = Q_t$as the two measurable system outputs are provided in References [3-4].

We obtained the active and reactive powers of synchronous generator 1 (DG1) from the MATLAB SimPower model. The parameters shown in the state space model are divided into two parts: generator parameters and power system network's parameters including line impedances. We calculated these parameters from our original microgrid model and obtained the synchronous generator's parameters from the Simulink block. The variables and constants of generator 1 are shown in *Table IX* in Appendix.

CHAPTER 4 EXTENDED KALMAN FILTER AND UNSCENTED KALMAN FILTER

4.1 EXTENDED KALMAN FILTER

The Kalman filter (KF) is an optimal recursive state estimator. It estimates the state of a discrete-time controlled process that is governed by a linear stochastic difference equations. The Extended Kalman filter (EKF) can be used to handle nonlinear systems by linearizing about the current mean state estimate.

A general nonlinear stochastic differential equation and measurement equation is in the following form [33].

$$\dot{\boldsymbol{x}} = \boldsymbol{f}(\boldsymbol{x}, t) + \boldsymbol{u}(t)$$

$$\boldsymbol{z} = \boldsymbol{h}(\boldsymbol{x}, t) + \boldsymbol{v}(t) \tag{4.1}$$

$\boldsymbol{u}(t)$ and $\boldsymbol{v}(t)$are both zero-mean white noise sequences and are mutually independent. The nonlinear equations lead to the discrete-time approximation:

$$\boldsymbol{x}_{k+1} = \boldsymbol{f}(\boldsymbol{x}_k, k) + \boldsymbol{w}_k$$

$$\boldsymbol{z}_{\boldsymbol{k}} = \boldsymbol{h}(\boldsymbol{x}_{\boldsymbol{k}}, \boldsymbol{k}) + \boldsymbol{v}_{\boldsymbol{k}} \tag{4.2}$$

where $\boldsymbol{x}_{k+1}$represents state vector, $\boldsymbol{f}$ is the nonlinear function of the states and inputs, $\boldsymbol{z}_k$is the measurement vector, $\boldsymbol{w}_k$ and $\boldsymbol{v}_{\boldsymbol{k}}$ are the process and measurement noise vectors, Q_k and R_k are the process and measurement noise covariance matrices, and k is the time step of the discrete model. The EKF can be applied to a nonlinear system through the following steps [33, 34]:

Step 1: Initialize the state vector and error covariance matrix.

Step 2: Compute the Kalman gain matrix from the error covariance and estimated measurement noise covariance.

$$K_k = P_k^- H_k^T (H_k P_k^- H_k^T + R_k)^{-1} \quad (4.3)$$

Step 3: Multiply the prediction error vector by the Kalman gain matrix to get state correction vector and update state vector.

$$\hat{\boldsymbol{x}}_{\mathrm{k}} = \hat{\boldsymbol{x}}_{\mathbf{k}}^- + K_k[\boldsymbol{z}_k - \boldsymbol{h}(x_k^-, k)] \quad (4.4)$$

Step 4: Update the error covarinace.

$$P_k = P_k^- (I - K_k H_k) \quad (4.5)$$

Step 5: Predict the new state vector and state covariance matrix.

$$\hat{\boldsymbol{x}}_{k+1}^- = \boldsymbol{f}(\boldsymbol{x}_k^+, k) \quad (4.6)$$

$$P_{\mathrm{k+1}}^- = F_k P_k F_k^T + Q_k \quad (4.7)$$

Linear approximation equations of system and measurement matrices are obtained through the Jacobians

$$F_{\boldsymbol{k}} = \frac{\partial \boldsymbol{f}_k}{\partial \boldsymbol{x}}, H_k = \frac{\partial \boldsymbol{h}_k}{\partial \boldsymbol{x}} \quad (4.8)$$

Because the EKF linearizes the system equations around each state estimate, it cannot capture the system nonlinearity and is a suboptimal filter [35].

4.2 GRADIENT CALCULATION

This section presents the Jacobians $F_k$and H_k for the synchronous generator and the linear approximation they provide. A simple discrete-time approximation of the model (4.1) is given by

$$\boldsymbol{x}(k) = \Delta t \times \boldsymbol{f}(\boldsymbol{x}(k-1), k-1) + \boldsymbol{x}(k-1) + \boldsymbol{w}(k-1) \quad (4.9)$$

The Jacobian $F_k = \left[f_{ij}(k)\right]$ is

$$F_k = [f_{ij}(k)] = \begin{bmatrix} 1 & \omega_0 \Delta t & 0 & 0 & 0 & 0 \\ f_{21} & f_{22} & f_{23} & 0 & 0 & 0 \\ f_{31} & 0 & f_{33} & 0 & f_{35} & 0 \\ f_{41} & 0 & 0 & f_{44} & 0 & f_{46} \\ f_{51} & 0 & f_{53} & 0 & f_{55} & 0 \\ f_{61} & 0 & 0 & f_{64} & 0 & f_{66} \end{bmatrix}$$

$$f_{21} = -\frac{\Delta t}{J}\left[\frac{v_b \times x_3}{x_{td}}\cos(x_1) + v_b^2\left(\frac{1}{x_{tq}} - \frac{1}{x_{td}}\right)\cos(2x_1)\right]$$

$$f_{22} = -\frac{\Delta t}{J} \times D + 1$$

$$f_{23} = -\frac{\Delta t}{J} \times \frac{v_b}{x_{td}}\sin(x_1)$$

$$f_{31} = \frac{\Delta t}{T'_{do}}\left[-(x_d - x'_d)\left(\frac{V_b}{x_{td}}\sin(\mathrm{x}_1) - \frac{\mathrm{x}'_\mathrm{d} - \mathrm{x}''_\mathrm{d}}{(\mathrm{x}'_\mathrm{d} - \mathrm{x}_\mathrm{ls})}\frac{V_b}{x_{td}}\sin(\mathrm{x}_1)\right)\right]$$

$$f_{33} = 1 + \frac{\Delta t}{T'_{do}}\left[-1 - (\mathrm{x}_\mathrm{d} - \mathrm{x}'_\mathrm{d})\left\{\frac{1}{x_{td}} - \frac{\mathrm{x}'_\mathrm{d} - \mathrm{x}''_\mathrm{d}}{(\mathrm{x}'_\mathrm{d} - \mathrm{x}_\mathrm{ls})}\frac{1}{x_{td}} - 1\right\}\right]$$

$$f_{35} = \frac{\Delta t}{T'_{do}}\left[-(x_d - x'_d)\left(\frac{\mathrm{x}'_\mathrm{d} - \mathrm{x}''_\mathrm{d}}{(\mathrm{x}'_\mathrm{d} - \mathrm{x}_\mathrm{ls})^2}\right)\right]$$

$$f_{41} = \frac{\Delta t}{T'_{qo}}\left[(x_q - x'_q)\left(\frac{V_b}{x_{tq}}\cos(\mathrm{x}_1) - \frac{\mathrm{x}'_\mathrm{q} - \mathrm{x}''_\mathrm{q}}{(\mathrm{x}'_\mathrm{q} - \mathrm{x}_\mathrm{ls})}\frac{V_b}{x_{tq}}\cos(\mathrm{x}_1)\right)\right]$$

$$f_{44} = 1 + \frac{\Delta t}{T'_{qo}}\left[-1 - (x_q - x'_q)\left(\frac{\mathrm{x}'_\mathrm{q} - \mathrm{x}''_\mathrm{q}}{(\mathrm{x}'_\mathrm{q} - \mathrm{x}_\mathrm{ls})^2}\right)\right]$$

$$f_{46} = \frac{\Delta t}{T'_{qo}}\left[-(x_q - x'_q)\left(\frac{\mathrm{x}'_\mathrm{q} - \mathrm{x}''_\mathrm{q}}{(\mathrm{x}'_\mathrm{q} - \mathrm{x}_\mathrm{ls})^2}\right)\right]$$

$$f_{51} = \frac{\Delta t}{T''_{do}}\left[-(x'_d - \mathrm{x}_\mathrm{ls})\left(\frac{V_b}{x_{td}}\sin(\mathrm{x}_1)\right)\right]$$

$$f_{53} = \frac{\Delta t}{T_{do}^{''}} \left[1 - (x_d^{'} - x_{ls}) \left(\frac{1}{x_{td}}\right)\right]$$

$$f_{55} = 1 - \frac{\Delta t}{T_{do}^{''}}$$

$$f_{61} = \frac{\Delta t}{T_{do}^{''}} \left[-(x_q^{'} - \mathrm{x_{ls}}) \left(\frac{V_b}{x_{tq}} \cos(\mathrm{x_1})\right)\right]$$

$$f_{64} = -\frac{\Delta t}{T_{qo}^{''}}$$

$$f_{66} = 1 - \frac{\Delta t}{T_{qo}^{''}}$$

The linearized measurement equation of the system is

$$\boldsymbol{z}_k = H_k \boldsymbol{x}_k + \boldsymbol{v}_k$$

where H_k is the Jacobian matrix

$$H_k = \left[h_{ij}\right] = \begin{bmatrix} h_{11} & 0 & h_{13} & 0 & 0 & 0 \\ h_{21} & 0 & h_{23} & 0 & 0 & 0 \end{bmatrix}$$

$$h_{11} = \frac{v_b}{x_{td}} x_3 \cos(x_1) + \frac{v_b^2}{2} \left(\frac{1}{x_{tq}} - \frac{1}{x_{td}}\right) 2\cos(2x_1)$$

$$h_{13} = \frac{v_b}{x_{td}} \sin(x_1)$$

$$h_{21} = -\frac{v_b}{x_{td}} x_3 \sin(x_1) - 2v_b^2 \left(\frac{1}{x_{tq}} - \frac{1}{x_{td}}\right) \sin(x_1) \cos(x_1)$$

$$h_{23} = \frac{v_b}{x_{td}} \cos(x_1)$$

4.3 UNSCENTED KALMAN FILTER

Nonlinear state estimation is complicated by the difficulty of nonlineary transforming a probability density function (pdf). The extended Kalman filter works on the principle that a linearized transformation of means and covariances is approximately equal to the true nonlinear transformation. If the nonlinearity is severe, then the approximation can be unsatisfactory. Better results can be obtained using the unscented Kalman filter (UKF) provided that the noise is additive and Guassian.

The UKF is based on the unscented transformation. The unscented transformation is based on two fundamental principles. First, it is easy to perform a nonlinear transformation on a single point. Second, it is possible to find a set of individual points in state space whose sample pdf approximates the true pdf of a state vector [21].

Suppose that we know the mean and covariance of a vector $\boldsymbol{x}$. We then find a set of deterministic vectors called sigma points. Then, we apply our known nonlinear function to each deterministic vector to obtain transformed vectors. The ensemble mean and covariance of the transformed vectors give a good estimate of the true mean and covariance of the nonlinear function. This is the key to unscented transformation. The unscented transformation can be generalized to give the unscented Kalman filter. The Kalman filter propagates the mean and covariance of a system using a time-update and a measurement update [36].

We assume that we are given an n state discrete time nonlinear system

$$\boldsymbol{x}_{k+1} = \boldsymbol{f}(\boldsymbol{x}_k, t_k) + \boldsymbol{w}_k$$

$$\boldsymbol{y}_k = \boldsymbol{h}(\boldsymbol{x}_k, t_k) + \boldsymbol{v}_k$$

with noise processes

$$\boldsymbol{w}_k \sim (0, Q_k)$$

$$\boldsymbol{v}_k \sim (0, R_k) \tag{4.7}$$

The UKF algorithm can be summarized as follows [36]:

Step 1: Initialize the UKF with

$$\hat{\boldsymbol{x}}_o^+ = E(\boldsymbol{x_o})$$

$$P_o^+ = E[(\boldsymbol{x}_o - \hat{\boldsymbol{x}}_o^+)(\boldsymbol{x}_o - \hat{\boldsymbol{x}}_o^+)^T] \tag{4.8}$$

Step 2: Propagate the state estimate and covariance from one measurement time to the next.

(a) To propagate from time step k−1 to k, first choose sigma points $\hat{\boldsymbol{x}}_{k-1}^{(i)}$, with appropriate changes since the current best guess for the mean and covariance of $\boldsymbol{x}_k$ are $\hat{\boldsymbol{x}}_{k-1}^+$ and P_{k-1}^+ :

$$\hat{\boldsymbol{x}}_{k-1}^{(i)} = \hat{\boldsymbol{x}}_{k-1}^+ + \tilde{\boldsymbol{x}}^{(i)} \qquad i = 1, \ldots\ldots\ldots\ldots, 2n$$

$$\tilde{\boldsymbol{x}}^{(i)} = \left(\sqrt{nP_{k-1}^+}\right)_i^T \qquad i = 1, \ldots\ldots\ldots\ldots, n$$

$$\tilde{\boldsymbol{x}}^{(n+i)} = -\left(\sqrt{nP_{k-1}^+}\right)_i^T \quad i = 1, \ldots\ldots\ldots\ldots, n \tag{4.9}$$

(b) Use the known nonlinear system equation $\boldsymbol{f}(.)$to transform the sigma points into $\hat{\boldsymbol{x}}_k^{(i)}$ vectors, with appropriate changes since our non linear transformation is $\boldsymbol{f}(.)$rather than $\boldsymbol{h}(.)$:

$$\hat{\boldsymbol{x}}_k^{(i)} = \boldsymbol{f}(\hat{\boldsymbol{x}}_{k-1}^{(i)}, t_k) \tag{4.10}$$

(c) Combine the $\hat{\boldsymbol{x}}_k^{(i)}$ vectors to obtain the *a priori* state estimate at time k.

$$\hat{\boldsymbol{x}}_k^- = \frac{1}{2n}\sum_{i=1}^{2n} \hat{\boldsymbol{x}}_k^{(i)} \tag{4.11}$$

(d) Estimate the *a priori* error covariance including the matrix Q_{k-1} to take the process noise into account:

$$P_k^- = \frac{1}{2n}\sum_{i=1}^{2n}\left(\hat{\boldsymbol{x}}_k^{(i)} - \hat{\boldsymbol{x}}_k^-\right)\left(\hat{\boldsymbol{x}}_k^{(i)} - \hat{\boldsymbol{x}}_k^-\right)^T + Q_{k-1} \tag{4.12}$$

Step 3: Update the measurement equations.

(a) Choose sigma points $\hat{\boldsymbol{x}}_k^{(i)}$, with appropriate changes since the current best guess for the mean and covariance of $\boldsymbol{x}_k$ are $\hat{\boldsymbol{x}}_k^-$ and P_k^- :

$$\hat{\boldsymbol{x}}_k^{(i)} = \hat{\boldsymbol{x}}_k^- + \tilde{\boldsymbol{x}}^{(i)} \qquad i = 1, \ldots\ldots\ldots\ldots, 2n$$

$$\tilde{\boldsymbol{x}}^{(i)} = \left(\sqrt{nP_k^-}\right)_i^T \qquad i = 1, \ldots\ldots\ldots\ldots, n$$

$$\tilde{\boldsymbol{x}}^{(n+i)} = -\left(\sqrt{nP_k^-}\right)_i^T \quad i = n+1, \ldots\ldots\ldots\ldots, 2n \tag{4.13}$$

(b) Use the known nonlinear measurement equation $\boldsymbol{h}(.)$to transform the sigma points into $\hat{\boldsymbol{y}}_k^{(i)}$ vectors:

$$\hat{\boldsymbol{y}}_k^{(i)} = \boldsymbol{h}(\hat{\boldsymbol{x}}_k^{(i)}, t_k) \tag{4.14}$$

(c) Combine the $\hat{\boldsymbol{y}}_k^{(i)}$ vectors to obtain the predicted measurement at time k.

$$\hat{\boldsymbol{y}}_k = \frac{1}{2n}\sum_{i=1}^{2n}\hat{\boldsymbol{y}}_k^{(i)} \tag{4.15}$$

(d) Estimate the covariance of the predicted measurement. However, we should add R_k to the end of the equation to take the measurement noise into account:

$$P_y = \frac{1}{2n}\sum_{i=1}^{2n}\left(\hat{\boldsymbol{y}}_k^{(i)} - \hat{\boldsymbol{y}}_k\right)\left(\hat{\boldsymbol{y}}_k^{(i)} - \hat{\boldsymbol{y}}_k\right)^T + R_k \tag{4.16}$$

(e) Estimate the cross covariance between $\hat{\boldsymbol{x}}_k^-$ and $\hat{\boldsymbol{y}}_k$.

$$P_{xy} = \frac{1}{2n}\sum_{i=1}^{2n}(\hat{\boldsymbol{x}}_k^{(i)} - \hat{\boldsymbol{x}}_k^-)(\hat{\boldsymbol{y}}_k^{(i)} - \hat{\boldsymbol{y}}_k)^T \tag{4.17}$$

(f) The measurement update of the state estimate can be performed using the normal Kalman filter equations as.

$$K_k = P_{xy} P_y^{-1}$$

$$\widehat{\boldsymbol{x}}_k^+ = \widehat{\boldsymbol{x}}_k^- + K_k(\boldsymbol{y}_k - \widehat{\boldsymbol{y}}_k)$$

$$P_k^+ = P_k^- - K_k P_y {K_k}^T \tag{4.18}$$

CHAPTER 5 NETWORKED CONTROL SYSTEM

5.1 INTRODUCTION

The past two decades have witnessed rapid development of smart sensors and actuators, such as bio-sensors in biomedicine [37], mobile sensor network for monitoring the health of civil infrastructures [38], and wireless sensor networks in smart home scenarios [39]. Since smart sensors and actuators, which are important components of control systems, provide more powerful computing and communicating abilities, control systems are experiencing a transition period from classical single-location systems into the so-called networked control systems(NCS). A communication network is used to close the control loop in NCS. Source distribution, reduced system wiring and increased system agility are among the prominent advantages of NCS [40]. At present NCS is getting extensive attentions from researchers and engineers from different research areas. Among the important applications of NCS is wide area control and monitoring of large-scale power system [41].

The earliest control systems were analog. Later, digital computers became powerful tools in control system design. In addition, microprocessor added a new dimension to the control system. Later distributed control system emerged in the 1970s. To satisfy the expanding needs of industrial applications, it became obvious that NCS is the only solution. Research in tele-operation with space projects and nuclear reactor power plants was made feasible only after the development of NCS. Later easy and cheap access to the Internet and the deployment of wireless networks aided the development of NCS. Today, distributed NCSs have emerged [36]. They are multi-disciplinary efforts whose aim is to produce a network structure and components that are capableof

integrating distributed sensors, distributed actuators, and distributed control algorithms over a communication network in a manner that is suitable for real-time applications [43].

When using communication networks, especially wireless networks, time delays and packet losses are unavoidable. These network associated problems can degrade the performance of NCS and can even make an NCS unstable. Although some NCS problems, such as time delays, have been extensively investigated, others are not well addressed [43-45]. For instance, protocols like TCP cannot ensure accurate real-time performance due to retransmission mechanism. However, protocols like UDP are popular for real-time performance, but have a much higher packet loss rate than TCP. Packet loss is a very important factor when investigating NCS stability and a high packet loss rate may destabilize the NCS [46].

5.2 NCS BASICS

The basic structure of a NCS is shown in Figure 5.1. The state of the plant is sensed by sensors and is sent to the controller over the network. Controller compares the state with reference model and computes control signals accordingly. Later the control signal is sent to the actuator through the network to be implemented at the plant [47].

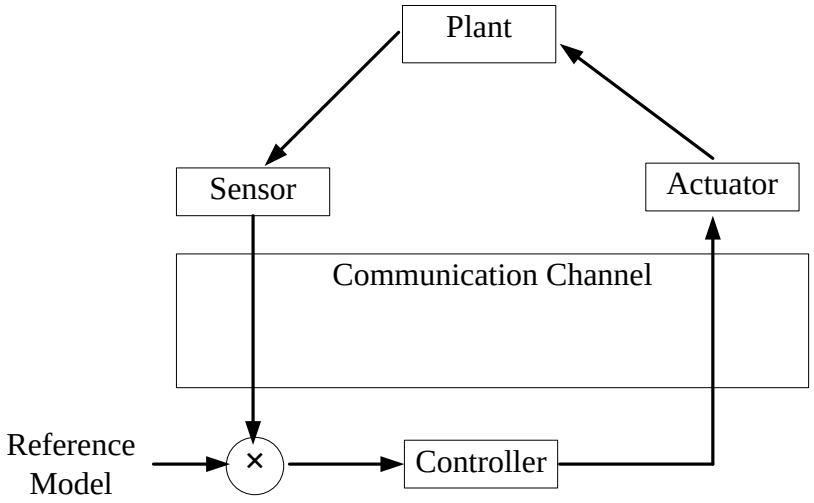

Figure 5.1: General structure of NCS.

The important capabilities of NCS are information acquisition from sensors, command from controllers, communication and network and control. NCS research comprises two main parts: control of network, and control over network [43]. Control of network involves study and research on communications and networks to make them suitable for real-time NCS. Control over network includes control strategies and control system design over the network to minimize the effect of adverse network parameters on NCS performance.

There are two major types of control systems under control over network. These are shared networked control system and remote control system. Detailed explanations, advantages and other related things to these connections are provided in [43]. The main challenges for NCS structure are the quality of service and quality of control. Quality of service is related to transmission rates, error rates and other characteristics can be measured, improved.

Quality of service can be degraded due to congestion and interference. Providing good quality of service and good quality of control for NCS are active research topics [47].

5.3 ADVANTAGES AND DISADVANTAGES OF NCS

NCS has several advantages and disadvantages. These advantages include:

(a) Flexibility: A network introduces lots of flexibility to control system and its resources. It extends and shares the network and its resources.

(b) Reduced Complexity: Introduction of control in networked system reduces systems' complexity.

(c) Data Sharing: NCS enables efficient data sharing when needed.

(d) Reduced Wiring: NCS eliminates unnecessary wiring usually needed for large control system.

(e) Extendibility: Addition of more sub control systems is easier in NCS. Also the network can be extended to central control system without large changes to its physical layout.

(f) Remote Controlled: The control part of the NCS can be on the remote side with the NCS connected to the physical system through a network.

Because it includes a communication network, NCS inherits some of the problems associated with the network including:

(a) Lack of Security: Since data is often transmitted through a shared network, it may be accessible to other network users. Therefore, special care must be taken in order to ensure security. To secure data, different cypher algorithms may be implemented.

(b) Bandwidth Allocation: NCS can create problems when the shared network bandwidth is limited. Bandwidth limitations can cause congestion and data loss due to packet dropping.

(c) Network Delays: Due to network congestion, data transmission may be delayed and the data may not be available when needed. This can destabilize the NCS if not identified and addressed. Many techniques are available to address this problem [48].

(d) Scheduling: Satisfactory NCS performance requires proper scheduling and data traffic management so as to optimally utilize the available bandwidth [49].

5.4 TIME DELAY AND PACKET DROP IN NCS

In NCS, spatially decentralized control nodes are connected by the communication network, of which the introduction leads to characteristics different from the traditional control. The basic problems in NCS design are network communication, control strategy and collaborative design [50]. The control strategy aims to design a controller that can tolerate communication delay, packet loss and sequential disorder. The communication delay can degrade system performance or even lead to instability. The delay can be fixed, random, bounded or unbounded depending on communication protocol, transmission rate and packet size [51]. A time-delay is called *short* if it is less than one sampling period and is called *long* if it exceeds one sampling period [52]. Researchers face difficulty with uncertainty of random delay and the serious lag caused by long time delay. To solve this problem various control strategies including deterministic control, random control, intelligent control, robust control, networked

predictive control, etc. have been proposed. For example, predictive control achieves stability, reliability and improves system performance significantly [51].

Another significant aspect in NCS is the possibility of data loss in transit through the network. Packet drop usually result from transmission errors in the physical network links or from buffer overflows due to congestion. Packet drop is far more common in wireless than in wired networks. Sometimes long transmission delays result in packet reordering, which can amount to packet drop out if the receiver discard outdated arrivals.

Delivery of packets is guaranteed in some reliable transmission protocols such as TCP. However, these protocols may not be good enough for NCS since transmission of old data is not generally useful [53].

5.5 PROPOSED ALGORITHM FOR TIME DELAY AND PACKET DROP

If the delivery of measurements to the estimator is delayed, the Kalman filter algorithm must be modified to make use of the delayed data. Several configurations of time delay are possible. One possibility is packets can arrive at the estimator in the order of their time stamps. Another possibility is the some packets reach the estimator ahead of data with earlier time stamps. The last possibility is that several packets with different time stamps reach the estimator at the same time. The Kalman filter update with multiple packets received at the same time can be performed by sorting the packets in accordance with the time order, then going back to the time corresponding to each packet to correct the state estimate. Our approach is to sort the data then correct the estimates with the Kalman filter as in the example shown in *Table I.*

As shown in the table, if data is lost, the Kalman filter is only able to predict the state. If data is delayed, then the predicted state at the time of the measurement is corrected using the delayed measurement. At $k = 1$, there is no drop or delay and the usual predictor/corrector Kalman filter is used. Data is lost at time $k = 2$ and $k = 3$ and the state can only be predicted without correction. At time $k = 4$, no measurement is received and again only prediction is possible, but the measurement $\boldsymbol{z}_4$ is not lost. The measurement $\boldsymbol{z}_4$ is received at $k = 5$ and is used to correct the predicted estimate at $k = 4$, then the estimate at $k = 5$ and $k = 6$ are predicted.

Table I Timeline for data and Kalman filter

No Drop/ Delay	Packet Drop	Delay	Receive Delayed Data	Receive Delayed Data
$k = 1$	$k = 2,3$	$k = 4$	$k = 5$	$k = 6$
Receive $\boldsymbol{z}_1$ Correct $\hat{\boldsymbol{x}}_1^+, P_1^+$	Predict $\hat{\boldsymbol{x}}_2^-, P_2^-$ Predict $\hat{\boldsymbol{x}}_3^-, P_3^-$	Predict $\hat{\boldsymbol{x}}_4^-, P_4^-$	Receive $\boldsymbol{z}_4$ Correct $\hat{\boldsymbol{x}}_4^+, P_4^+$ using $\hat{\boldsymbol{x}}_4^-, P_4^-$ Predict $\hat{\boldsymbol{x}}_5^-, P_5^-$,	Receive $\boldsymbol{z}_3$ Correct $\hat{\boldsymbol{x}}_3^+, P_3^+$ using $\hat{\boldsymbol{x}}_3^-, P_3^-$ Predict $\hat{\boldsymbol{x}}_4^-, P_4^-$ $\hat{\boldsymbol{x}}_5^-, P_5^-$, $\hat{\boldsymbol{x}}_6^-, P_6^-$

CHAPTER 6 ROBUST STATE ESTIMATE

6.1 INTRODUCTION

Detection, identification and elimination of errors which may appear in measurements, network models or parameters are among the main reasons behind using state estimators. An estimator is statistically robust when it remains insensitive to major deviations in a limited number of measurements [54]. Unfortunately, robustness is achieved at the cost of high computational complexity. A state estimator can track power system dynamics with the use of wide area synchrophasor measurements. Real-time control schemes can then be implemented using the estimated states. The extended Kalman filter can be modified to cope with large disturbances in measurements [55]. Netto et al. developed a new generalized maximum likelihood extended Kalman filter (GM-EKF) that exhibits good statistical efficiency under Gaussian process and measurement noises [12]. The GM-EKF is capable of bounding the influence of vertical outliers and bad leverage points, identified by projection statistics. A batch mode regression form is derived that is implemented in GM-EKF. This thesis uses the GM-EKF methodology to obtain a robust state estimator.

6.2 BATCH MODE REGRESSION FORM

Consider the state equation of Equation (4.2) with the initial estimated state vector$\hat{\boldsymbol{x}}_{(0|0)}$, and with estimation error covariance matrix, $P_{(0|0)}$. The estimates are updated through

$$\hat{\boldsymbol{x}}_{(k|k-1)} = \boldsymbol{f}(\hat{\boldsymbol{x}}_{(k-1|k-1)}) \tag{6.1}$$

$$P_{(k|k-1)} = F_{k-1}P_{(k-1|k-1)}F_{k-1}^{T} + W_{k-1} \tag{6.2}$$

where the Jacobian matrices F and H are defined as

$$F = \frac{\partial \boldsymbol{f}}{\partial \boldsymbol{x}} \quad , \qquad H = \frac{\partial \boldsymbol{g}}{\partial \boldsymbol{x}}$$

$\boldsymbol{f}$ is a vector of state dynamics whereas $\boldsymbol{g}$ is a vector of measurement equations.

$\boldsymbol{g}(\boldsymbol{x}_k, \boldsymbol{v}_k)$ is linearized around the predicted state vector$\widehat{\boldsymbol{x}}_{(k|k-1)}$ to obtain

$$\boldsymbol{z}_k = \boldsymbol{g}\left(\widehat{\boldsymbol{x}}_{(k|k-1)}\right) + H_k\left(\widehat{\boldsymbol{x}}_k - \widehat{\boldsymbol{x}}_{(k|k-1)}\right) + \boldsymbol{v}_k \tag{6.3}$$

In addition, we define

$$\widehat{\boldsymbol{x}}_{(k|k-1)} = \boldsymbol{x}_k - \boldsymbol{\delta}_{(k|k-1)} \tag{6.4}$$

$\boldsymbol{\delta}_{(k|k-1)}$ is the prediction error.

Combining Equations (6.3-6.4) gives a new measurement equation

$$\begin{bmatrix} \boldsymbol{z}_k - \boldsymbol{g}\left(\widehat{\boldsymbol{x}}_{(k|k-1)}\right) + H_k\left(\widehat{\boldsymbol{x}}_{(k|k-1)}\right) \\ \widehat{\boldsymbol{x}}_{(k|k-1)} \end{bmatrix} = \begin{bmatrix} H_k \\ I \end{bmatrix} \boldsymbol{x}_k + \begin{bmatrix} \boldsymbol{v}_k \\ -\boldsymbol{\delta}_{(k|k-1)} \end{bmatrix} \tag{6.5}$$

Equation (6.5) can be written as

$$\tilde{\boldsymbol{z}}_k = \widetilde{H}_k \boldsymbol{x}_k + \tilde{\boldsymbol{e}}_k \tag{6.6}$$

and used in the Kalman filter algorithm with the error covariance matrix

$$\tilde{R}_k = \begin{bmatrix} R_k & \mathbf{0} \\ \mathbf{0} & P_{(k|k-1)} \end{bmatrix} = S_k S_k^T \tag{6.7}$$

6.3 OUTLIER IDENTIFICATION

It is necessary to detect the outliers and suppress them for getting a robust state estimator. This is performed by using projection statistics algorithm. Projection statistics are calculated by using the matrix

$$Z = \begin{bmatrix} \boldsymbol{z}_{k-1} - \boldsymbol{g}\left(\widehat{\boldsymbol{x}}_{(k-1|k-2)}\right) & \boldsymbol{z}_k - \boldsymbol{g}\left(\widehat{\boldsymbol{x}}_{(k|k-1)}\right) \\ \widehat{\boldsymbol{x}}_{(k-1|k-2)} & \widehat{\boldsymbol{x}}_{(k|k-1)} \end{bmatrix} \tag{6.8}$$

$Z \in R^{m' \times 2}$,where $m' = m + n$.

m = number of measurements and n = number of state variables.

Each i^{th} computed projection statistic (PS_i) is compared with a given threshold value. The flagged outliers are weighted using the weight function

$$\overline{w}_i = \min\left(1,\ \frac{d^2}{PS_i^2}\right) \tag{6.9}$$

$d = 1.5$is chosen for good statistical efficiency [12].

Robust prewhitening is achieved by multiplying Equation (6.6) by $S_k^{-1}$to obtain

$$S_k^{-1}\tilde{\boldsymbol{z}}_k = S_k^{-1}\widetilde{H}_k\boldsymbol{x}_k + S_k^{-1}\tilde{\boldsymbol{e}}_k \tag{6.10}$$

Equation (6.10) is rewritten in a compact form as

$$\boldsymbol{y}_k = A_k\boldsymbol{x}_k + \boldsymbol{\zeta}_k \tag{6.11}$$

6.4 ROBUST FILTERING

The GM estimator bounds the influence of outliers by minimizing the effect of objective function given by

$$J(\boldsymbol{x}) = \sum_{i=1}^{m} \overline{w}_i^2\, \rho(rs_i) \tag{6.12}$$

The Huber ρ function is defined by.

$$\rho(rs_i) = \begin{cases} 0.5\, rs_i^2 & |rs_i| \le c \\ c|rs_i| - 0.5\, c^2, & otherwise \end{cases}$$

Setting the value of c equal to 1.5 gives high statistical efficiency [10].

The standardized residual $rs_i$is defined as

$$rs_i = r_i/(s\,\overline{w_i}) \tag{6.13}$$

s_i is a robust estimator of scale and defined as follows

$$s_i = 1.4826\, b'_m\, median_i|r_i|$$

Croux and Rousseeuw suggested setting the value of parameter b'_m as shown in *Table II* if $m' \le 9$ and to $b'_m = \left[\frac{m'}{m'-0.8}\right]$ otherwise [56].

Table II Parameter b'_m for $m' \leq 9$

m'	2	3	4	5	6	7	8	9
b'_m	1.196	1.495	1.363	1.206	1.200	1.140	1.129	1.107

The residual vector $\boldsymbol{r}_i$ is defined as $\boldsymbol{r}_i = \boldsymbol{y}_i - \boldsymbol{a}_i^T \hat{\boldsymbol{x}}$

where $\boldsymbol{a}_i$ is the i^{th} column vector of the matrix A_k^T.

Iteratively updating the state with the reweighted least squares (IRLS) algorithm gives

$$\hat{\boldsymbol{x}}_{(k|k)}^{j+1} = \left(A_k^T Q^j A_k\right)^{-1} A_k^T Q^j y_k \tag{6.14}$$

where,

$Q = diag(\boldsymbol{q}(rs_i))$

$$\boldsymbol{q}(rs_i) = \frac{\psi(rs_i)}{rs_i}$$

$$\psi(rs_i) = \frac{\partial \rho(rs_i)}{\partial rs_i}$$

With every update of the state estimate, the error covariance matrix must be updated. GM-EKF uses the expression for error covariance obtained from the total influence function [14]

$$P_{(k|k)} = \frac{\mathrm{E}_\phi[\psi^2(rs_i)]}{\{\mathrm{E}_\phi[\psi'(rs_i)]\}^2} (A_k^T A_k)^{-1} (A_k^T Q_w A_k)(A_k^T A_k)^{-1} \tag{6.15}$$

where$Q_w = diag(\overline{w}_i{}^2)$. In Equation (6.15), $\frac{\mathrm{E}_\phi[\psi^2(rs_i)]}{\{\mathrm{E}_\phi[\psi'(rs_i)]\}^2}$, is equal to 1.0369 for $c = 1.5$

6.5 UKF STATE ESTIMATOR WITH BAD DATA DETECTION

Bad data results from meter biases, topology errors, communication failure, false data injection etc.[57]. State estimation including bad data may result in unsatisfactory state

estimates. It is not uncommon to obtain estimation results that diverge from the actual values. Therefore, it is necessary to detect the bad data and modify the estimator such that it provides satisfactory results. Bad data detection is usually based on the fact that the ratio between the deviation of the actual measurement from the estimate of the measurement and the expected standard deviation of the estimate remains below a threshold value in the absence of bad data. If the ratio exceeds the threshold value, the actual measurement is detected as bad data. This ratio is called the normalized innovation ratio [58]. Assume a measurement vector, $\boldsymbol{y} = [P, Q]^T$. P and Q are active and reactive powers, respectively. Consider predicted measurement as $\hat{\boldsymbol{y}}$ and error covariance matrix as P_{err}. P_{err} is defined as follows

$$P_{err} = \begin{bmatrix} P_{11} & P_{12} \\ P_{21} & P_{22} \end{bmatrix}$$

The innovation or residual vector is calculated as $\boldsymbol{r} = \boldsymbol{y} - \hat{\boldsymbol{y}} = \begin{bmatrix} r_1 \\ r_2 \end{bmatrix}$.

The normalized residuals are obtain as in the form

$$r_{n1} = \frac{r_1}{\sqrt{P_{11}}}, r_{n2} = \frac{r_2}{\sqrt{P_{22}}}$$

For bad data, $|r_{n1}| > r_o$ and $|r_{n2}| > r_o$.Here,r_o is the threshold value for detecting bad data. The threshold, r_o depends on the type of system and type of measurements and can be calculated offline [59,60].For the system in our case study, offline simulations gaver_o equal to 30. Therefore, a measurement is detected as bad measurement if the corresponding normalized innovation value exceeds r_o in a given sample. This method of detecting bad data is not flawless. The main weakness of this approach results from the fact that they use detection tests which is based on least

squares residuals prone to the masking effects of multiple bad data [19].In our case, we used outliers in one measurement to avoid the masking effects of multiple bad data in bad data detection.

We propose two methods for state estimation using the unscented Kalman filter with bad data. Upon detecting a bad measurement we replace the bad measurement with(i) the predicted measurement, or (ii) the last uncorrupted measurement. Simulation results based on these two methods are provide in Chapter 7 and compared with the GM-EKF.

CHAPTER 7: SIMULATION RESULTS

This chapter presents simulations of the microgrid of Section 2.3. In the simulations, active and reactive powers are the two output measurements while the inputs are field voltage E_{fd} and mechanical torque T_m.All simulations use zero initial state $\boldsymbol{x}_0$ and an initial error covariance matrix $P_0 = 100I_6$.The values of the noise statistics are as follows: for the state noise we set $w_k \sim (\mathbf{0}, Q_k) = (\mathbf{0}, 0.01I_6)$ and for measurement noise we set$v_k \sim (0, R_k) = (0, 0.01I_2)$.

We first consider six scenarios with a sampling frequency of 1 kHz and compare the performance of the estimators in each case. For the first scenario, the microgrid is operating normally with no faults or disturbances. In the second scenario, we consider the effect of a fault at the PCC in the microgrid. In the third scenario, we examine the effects of a failure of the second generator of the microgrid. The fourth scenario shows the effect of a fault that drops load 2 of the microgrid. The fifth scenario includes data loss or delay and uses our proposed scheme to utilize the delay data. The sixth scenario includes bad data in the measurements and simulates the GM-EKF and two robust UKFs.

We also present simulations of the first four scenarios for the GM-EKF and the two robust UKFs at the PMU frequency of 50 Hz with both bad data and data loss or delay due to network congestion. These simulations require the use of second order Runge-Kutta discretization of the microgrid model, while the simpler Euler approximation was adequate for the higher frequency of 1 kHz. In addition, the simulations required 10 prediction steps for each sampling period to reduce the numerical errors associated with the approximation of the derivative.

For each simulation scenario that we present, we include a table that summarizes the results of 500 Monte Carlo simulations. The table includes the maximum error, the minimum error and the average error for our estimates of the state variables excluding the rotor angle, which is presented separately because it is in radians while the rest are per unit.

7.1 NORMAL MICROGRID OPERATION

The state estimation results for synchronous generator-1 are shown in Figure 7.1 – Figure 7.6. The simulation results show that the state estimates follow the actual states. In most cases, the UKF provides better estimation than the EKF. In a few cases, as in the cases with d transient voltage and q axis second damper flux, the estimates are very close to each other. This verifies the effectiveness of the UKF in addition to eliminating the limitations of the linearization process required by the traditional EKF.

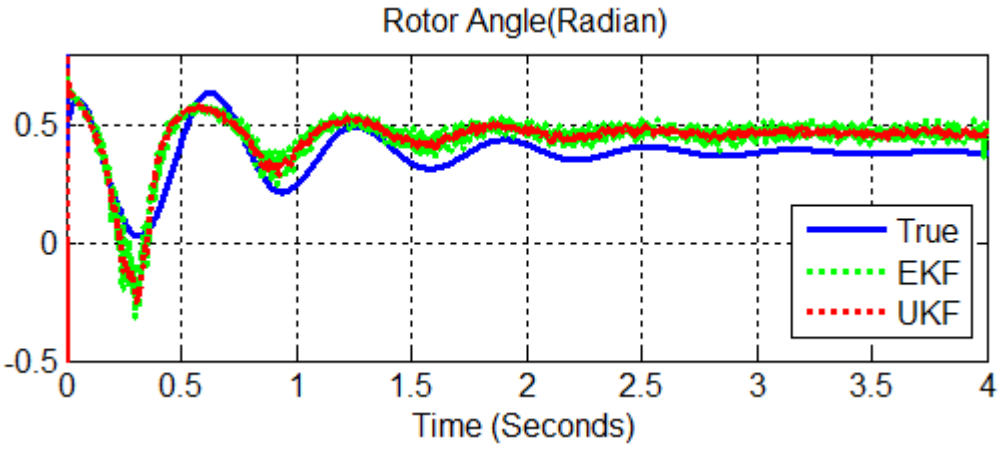

Figure 7.1 Rotor angle and its estimates.

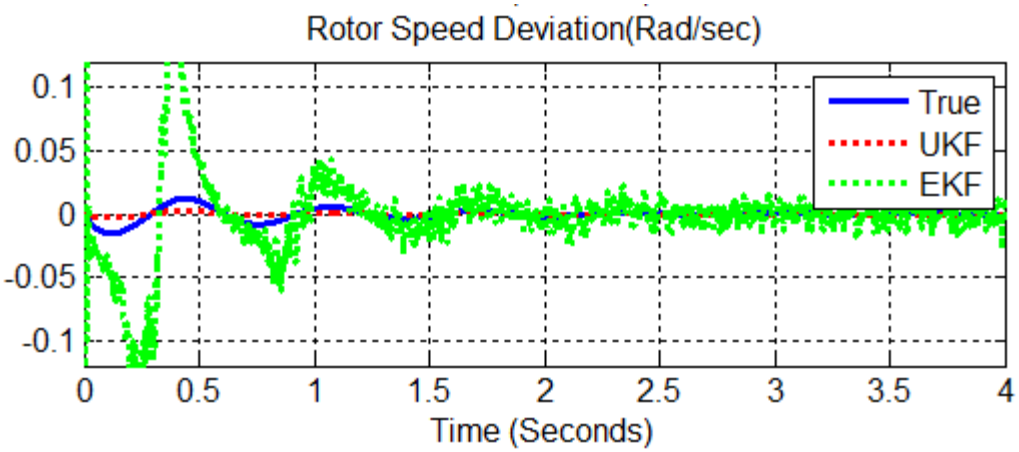

Figure 7.2 Rotor speed deviation from the synchronous speed and its estimates.

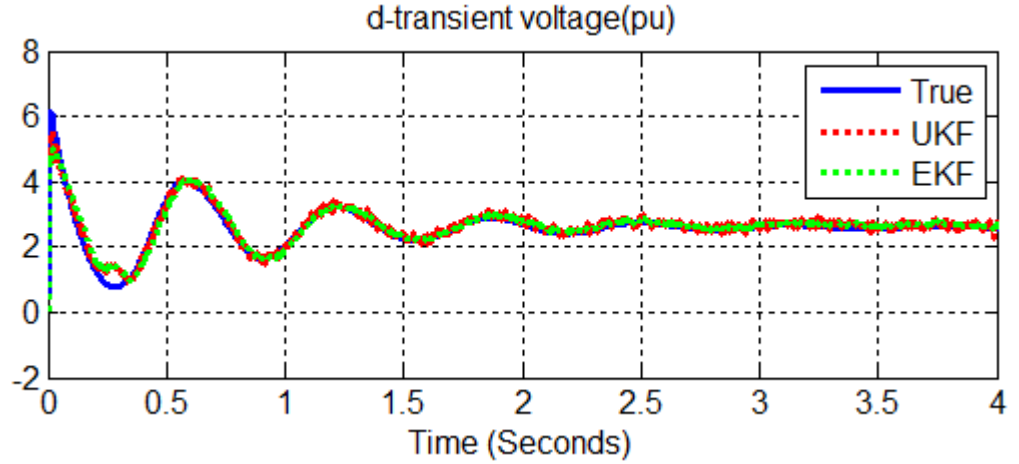

Figure 7.3 d-axis transient voltage and its estimates.

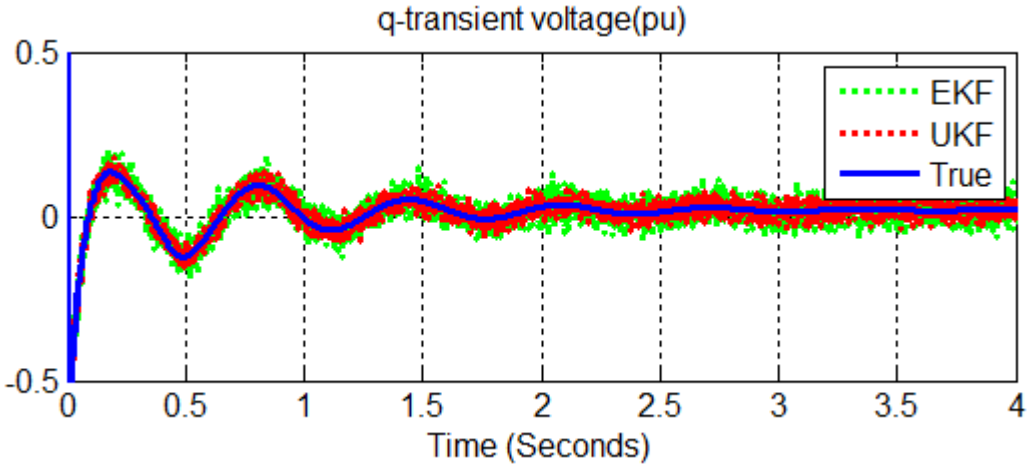

Figure 7.4 q-axis transient voltage and its estimates.

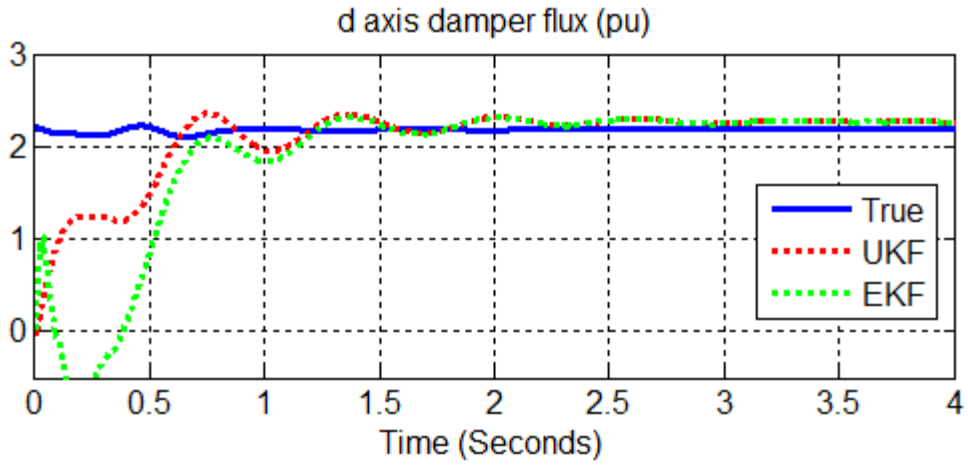

Figure 7.5 d- axis damper flux and its estimates.

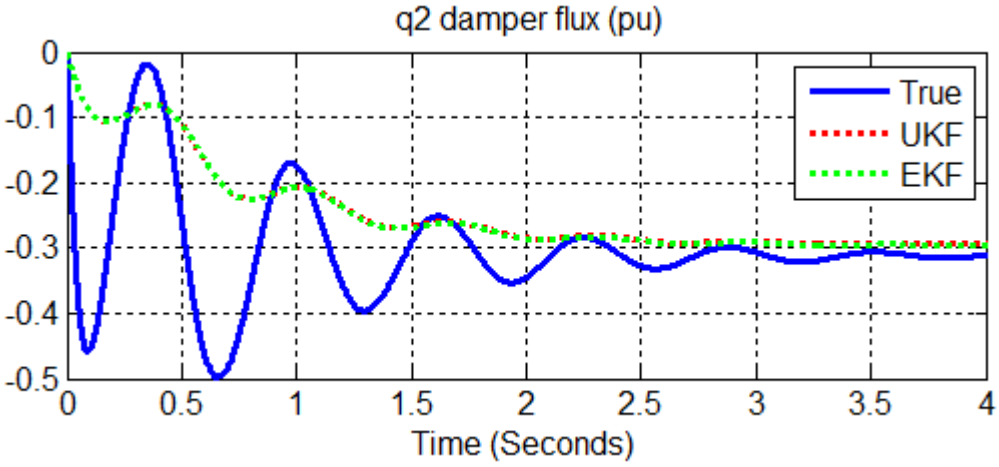

Figure 7.6 q- axis second damper flux and its estimates.

The estimated outputs (measurements) are shown in Figure 7.7 - Figure 7.8. From these figures, it is observed that the Kalman filter effectively filters out the noise from the measurements. The figures also show that the estimator performs with good accuracy, both in state estimation and filtering noise from measurements.

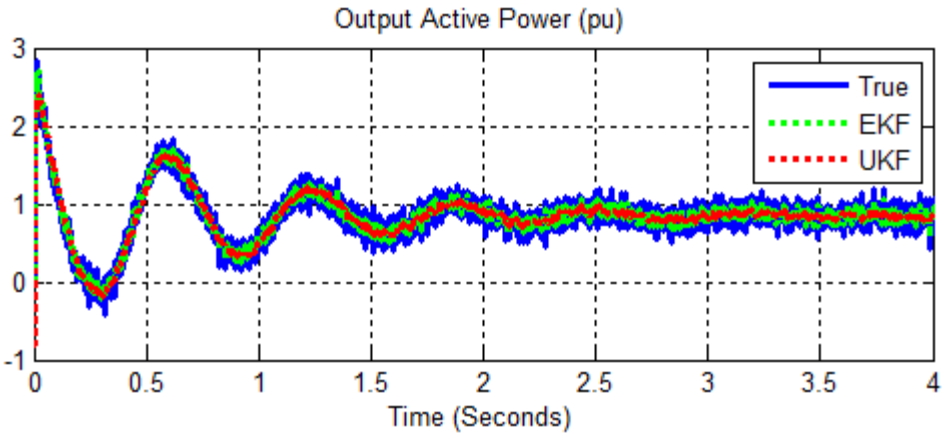

Figure 7.7 Noisy measurement and estimated active power of synchronous generator-1.

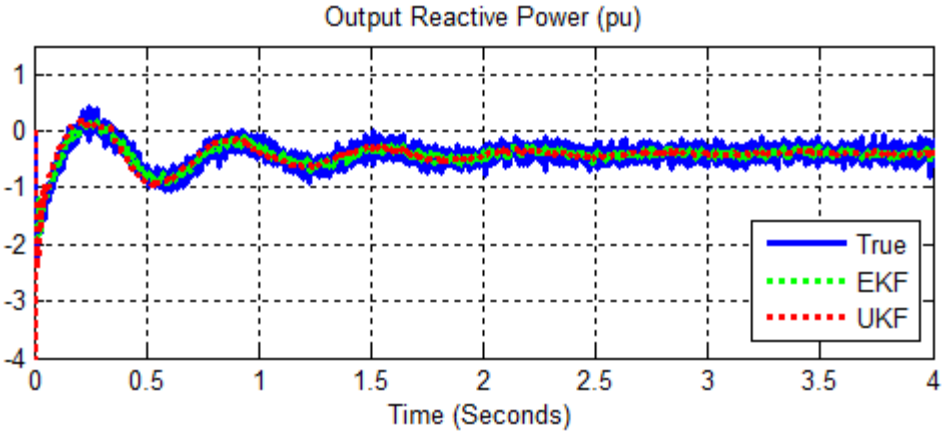

Figure 7.8 Noisy measurement and estimated reactive power of synchronous generator-1.

To compare the root mean square (RMS) error of the EKF to the RMS of the UKF, we ran a Monte Carlo simulation for 500 times. The simulation was performed from 5 second to 10 second. Figure 7.9 - 7.10 show the box plot of RMS errors for both EKF and the UKF. *Table III* shows the maximum, minimum and standard deviation of the RMS errors and rotor angle RMS errors for EKF and UKF. From the figures and table, we see that the EKF has a greater state estimation error than the UKF.

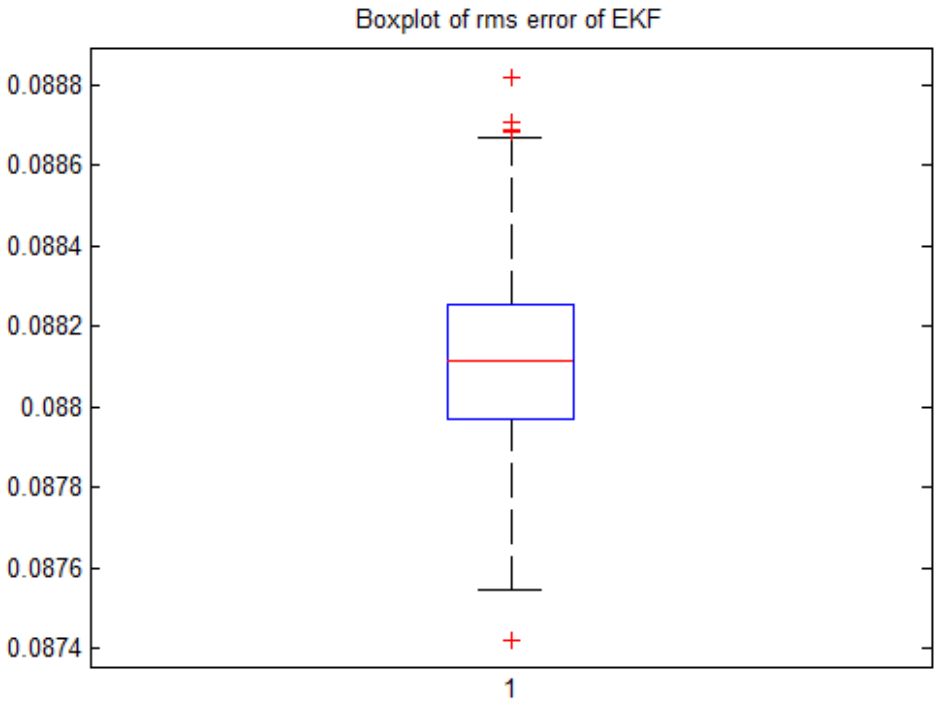

Figure 7.9 Box plot of RMS error for the EKF at normal microgrid.

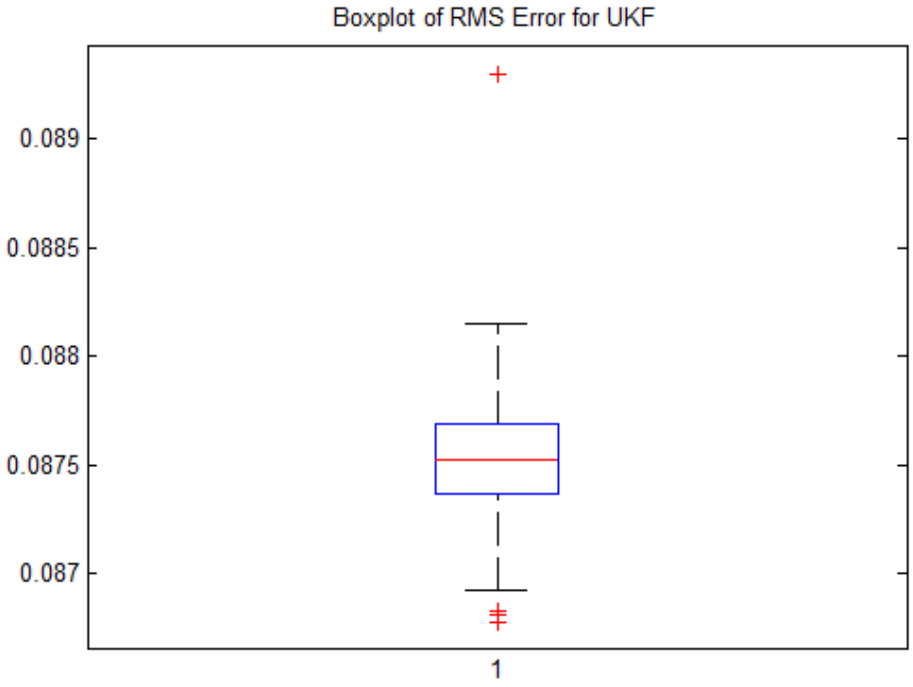

Figure 7.10 Box plot of RMS error for the UKF at normal microgrid.

Table III Comparison of RMS errors for EKF and UKF

Filter	RMSE (Max.)	RMSE(Min)	Standard Deviation	RMSE of Rotor Angle (Max)	RMSE of Rotor Angle (Min)	Standard Deviation
UKF	0.0893	0.0868	4.04e-04	0.0866	0.0861	7.82e-05
EKF	0.0888	0.0874	2.20e-04	0.0867	0.0863	1.87e-05

7.2 FAULT AT PCC

In order to check the effectiveness of the EKF and UKF under network fault disturbance, we simulated a 3-phase to ground fault at the microgrid PCC after 5 s and cleared after 5.1 s. The Simulink model settings and estimator initial values are the same as in the first simulation. Simulation results show that the fault has significant impact on the UKF estimator. After clearing the fault, the estimator converges quickly to the steady state.

We highlight the performance of the state estimator at the time of the fault and after clearing the fault by showing simulation results over a shorter time period that bounds the two events. The simulation results are shown in Figure 7.11 -Figure 7.16. The results show that the estimator generates good estimates under PCC fault, exhibits a discontinuity immediately after the fault occurs, then resumes tracking the true values after the fault is cleared.

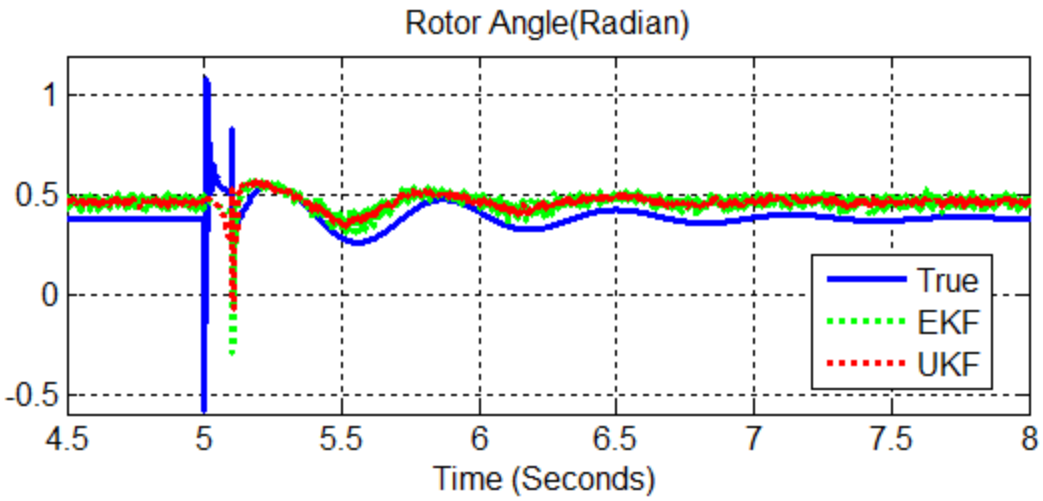

(a) From time interval 4.5 to 8s.

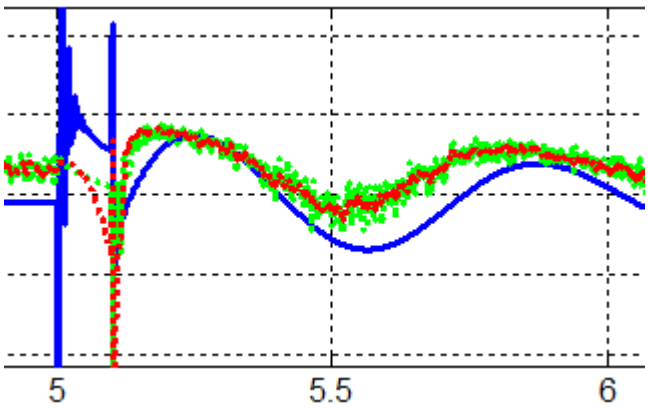

(b) From time interval 5 to 6s.

Figure 7.11 Rotor angle and its estimates under faulty condition.

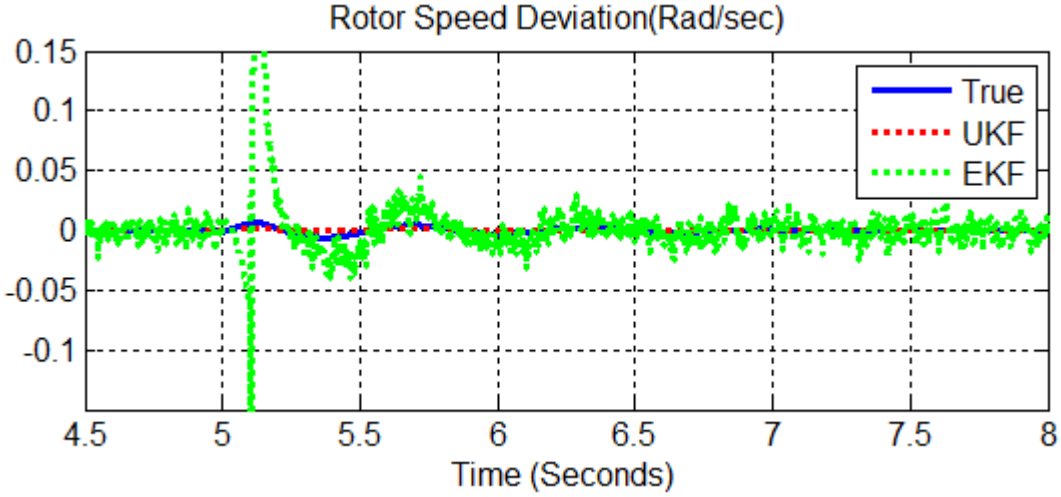

(a) From time interval 4.5 to 8s.

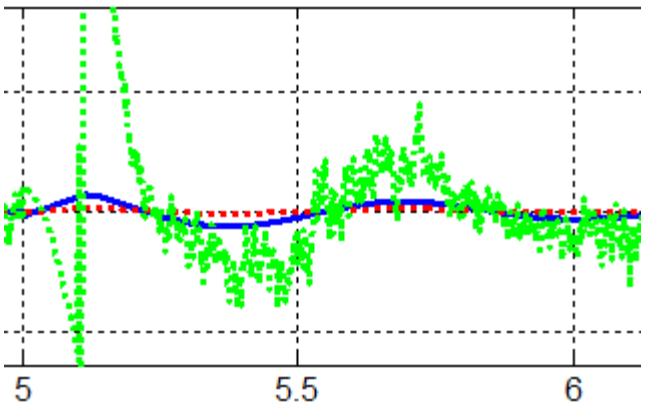

(b) From time interval 5 to 6s.

Figure 7.12Rotor speed deviation and its estimates under faulty condition.

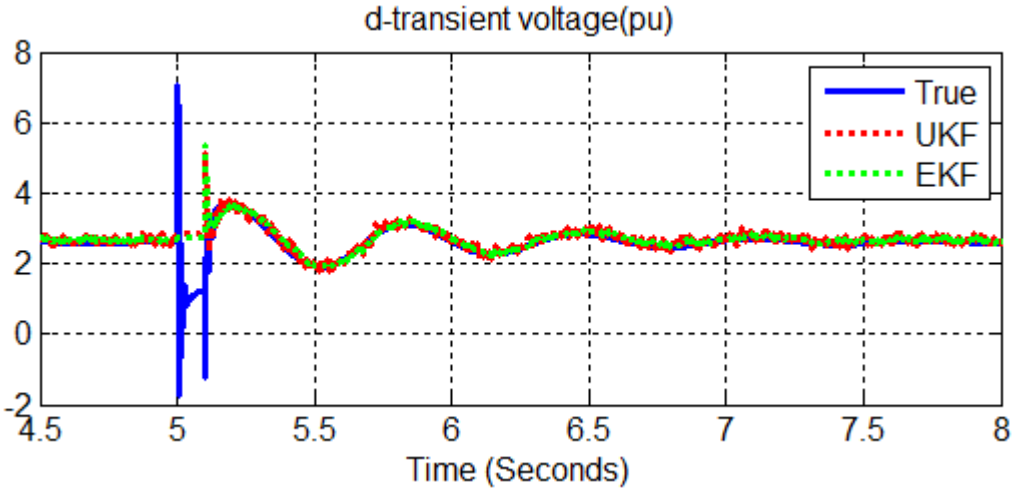

(a) From time interval 4.5 to 8s.

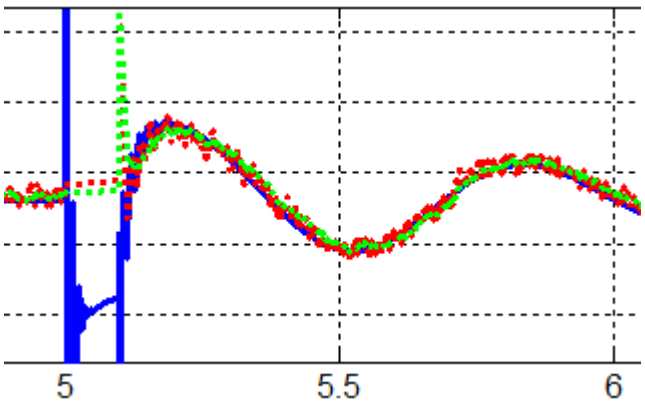

(b) From time interval 5 to 6s.

Figure 7.13 d-axis transient voltage and its estimates under faulty condition.

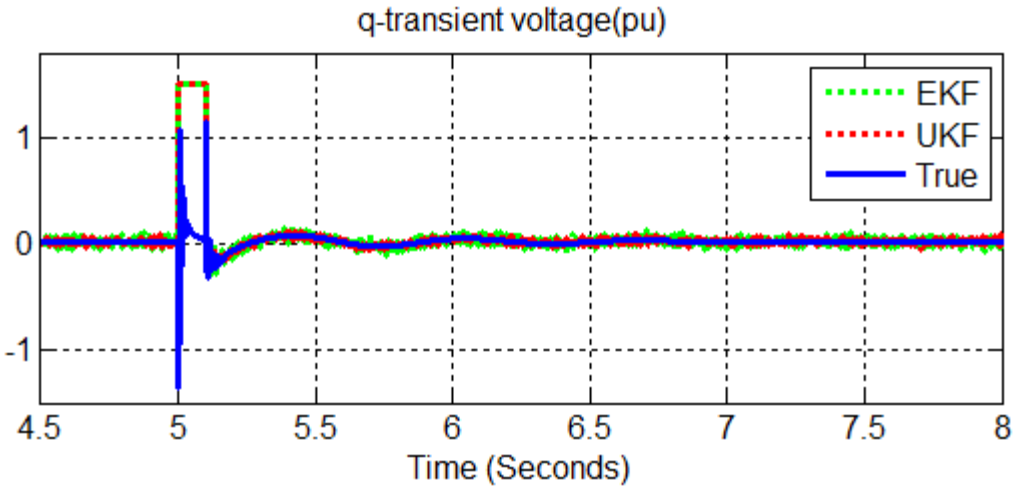

(a) From time interval 4.5 to 8s.

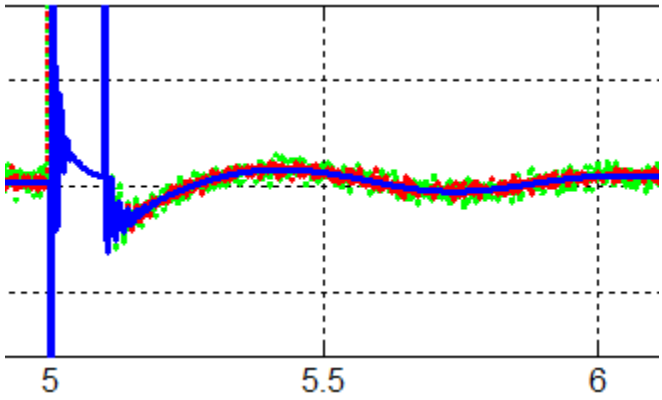

(b) From time interval 5 to 6s.

Figure 7.14 q-axis transient voltage and its estimates under faulty condition.

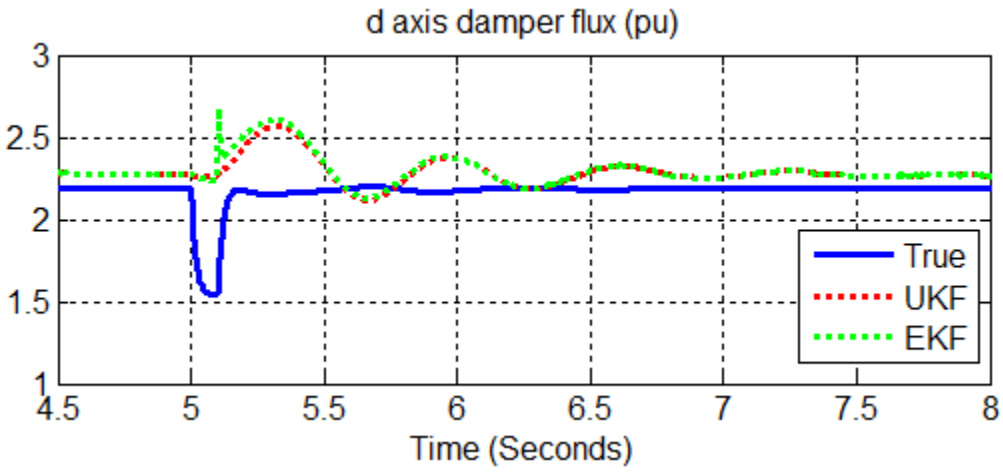

(a) From time interval 4.5 to 8s.

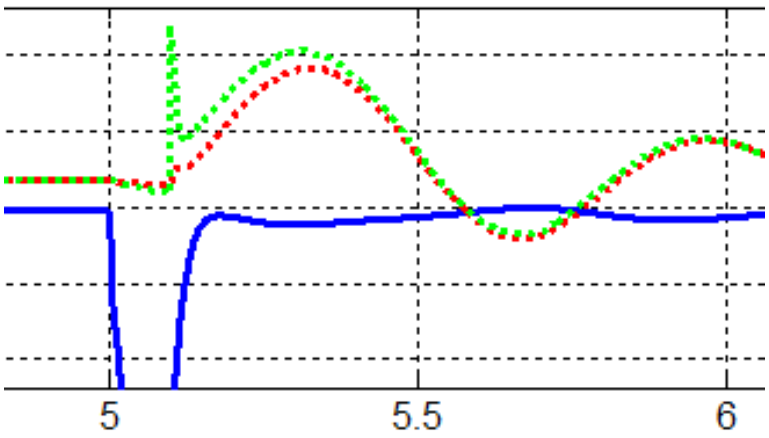

(b) From time interval 5 to 6s.

Figure 7.15 d-axis damper flux and its estimates under faulty condition.

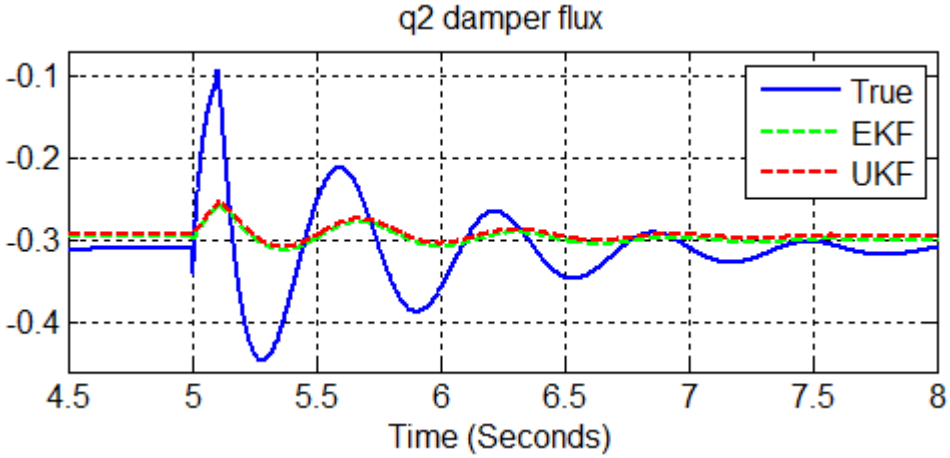

(a) From time interval 4.5 to 8s.

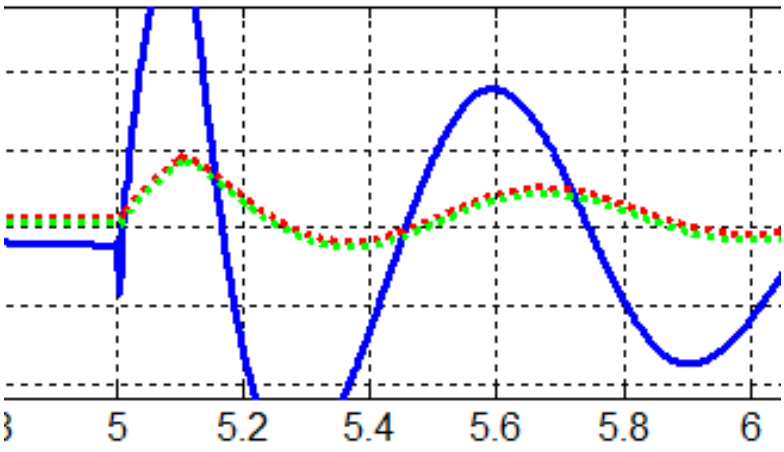

(b) From time interval 5 to 6s.

Figure 7.16 q-axis second damper flux and its estimates under faulty condition.

The estimated outputs (measurement) for this faulty condition are shown in Fig. 7.17 - Fig. 7.18. From Figure 7.17, the Kalman filter filters the noise from the noisy measurement of the active power in normal operation but fails to do so during the fault period. In Figure 7.18, the results for the reactive power are similar to those for the active power. This is because, during the period of the fault, the network topology and parameters are no longer the same as in normal operation. Since the Kalman filter uses the nominal parameter values, it cannot follow the true system dynamics. When the fault is cleared, the network is restored and Kalman filter performs well as before.

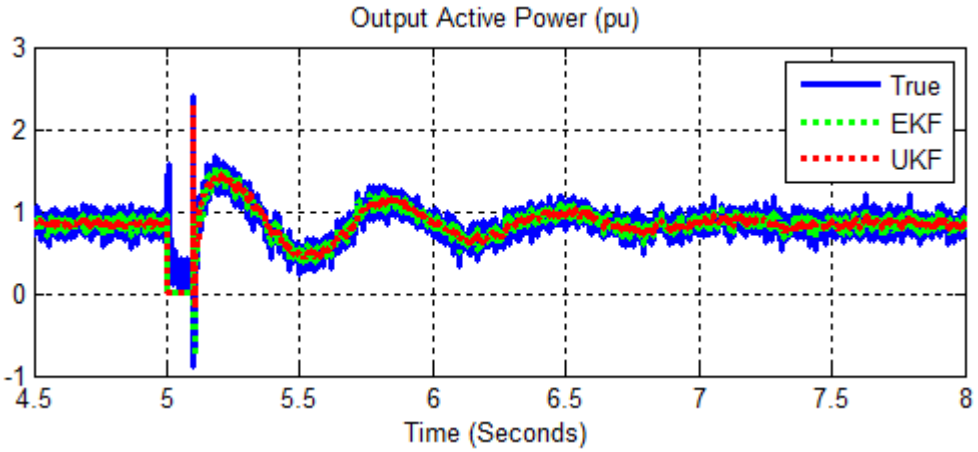

(a) From time interval 4.5 to 8s.

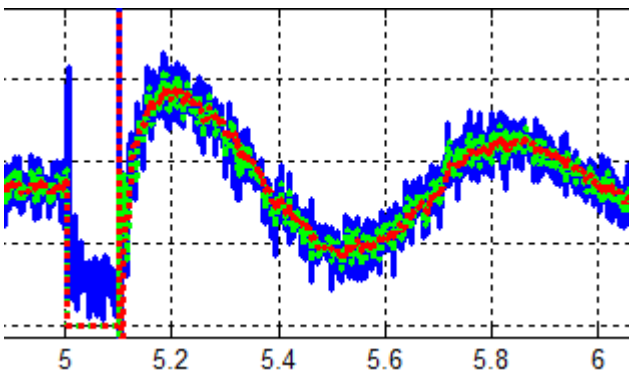

(b) From time interval 5 to 6s.

Figure 7.17 Active power of synchronous generator-1 under faulty condition.

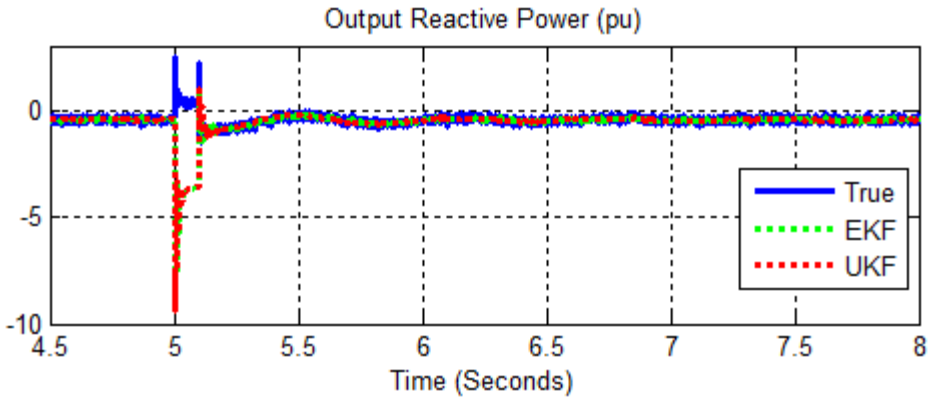

(a) From time interval 4.5 to 8s.

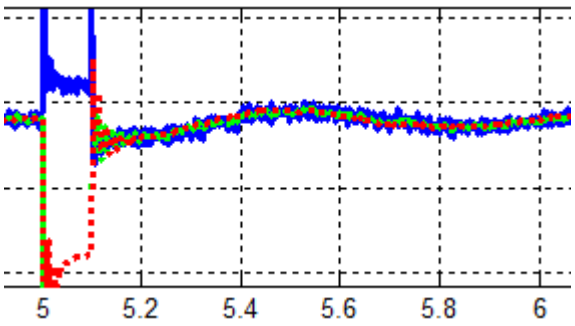

(b) From time interval 5 to 6s.

Figure 7.18 Reactive power of synchronous generator-1 and its estimates under faulty condition.

The box plots of errors obtained from our Monte Carlo simulations are shown in Figure 7.19-7.20. We calculated the RMS errors from 5 second to 10 second and the results are shown in *Table IV*. It is clear from the box plots and *Table IV* that the errors corresponding to EKF are larger than that of UKF under the faulty condition.

Table IV Comparison of RMS errors for EKF and UKF

Filter	RMSE (Max.)	RMSE(Min)	Standard Deviation	RMSE of Rotor Angle (Max)	RMSE of Rotor Angle (Min)	Standard Deviation
EKF	0.5066	0.4766	0.0042	0.0914	0.0900	6.11e-05
UKF	0.3470	0.3430	6.34e-04	0.0907	0.0898	1.18e-04

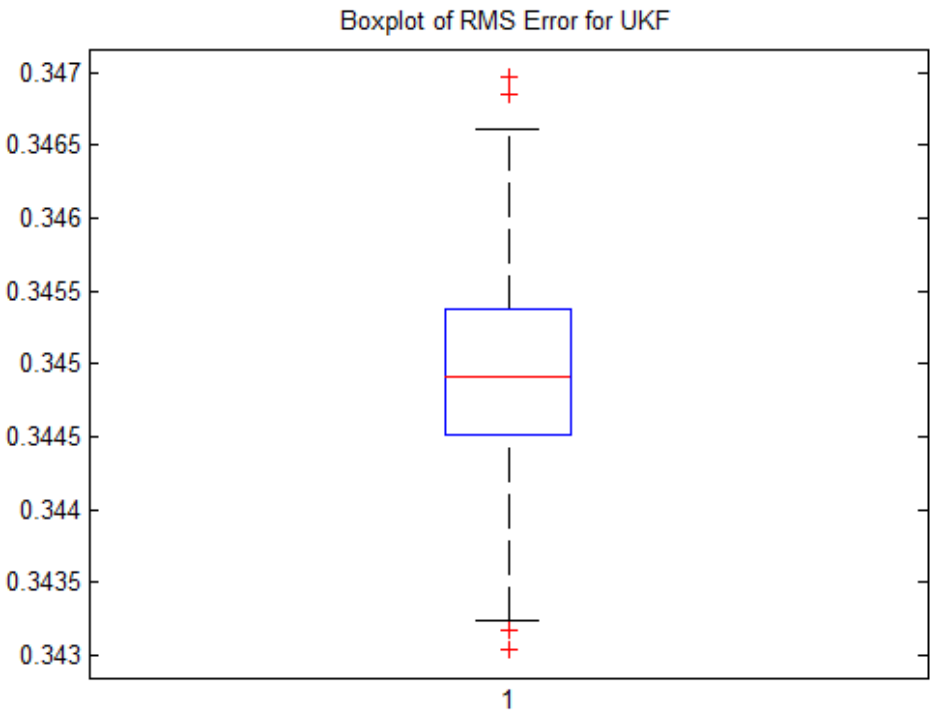

Figure 7.19 Box plot of RMS error for UKF with fault at PCC.

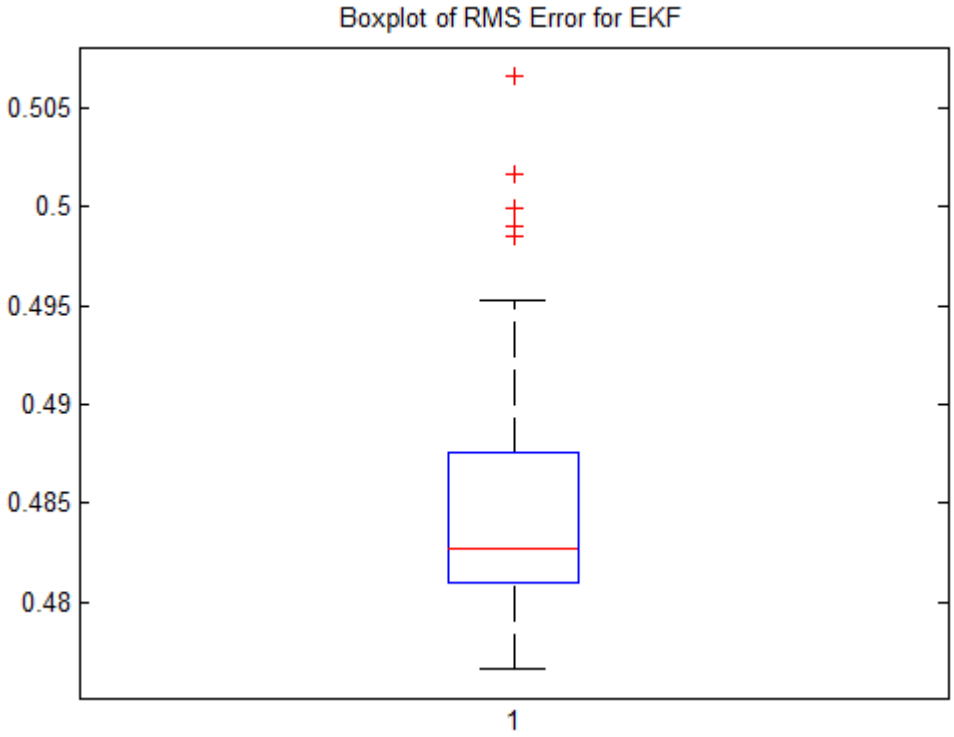

Figure 7.20 Box plot of RMS error for EKF with fault at PCC.

7.3 LOSS OF GENERATOR

We simulated a fault in the line that connects generator 2 to the microgrid to show the performance of the EKF and the UKF subject to loss of generator, The fault is applied at 4.0 s and cleared at 4.1 s and the system becomes stable after the fault is cleared. Both state estimators performed satisfactorily and the estimated results track the actual values of states even after the generator loss. This is validated by the simulation results presented in Figures 7.21-7.26.

The result of 500 Monte Carlo simulations are shown in the box plots of Figure 7.27-Figure 7.28 and in Table V. The figures are the box plots of RMS errors for EKF and UKF. Table V shows the RMS errors calculated for the simulation period of 3.5 second to 10 second. From Table V and the box plots we observe that the EKF results in larger errors than the UKF.

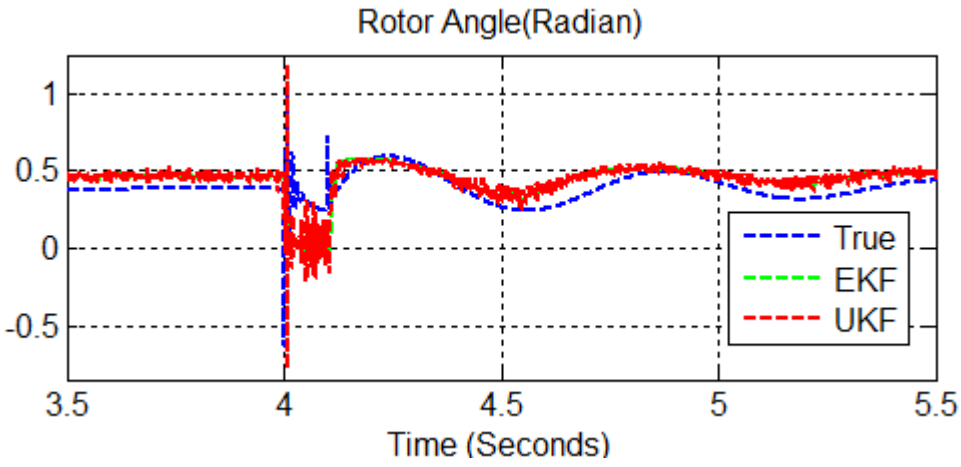

(a) From time interval 3.5 to 5.5s.

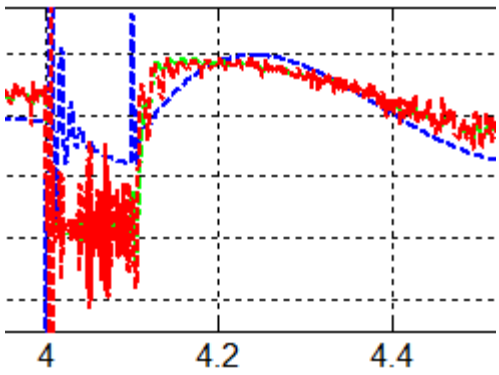

(b) From time interval 4 to 4.4s.

Figure 7.21 Rotor angle and its estimates with loss of generator.

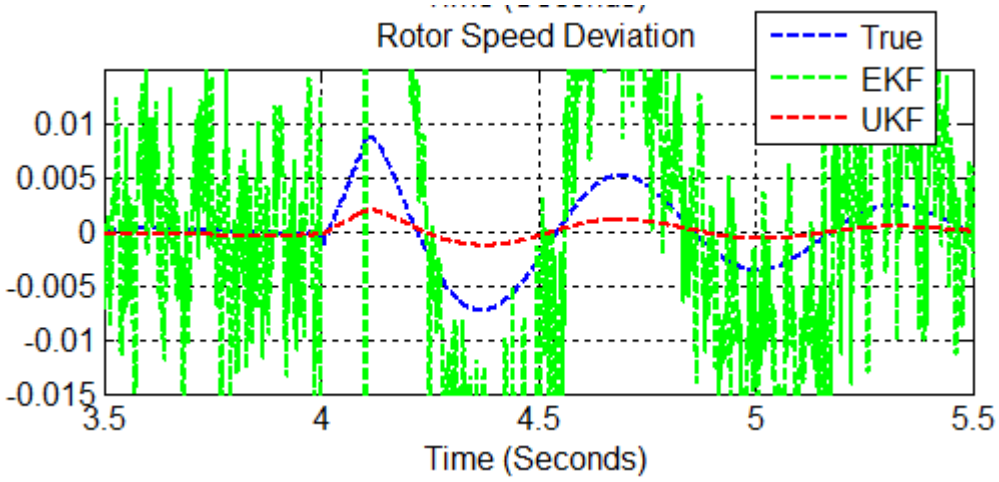

Figure 7.22Rotor speed deviation and its estimates with loss of generator.

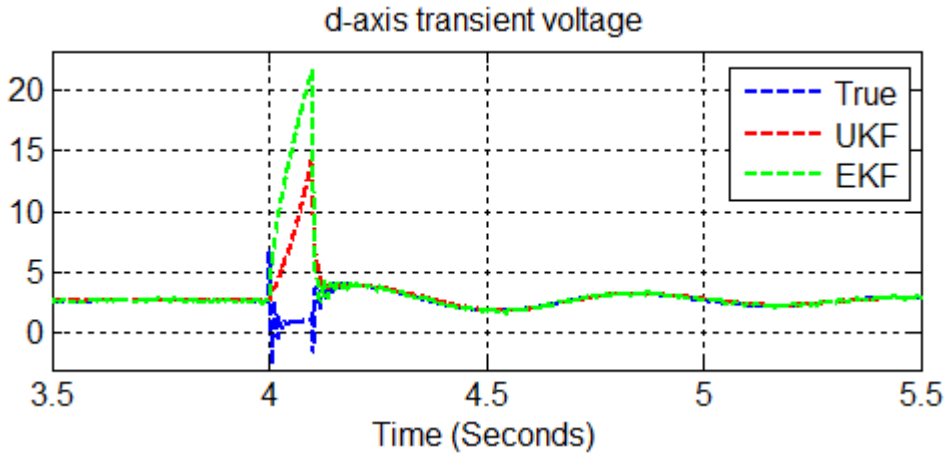

(a) From time interval 3.5 to 5.5s.

(b)

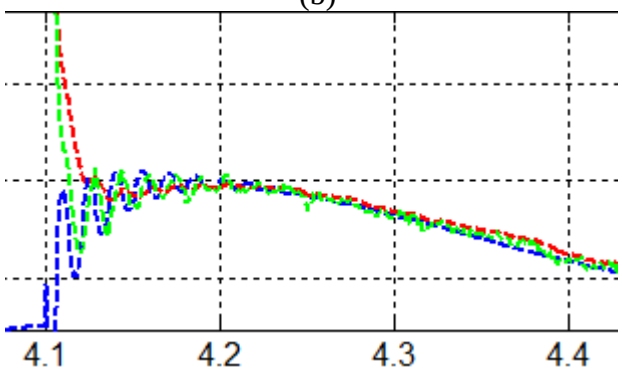

(b) From time interval 4.1 to 4.4s.

Figure 7.23 d-axis transient voltage and its estimates with loss of generator.

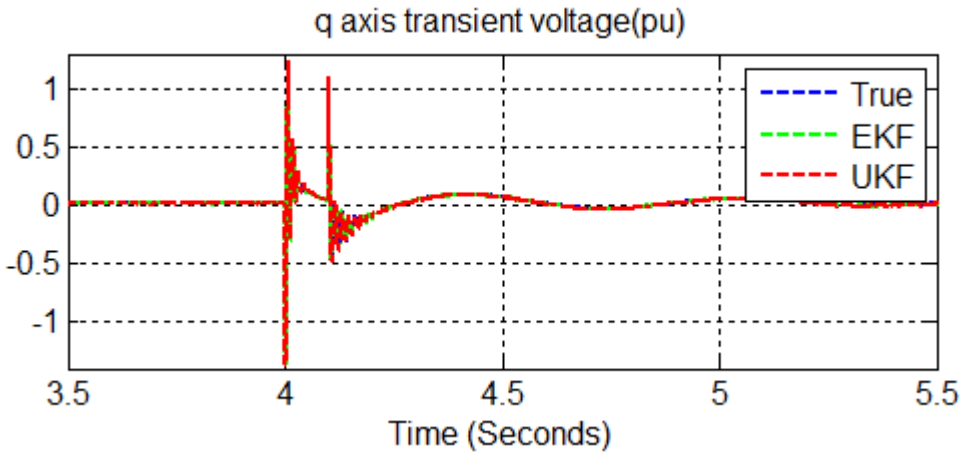

(a) From time interval 3.5 to 5.5s.

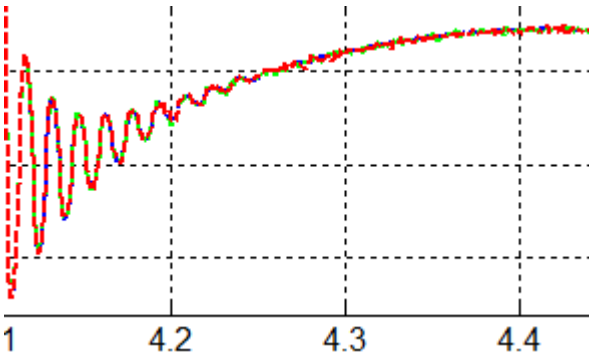

(b) From time interval 4.1 to 4.4s.

Figure 7.24 q-axis transient voltage and its estimates with loss of generator

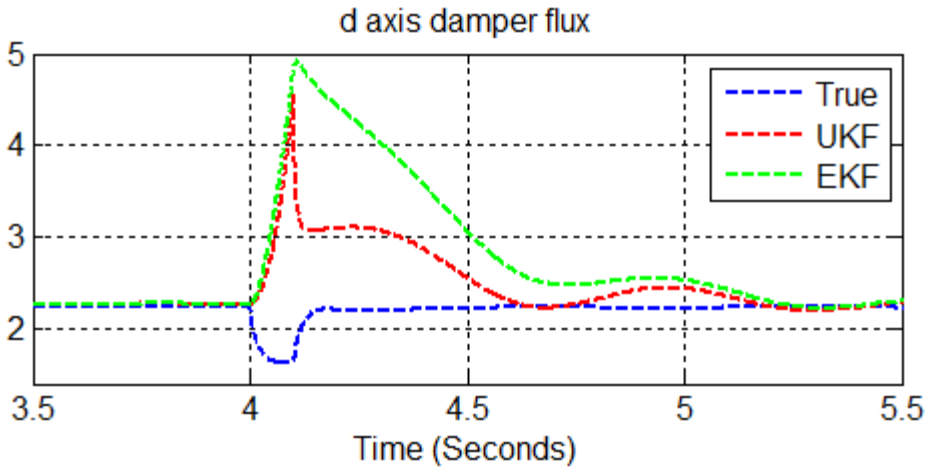

Figure 7.25 d-axis damper flux and its estimates with loss of generator.

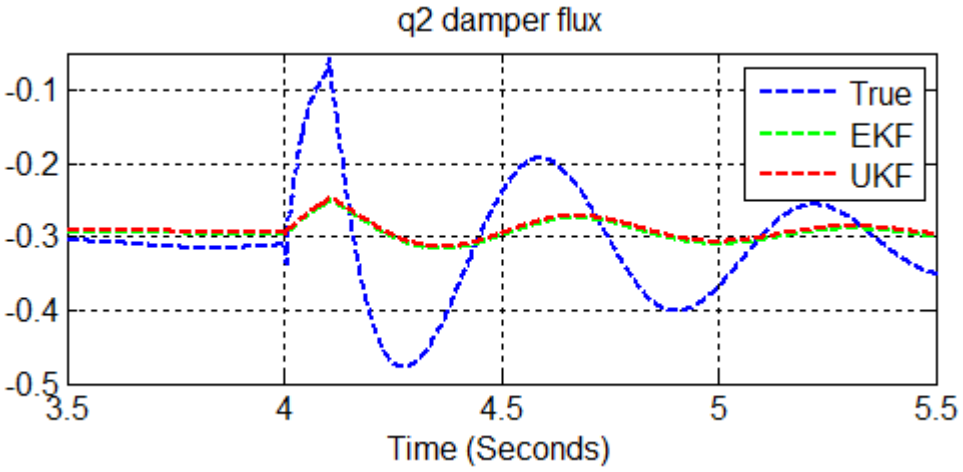

Figure 7.26 q-axis second damper flux and its estimates with loss of generator.

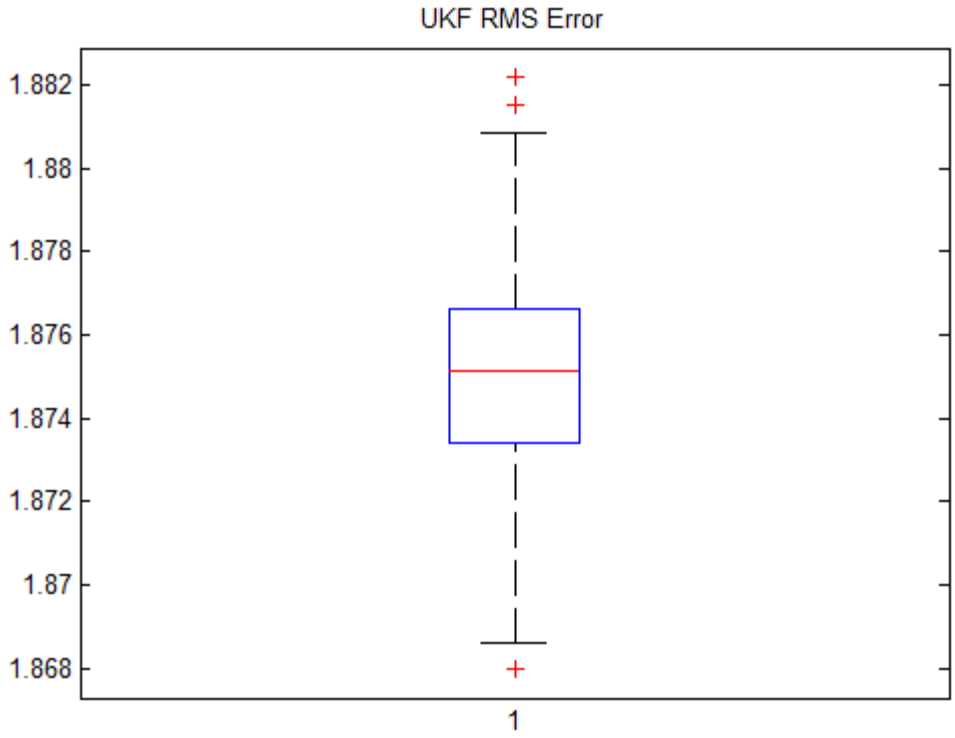

Figure 7.27 Box plot of UKF RMS error with loss of generator.

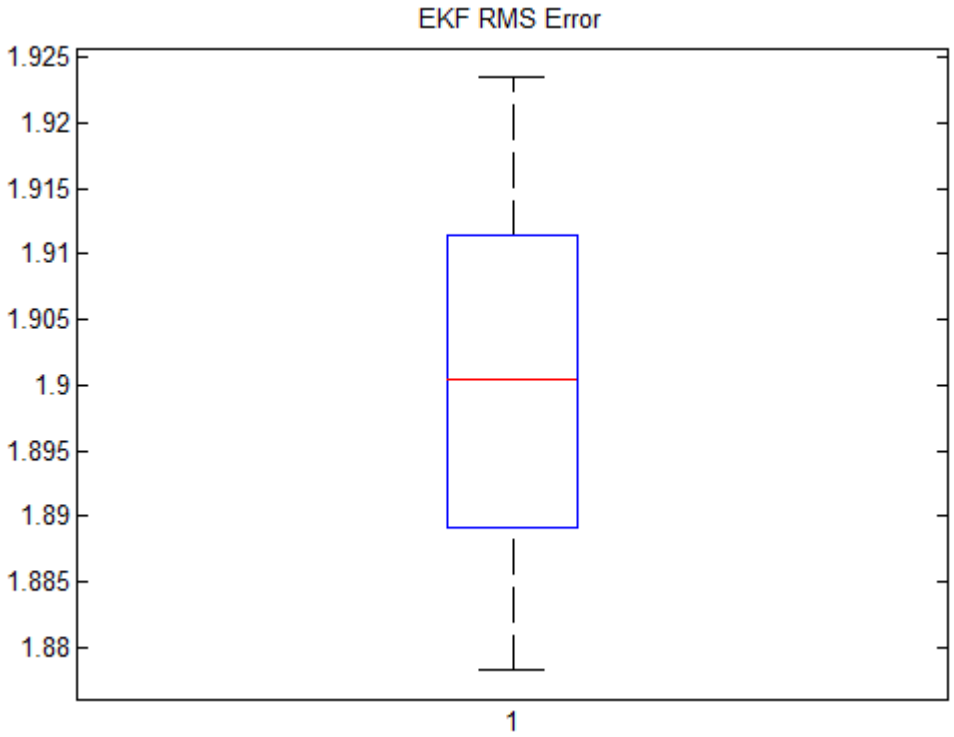

Figure 7.28 Box plot of EKF RMS error with loss of generator.

Table V Comparison of RMS errors for EKF and UKF

Filter	RMSE (Max.)	RMSE(Min)	Standard Deviation	RMSE of Rotor Angle (Max)	RMSE of Rotor Angle (Min)	Standard Deviation
UKF	1.8822	1.8680	0.0024	0.1021	0.0711	0.0044
EKF	1.9235	1.8783	0.0129	0.1033	0.0829	0.0060

7.4 LOSS OF LOAD

We simulated a fault in the line connecting load 2 to the adjacent transformer after 4.5 s and cleared it at 4.6 s to show the performance of EKF and the UKF subject to loss of load. As in other scenarios, the filter estimates have large errors during the fault but track the actual state values after the fault is cleared. Simulation results presented in Figures 7.29-7.34show the performance of both EKF and UKF under loss of load in the microgrid. The simulation results show that both filters can generate estimated states with an appropriate accuracy.

To compare the RMS errors of EKF and UKF under loss of load, we calculated the RMS errors from the results 500 Monte Carlo simulations from 4 to 10s and the results are summarized in the box plots of Figure 7.35, Figure 7.36 and in *Table VI*. In this case, the RMS errors for the UKF are similar to those for the EKF.

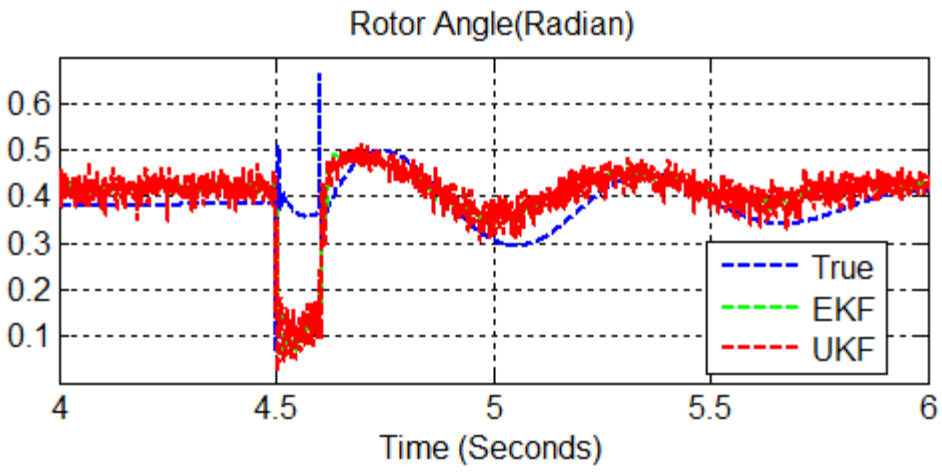

(a) From time interval 4 to 6s.

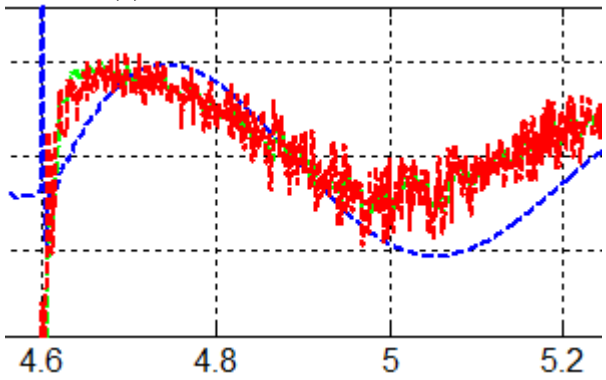

(b) From time interval 4.6 to 5.2s.

Figure 7.29 Rotor angle and its estimates with loss of load.

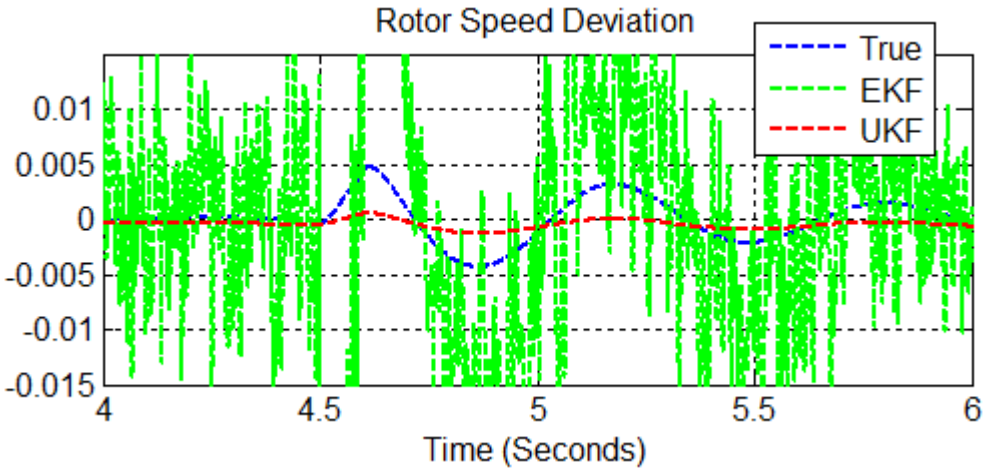

Figure 7.30 Rotor speed deviation and its estimates with loss of load.

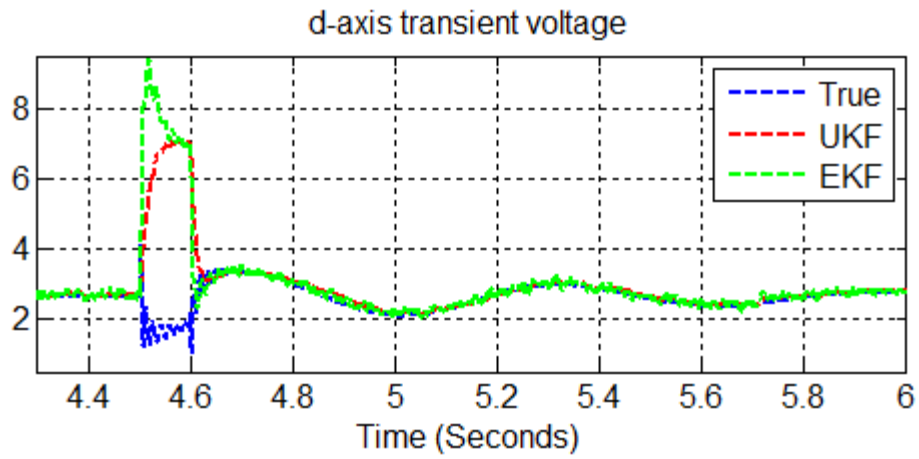

(a) From time interval 4.4 to 6s.

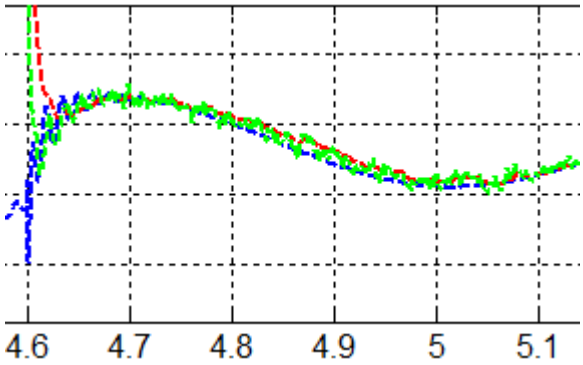

(b) From time interval 4.6 to 5.1s.

Figure 7.31 d-axis transient voltage and its estimates with loss of load.

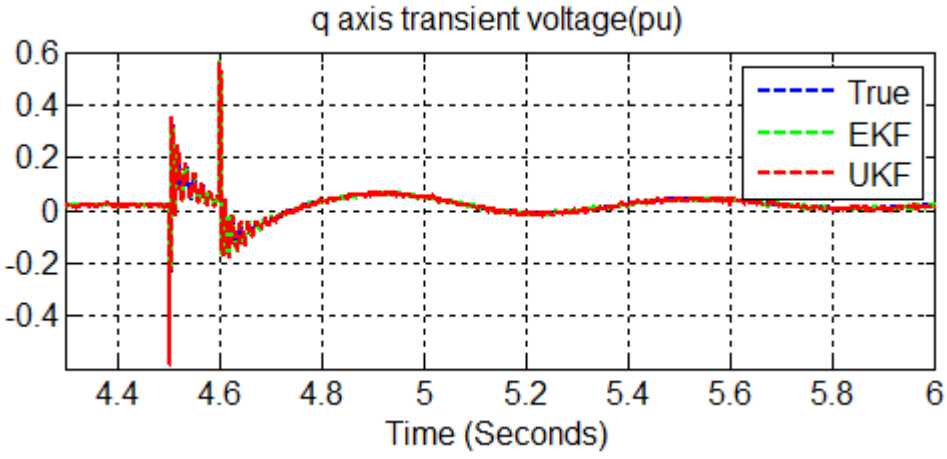

(a) From time interval 4.4 to 6s.

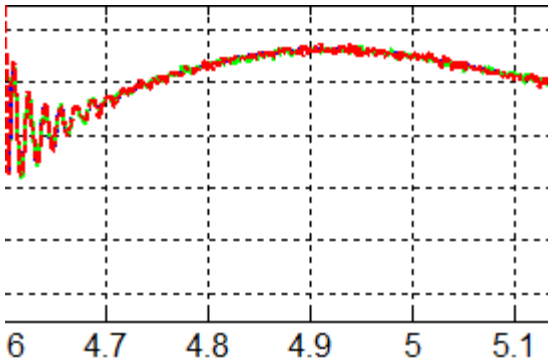

(b) From time interval 4.6 to 5.1s.

Figure 7.32 q-axis transient voltage and its estimates with loss of load.

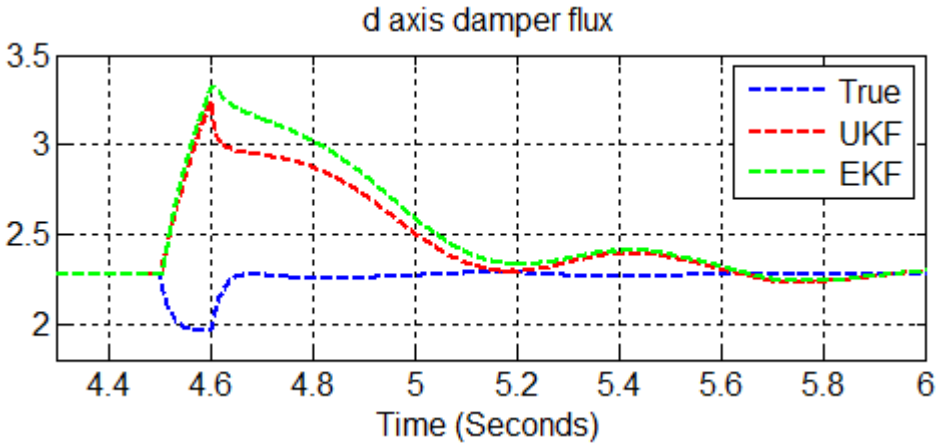

Figure 7.33 d-axis damper flux and its estimates with loss of load.

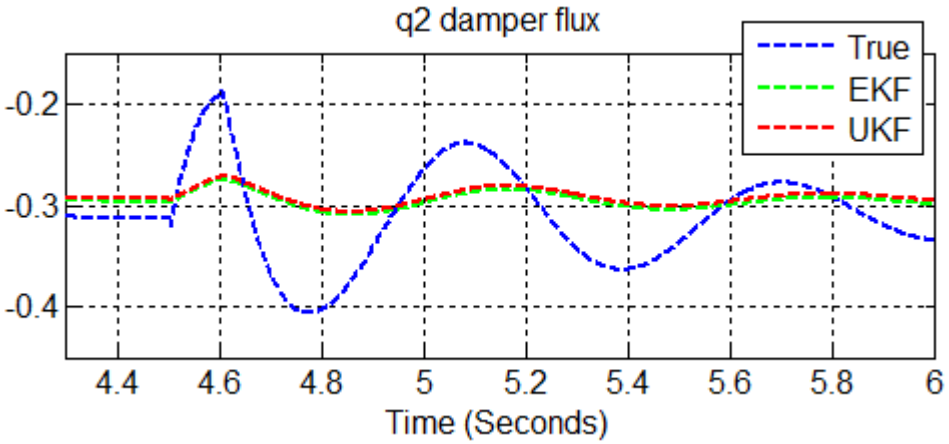

(a) From time interval 4.4 to 6s.

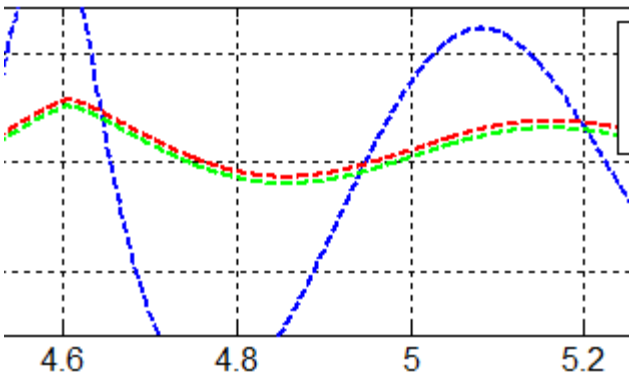

(b) From time interval 4.6 to 5.2s.

Figure 7.34 q-axis second damper flux and its estimates with loss of load.

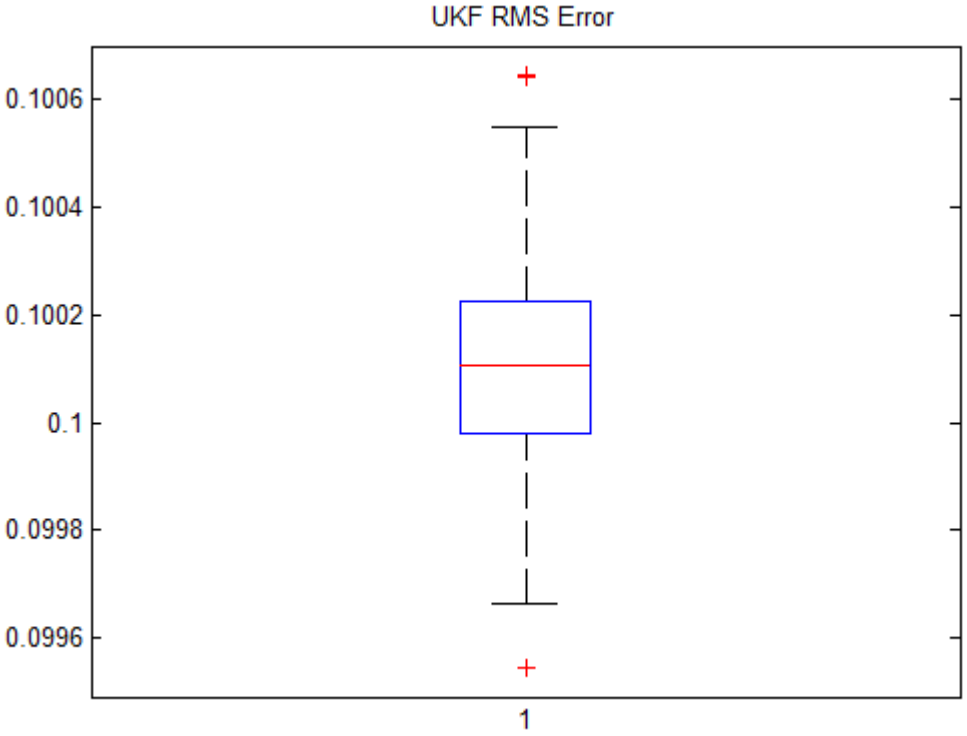

Figure 7.35 UKF RMS error with loss of load.

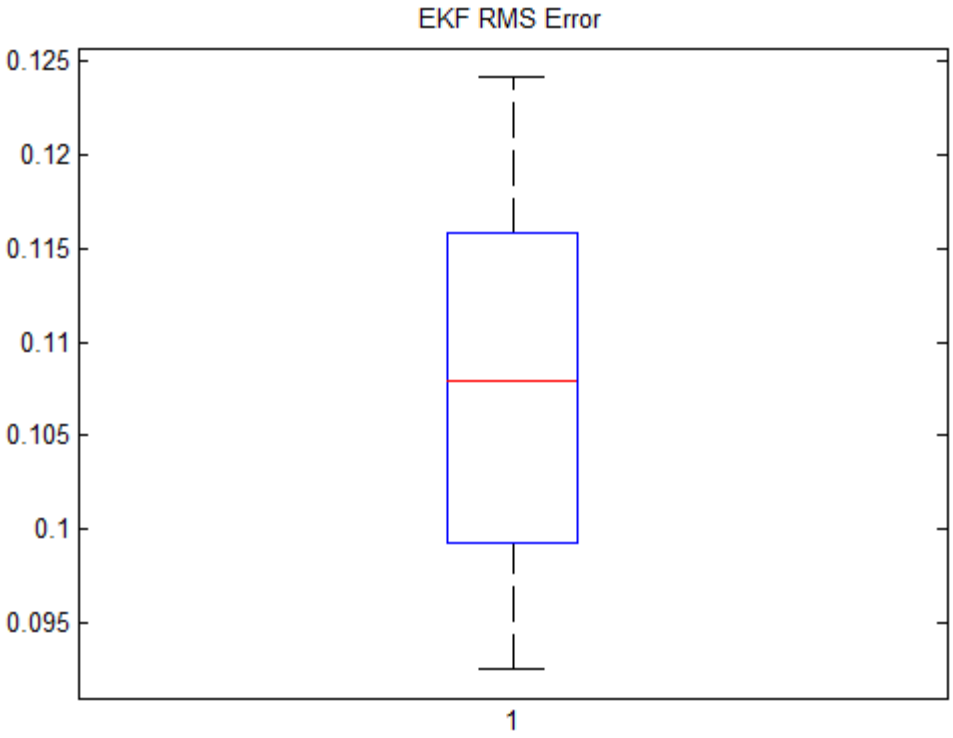

Figure 7.36 EKF RMS error with loss of load.

Table VI Comparison of RMS errors of EKF and UKF with loss of load.

Filter	RMSE (Max.)	RMSE(Min)	Standard Deviation	RMSE of Rotor Angle (Max)	RMSE of Rotor Angle (Min)	Standard Deviation
UKF	0.1006	0.0995	1.87e-04	0.0966	0.0725	0.0039
EKF	0.1241	0.0926	0.009	0.0992	0.0852	0.004

7.5 PACKET LOSS AND TIME DELAY

In this scenario, we assume that the measurement data are transmitted through a communication channel to the estimator. At each time step, two measurements are sent in a single packet. The packet can reach the estimator in time, reach it after a time delay, or can be lost. In this thesis, it is assumed that the packet loss is a Bernoulli

random process with parameter $p = 0.9$. The packet time delay is a binomial random process with parameters $(n, p) = (3, 0.4)$.

The state estimation results are given in Figure 7.37 - Figure 7.42 with packet loss and delay while microgrid is operating normally. With 10% packet loss and with random delay, the simulation results are almost the same as in Figure 7.1 - Figure 7.6. The results are obtained using the algorithm of Chapter 5. From Figure 7.37, the estimated rotor angle tracks the actual values. This is true for other state estimates because 10% packet drop can be tolerated by the Kalman filter. However, packet loss probability has a critical value above which the performance of the Kalman filter starts to deteriorate.

The simulation results show that both the EKF and UKF estimation results are satisfactory with packet loss and time delay. In some cases (here rotor speed deviation and q axis second damper flux), estimation with UKF is significantly better than the EKF. Other estimation results are similar for both filters.

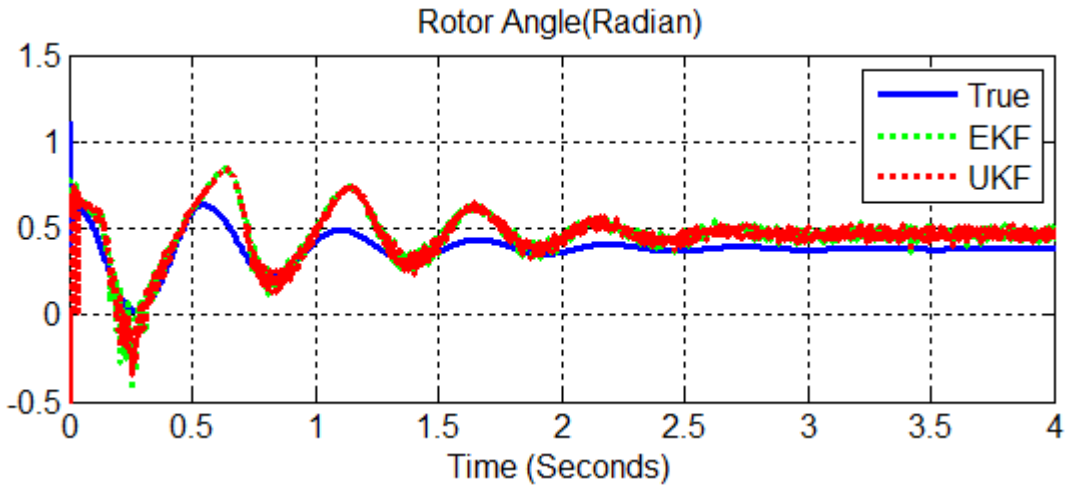

Figure 7.37 Rotor angle and its estimates with packet loss and time delay.

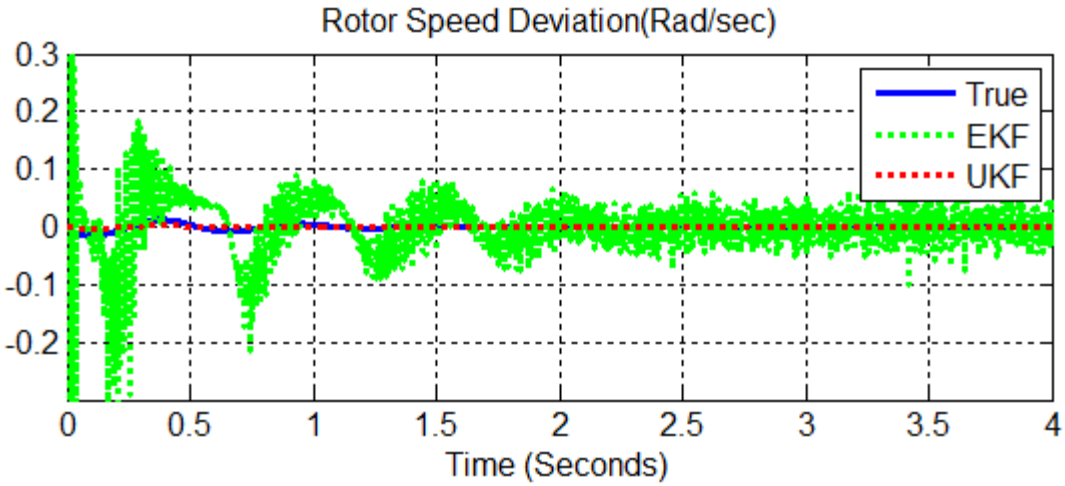

Figure 7.38 Rotor speed deviation and its estimates with packet loss and time delay.

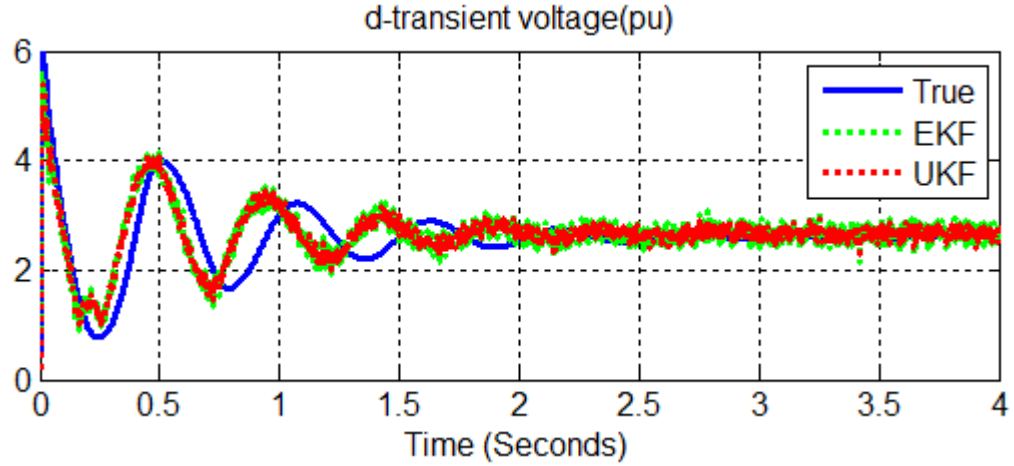

Figure 7.39 d-axis transient voltage and its estimates with packet loss and time delay.

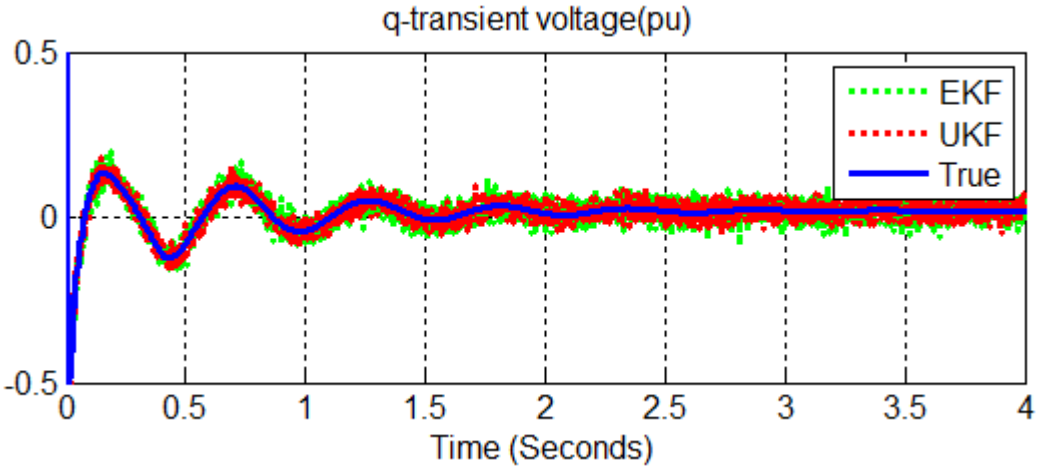

Figure 7.40 q-axis transient voltage and its estimates with packet loss and time delay.

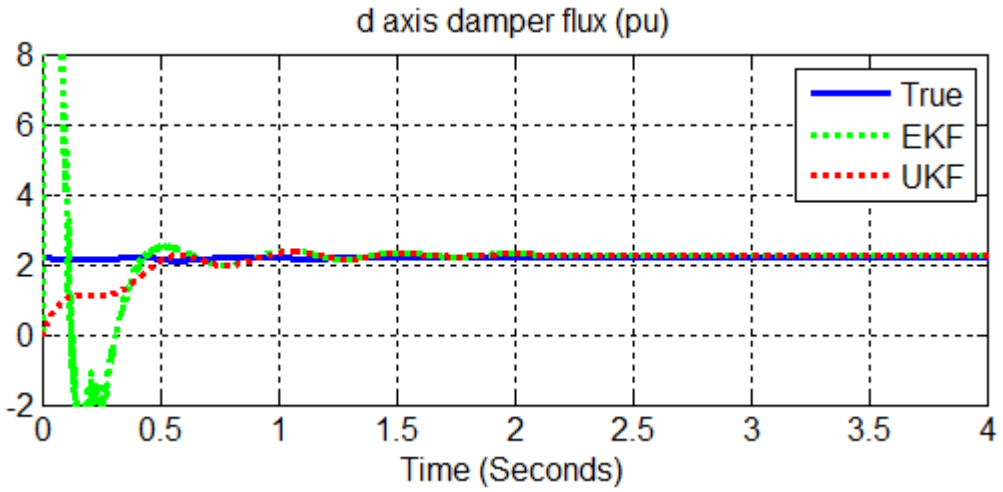

Figure 7.41 d-axis damper flux and its estimates with packet loss and time delay.

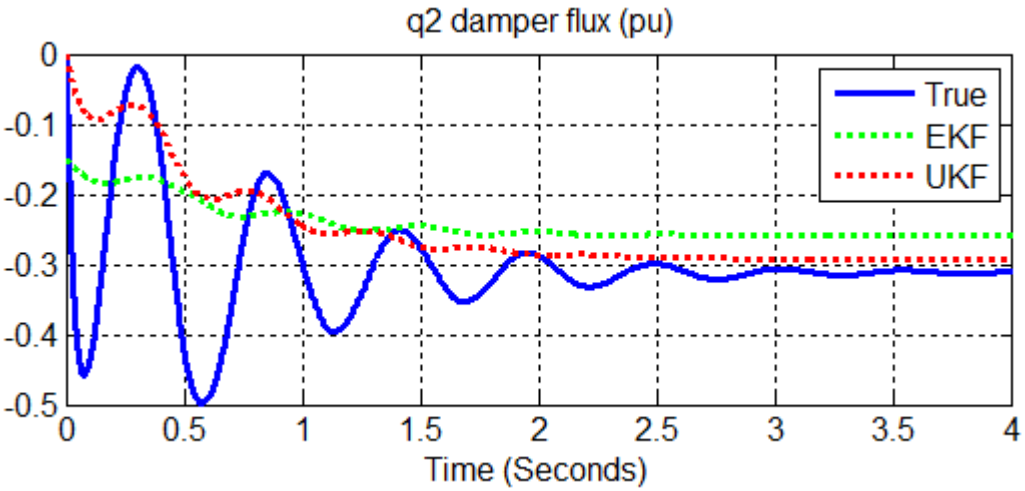

Figure 7.42 q-axis second damper flux and its estimates with packet loss and time delay.

We observe from Figure 7.37 - Figure 7.42 that the state estimates with 10% packet loss and randomly delayed packets approach those with no packet loss. Implementing the algorithm of Chapter 5 requires extra memory to store predicted values for each time step for use in the corrector when measurements become available. This increase in the cost associated with this Kalman filter is justifiable given the reduction in the estimation errors.

We ran 500 Monte Carlo simulations and calculated RMS errors for the entire simulation duration of 10 s. In this scenario, the RMS errors for the EKF and the UKF are similar

Table VII Comparison of RMS errors of EKF and UKF

Filter	RMSE (Max.)	RMSE(Min)	Standard Deviation	RMSE of Rotor Angle (Max)	RMSE of Rotor Angle (Min)	Standard Deviation
UKF	1.1560	1.1050	0.0146	0.0924	0.0913	0.0041
EKF	1.3738	1.1251	0.0725	0.0921	0.0935	0.0057

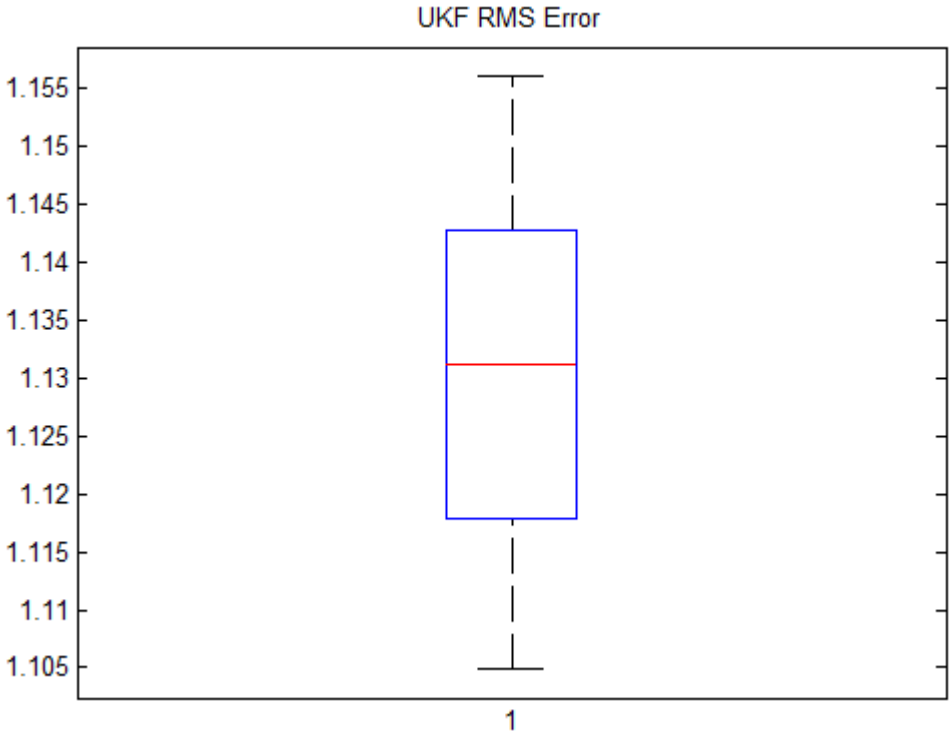

Figure 7.43 Box plot of UKF RMS error with packet loss and time delay.

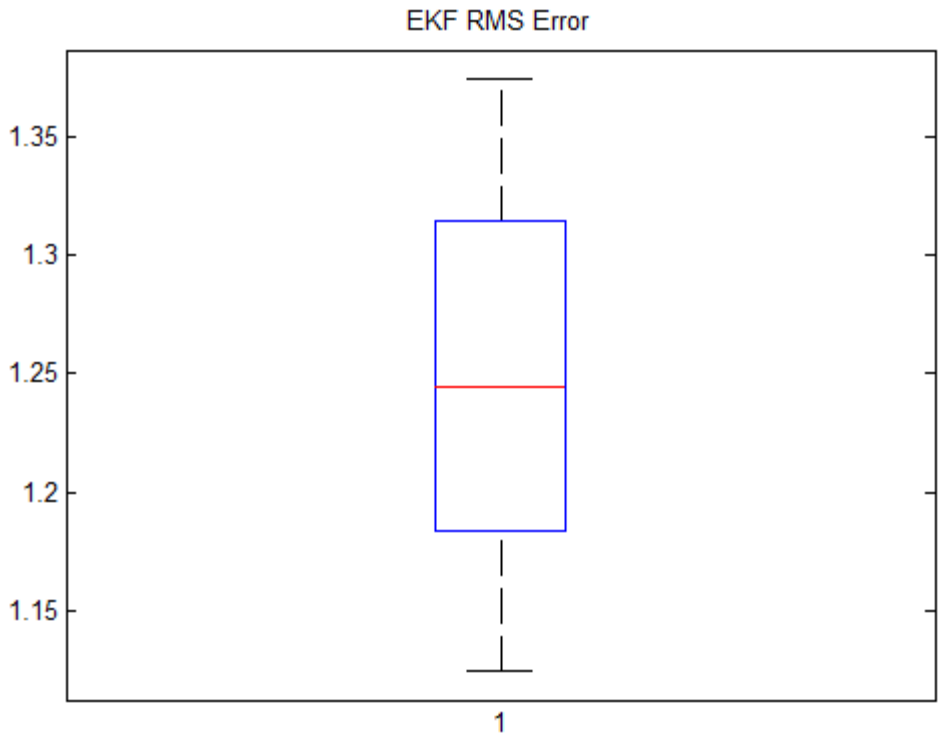

Figure 7.44 Box plot of EKF RMS error with packet loss and time delay.

7.6 ROBUST STATE ESTIMATION

Gross errors in the measurements and sudden changes of states caused by sudden load changes and network topology errors are considered as bad data. It is not uncommon for bad data or outliers to appear in measurement data and be transmitted through the communication network due to sensor errors. Outliers can seriously degrade the performance of conventional state estimators using nonlinear filters such as EKF and the UKF [61]. Robust state estimators, such as the GM-EKF allow dynamic state estimation in the presence of outliers in measurements. For the GM-EKF, the detection of outliers is carried out by using projection statistics. The bad data are weighted down and used in state estimation but not discarded.

We introduced 6 outliers in the active power measurements with values set equal to 50 for 6 consecutive samples of active power starting at time$t$ =2.5 s. This represents a gross measurement error since the active power injections are below 2.8 per unit at all times. State estimation results from the EKF, the UKF and the GM-EKF subject to measurements with bad data are presented in Figure 7.109- Figure 7.114. We present the simulations in two plots for each state. Each figure includes two plots, one shows the entire plot and the other shows a close-up of the outlier.

We observe that the larger the magnitude of the outlier, the worse the estimation results from the EKF and UKF. However, the GM-EKF exhibits good state estimation by weighting down the outliers. A drawback of the GM-EKF is that it loses tracking capability when the system nonlinearities are severe. This occurs when power system is under too much stress or undergoing a large variation in system states following a large disturbance [12].

Simulation results from the EKF, UKF and GM-EKF are presented along with the true values for comparison. If the figure legends, the GM-EKF is referred to as the REKF. The state estimates diverge from the true values when the outlier is included in the measurements at 2.5 s. This is the case with EKF and UKF as seen in Figures 7.45 - Figure 7.49. However, the estimates are not equally affected by bad data. For example, Figure 7.50 show that the effects of outliers on the estimates from the EKF and the UKF are small.

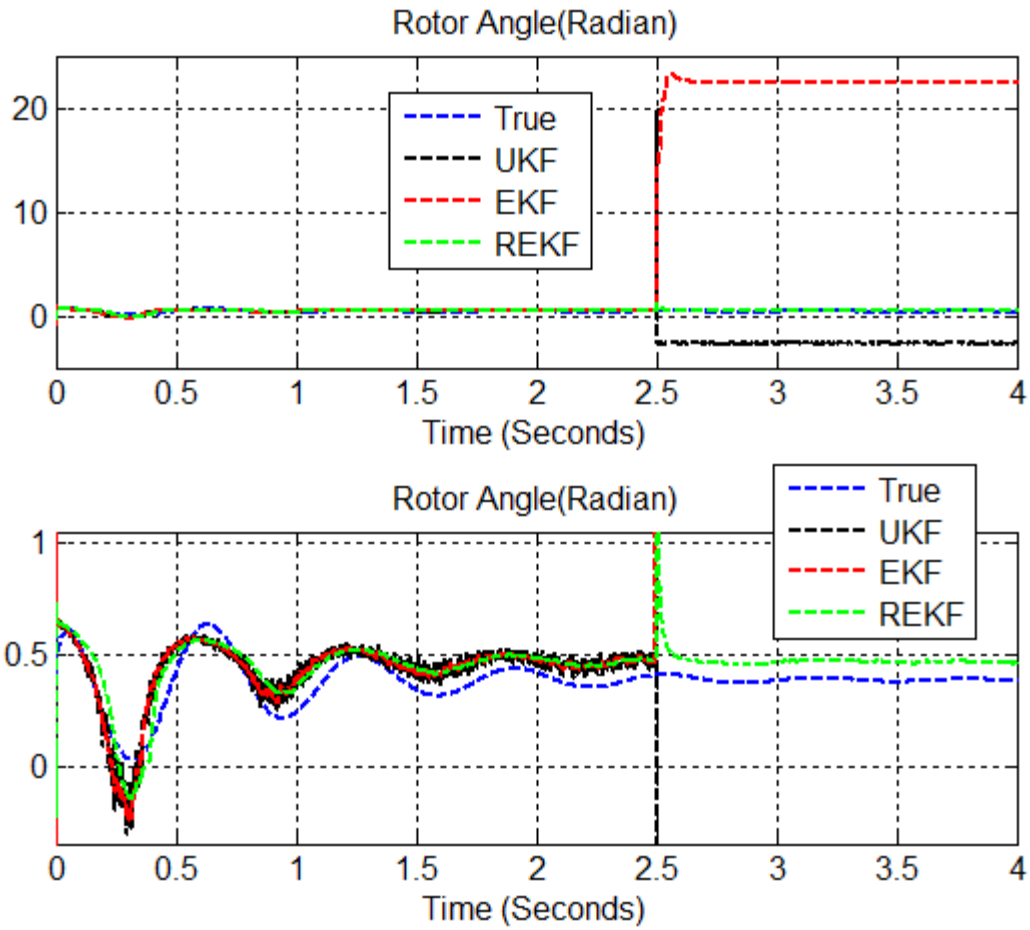

Figure 7.45 Rotor angle and its estimates with outliers.

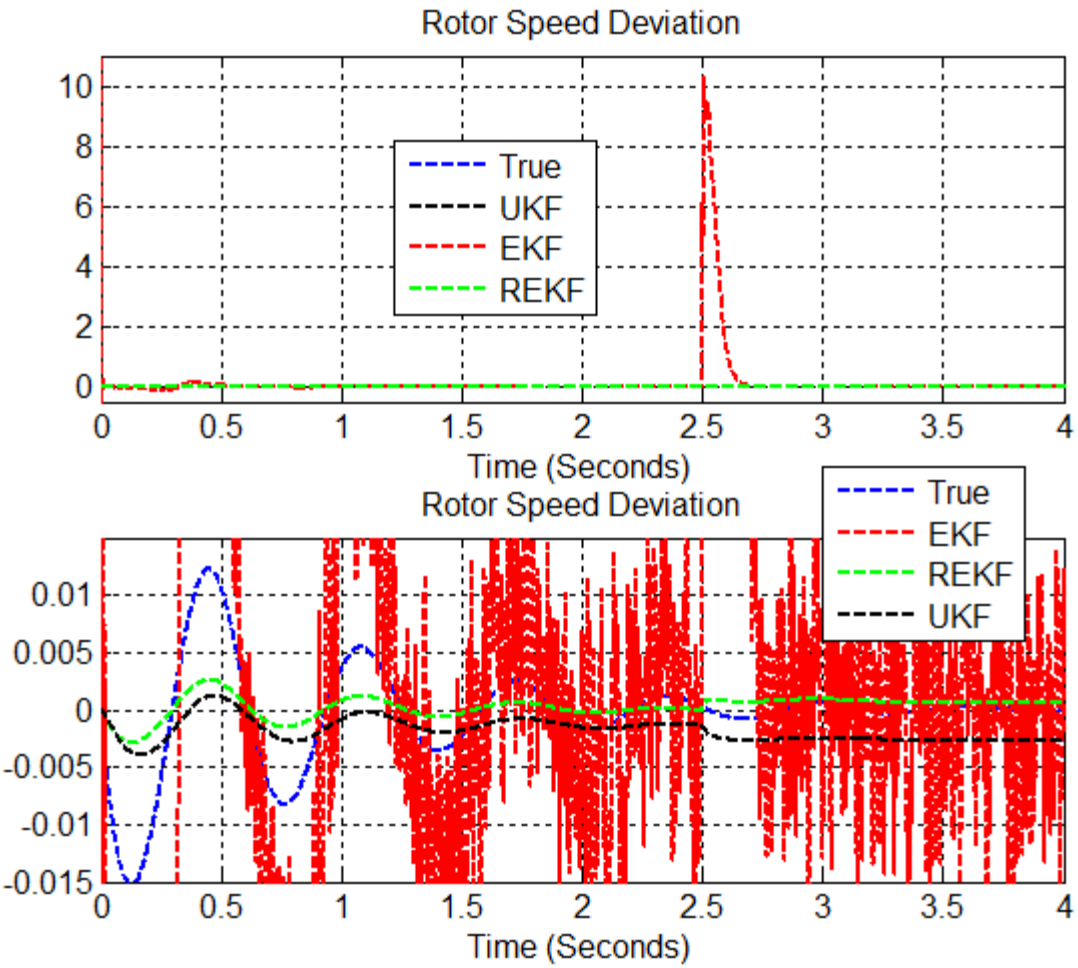

Figure 7.46 Rotor speed deviation and its estimates with outliers.

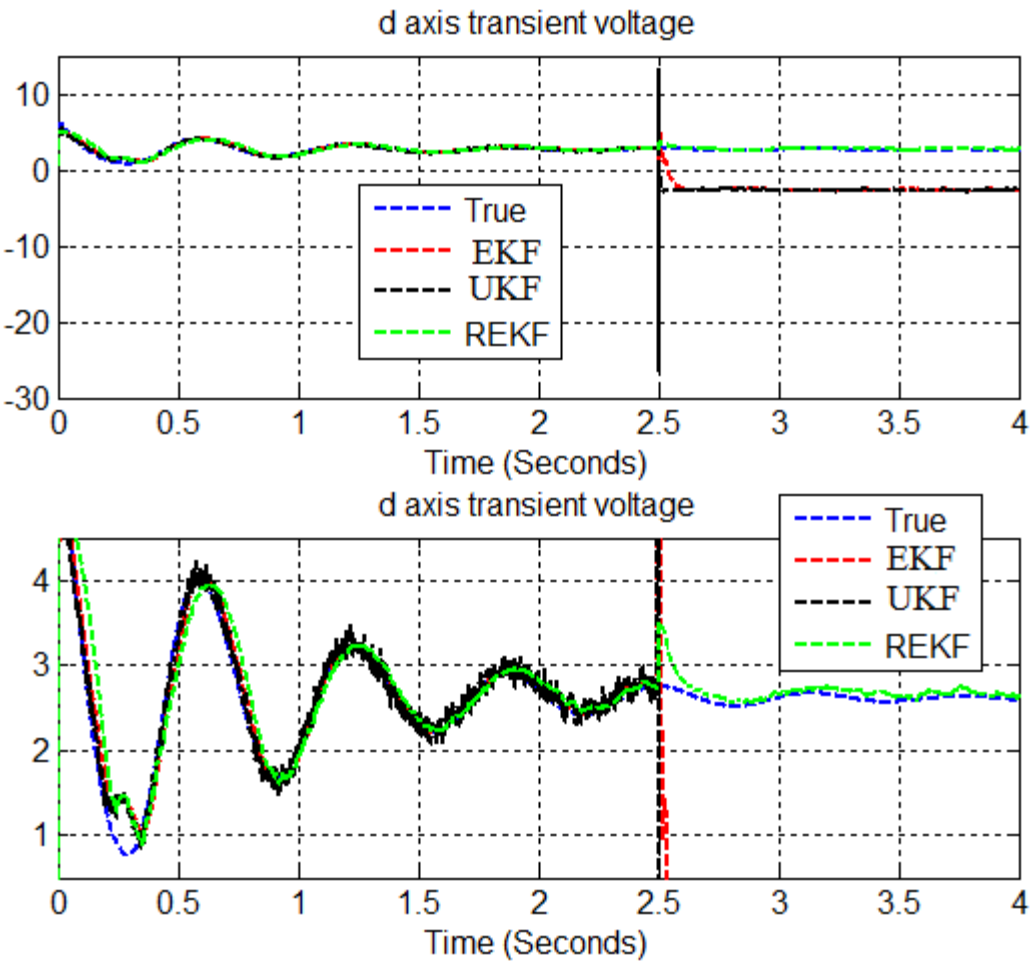

Figure 7.47 d-axis transient voltage and its estimates with outliers.

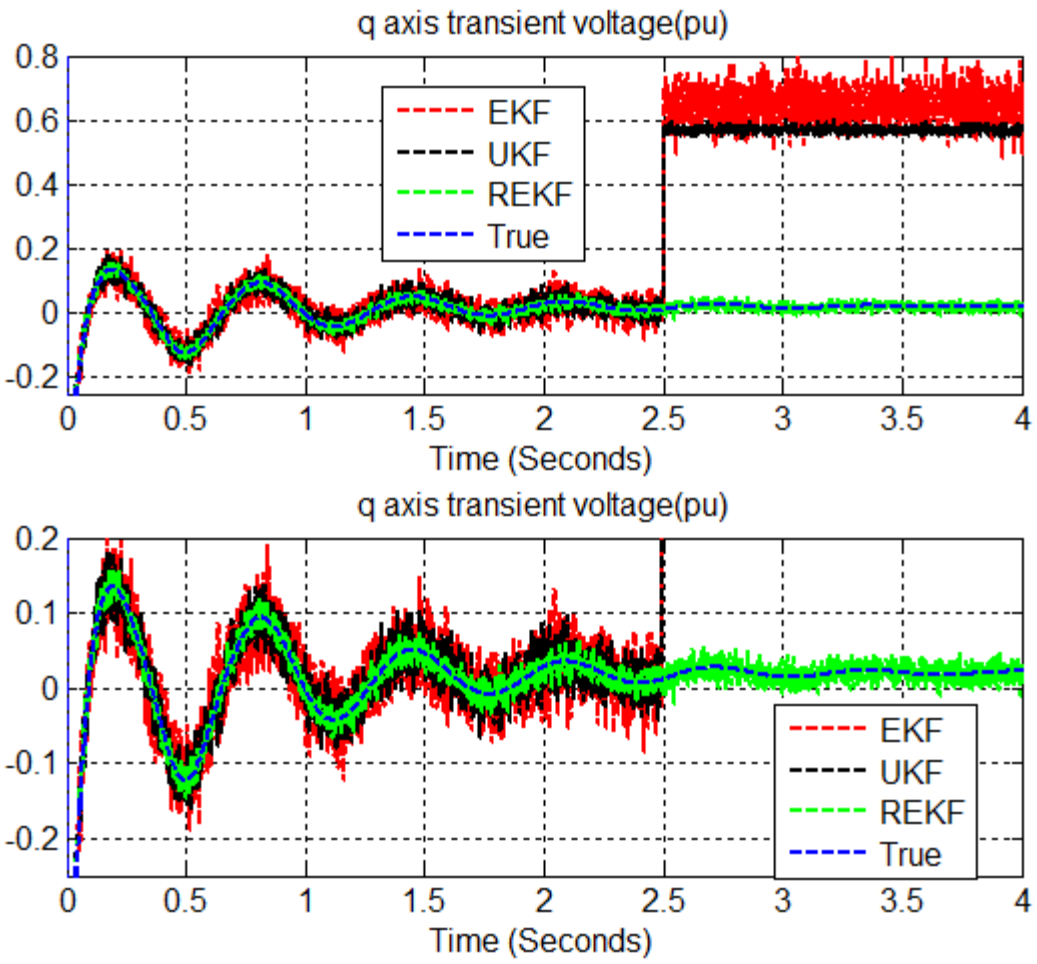

Figure 7.48 q-axis transient voltage and its estimates with outliers.

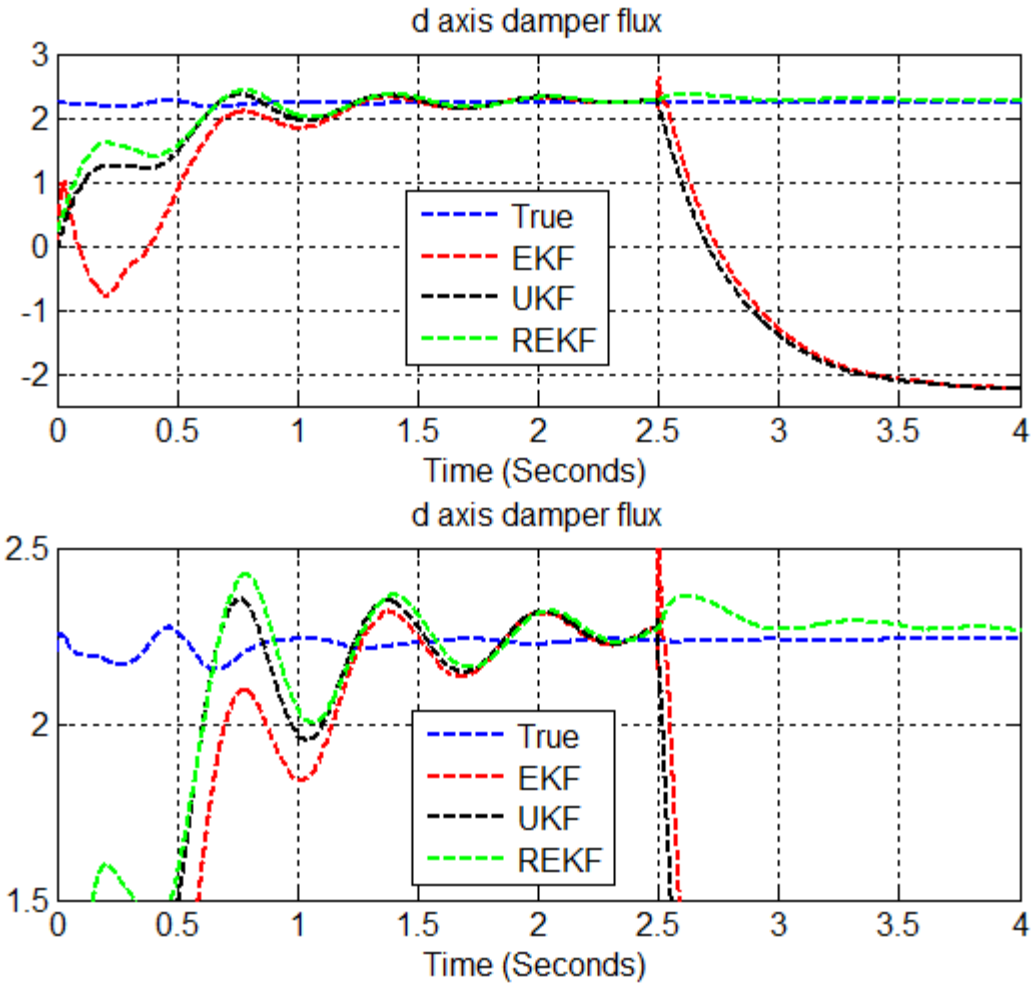

Figure 7.49 d-axis damper flux and its estimates with outliers.

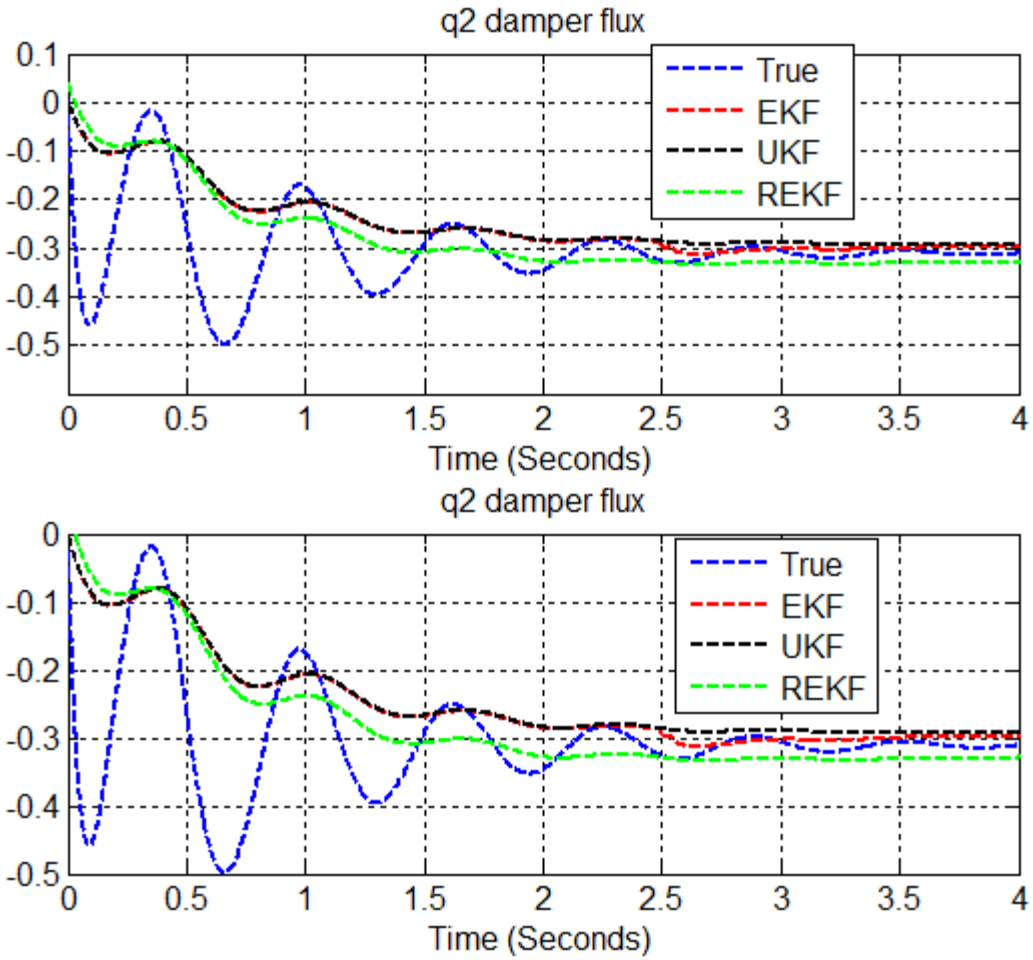

Figure 7.50 q-axis second damper flux and its estimates with outliers.

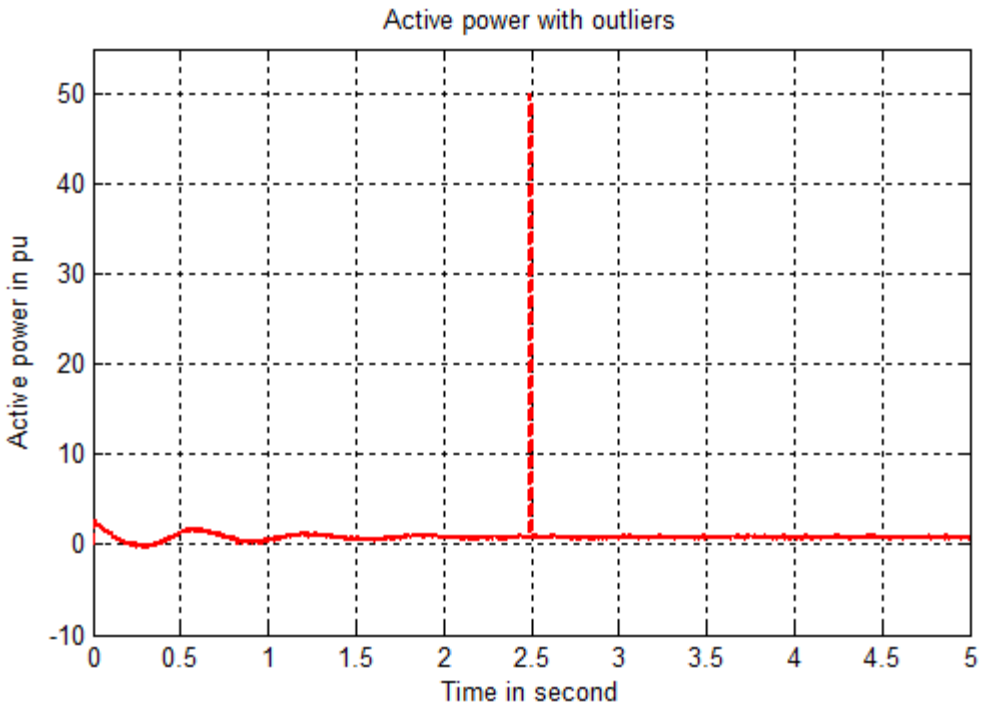

Figure 7.51 Active power with outliers.

7.7 UKF and GM-EKF WITH BAD DATA

In this section, we present simulation results subject to bad data for the GM-EKF together with the UKF using two different approaches. The first approach replaces the bad data with the predicted measurements, and is referred to as the KLM. The second approach replaces the bad data with the last good measurement, and is referred to as the KPM. We inserted 10 outliers of 100per unit (pu) in 10 consecutive active power samples starting from 2 s. Those are well above the actual active power values of below 1 pu. The active power measurement with outlier is shown in Figure 7.55. We ran 500 Monte Carlo simulations of the three robust estimators.

We observe that both UKF state estimates are better than the GM-EKF estimates as shown in Figures 7.52-7.54. This is particularly the case at time 2 s when we inserted outliers where the GM-EKF exhibits a larger spike in its estimates of several states. For

example in rotor angle, d-axis transient voltage and d-axis damper flux, the GM-EKF takes longer times to track the actual states. In contrast, the robust UKFs do not show larger spikes with bad data. Our 500 Monte Carlo simulations show that the UKFs also provide better performance in terms of RMS errors than the GM-EKF, as observed from *Table VIII*. This shows that the modified UKF can perform better than the GM-EKF subject to bad data.

Table VIII Comparison of RMS error for various estimators

Filter	RMSE (Max.)	RMSE(Min)	Standard Deviation	RMSE of Rotor Angle (Max)	RMSE of Rotor Angle (Min)	Standard Deviation
KLM	0.0889	0.0874	2.34e-04	0.0997	0.0760	0.0043
KPM	0.0887	0.0875	2.21e-04	0.0989	0.0741	0.0044
GM-EKF	0.1346	0.1336	2.21e-04	0.0883	0.0843	9.64e-04

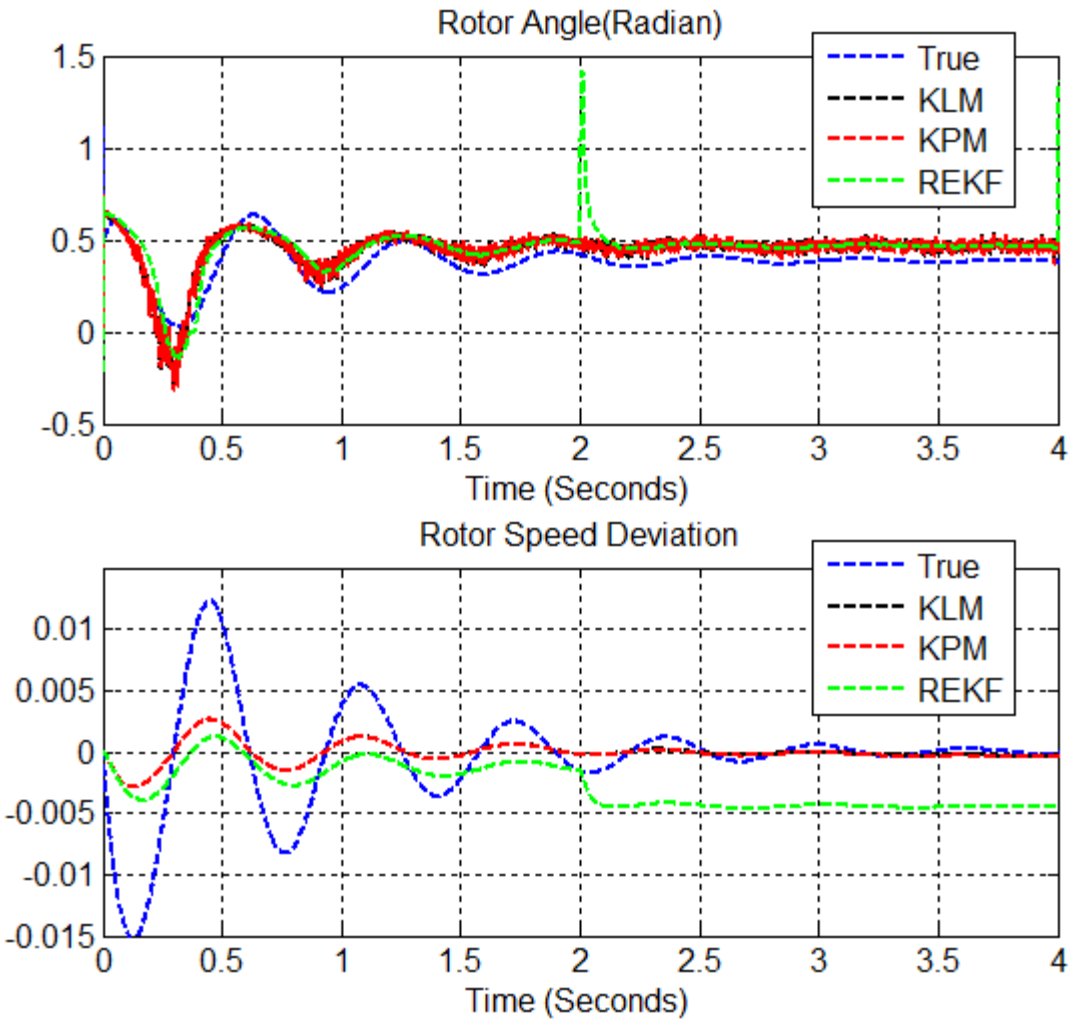

Figure 7.52 Rotor angle, rotor speed deviation and their estimates with bad data.

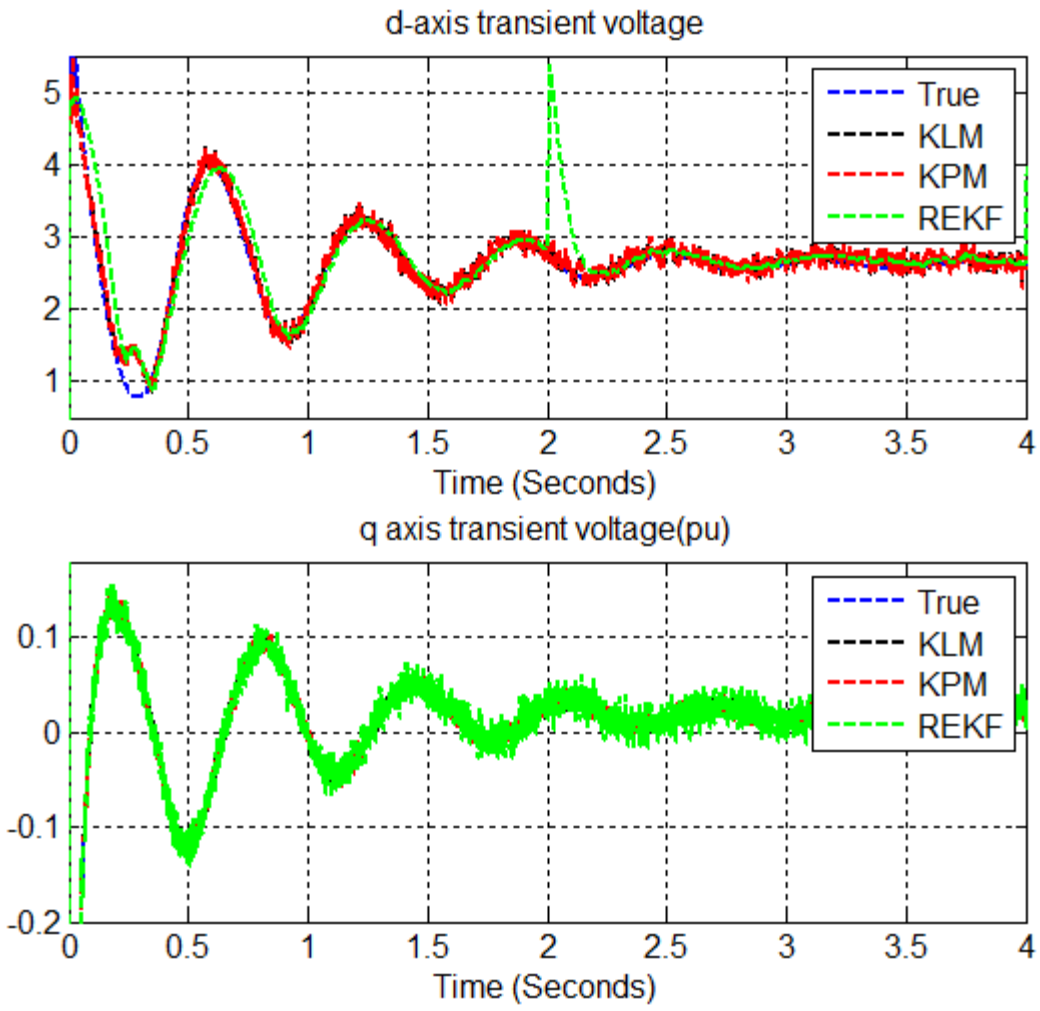

Figure 7.53 d-axis, q-axis transient voltage and their estimates with bad data.

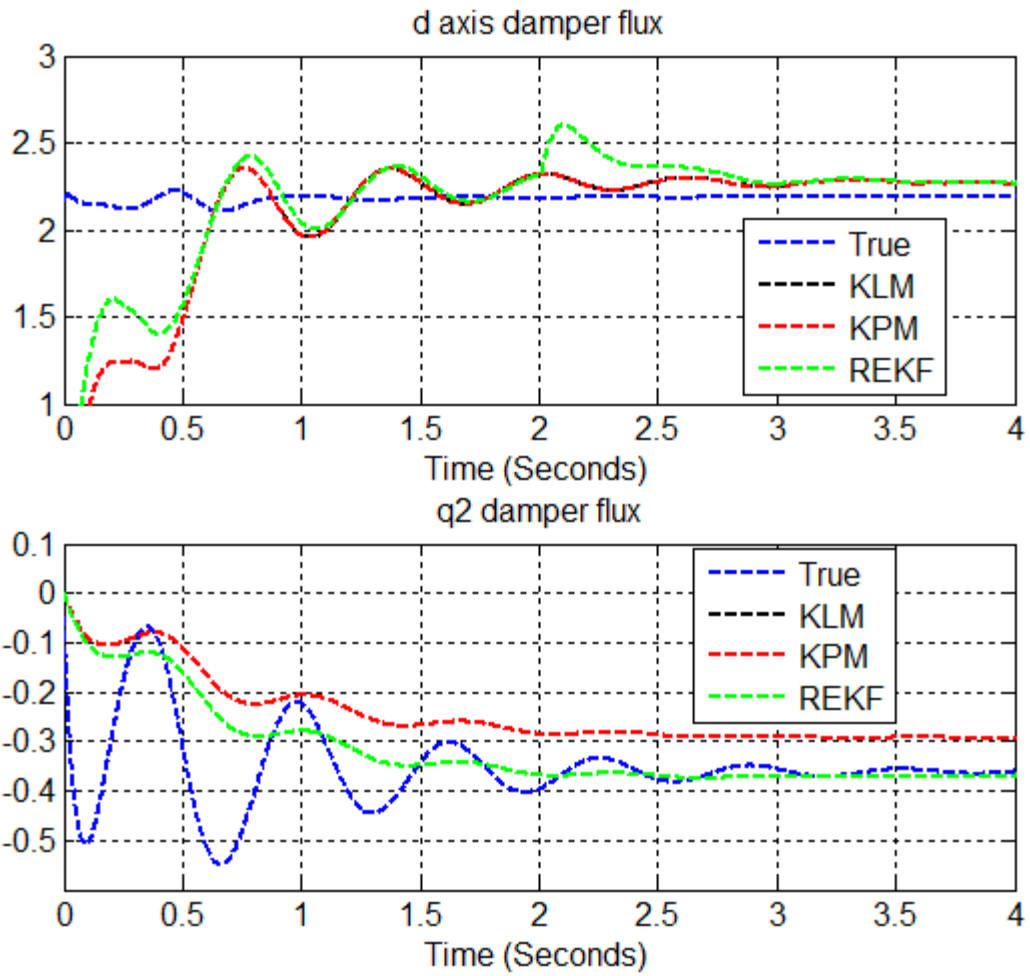

Figure 7.54 d-axis damper flux, q-axis second damper flux and their estimates with bad data.

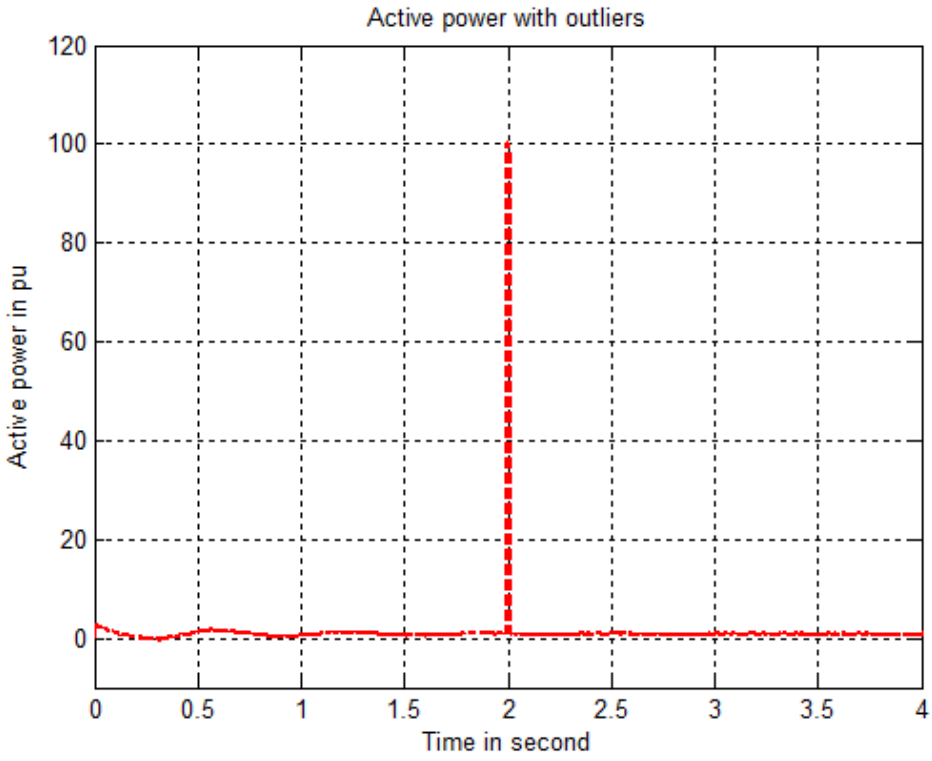

Figure 7.55 Active power with outliers.

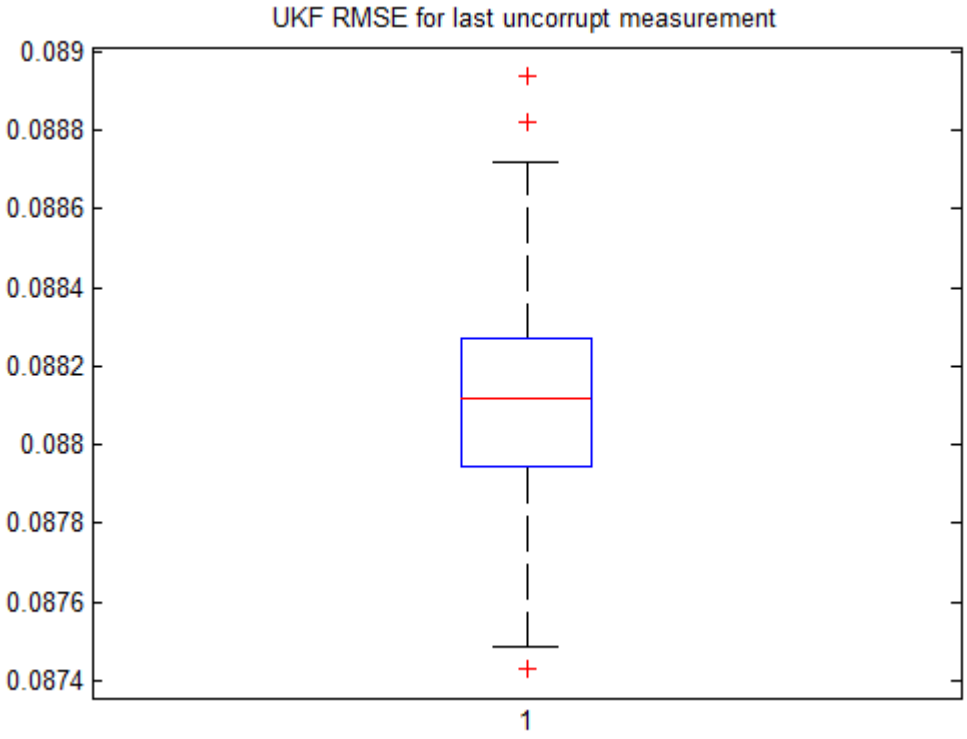

Figure 7.56 Box plot of RMS error for UKF with uncorrupt measurement.

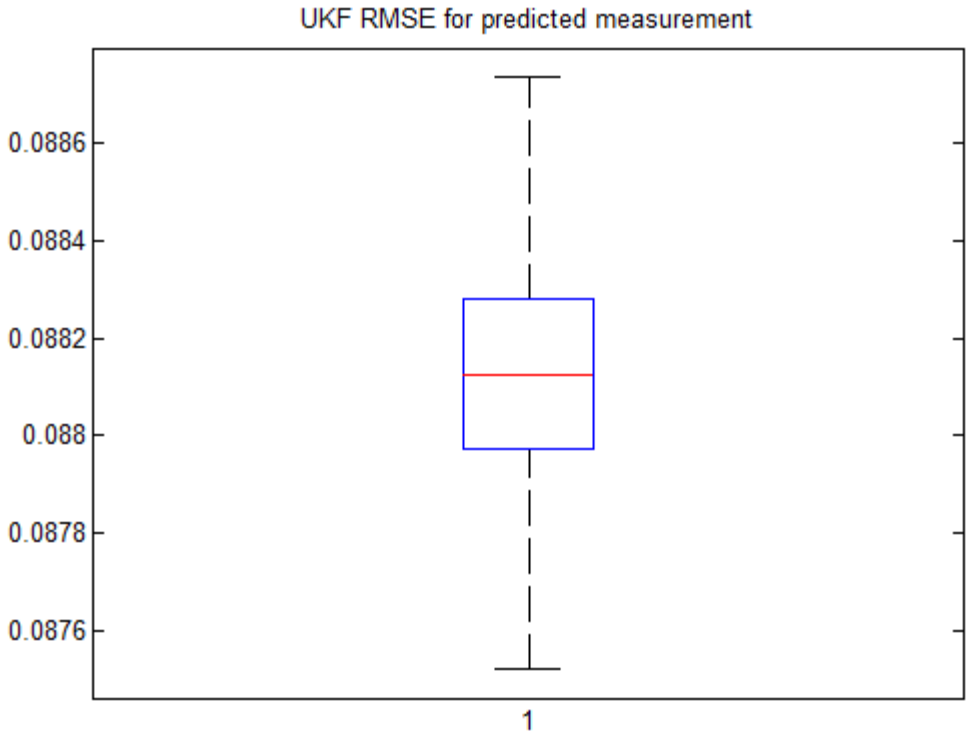

Figure 7.57 Box plot of RMS error for UKF with predicted measurement.

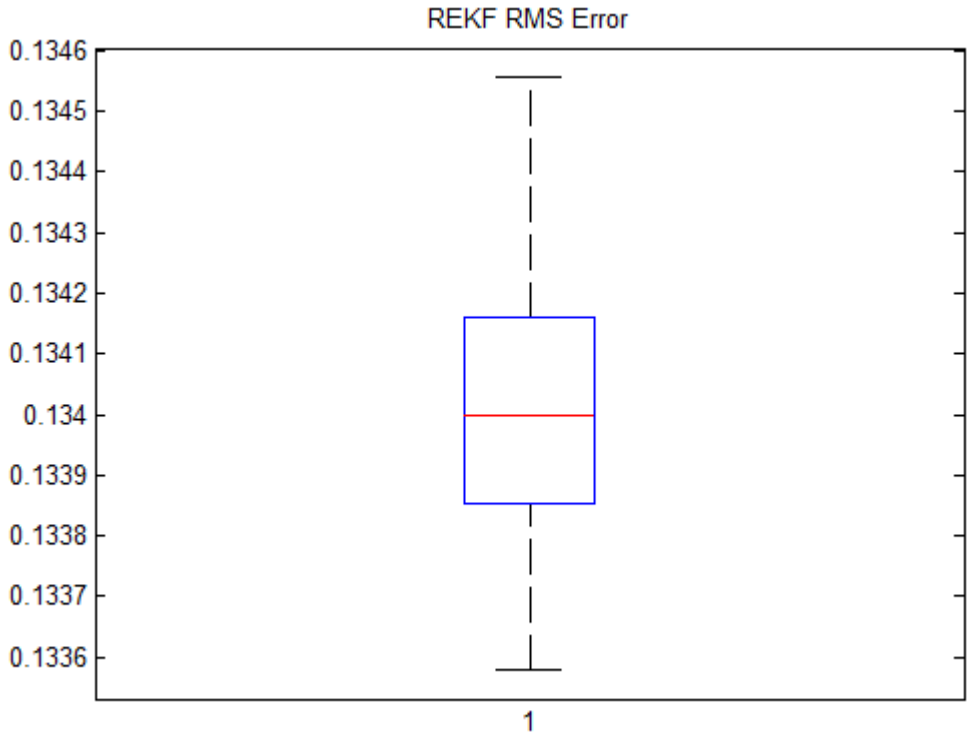

Figure 7.58 Box plot of RMS error for GM-EKF.

7.8 NORMAL MICROGRID OPERATION AND PMU MEASUREMENTS

This section provides state estimation results for a sampling frequency of 50 Hz for the EKF and the UKF under normal operation. The simulation results show the true and estimated values of the state variable in Figure 7.59- Figure 7.64. From the figures, we observe that the state estimates track the true values of the states satisfactorily using the PMUs data. Figure 7.65- Figure 7.66 show the RMS errors for the UKF and the EKF respectively. As expected the RMS errors for the EKF is larger than those of the UKF. Table IV shows the maximum, minimum and standard deviation of the RMS errors and rotor angle RMS errors for the EKF and the UKF. From the figures and Table IX, we see that state estimation errors are greater for the EKF than for the UKF.

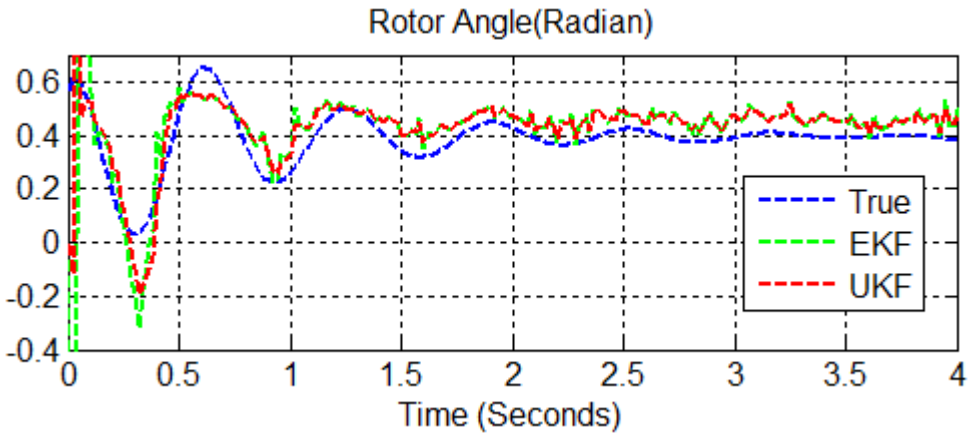

Figure 7.59 Rotor angle and its estimates at 50 Hz

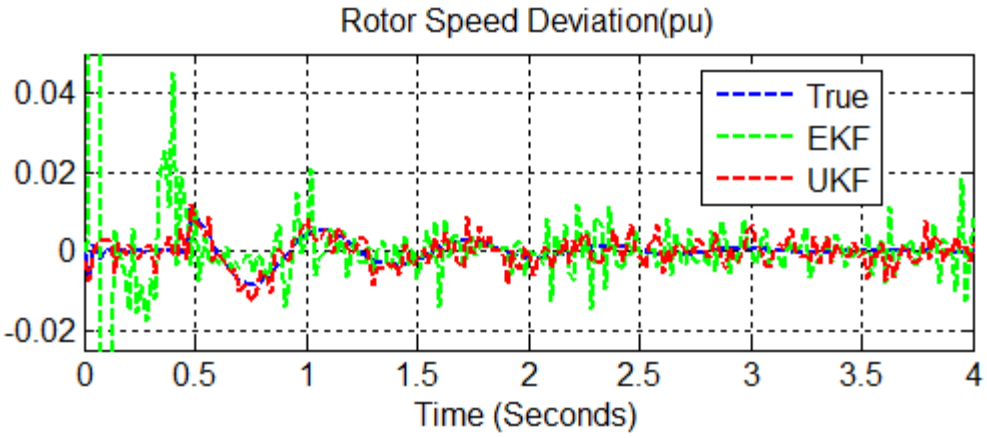

Figure 7.60 Rotor speed deviation and its estimates at 50 Hz

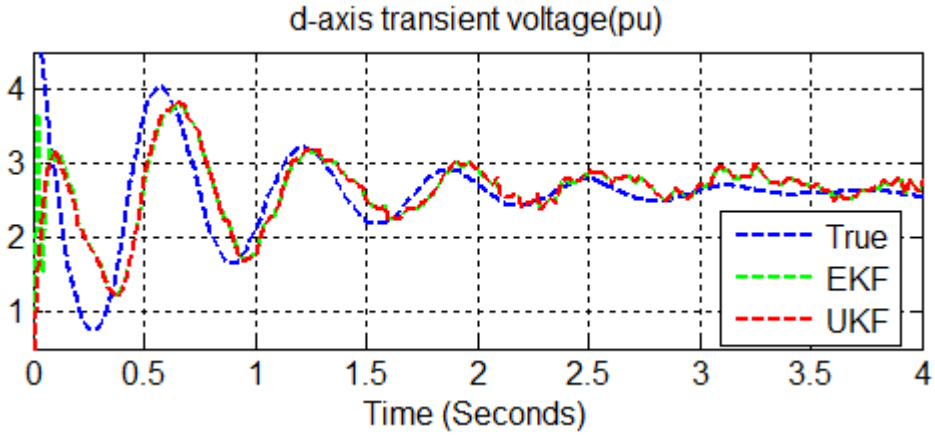

Figure 7.61 d-axis transient voltage and its estimates at 50 Hz

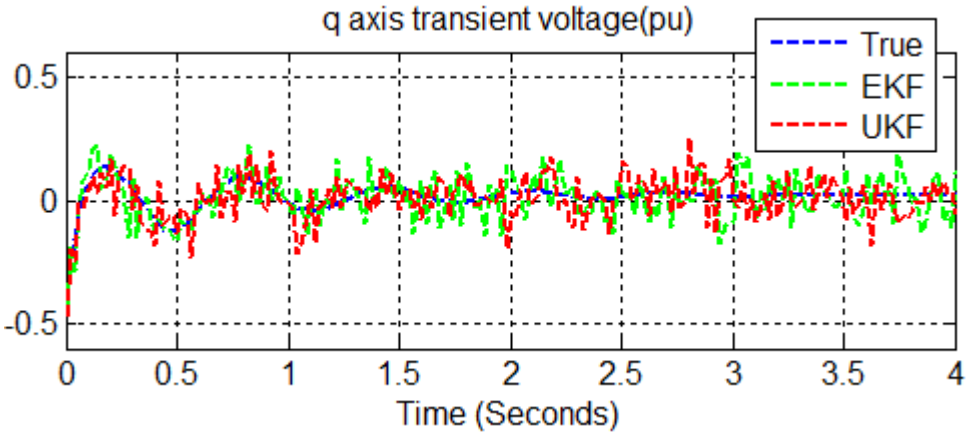

Figure 7.62 q-axis transient voltage and its estimates at 50 Hz

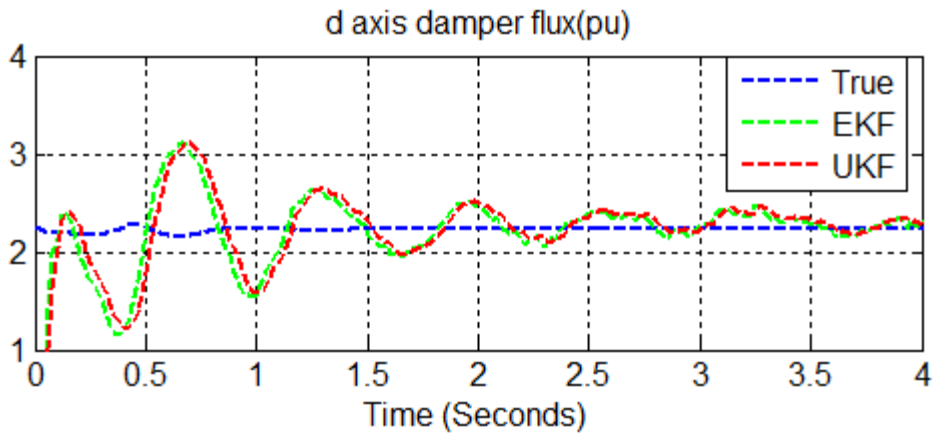

Figure 7.63 d-axis damper flux and its estimates at 50 Hz

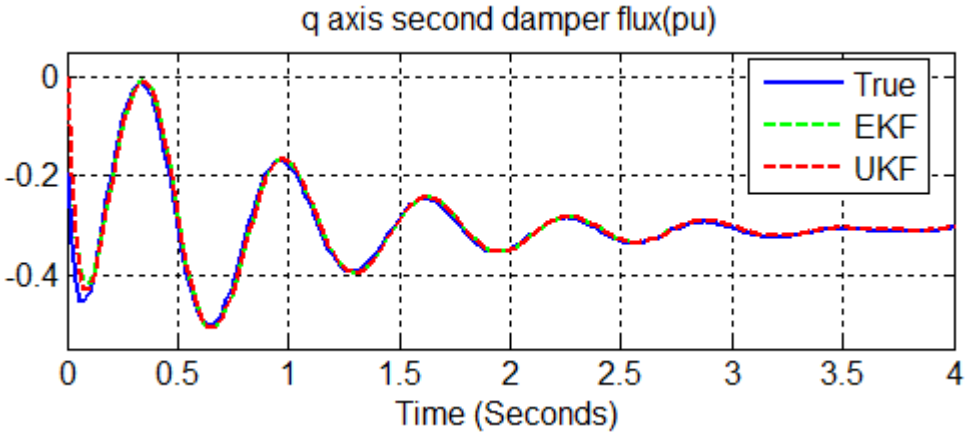

Figure 7.64 q-axis second damper flux and its estimates at 50 Hz

Table IX Comparison of RMS errors for EKF and UKF

Filter	RMSE (Max.)	RMSE(Min)	Standard Deviation	RMSE of Rotor Angle (Max)	RMSE of Rotor Angle (Min)	Standard Deviation
UKF	0.5007	0.4782	0.0036	0.1952	0.0124	0.0400
EKF	0.4954	0.4674	0.0053	0.1967	0.0042	0.0353

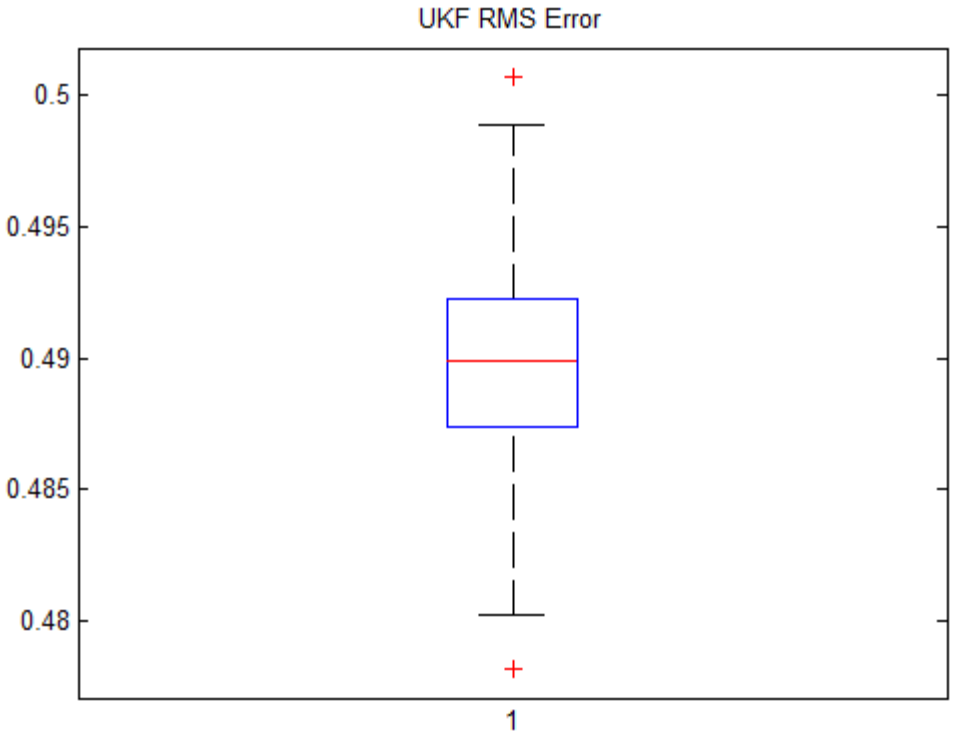

Figure 7.65 Box plot of UKF RMS error at 50 Hz

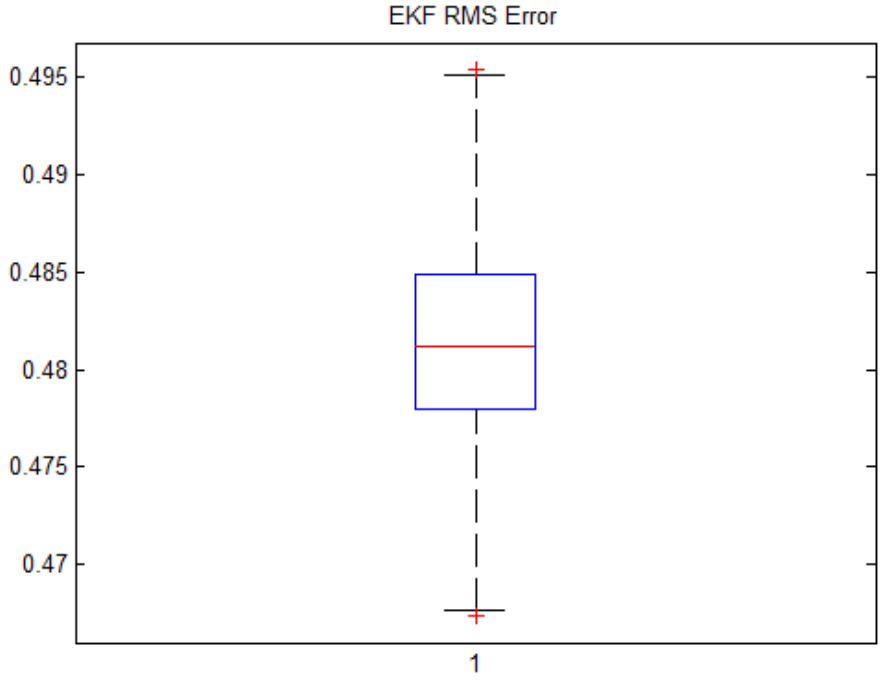

Figure 7.66 Box plot of EKF RMS error at 50 Hz

7.9 FAULT AT PCC AND PMU MEASUREMENTS

As in Section 7.2, we simulated a 3-phase-to-ground fault at the PCC after 5 s and cleared it at 5.1 s for both the EKF and the UKF at the PMU frequency of 50 Hz. Figure 7.67 – Figure 7.72 show that the filters cannot track the true states during the fault but quickly converge to the steady state after the fault is cleared. The RMS errors obtained from 500 Monte Carlo simulation are provided in box plots in Figure 7.35-Figure 7.36 and in Table X. Although the errors are small for both filters, the UKF provides better results.

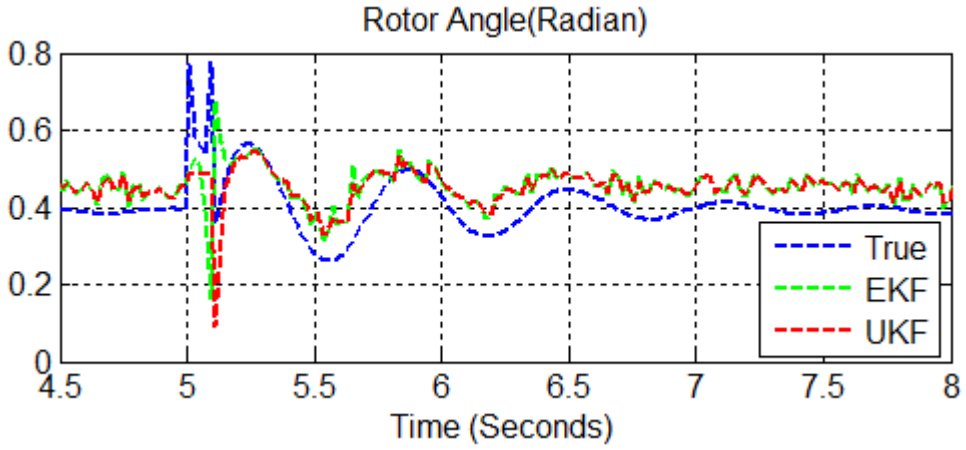

Figure 7.67 Rotor angle and its estimates with fault at 50 Hz.

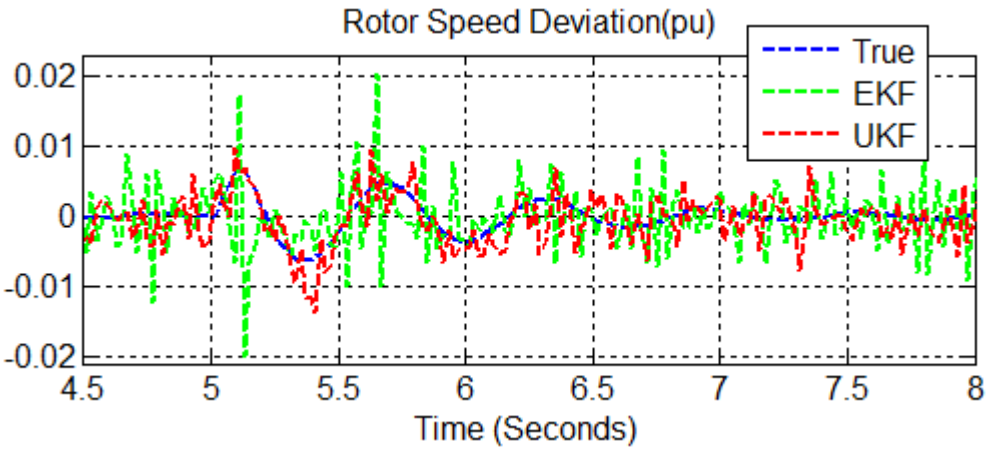

Figure 7.68 Rotor speed deviation and its estimates with fault at 50 Hz.

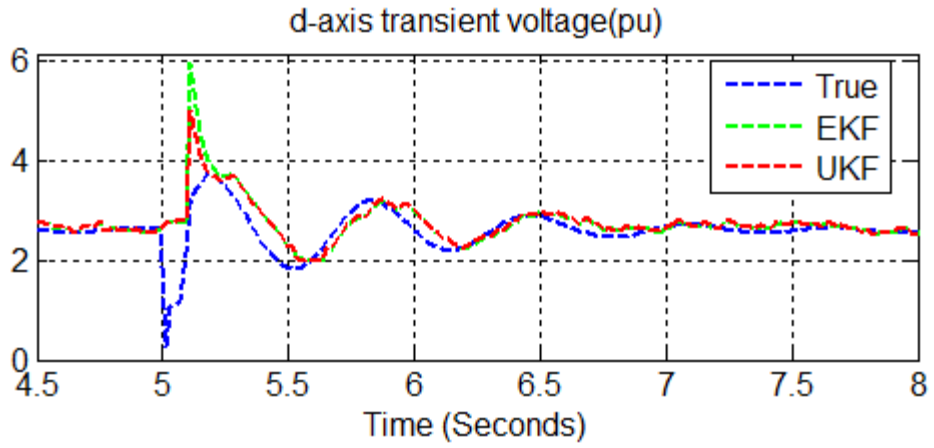

Figure 7.69 d-axis transient voltage and its estimates with fault at 50 Hz.

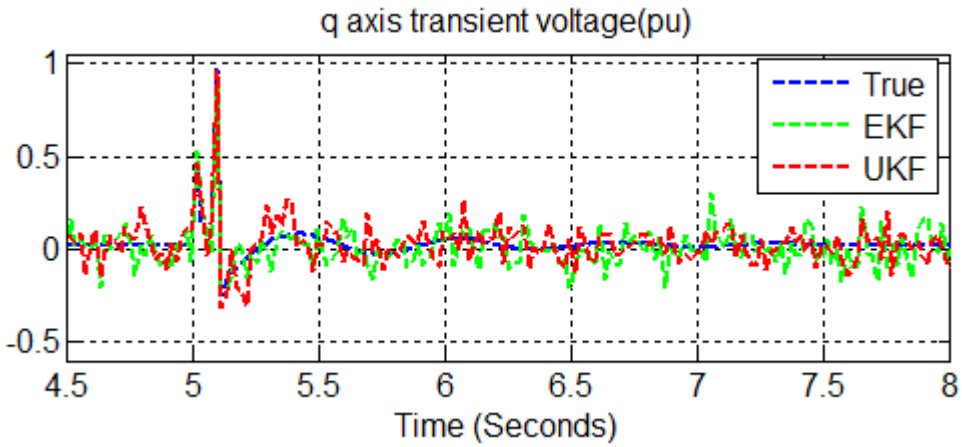

Figure 7.70 q-axis transient voltage and its estimates with fault at 50 Hz.

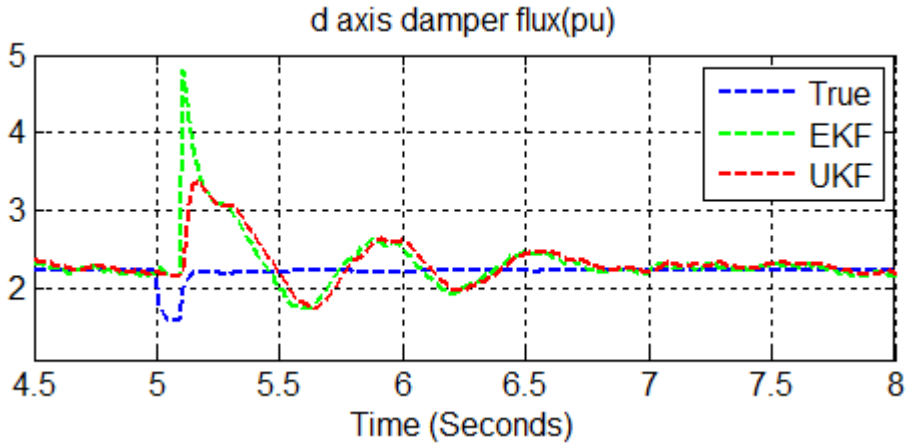

Figure 7.71 d-axis damper flux and its estimates under with fault at 50 Hz.

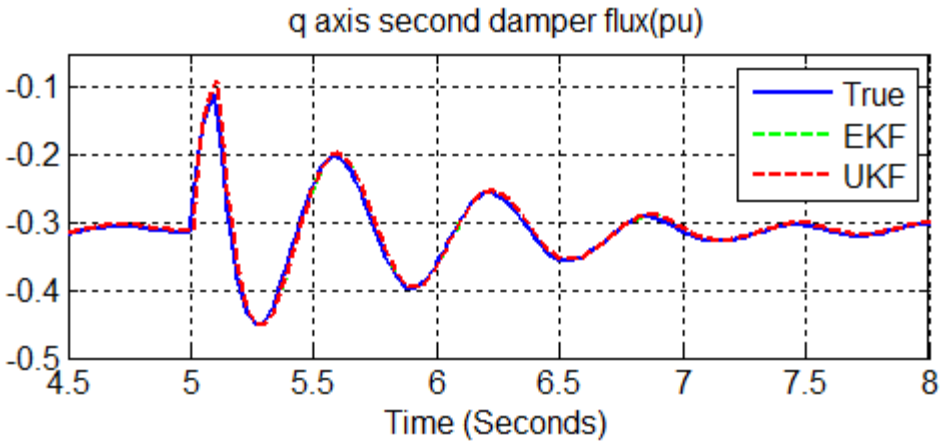

Figure 7.72 q-axis second damper flux and its estimates with fault at 50 Hz.

Table X Comparison of RMS errors for EKF and UKF

Filter	RMSE (Max.)	RMSE(Min)	Standard Deviation	RMSE of Rotor Angle (Max)	RMSE of Rotor Angle (Min)	Standard Deviation
UKF	0.5820	0.5534	0.0047	0.2059	0.0152	0.0403
EKF	0.6146	0.5716	0.0063	0.1796	0.0044	0.0340

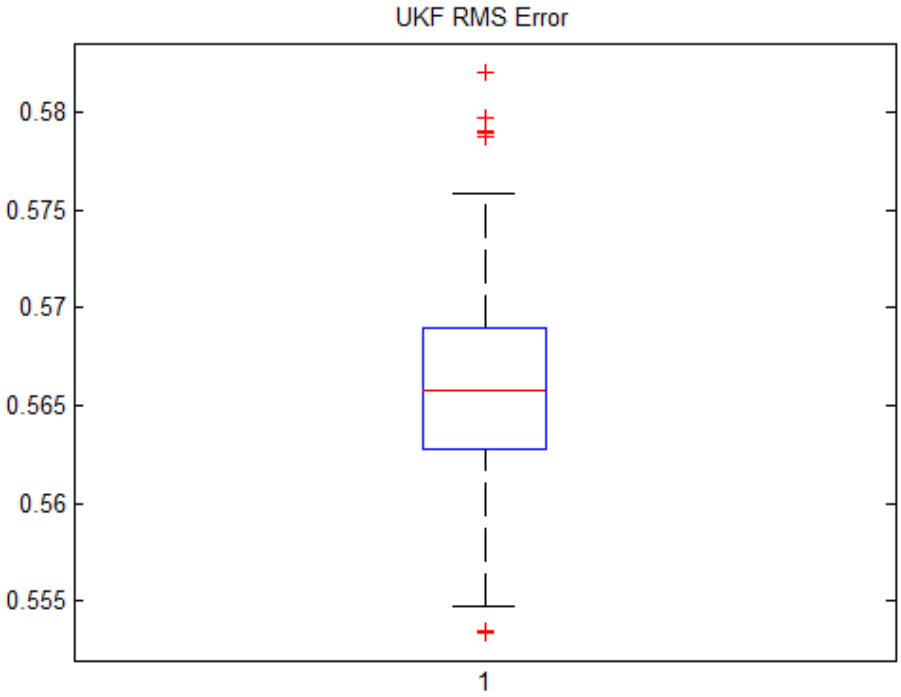

Figure 7.73 Box plot of UKF RMS error with fault at 50 Hz

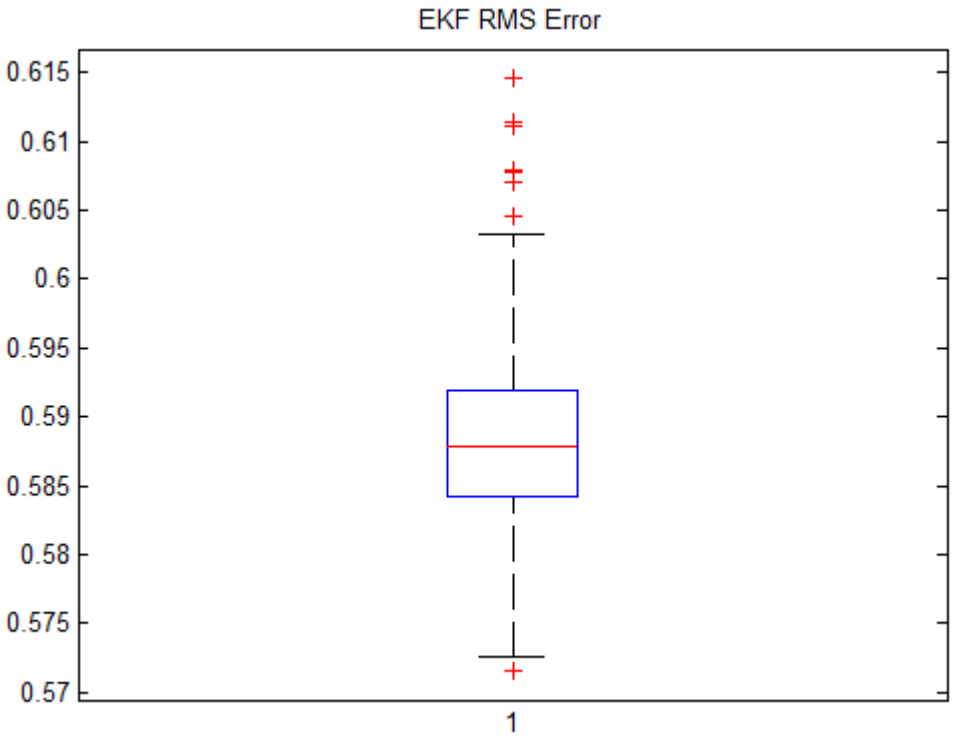

Figure 7.74 Box plot of EKF RMS error with fault at 50 Hz

7.10 LOSS OF GENERATOR AND PMU MEASUREMENTS

This scenario considers the effects of generator failure on the estimators with PMU measurements at a frequency of 50 Hz. As in Section 7.3, we assume the failure of generator 2 after 4 s. We again obtained satisfactory results from the EKF and the UKF estimators as demonstrated by the results in Figure 7.75 – Figure 7.80. Monte Carlo based RMS errors are presented in the box plots of Figure 7.81- Figure 7.82. The box plots along with *Table XI* demonstrates once again the lower error of the UKF as compared to the EKF.

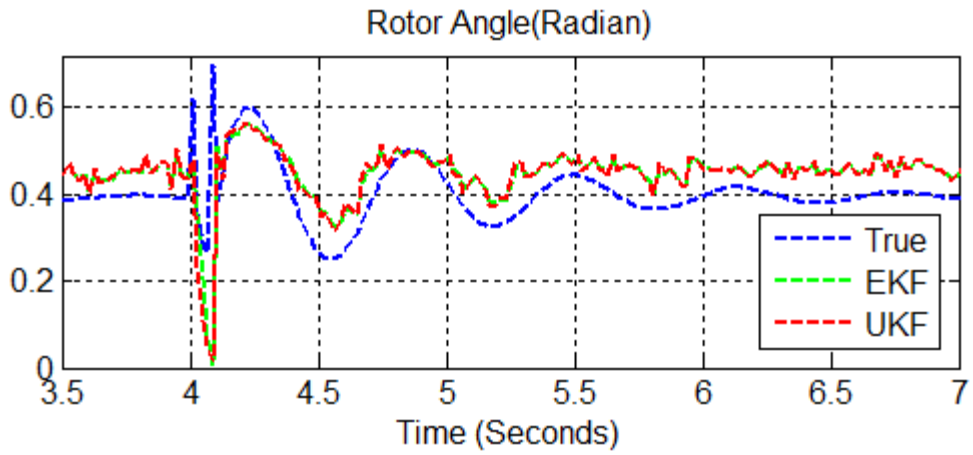

Figure 7.75 Rotor angle and its estimates with loss of generator at 50 Hz.

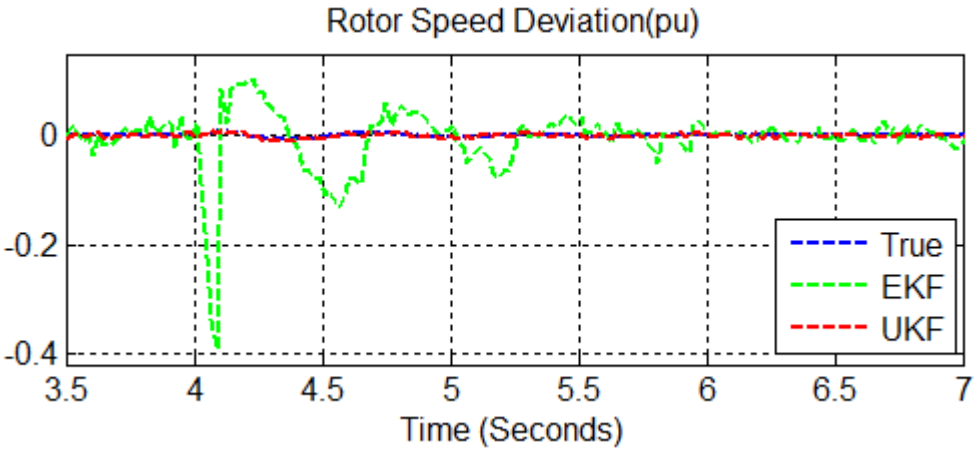

Figure 7.76 Rotor speed deviation and its estimates with loss of generator at 50 Hz.

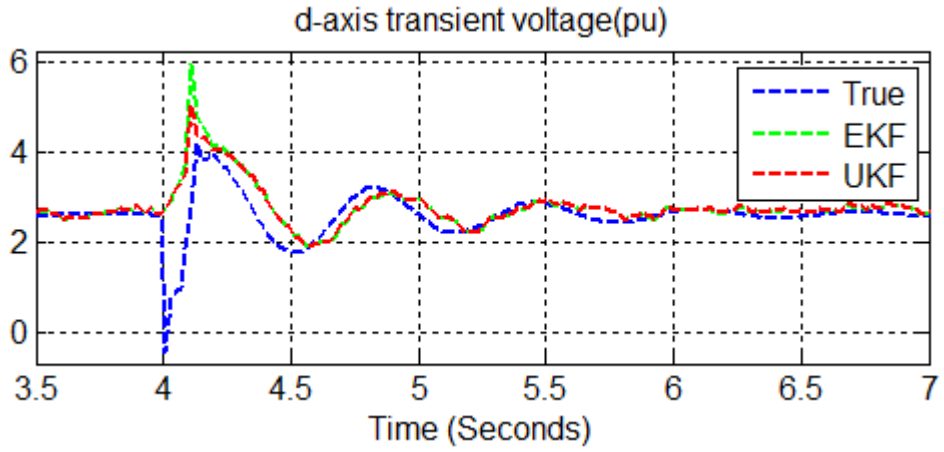

Figure 7.77 d-axis transient voltage and its estimates with loss of generator at 50 Hz.

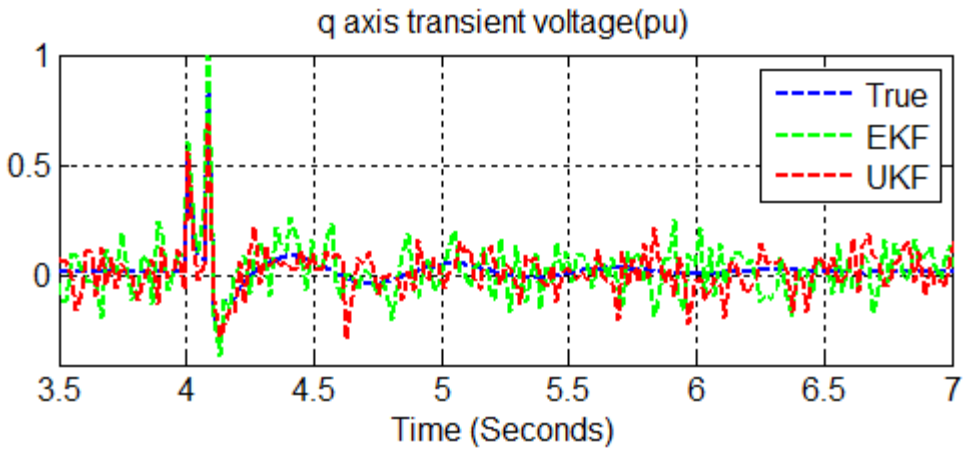

Figure 7.78 q-axis transient voltage and its estimates with loss of generator at 50 Hz.

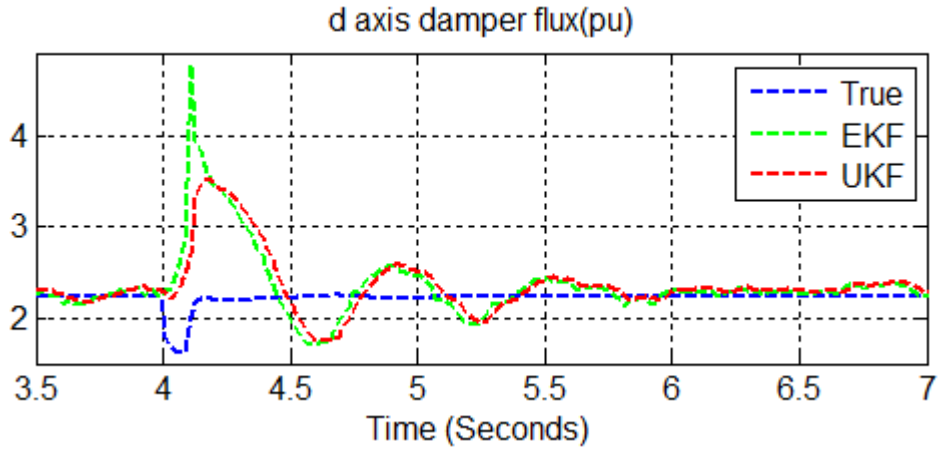

Figure 7.79 d-axis damper flux and its estimates with loss of generator at 50 Hz.

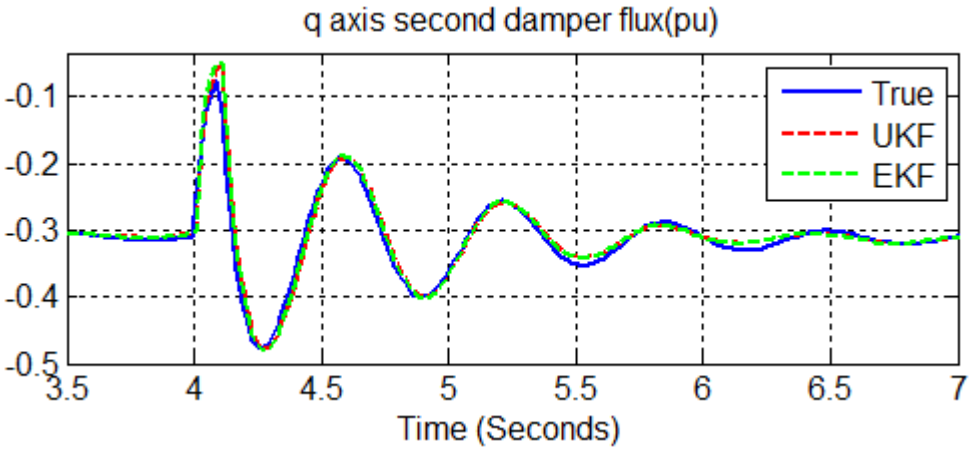

Figure 7.80 q-axis second damper flux and its estimates with loss of generator at 50 Hz.

Table XI Comparison of RMS errors for EKF and UKF

Filter	RMSE (Max.)	RMSE(Min)	Standard Deviation	RMSE of Rotor Angle (Max)	RMSE of Rotor Angle (Min)	Standard Deviation
UKF	0.6137	0.5843	0.005	0.1827	0.0013	0.0411
EKF	0.6414	0.6035	0.0063	0.1720	0.0019	0.0349

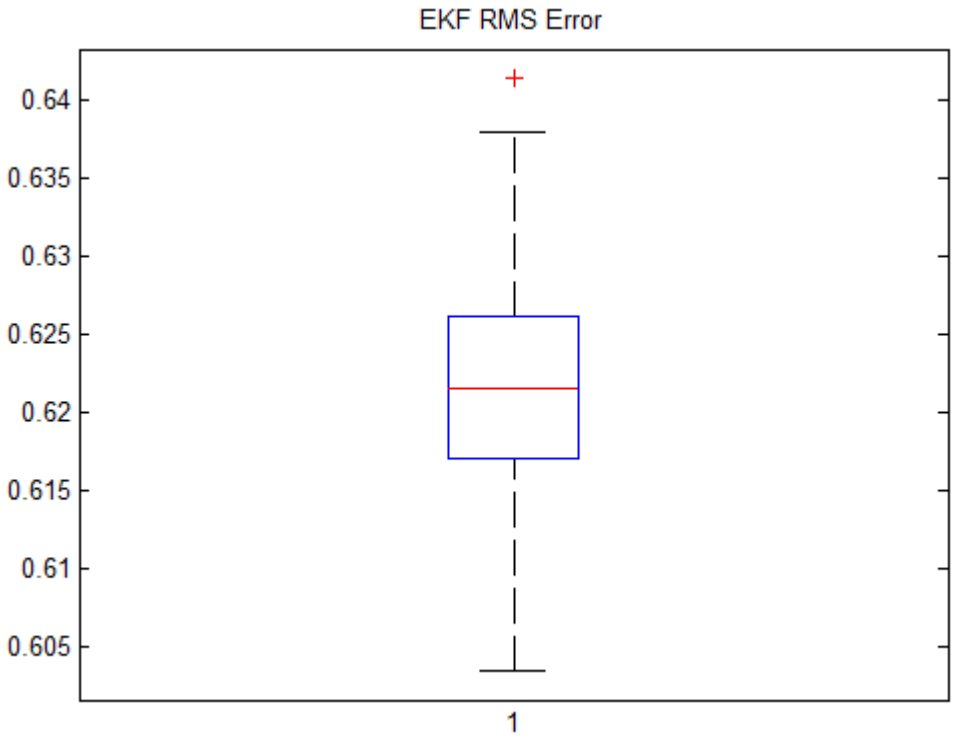

Figure 7.81 Box plot of EKF RMS error with loss of generator at 50 Hz.

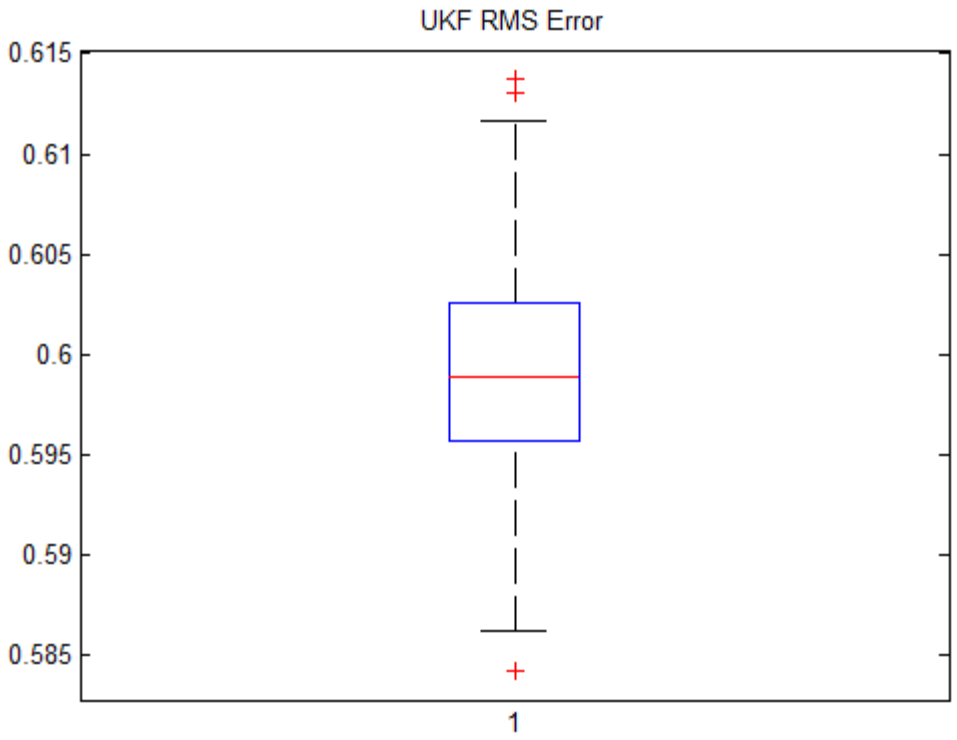

Figure 7.82 Box plot of UKF RMS error with loss of generator at 50 Hz.

7.11 LOSS OF LOAD AND PMU MEASUREMENTS

We investigate the performance of the EKF and the UKF following the loss of load 2 after 4.5 s using PMUs measurements. The state estimation results based on this scenario are provided in Figures 7.83 – 7.88. We present the RMS errors based on 500 Monte Carlo simulations in *Table XII* and Figure 7.89- Figure 7.90. The result show that the UKF and EKF results are similar.

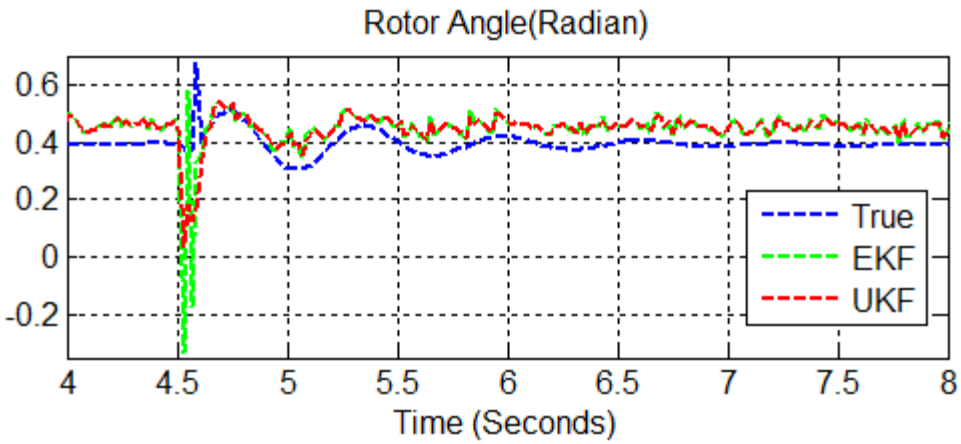

Figure 7.83 Rotor angle and its estimates with loss of load at 50 Hz.

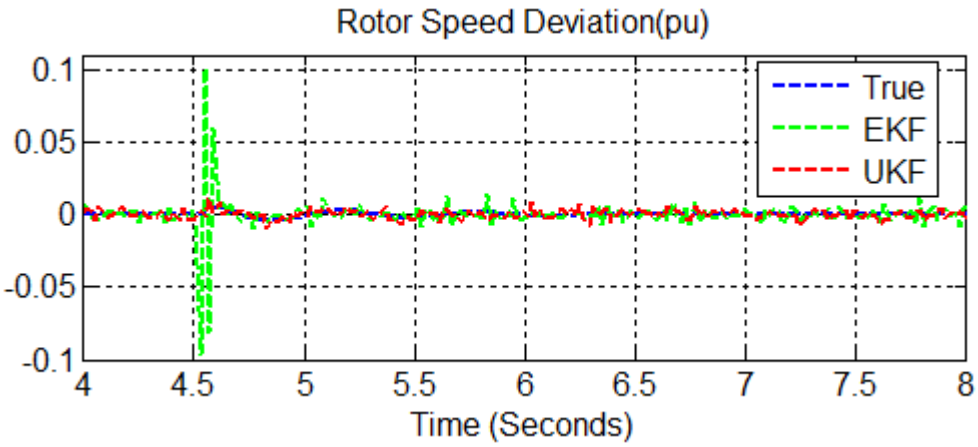

Figure 7.84 Rotor speed deviation from and its estimates with loss of load at 50 Hz.

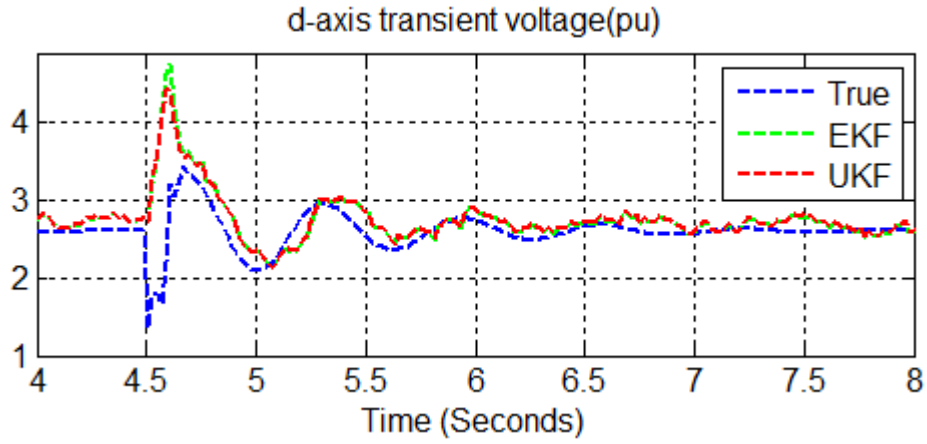

Figure 7.85 d-axis transient voltage and its estimates with loss of load at 50 Hz.

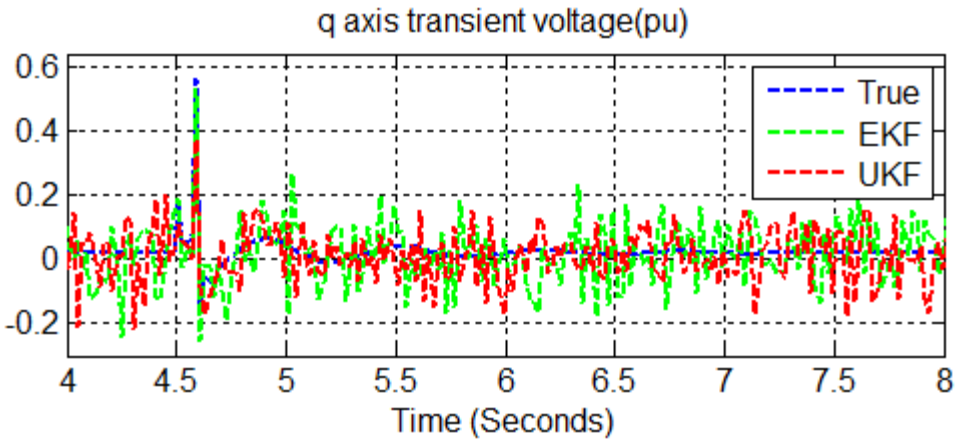

Figure 7.86 q-axis transient voltage and its estimates with loss of load at 50 Hz.

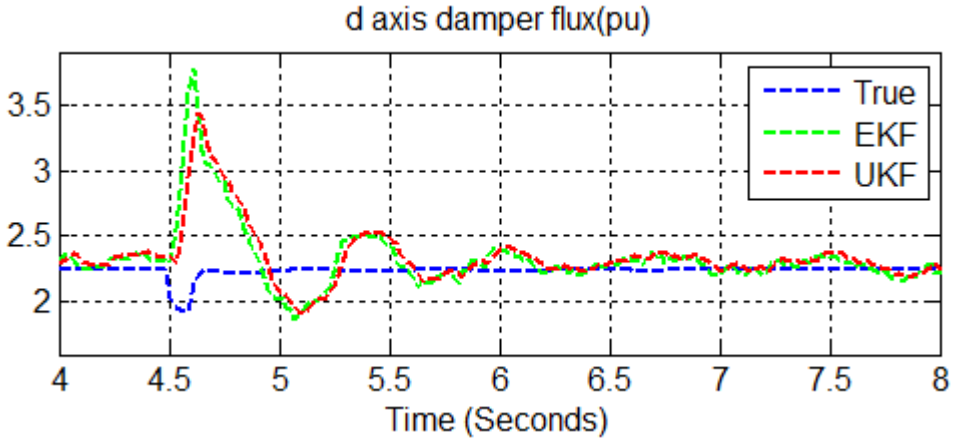

Figure 7.87 d-axis damper flux and its estimates with loss of load at 50 Hz.

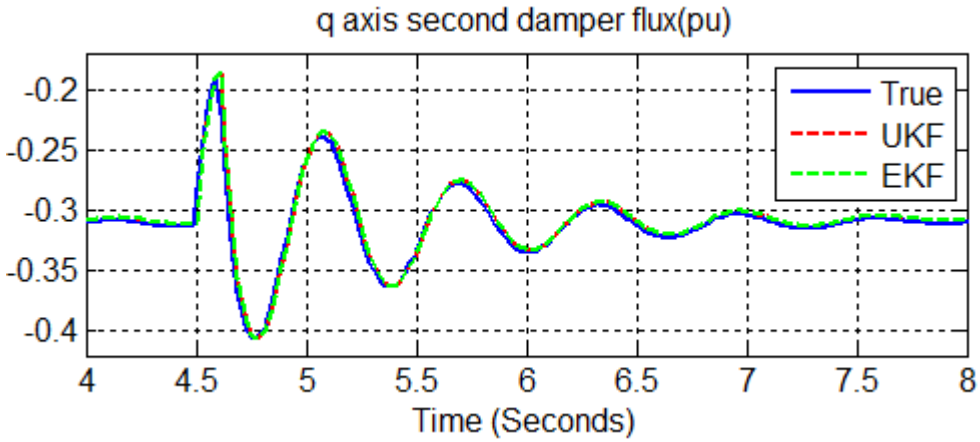

Figure 7.88 q-axis second damper flux and its estimates with loss of load at 50 Hz.

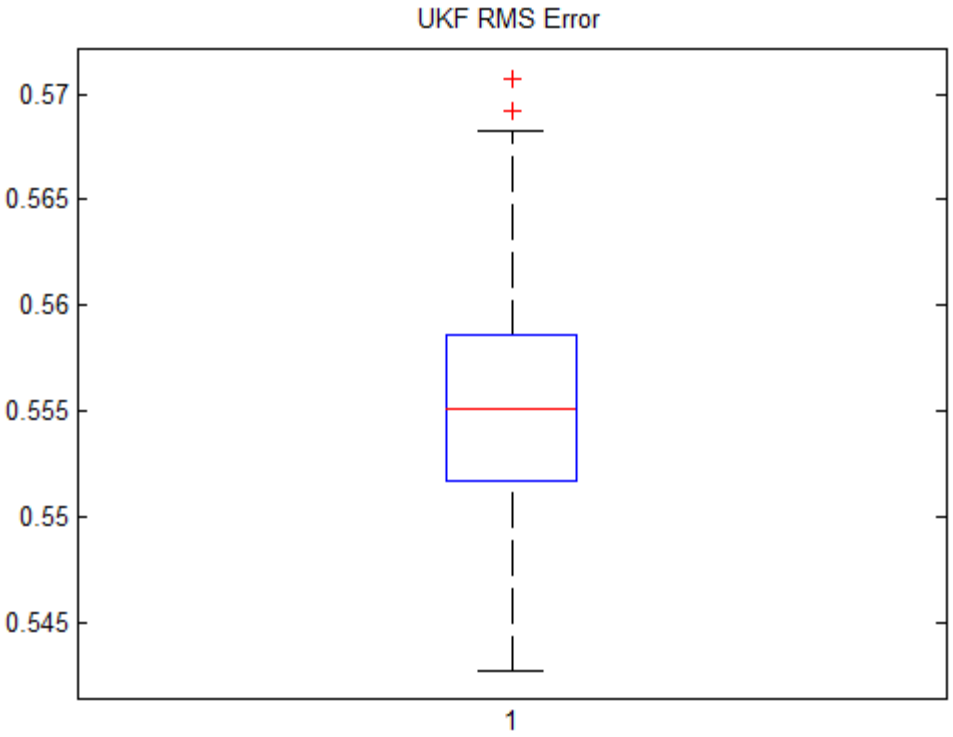

Figure 7.89 Box plot of UKF RMS error with loss of load at 50 Hz.

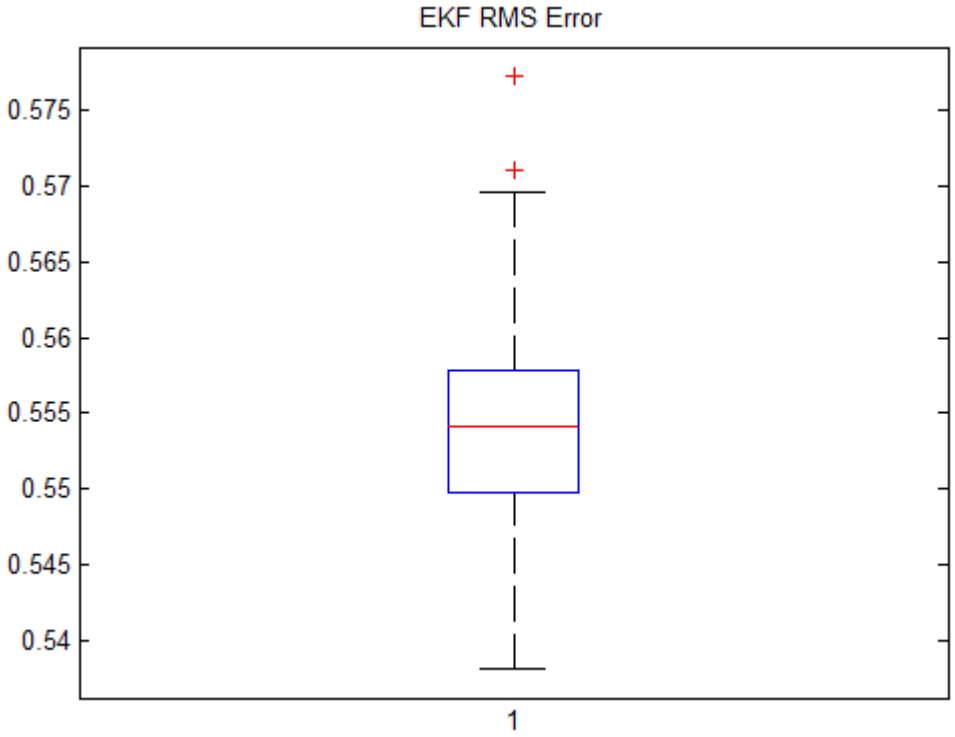

Figure 7.90 Box plot of EKF RMS error with loss of load at 50 Hz.

Table XII Comparison of RMS errors for EKF and UKF

Filter	RMSE (Max.)	RMSE(Min)	Standard Deviation	RMSE of Rotor Angle (Max)	RMSE of Rotor Angle (Min)	Standard Deviation
UKF	0.5707	0.5427	0.0050	0.2001	0.0023	0.0408
EKF	0.5773	0.5382	0.0061	0.1673	0.0024	0.0335

7.12 PACKET LOSS AND TIME DELAY WITH PMU MEASUREMENTS

We analyze the effectiveness of our KF approach for dealing with packet loss or delay (Section 5.5) with the distributions mentioned in Section 7.5. We consider a normally operating microgrid with PMU measurements at a sampling frequency of 50 Hz. The results are provided in Figure 7.91- Figure 7.96. From Figures 7.91- 7.96, we observe that the effects of packet delay are reduced but not eliminated. This is particularly true of the estimate of the rotor angle where the estimation error is significant. Nevertheless, the provided RMS errors demonstrate that the approach of Section 5.5 improves filter accuracy.

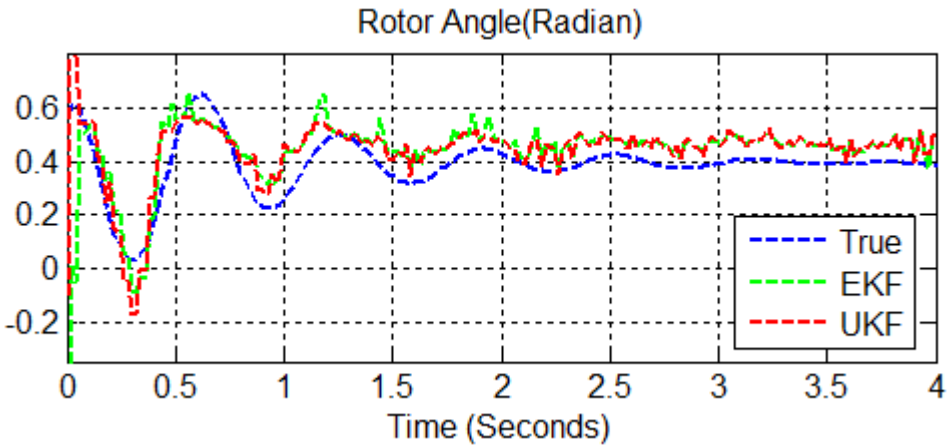

Figure 7.91 Rotor angle and its estimates with packet loss and time delay at 50 Hz.

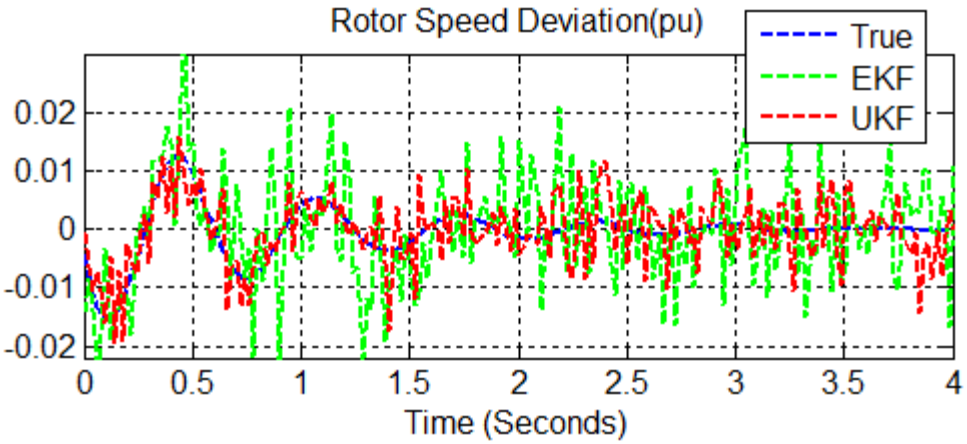

Figure 7.92Rotor speed deviation and its estimates with packet loss and time delay at 50 Hz.

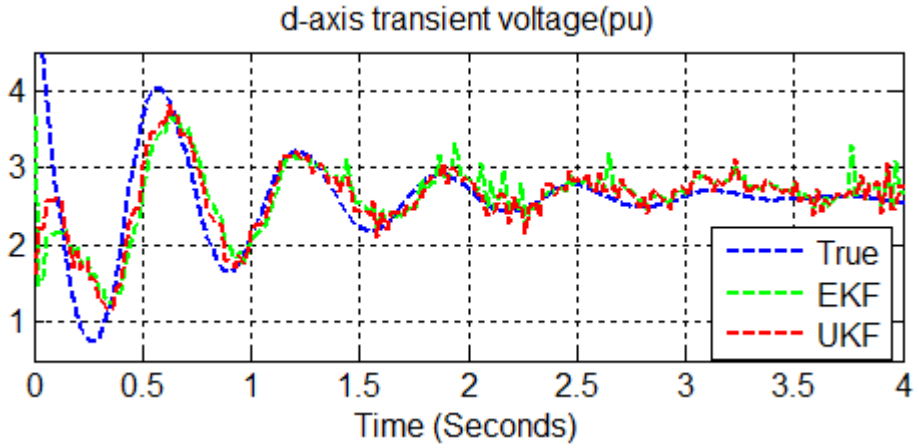

Figure 7.93 d-axis trans. voltage and its est. with packet loss and time delay at 50 Hz.

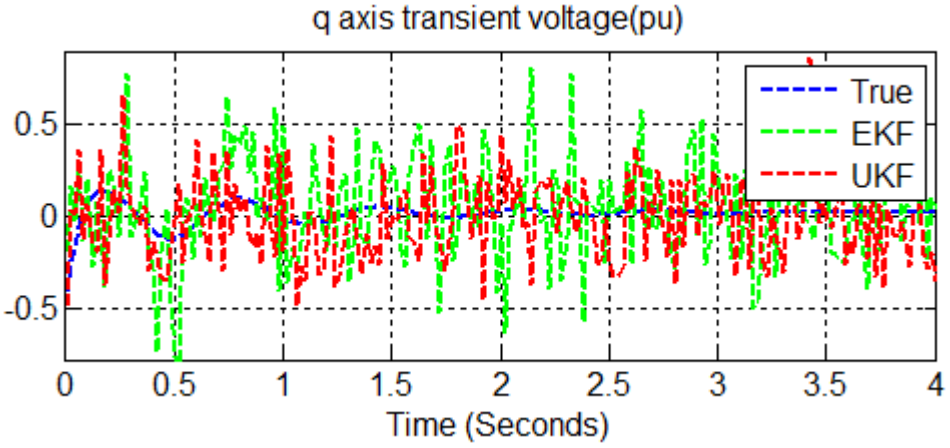

Figure 7.94 q-axis transient voltage and its estimates with packet loss and time delay at 50 Hz.

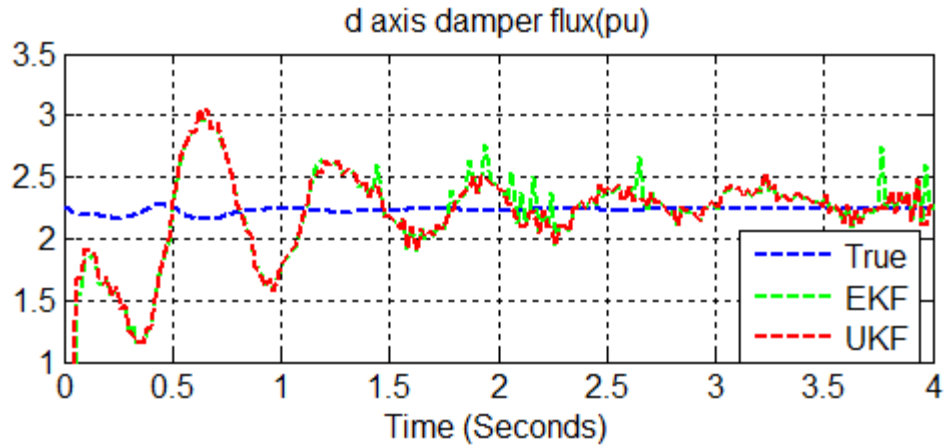

Figure 7.95 d-axis damper flux and its estimates with packet loss and time delay at 50 Hz.

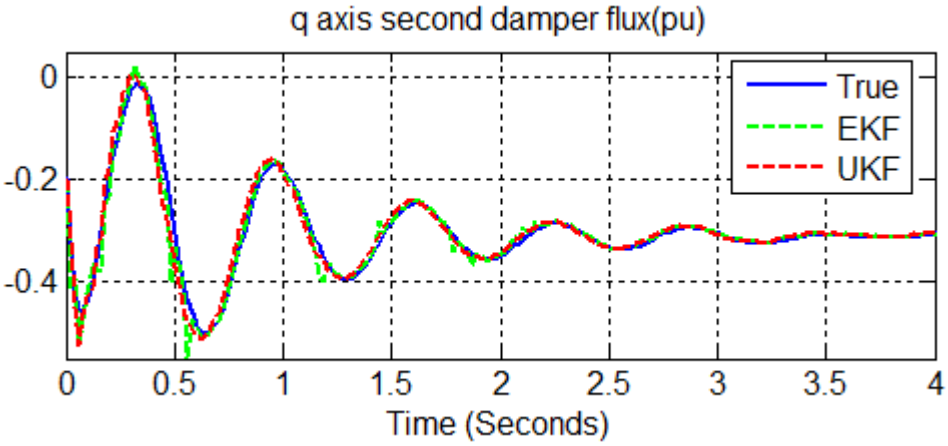

Figure 7.96 q-axis second damper flux and its estimates with packet loss and time delay at 50 Hz.

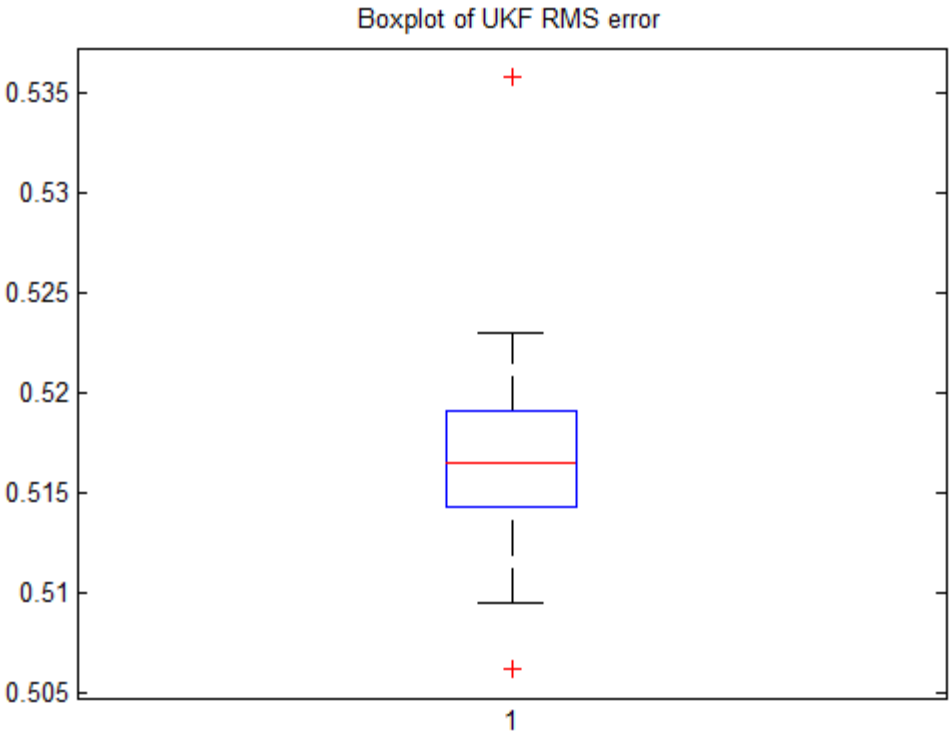

Figure 7.97 Box plot of UKF RMS error with packet loss and time delay at 50 Hz.

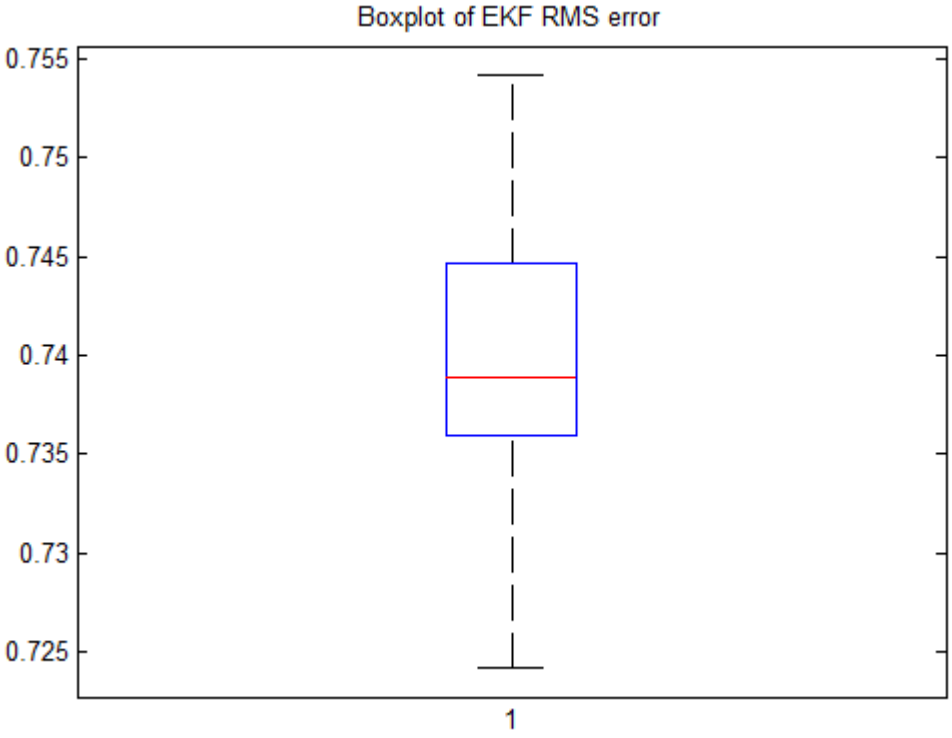

Figure 7.98 Box plot of EKF RMS error with packet loss and time delay at 50 Hz.

Table XIII Comparison of RMS errors for EKF and UKF

Filter	RMSE (Max.)	RMSE(Min)	Standard Deviation	RMSE of Rotor Angle (Max)	RMSE of Rotor Angle (Min)	Standard Deviation
UKF	0.5358	0.5063	0.0043	0.1740	0.0047	0.0370
EKF	0.7542	0.7242	0.0070	0.2028	0.0084	0.0448

7.13 FAULT AT PCC, PACKET LOSS, AND DELAY WITH PMU MEASUREMENTS

In this section, we consider the effects of a fault at the PCC with packet drop and delay using the distributions defined in Section 7.5. A three phase to ground fault occurs at 5 s and is cleared at 5.1 s. The results of 500 Monte Carlo simulations are given in the box plots of Figures 7.105 and 7.106 and in Table XIV. Again, the results presented in Figure 7.99 – Figure 7.104 demonstrate the effectiveness of our proposed method.

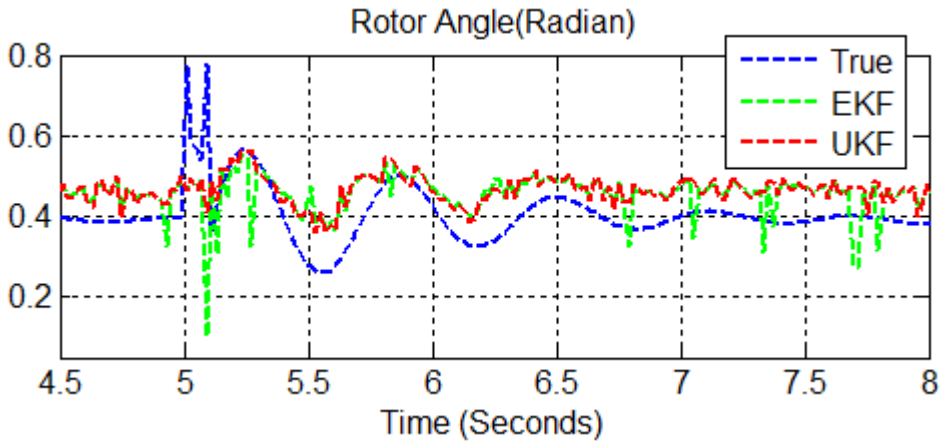

Figure 7.99 Rotor angle and its estimates with fault, packet loss and delay at 50 Hz.

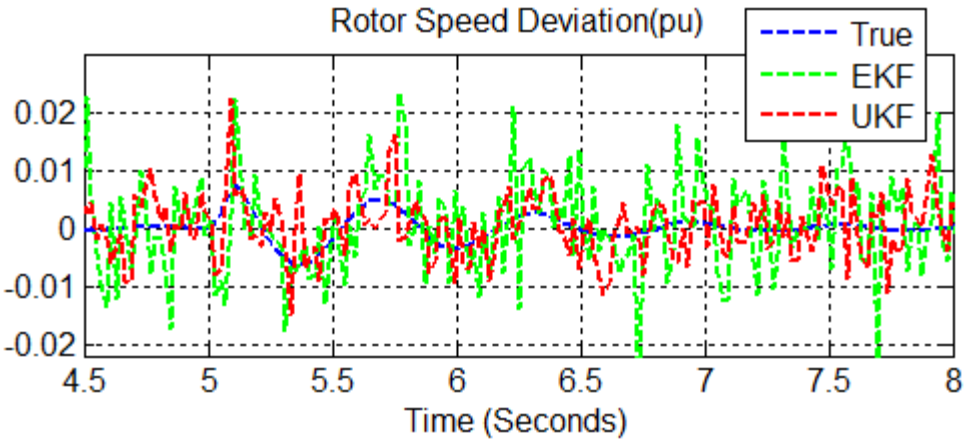

Figure 7.100 Rotor speed deviation from and its estimates with fault, packet loss and delay at 50 Hz.

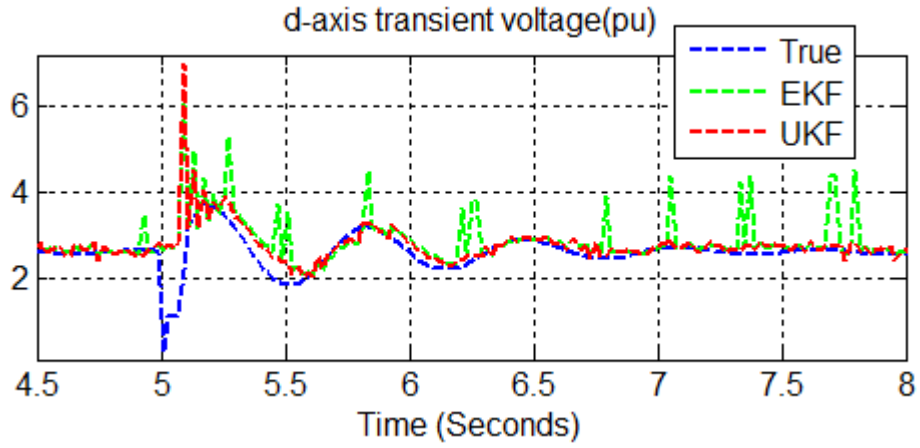

Figure 7.101 d-axis transient voltage and its estimates with fault, packet loss and delay at 50 Hz.

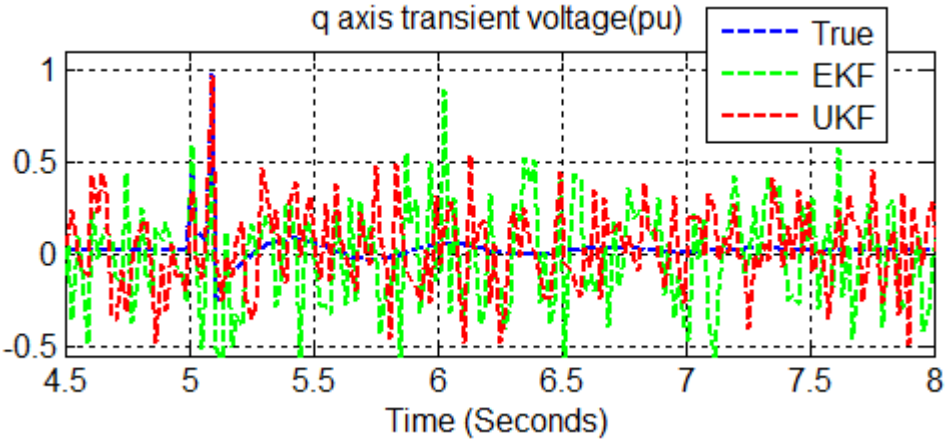

Figure 7.102 q-axis transient voltage and its estimates with fault, packet loss and delay at 50 Hz.

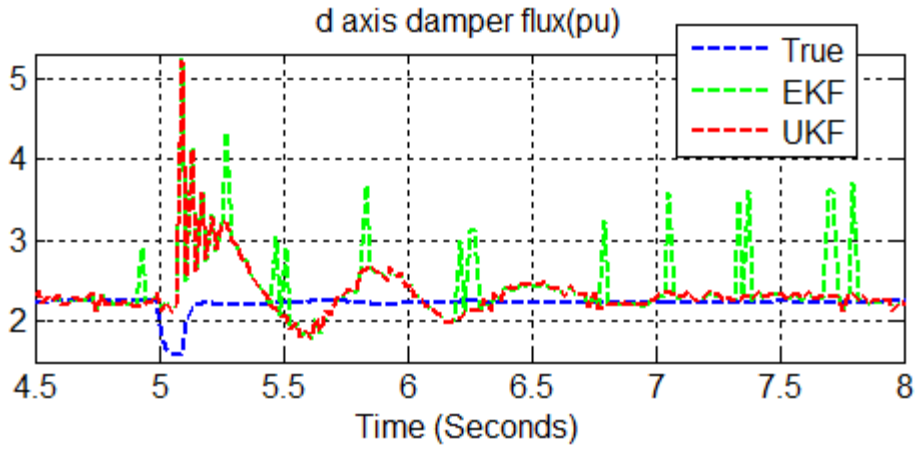

Figure 7.103 d-axis damper flux and its estimates with fault, packet loss and delay at 50 Hz.

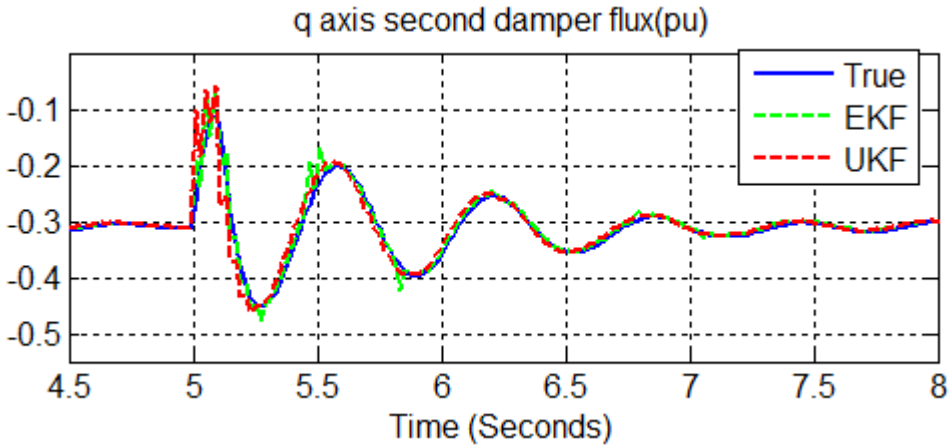

Figure 7.104 q-axis second damper flux and its estimates with fault, packet loss and delay at 50 Hz.

Table XIV Comparison of RMS errors for EKF and UKF

Filter	RMSE (Max.)	RMSE(Min)	Standard Deviation	RMSE of Rotor Angle (Max)	RMSE of Rotor Angle (Min)	Standard Deviation
UKF	0.6822	0.6243	0.0132	0.1886	0.0014	0.0402
EKF	0.9225	0.8903	0.0070	0.3141	0.0652	0.0528

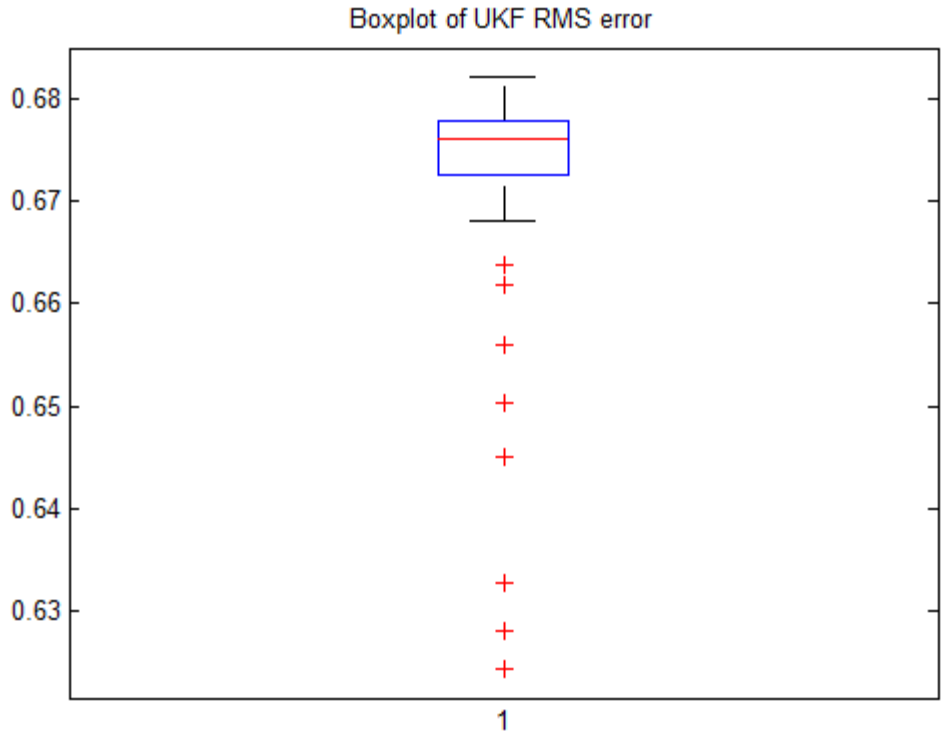

Figure 7.105 UKF RMS error with fault, packet loss and delay at 50 Hz.

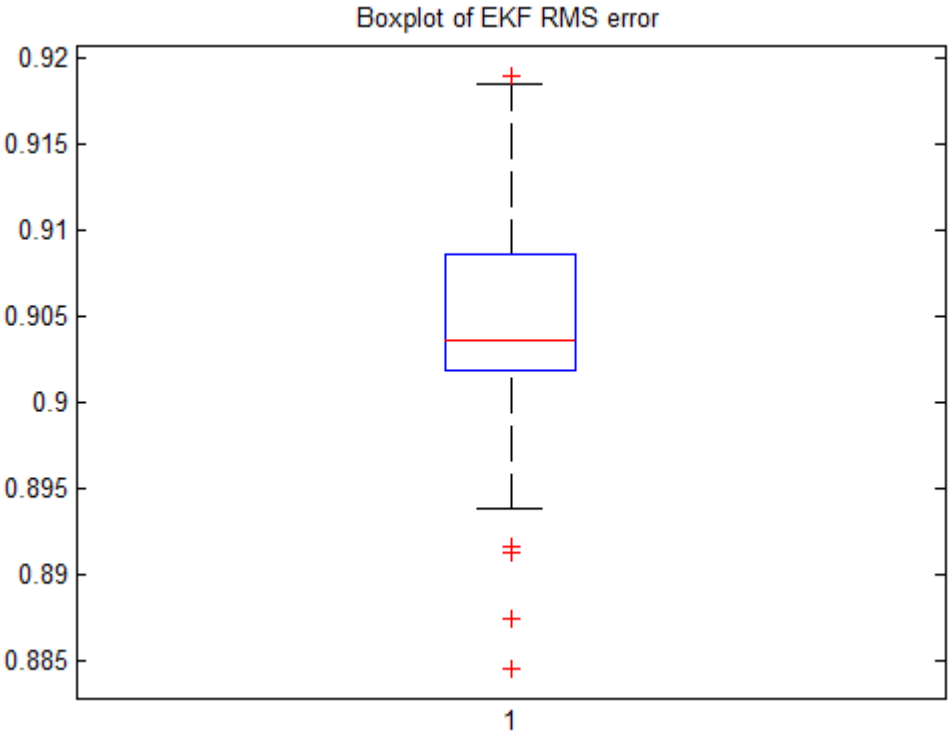

Figure 7.106 EKF RMS error with fault, packet loss and delay at 50 Hz.

7.14 GENERATOR LOSS, PACKET LOSS AND TIME DELAY WITH PMU MEASUREMENTS

In this section, we consider generator loss with packet drop and delay and with the PMU sampling frequency of 50 Hz and the packet drop and delay distributions of Section 7.5. Simulation results are provided in Figure 7.107- Figure 7.112. The results of 500 Monte Carlo simulations given in the box plots of Figures 7.113 and 7.114 and in Table XV show that our results are acceptable.

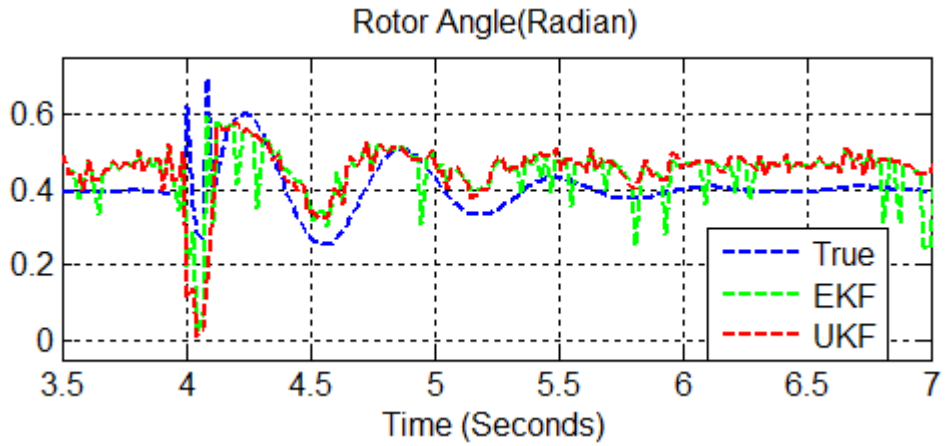

Figure 7.107 Rotor angle and its estimates with gen. loss, packet loss and delay at 50 Hz.

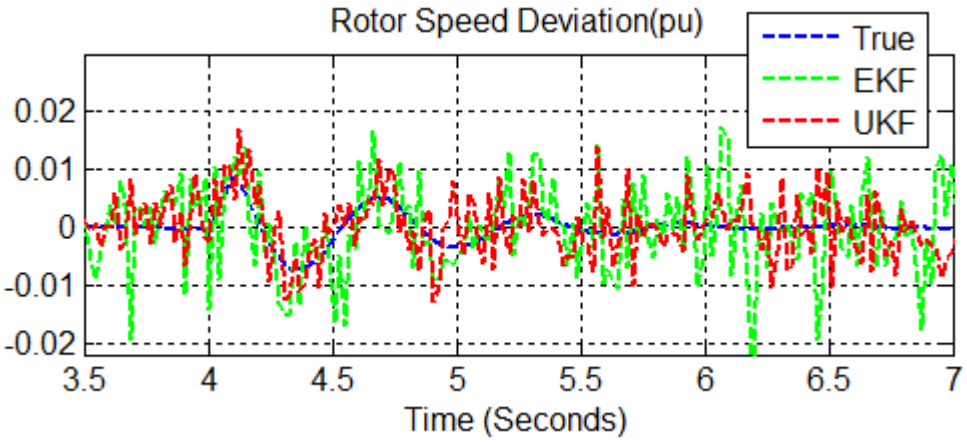

Figure 7.108 Rotor speed deviation and its estimates with gen. loss, packet loss and delay at 50 Hz.

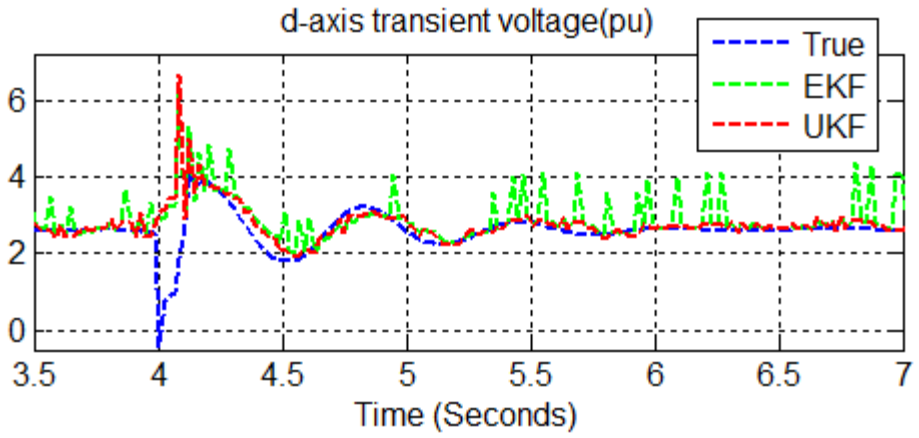

Figure 7.109 d-axis transient voltage and its estimates gen. loss, packet loss and delay at 50 Hz.

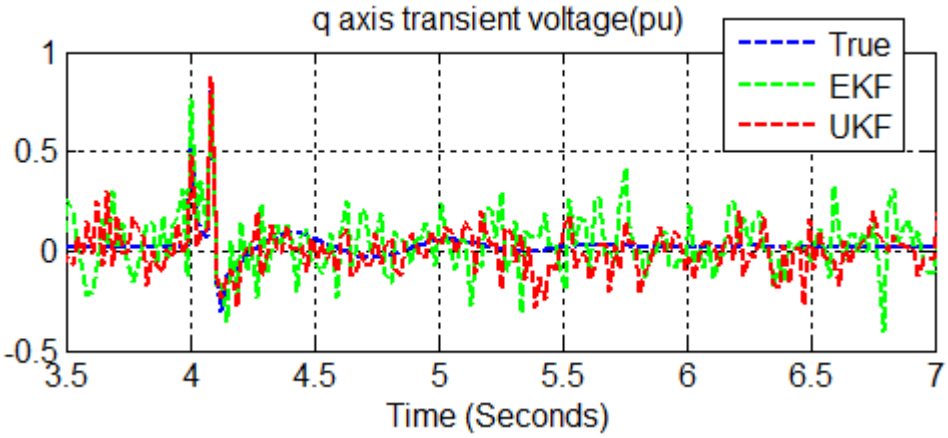

Figure 7.110 q-axis transient voltage and its estimates gen. loss, packet loss and delay at 50 Hz.

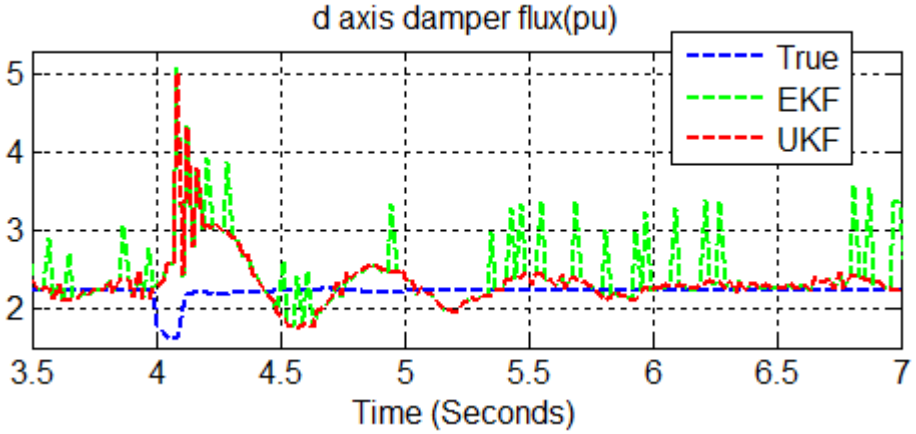

Figure 7.111 d-axis damper flux and its estimates gen. loss, packet loss and delay at 50 Hz.

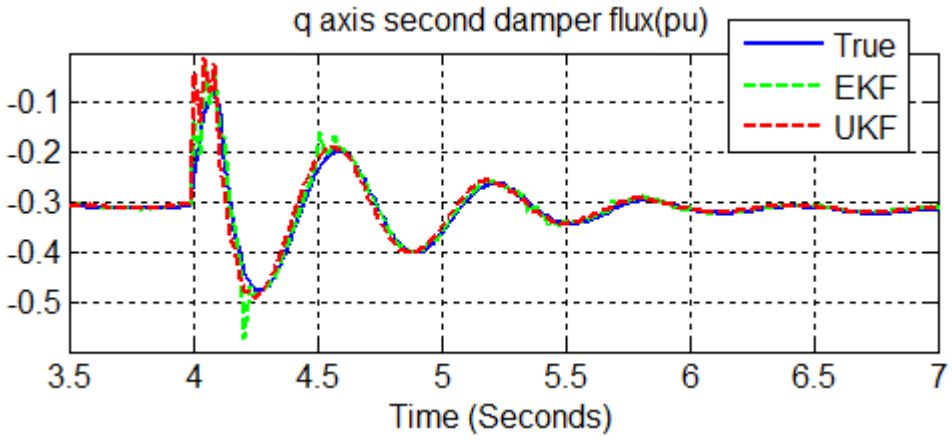

Figure 7.112 q-axis second damper flux and its estimates gen. loss, packet loss and delay at 50 Hz.

Table XV Comparison of RMS errors for EKF and UKF with a sampling frequency of 50 Hz.

Filter	RMSE (Max.)	RMSE(Min)	Standard Deviation	RMSE of Rotor Angle (Max)	RMSE of Rotor Angle (Min)	Standard Deviation
UKF	0.7201	0.6055	0.0324	0.1741	0.0007	0.0405
EKF	0.7321	0.6986	0.0074	0.2355	0.0138	0.0450

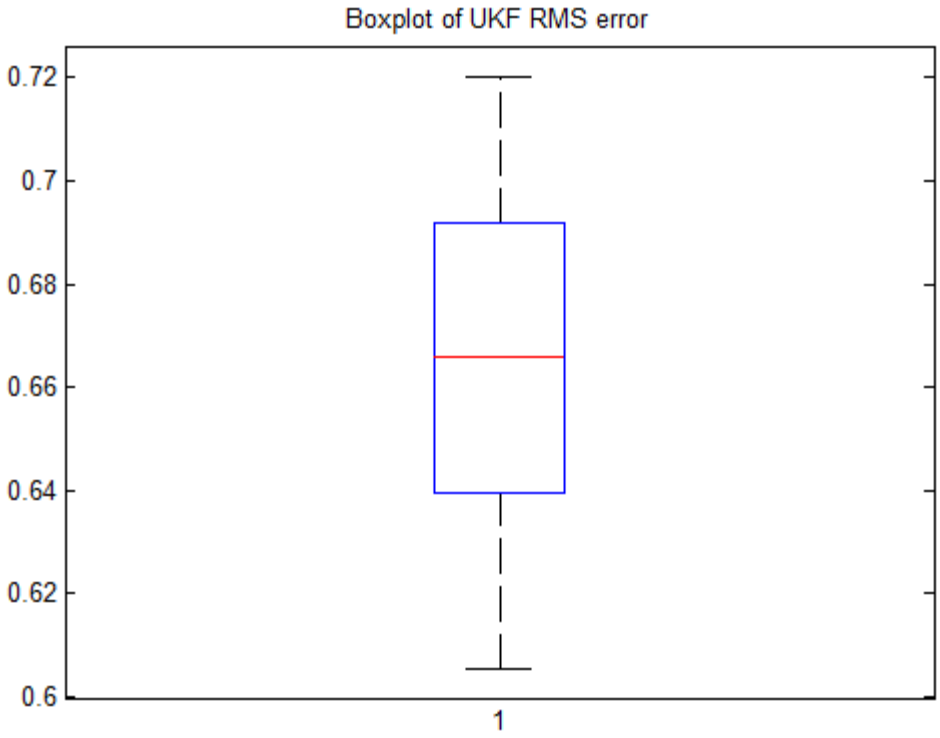

Figure 7.113 UKF RMS error with gen. loss, packet loss and delay at 50 Hz.

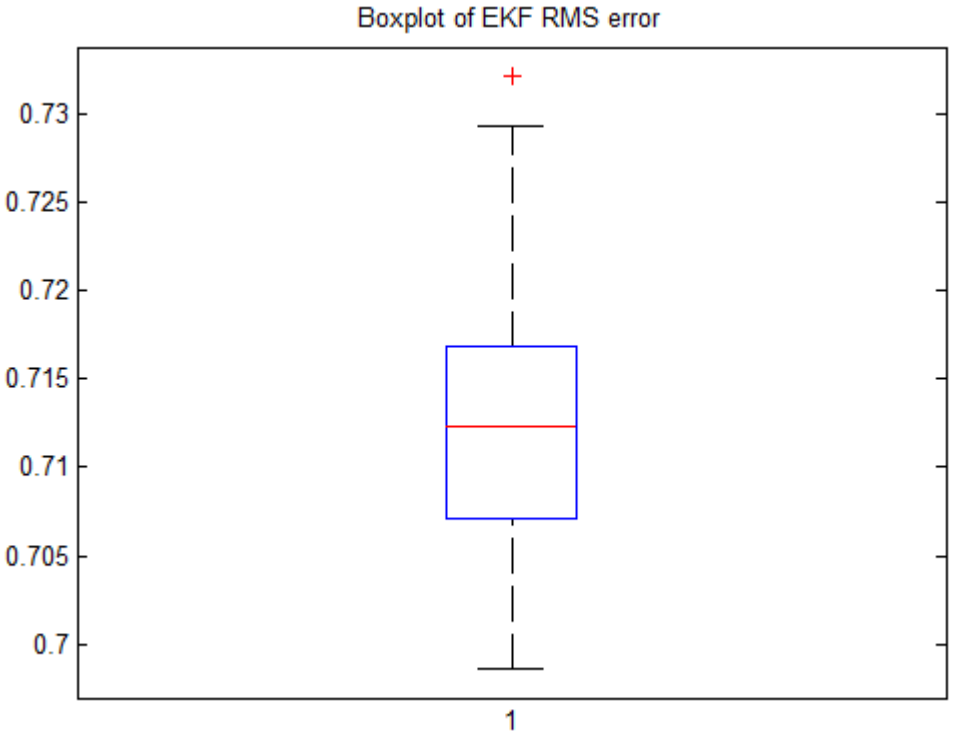

Figure 7.114 EKF RMS error gen. loss, packet loss and delay at 50 Hz.

7.15 LOAD LOSS, PACKET LOSS, AND TIME DELAY USING PMUMEASUREMENTS

We consider the effects of the loss of load 2 after 4.5 s with the PMU sampling frequency of 50 Hz and the packet drop and delay distributions of Section 7.5. Simulation results provided in Figure 7.115- Figure 7.120 demonstrate the effectiveness of our proposed method. The RMS errors corresponding to the EKF and the UKF are also provided in Figure 7.121-Figure 7.122. The results of 500 Monte Carlo simulations given in the box plots of Figures 7.121 and 7.122 and in Table XVI show that our results are acceptable for both filters.

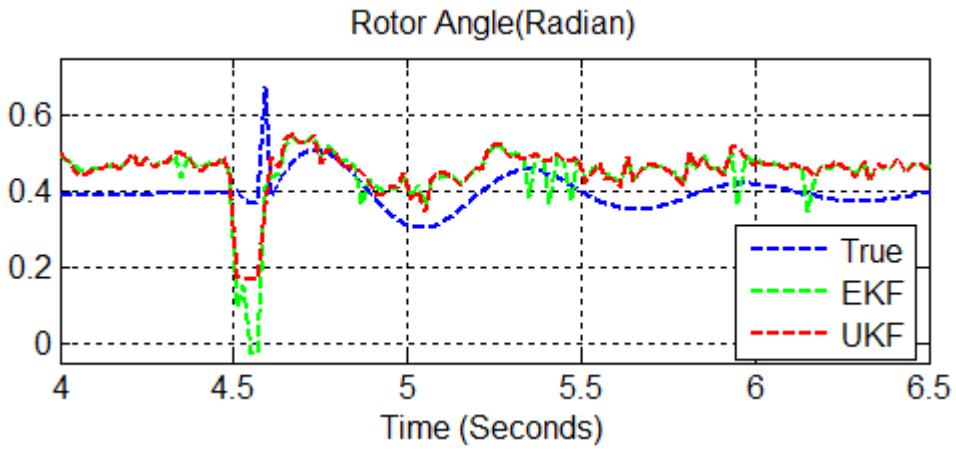

Figure 7.115 Rotor angle and its estimates with load loss, packet loss and delay at 50 Hz.

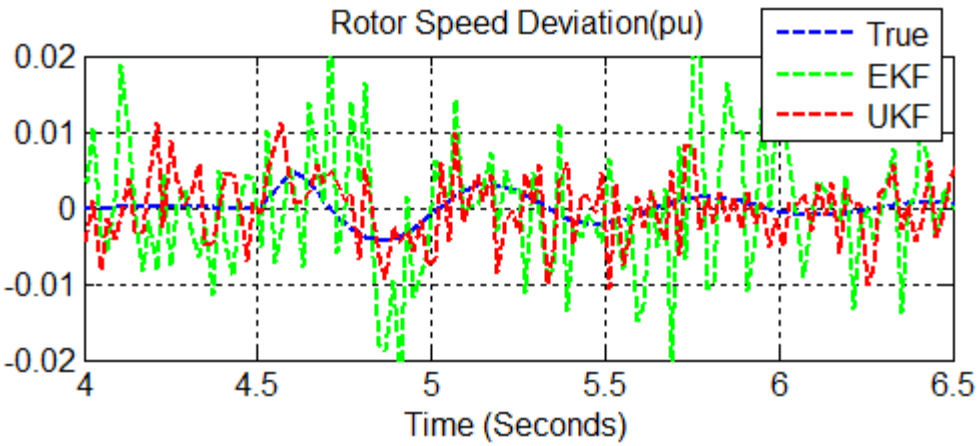

Figure 7.116 Rotor speed deviation and its estimates with load loss, packet loss and delay at 50 Hz.

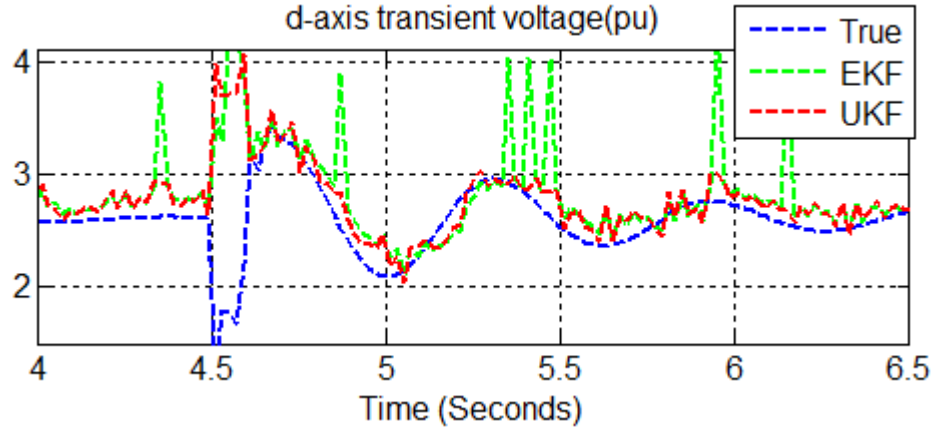

Figure 7.117 d-axis transient voltage and its estimates with load loss, packet loss and delay at 50 Hz.

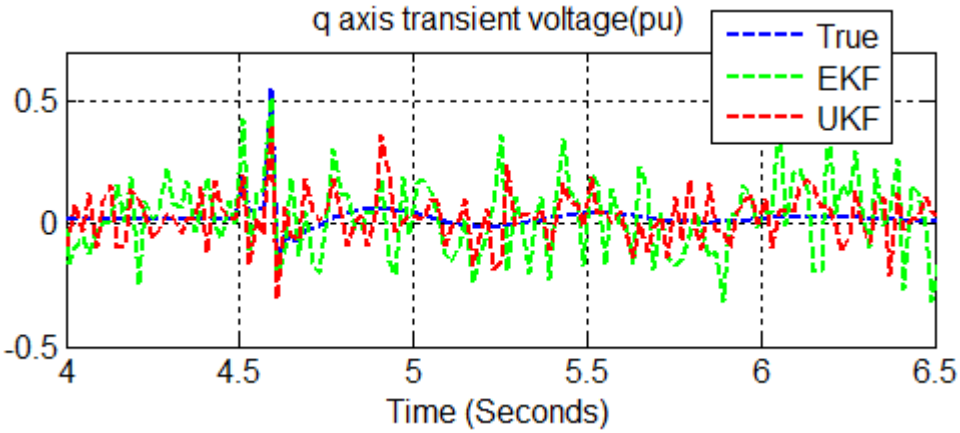

Figure 7.118 q-axis transient voltage and its estimates with load loss, packet loss and delay at 50 Hz.

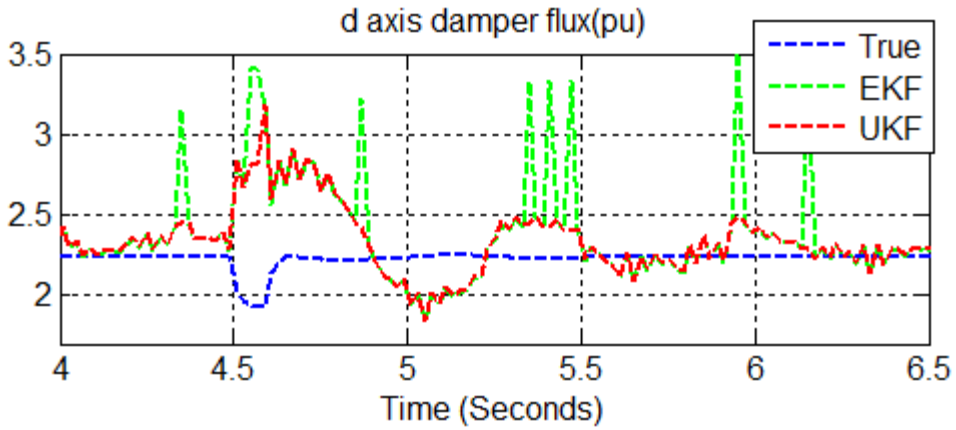

Figure 7.119 d-axis damper flux and its estimates with load loss, packet loss and delay at 50 Hz.

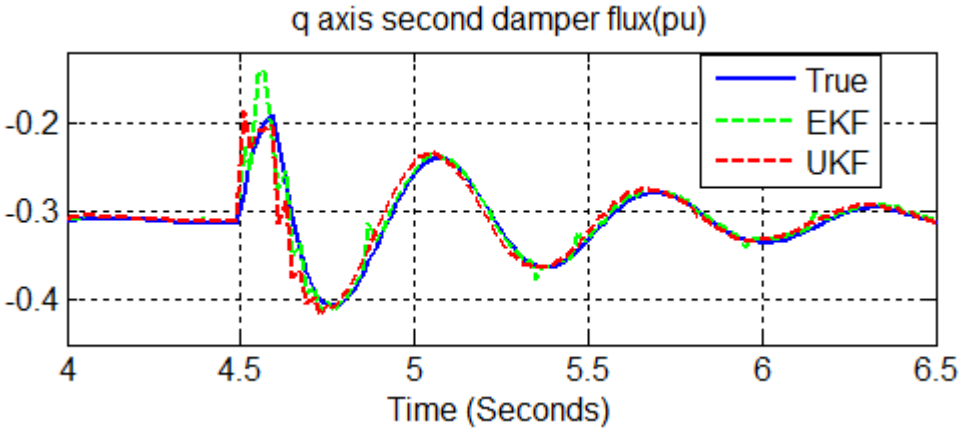

Figure 7.120 q-axis second damper flux and its estimates with load loss, packet loss and delay at 50 Hz.

Table XVI Comparison of RMS errors for EKF and UKF

Filter	RMSE (Max.)	RMSE(Min)	Standard Deviation	RMSE of Rotor Angle (Max)	RMSE of Rotor Angle (Min)	Standard Deviation
UKF	0.7610	0.5340	0.0595	0.1625	0.0081	0.0374
EKF	0.7613	0.7258	0.0078	0.1745	0.0173	0.0362

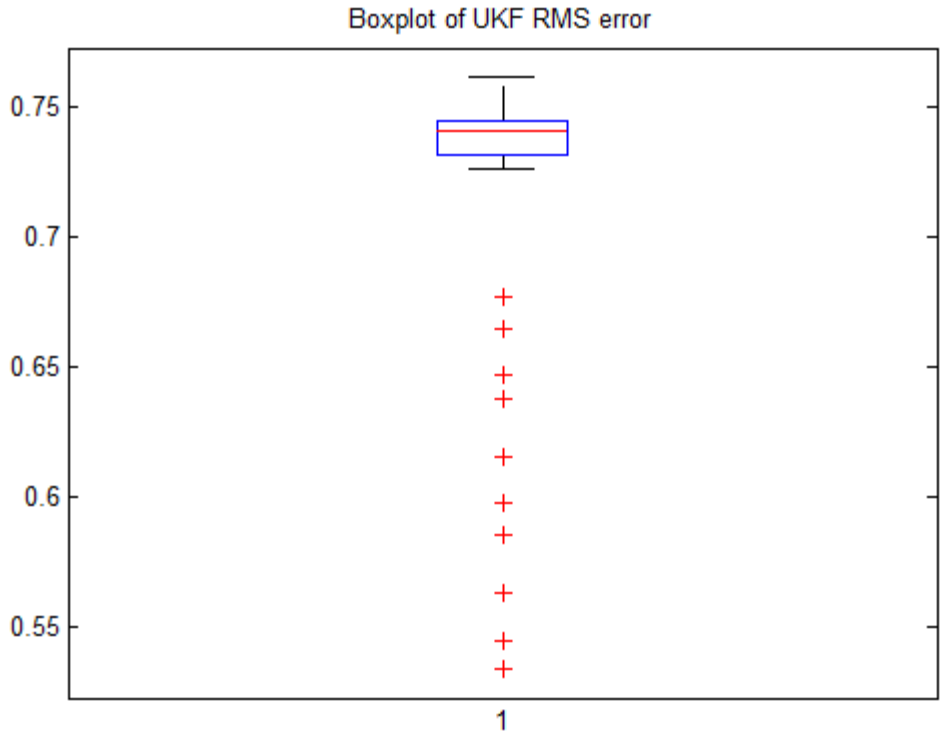

Figure 7.121 UKF RMS error with load loss, packet loss and delay at 50 Hz.

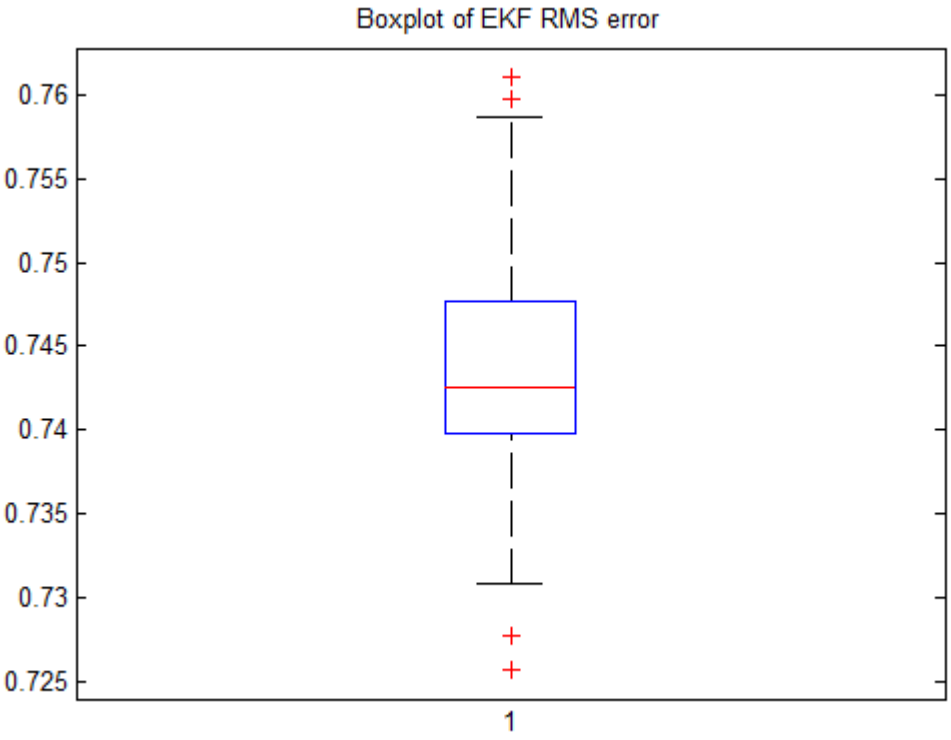

Figure 7.122 EKF RMS error with load loss, packet loss and delay at 50 Hz.

7.16 NORMAL MICROGRIDOPERATION WITH BAD DATA AND PMU MEASUREMENT

We investigate the performance of the robust state estimators, the two UKFs, and the GM-EKF using PMU data with outliers under normal operation. We introduced six consecutive outliers with values equal to 50 pu in active power starting at 4 seconds. Active power with bad data are presented in Figure 7.129. The nominal values of active power were below 2 (pu). The three robust state estimators were run using the measurements with bad data and the estimation results are provided in Figure 7.123- Figure 7.128.

Based on the results of Figure 7.123- Figure 7.128, we conclude that performance of the robust UKFs is better in dealing with the bad data than the GM-EKF. While the GM-EKF exhibits a large state estimation error when it faces bad data, the robust UKFs does not. The improved performance of the robust UKFs is also demonstrated by the RMS errors, based on 500 Monte Carlo simulations, presented in *Table XVII* and the box plots of Figure 7.131- Figure 7.132. Note that the effects of bad data are not equal for all state estimates. For example, in Figure 7.126 and Figure 7.128 the three estimators are performing with good accuracy.

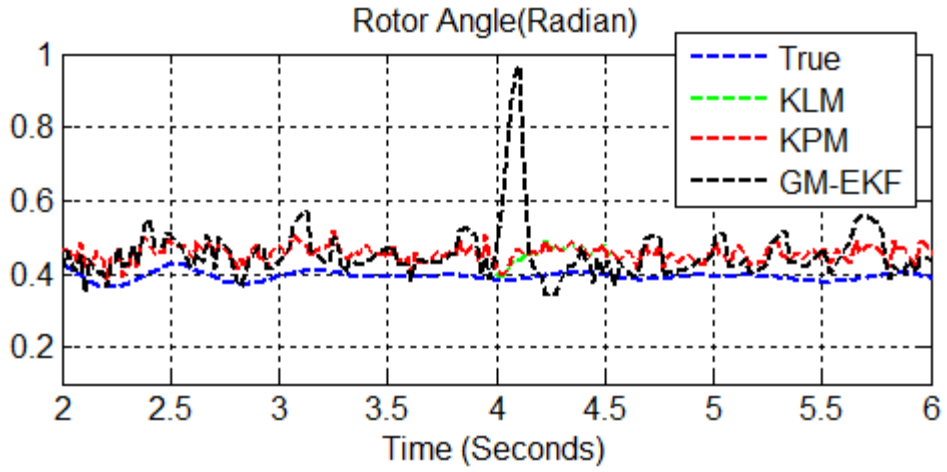

Figure 7.123 Rotor angle and its estimates with bad data at 50 Hz.

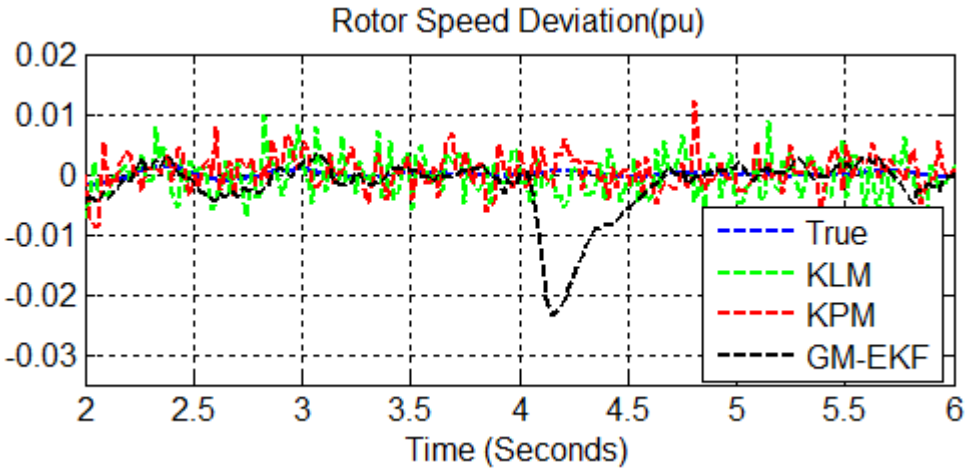

Figure 7.124 Rotor speed deviation and its estimates with bad data at 50 Hz.

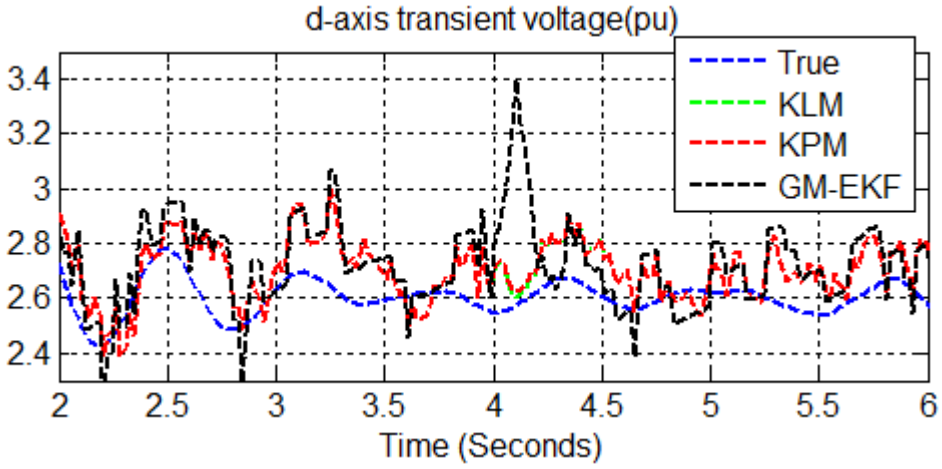

Figure 7.125 d-axis transient voltage and its estimates with bad data at 50 Hz.

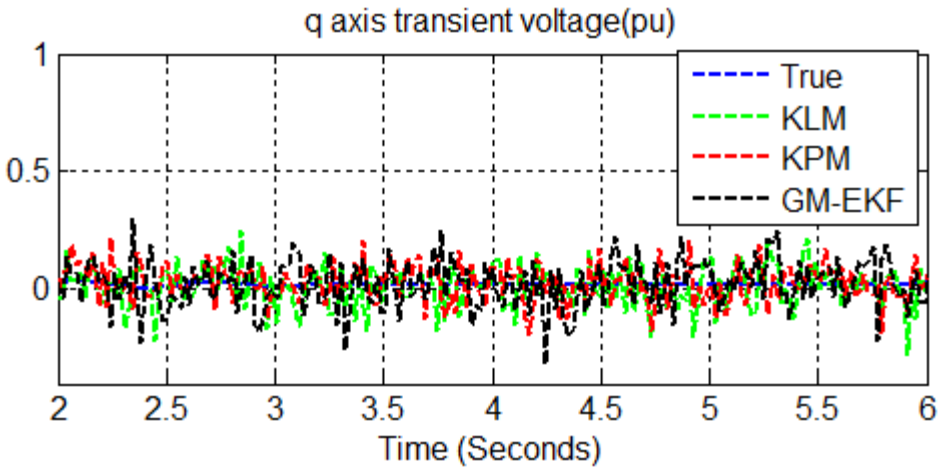

Figure 7.126 q-axis transient voltage and its estimates with bad data at 50 Hz.

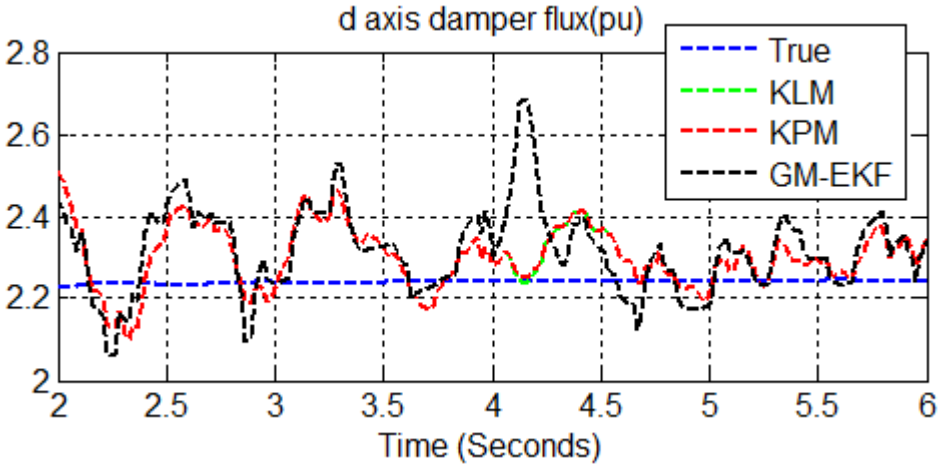

Figure 7.127 d-axis damper flux and its estimates with bad data at 50 Hz.

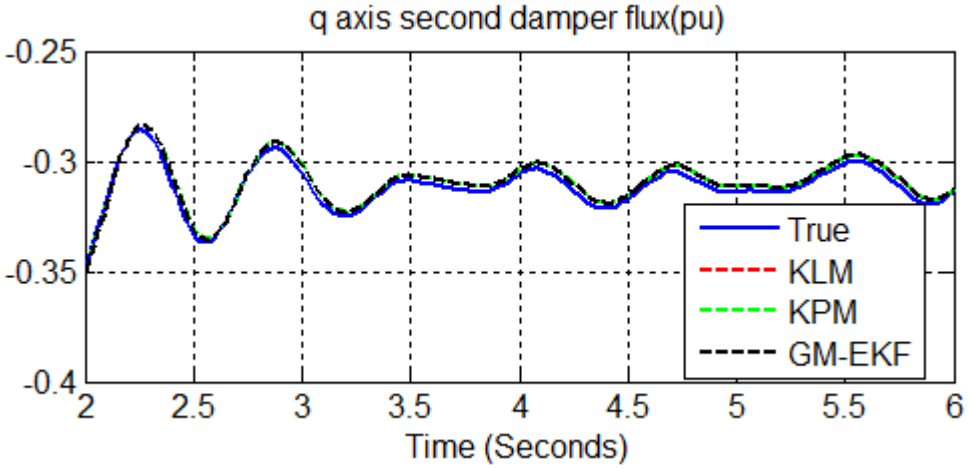

Figure 7.128 q-axis second damper flux and its estimates with bad data at 50 Hz.

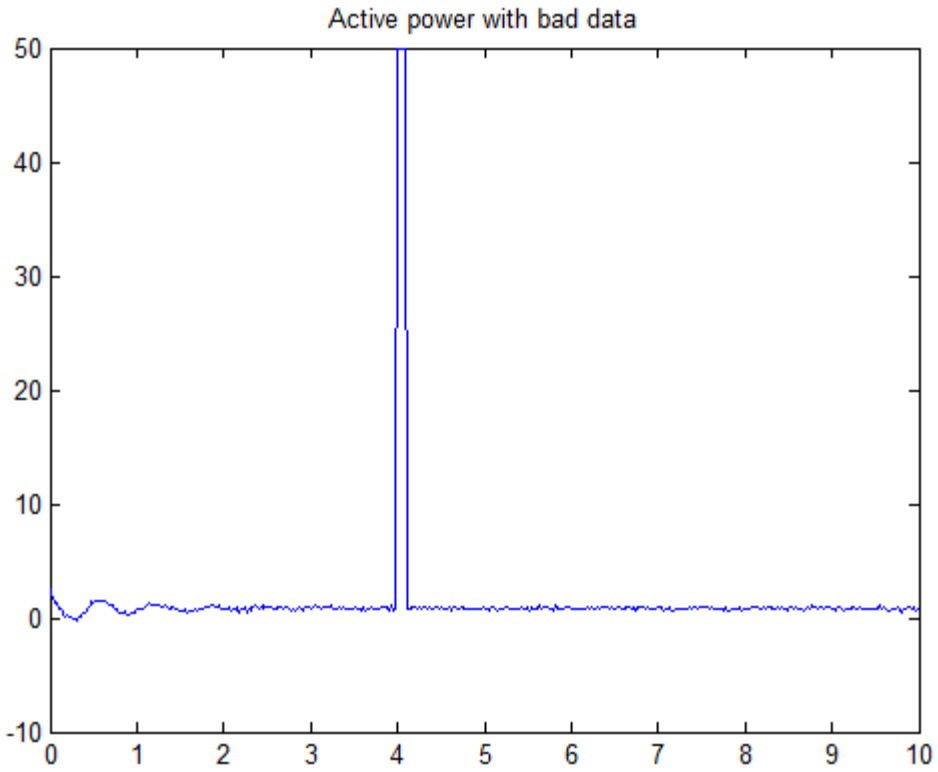

Figure 7.129 Active power with bad data

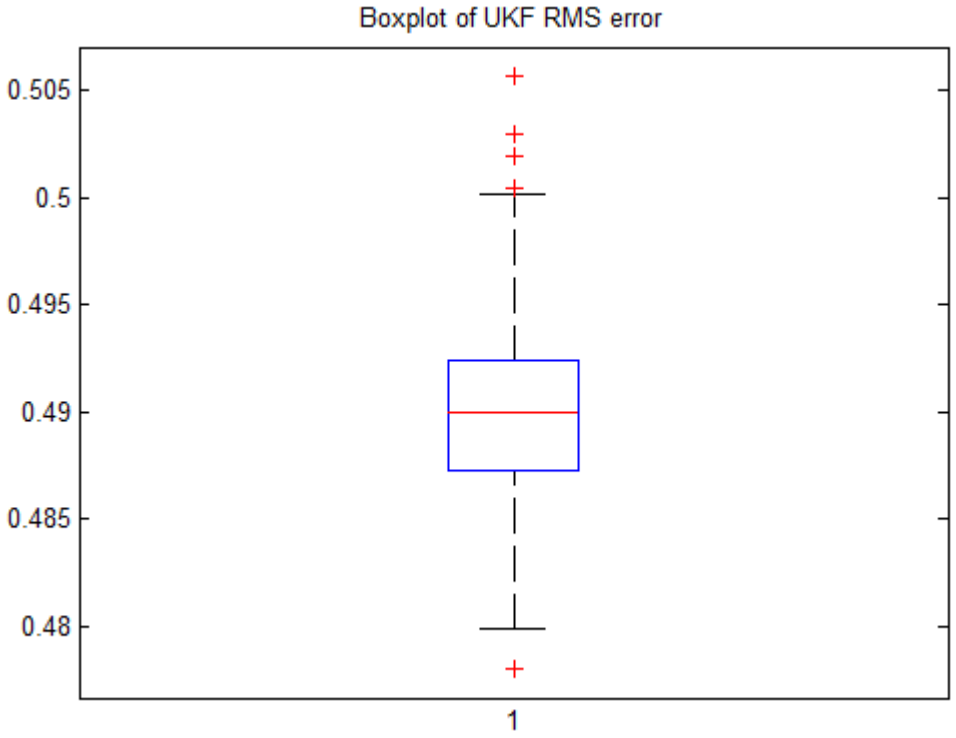

Figure 7.130 UKF RMS error with predicted measurement with bad data at 50 Hz.

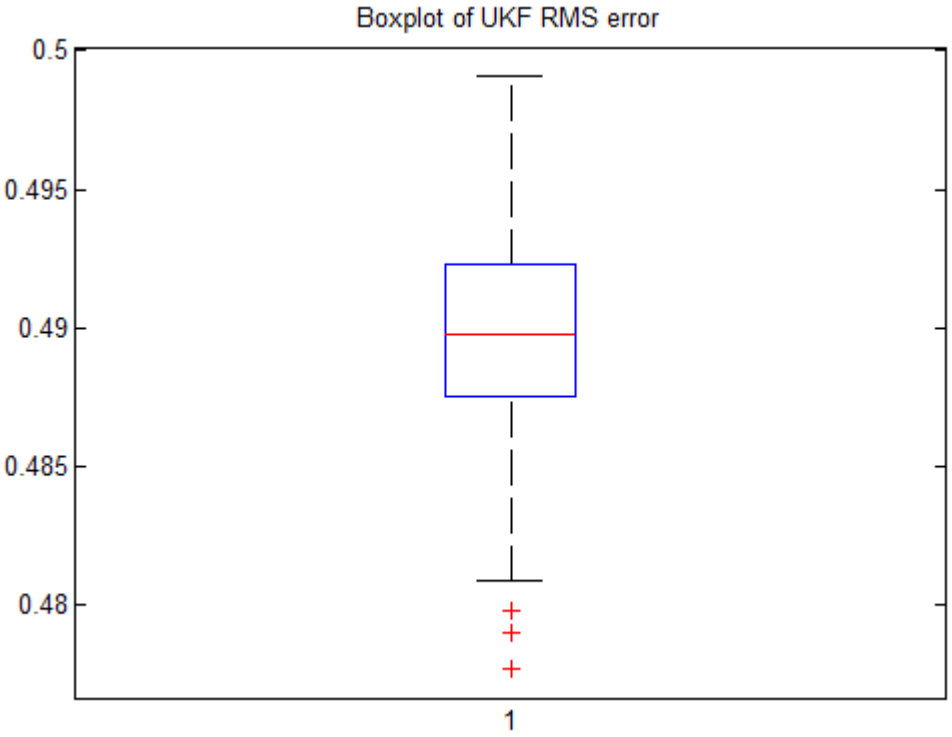

Figure 7.131 UKF RMS error with last uncorrupted measurement with bad data at 50 Hz.

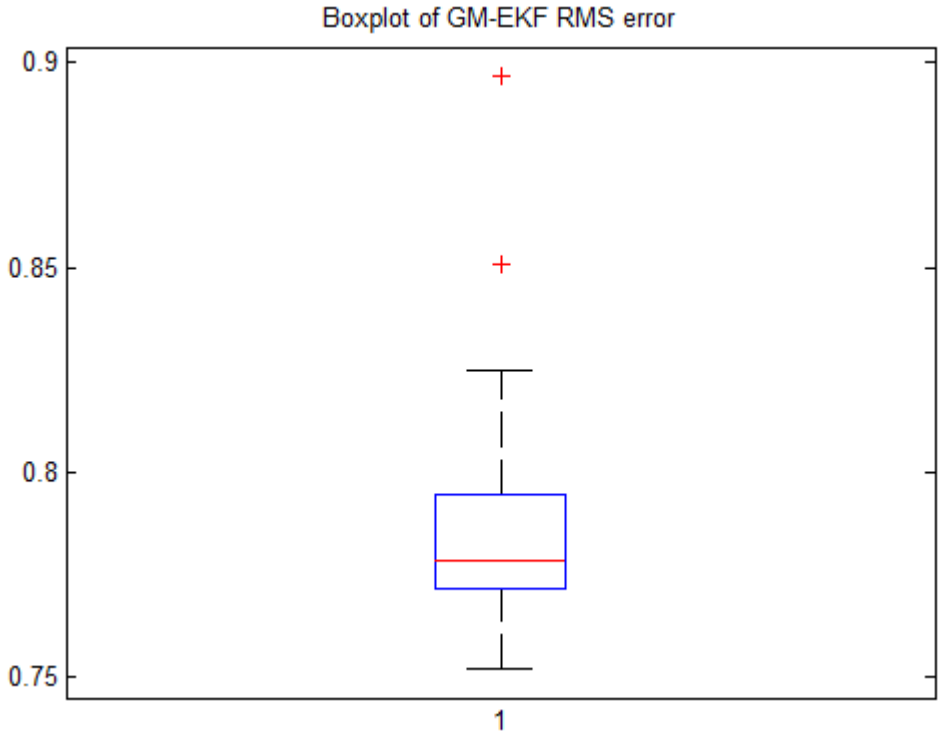

Figure 7.132 Box plot of GM-EKF RMS error with bad data at 50 Hz.

Table XVII Comparison of RMS errors for the EKF, the UKF and the GM-EKF

Filter	RMSE (Max.)	RMSE(Min)	Standard Deviation	RMSE of Rotor Angle (Max)	RMSE of Rotor Angle (Min)	Standard Deviation
KPM	0.5056	0.4781	0.0039	0.1875	0.0016	0.0350
KLM	0.4991	0.4777	0.0036	0.1809	0.0013	0.0352
GM-EKF	0.8966	0.7523	0.0252	0.1904	0.0002	0.0530

7.17 FAULT AT PCC, BAD DATA AND PMU MEASUREMENT

In this section, we analyze the performance of the robust estimators under the condition of fault at PCC and bad data in measurements at the PMU sampling frequency of 50 Hz. A three phase to ground fault is applied at 5 s and cleared at 5.1 s. Together with the fault, we introduce six consecutive outliers in the active power measurements starting at 6 s (Figure 7.139). The results obtained from the GM-EKF, and the robust UKFs are presented in Figure 7.133- Figure 7.138.

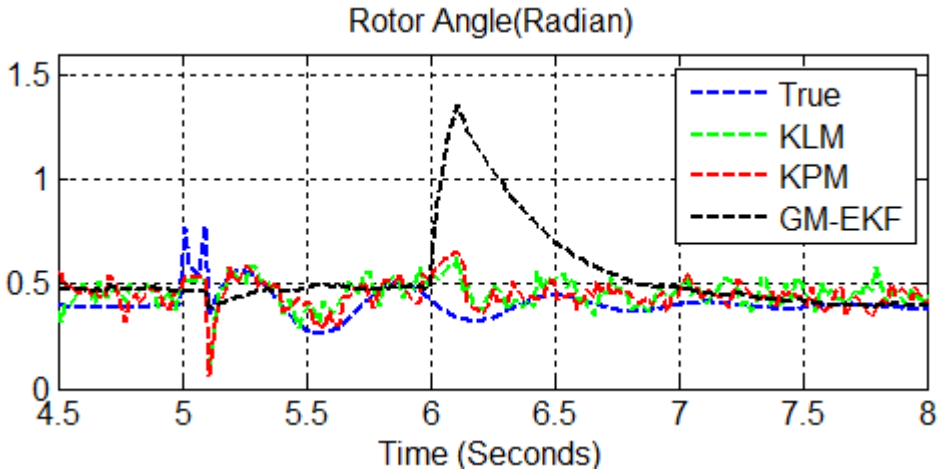

Figure 7.133 Rotor angle and its estimates with fault, bad data at 50 Hz.

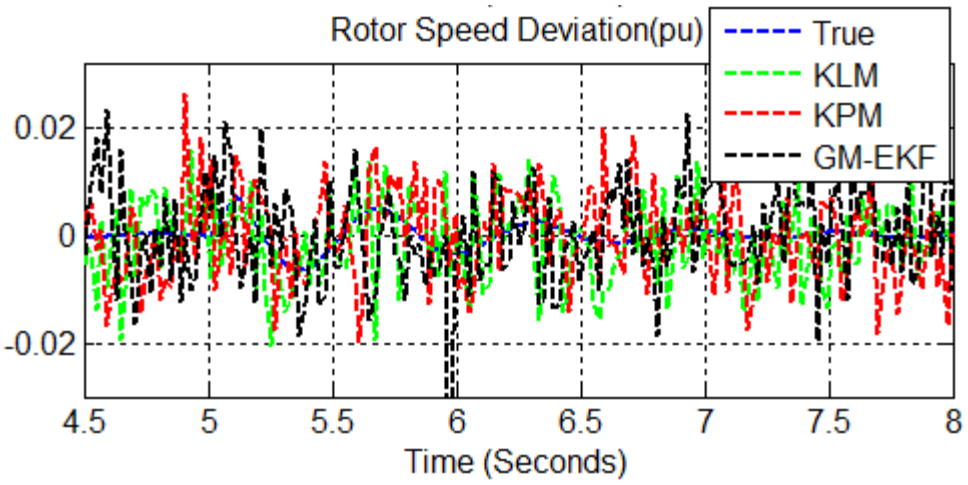

Figure 7.134 Rotor speed deviation and its estimates with fault, bad data at 50 Hz.

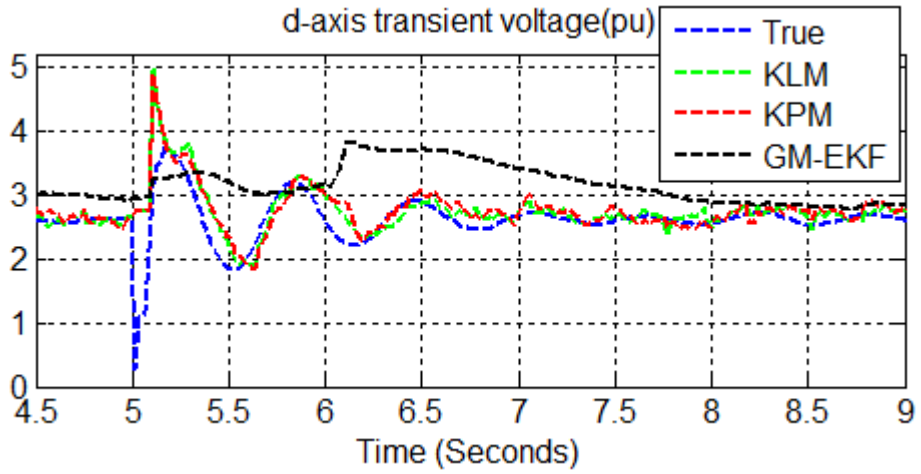

Figure 7.135 d-axis transient voltage and its estimates with fault, bad data at 50 Hz.

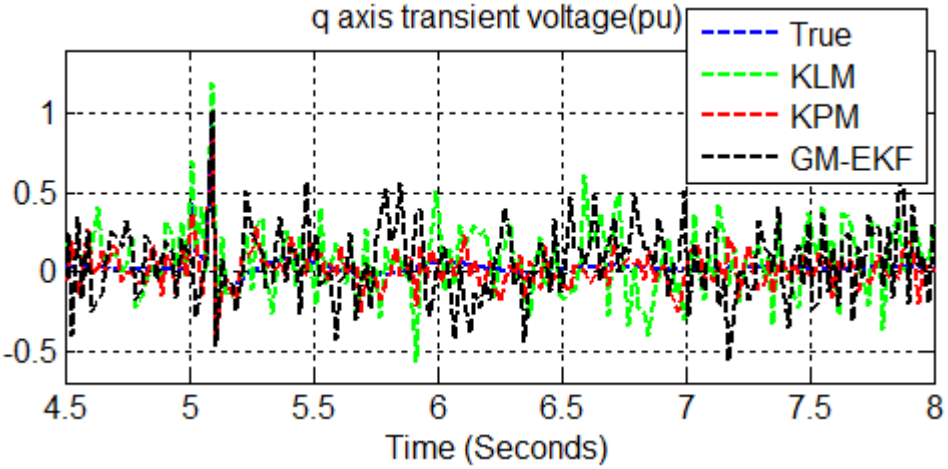

Figure 7.136 q-axis transient voltage and its estimates with fault, bad data at 50 Hz.

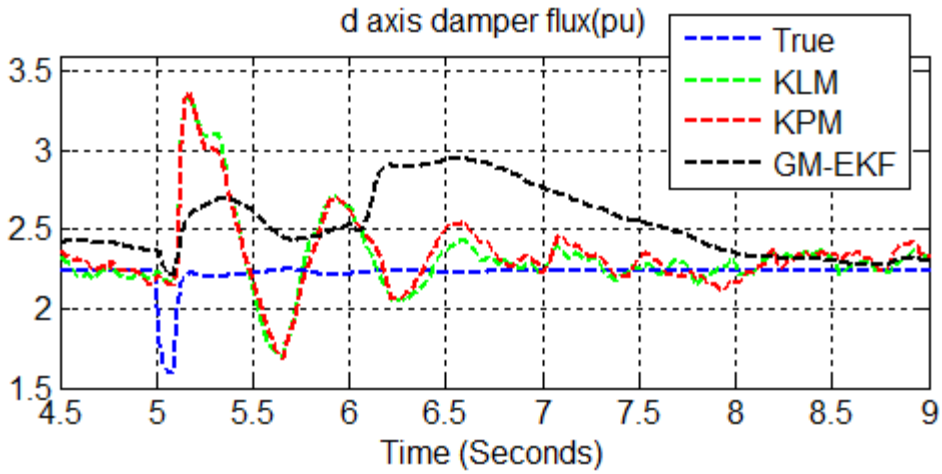

Figure 7.137 d-axis damper flux and its estimates with fault, bad data at 50 Hz.

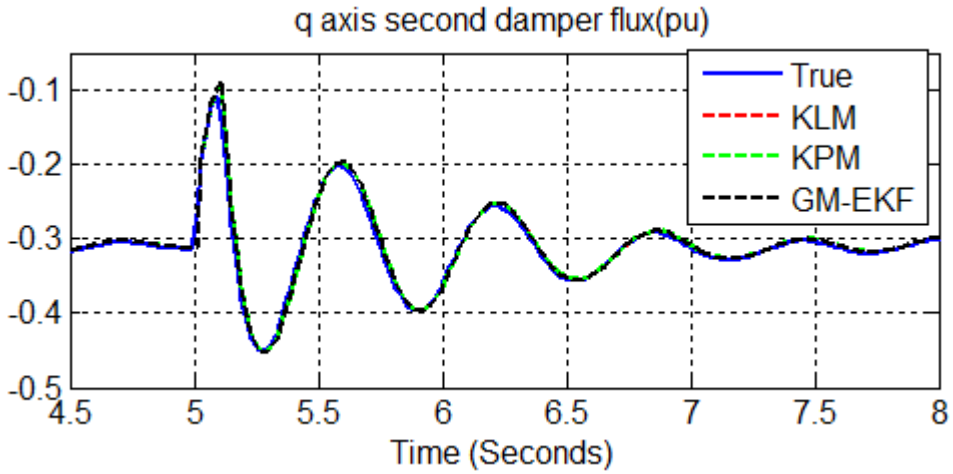

Figure 7.138 q-axis second damper flux and its estimates with fault, bad data at 50 Hz.

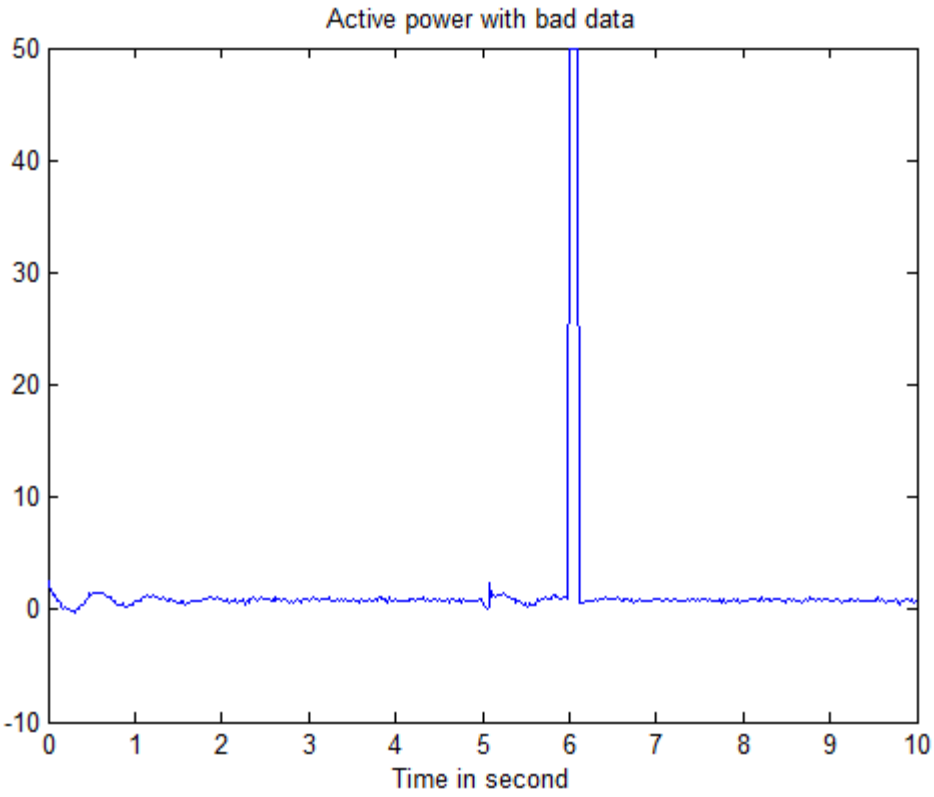

Figure 7.139 Active power with bad data

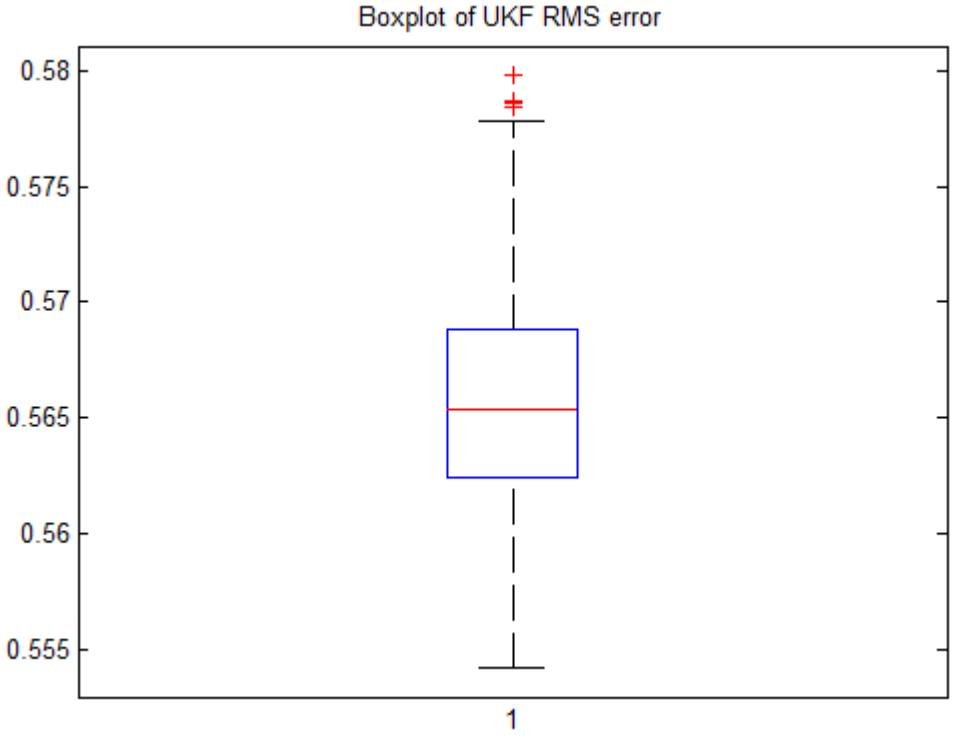

Figure 7.140 UKF RMS error with predicted measurement with fault, bad data at 50 Hz.

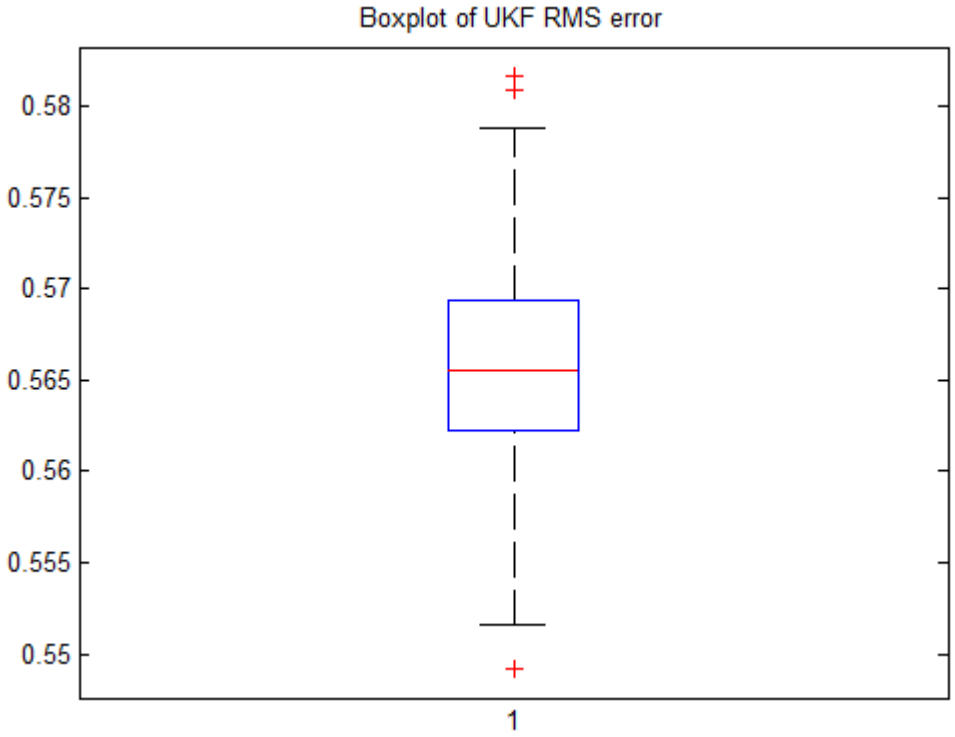

Figure 7.141 UKF RMS error with last uncorrupted measurement with fault, bad data at 50 Hz.

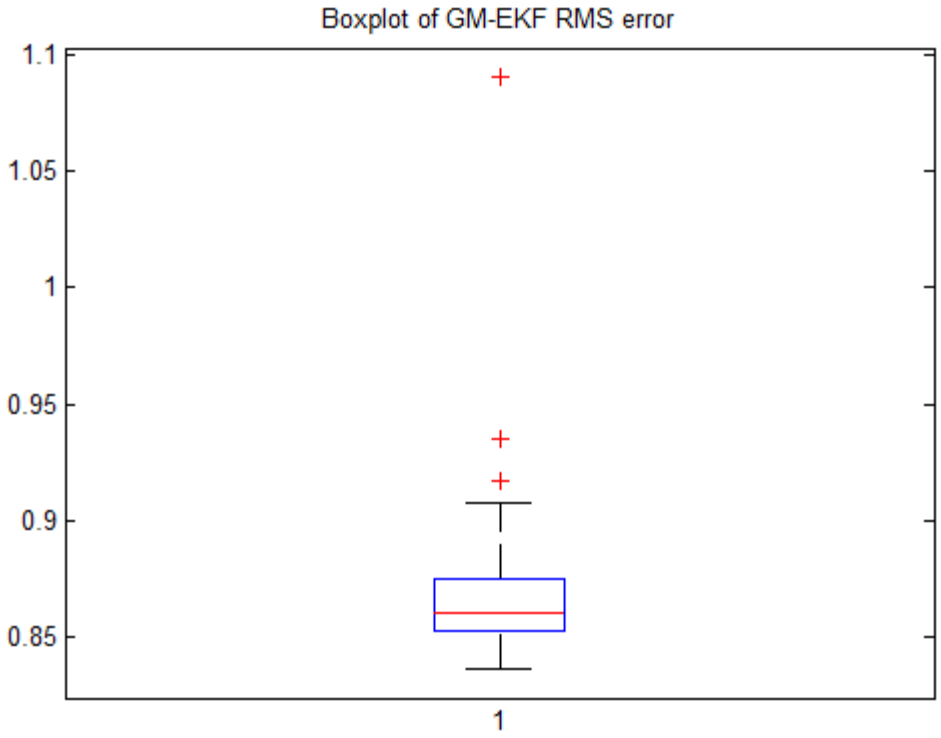

Figure 7.142 GM-EKF RMS error with fault, bad data at 50 Hz.

Table XVIII Comparison of RMS errors for the KPM, KLM and the GM-EKF

Filter	RMSE (Max.)	RMSE(Min)	Standard Deviation	RMSE of Rotor Angle (Max)	RMSE of Rotor Angle (Min)	Standard Deviation
UKF (PM)	0.5798	0.5543	0.0048	0.2045	0.0098	0.0342
UKF (LM)	0.5816	0.5492	0.0052	0.1673	0.0205	0.0352
GM-EKF	1.0903	0.8365	0.0382	0.2042	0.0770	0.0061

Once again, we obtain superior performance from the robust UKFs to the GM-EKF. The GM-EKF starts deviating from the true values as it faces bad data in measurements. It also takes a longer time to recover to the actual states than the robust UKFs. The results of 500 Monte Carlo simulation shown in *Table XVIII* demonstrate

the larger RMS errors associated with the GM-EKF. The results of Figure 7.136 and Figure 7.138 are not significantly affected by bad data.

7.18 GENERATOR LOSS, BAD DATA AND PMU MEASUREMENT

We investigate the performance of robust estimators under loss of generator and bad data. We simulated the loss of the second synchronous generator at 4 s with the PMU sampling frequency of 50 Hz for measurements of active and reactive power. Six outliers were introduced in active power as shown in Figure 7.149. Simulation results from the robust state estimators are provided in Figure 7.143- Figure 7.148.

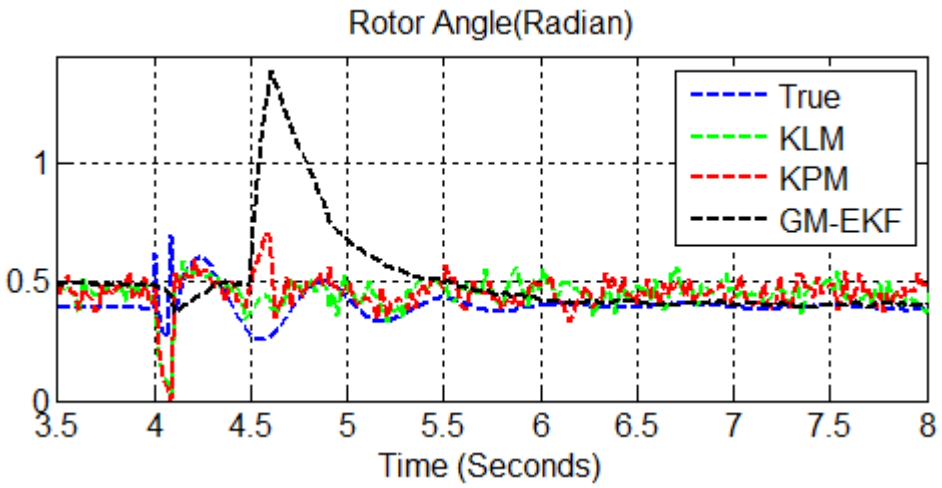

Figure 7.143 Rotor angle and its estimates with gen. loss, bad data at 50 Hz.

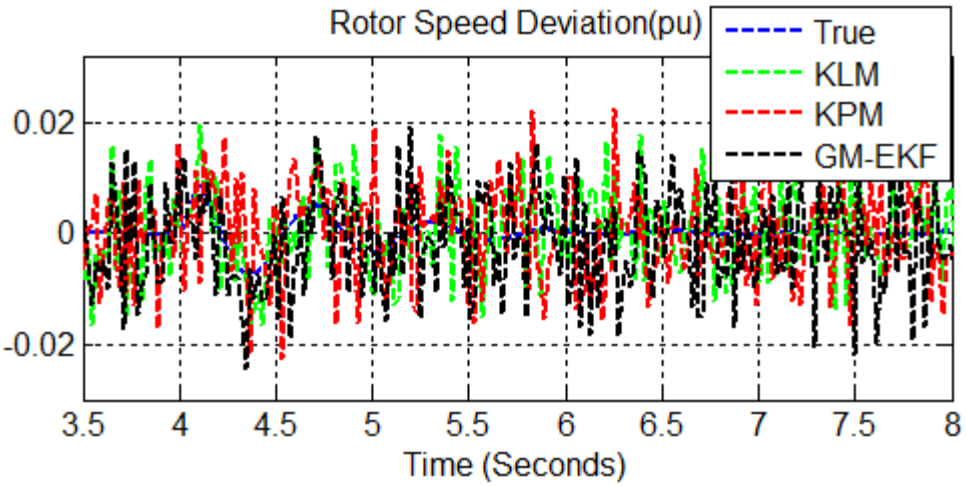

Figure 7.144 Rotor speed deviation and its estimates with gen. loss, bad data at 50 Hz.

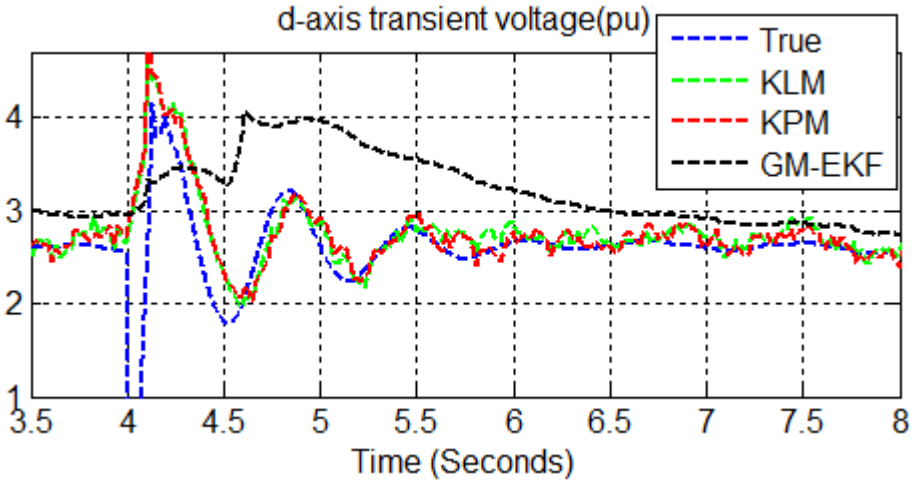

Figure 7.145 d-axis transient voltage and its estimates with gen. loss, bad data at 50 Hz.

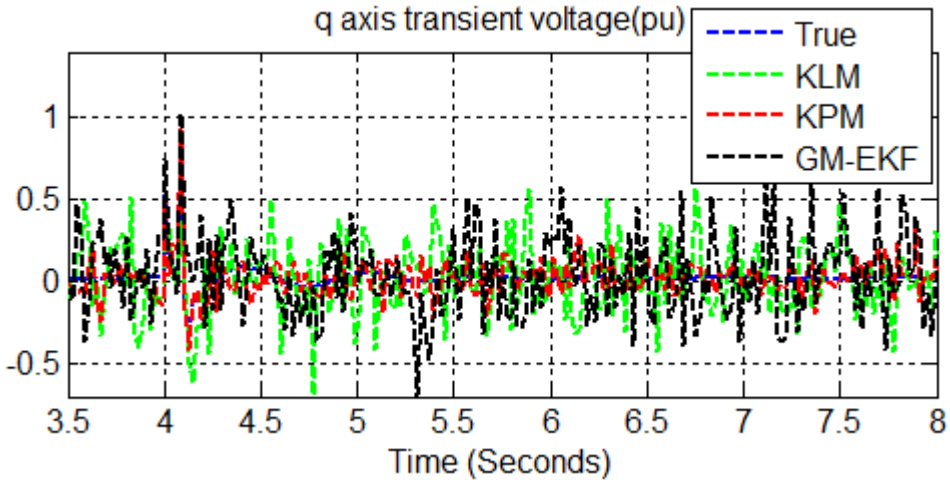

Figure 7.146 q-axis transient voltage and its estimates with gen. loss, bad data at 50 Hz.

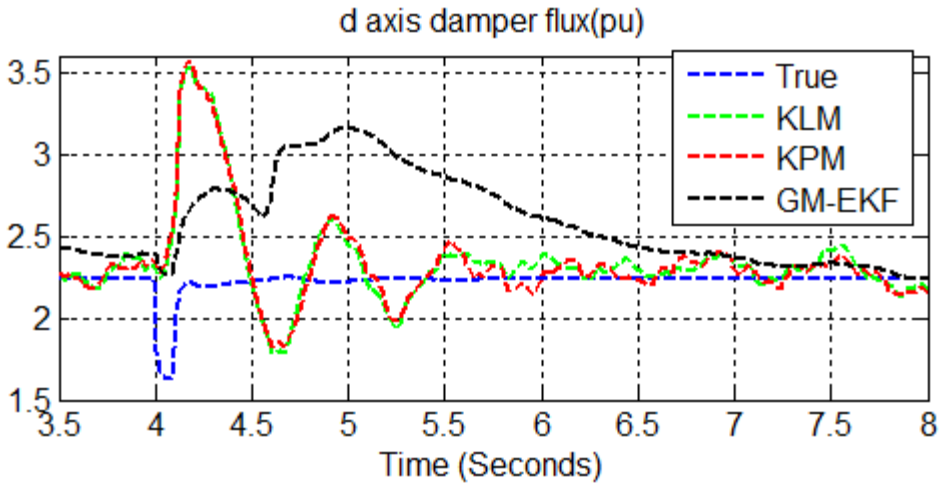

Figure 7.147 d-axis damper flux and its estimates with gen. loss, bad data at 50 Hz.

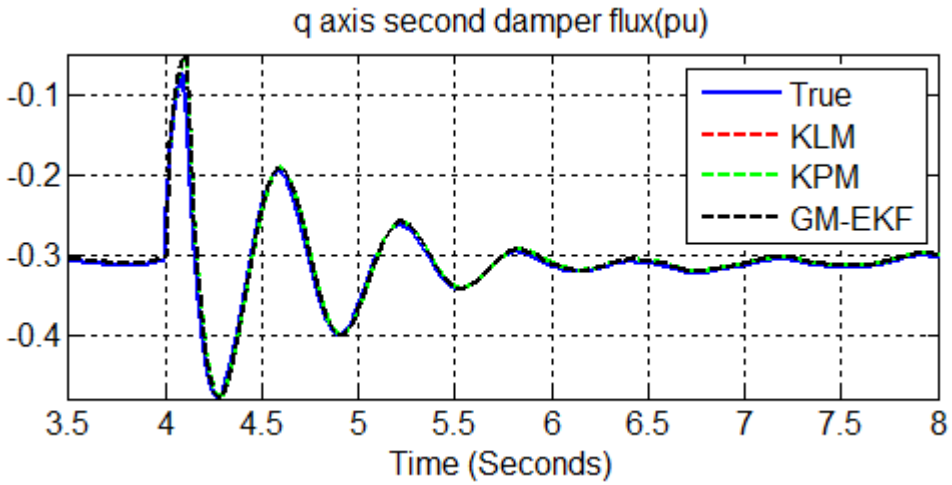

Figure 7.148 q-axis second damper flux and its estimates with gen. loss, bad data at 50 Hz.

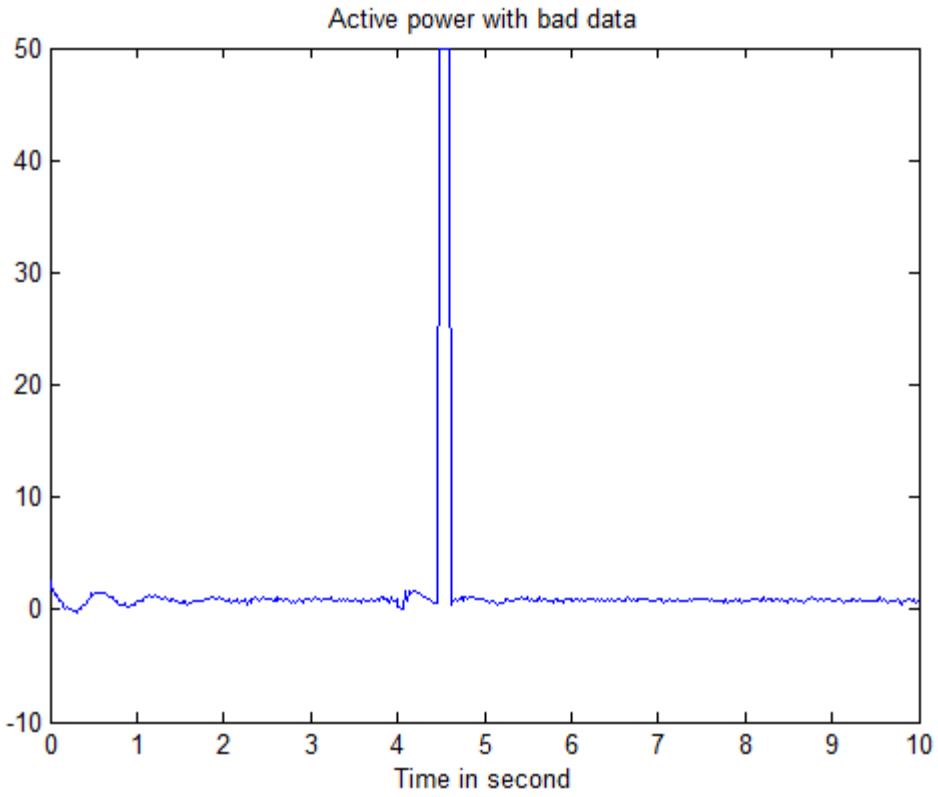

Figure 7.149 Active power with bad data

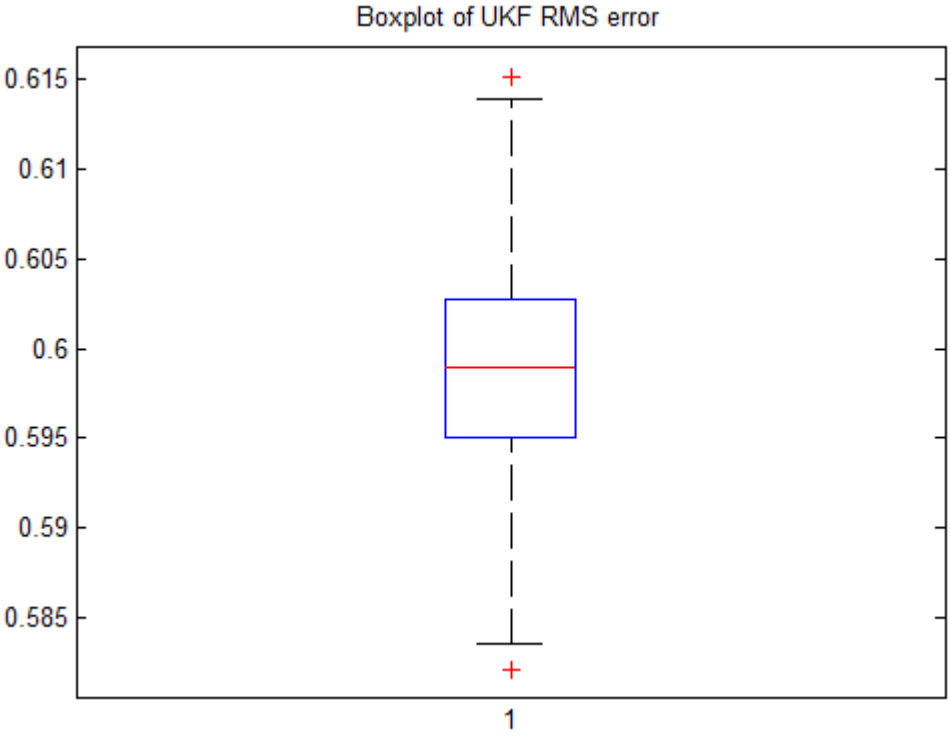

Figure 7.150 KPM-UKF RMS error with generator loss and bad data at 50 Hz.

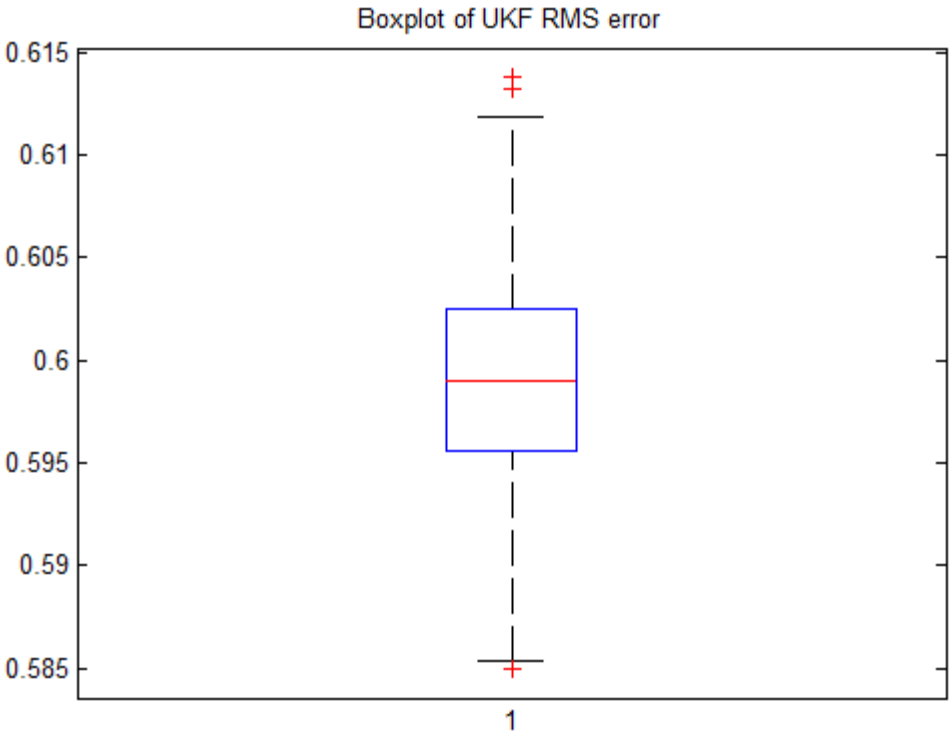

Figure 7.151 KLM-UKF RMS error with generator loss, bad data at 50 Hz.

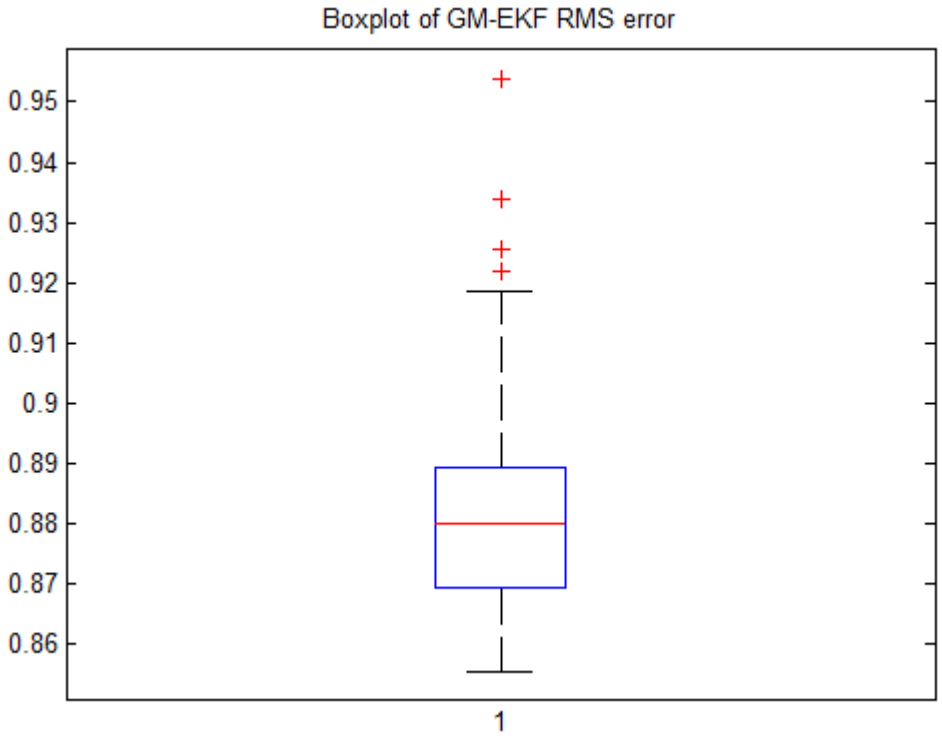

Figure 7.152 GM-EKF RMS error with gen. loss, bad data at 50 Hz.

Table XIX Comparison of RMS errors for the KPM, the KLM and the GM-EKF

Filter	RMSE (Max.)	RMSE(Min)	Standard Deviation	RMSE of Rotor Angle (Max)	RMSE of Rotor Angle (Min)	Standard Deviation
UKF (PM)	0.6151	0.5821	0.0050	0.1806	0.0042	0.0323
UKF (LM)	0.6138	0.5850	0.0063	0.1596	0.0036	0.0342
GM-EKF	0.9537	0.8556	0.0209	6.5055	0.0034	0.9182

Based on the results of Figure 7.143- Figure 7.148 and 500 Monte Carlo simulation results (*Table XIX* and box plots Figure 7.151- Figure 7.152), we conclude the robust UKFs perform better than the GM-EKF. Again, not all of state estimates are equally affected by bad data in PMU measurements.

7.19 LOAD LOSS, BAD DATA AND PMU MEASUREMENT

In this section, we examine the performance of the robust UKFs and the GM-EKF under loss of load and bad data with the PMU frequency of 50 Hz. As in Section 7.4, we simulate the loss of the second load at 4.5 s. Six outliers are introduced in active power as shown in Figure 7.159. Simulation results for the robust state estimators subject the bad data and loss of load are presented in Figure 7.153- Figure 7.158. The robust UKFs provide better tracking of the true states than the GM-EKF. This is particularly true for the plots of the rotor angle, the d-axis transient voltage, and d-axis damper flux.

The results of 500 Monte Carlo simulations are provided in the box plots of Figure 7.161- Figure 7.162 and *Table XX*. The errors for the robust UKFs are significantly smaller than the errors for the GM-EKF. The results show that with bad data and load

loss, at the PMU sampling frequency of 50 Hz, the robust UKFs perform better than the GM-EKF.

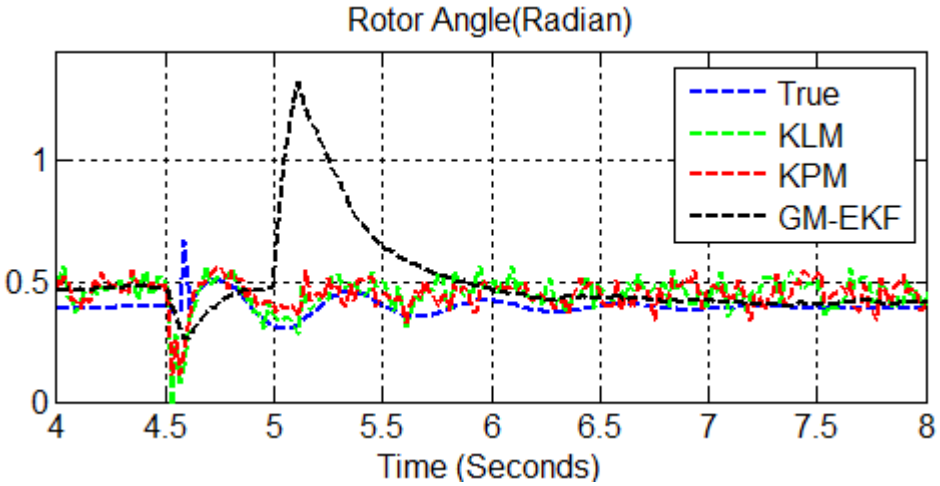

Figure 7.153 Rotor angle and its estimates with load loss, bad data at 50 Hz.

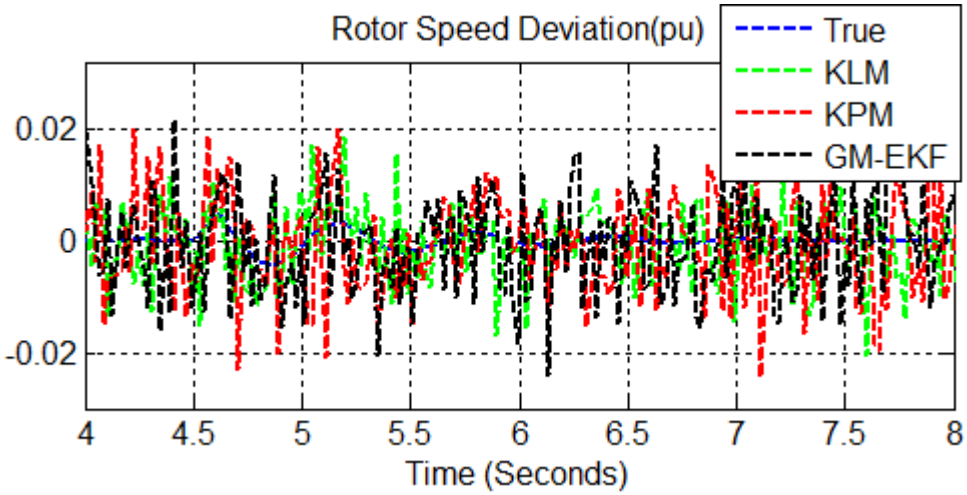

Figure 7.154 Rotor speed deviation and its estimates with load loss, bad data at 50 Hz.

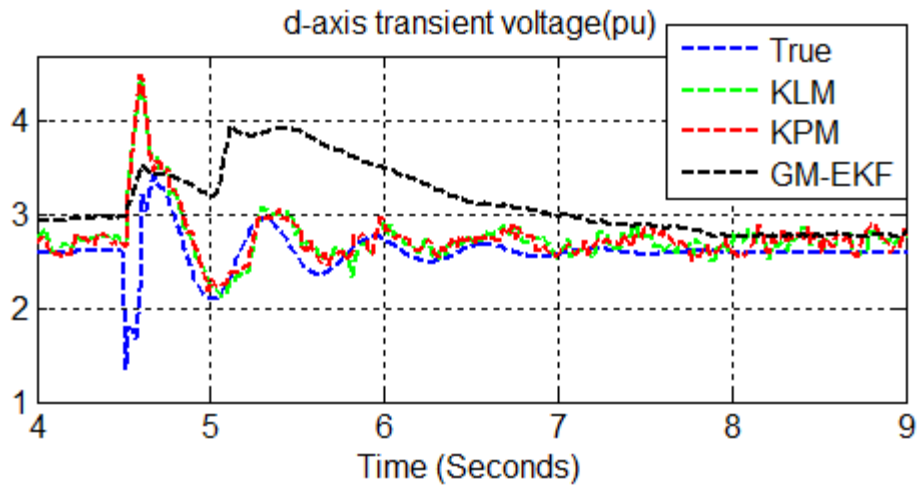

Figure 7.155 d-axis transient voltage and its estimates with load loss, bad data at 50 Hz.

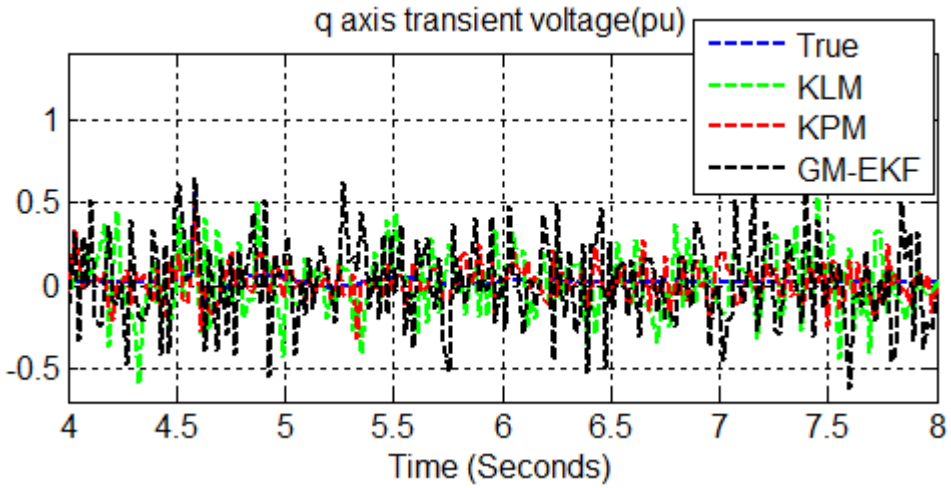

Figure 7.156 q-axis transient voltage and its estimates with load loss, bad data at 50 Hz.

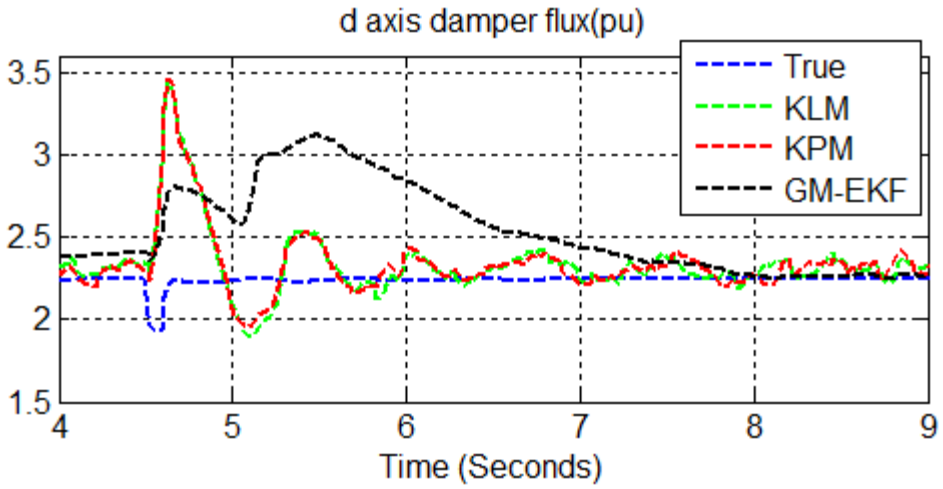

Figure 7.157 d-axis damper flux and its estimates with load loss, bad data at 50 Hz.

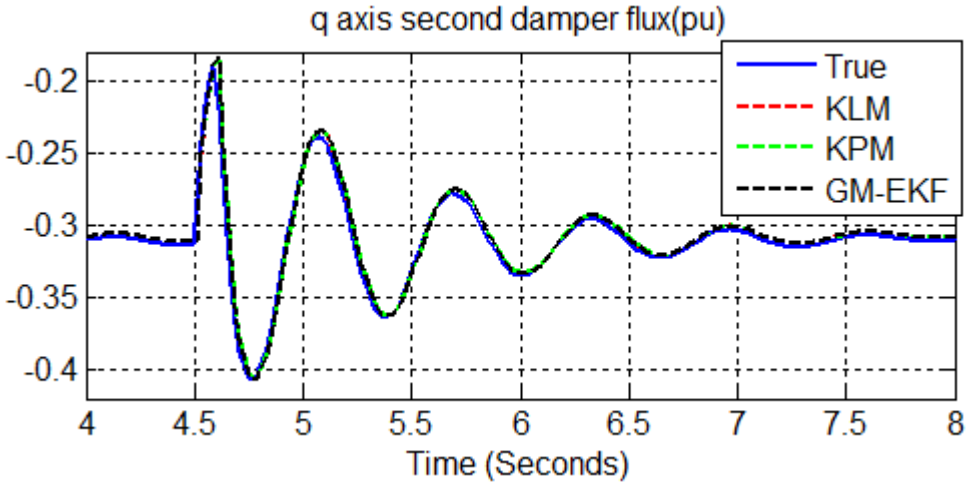

Figure 7.158 q-axis second damper flux and its estimates with load loss, bad data at 50 Hz.

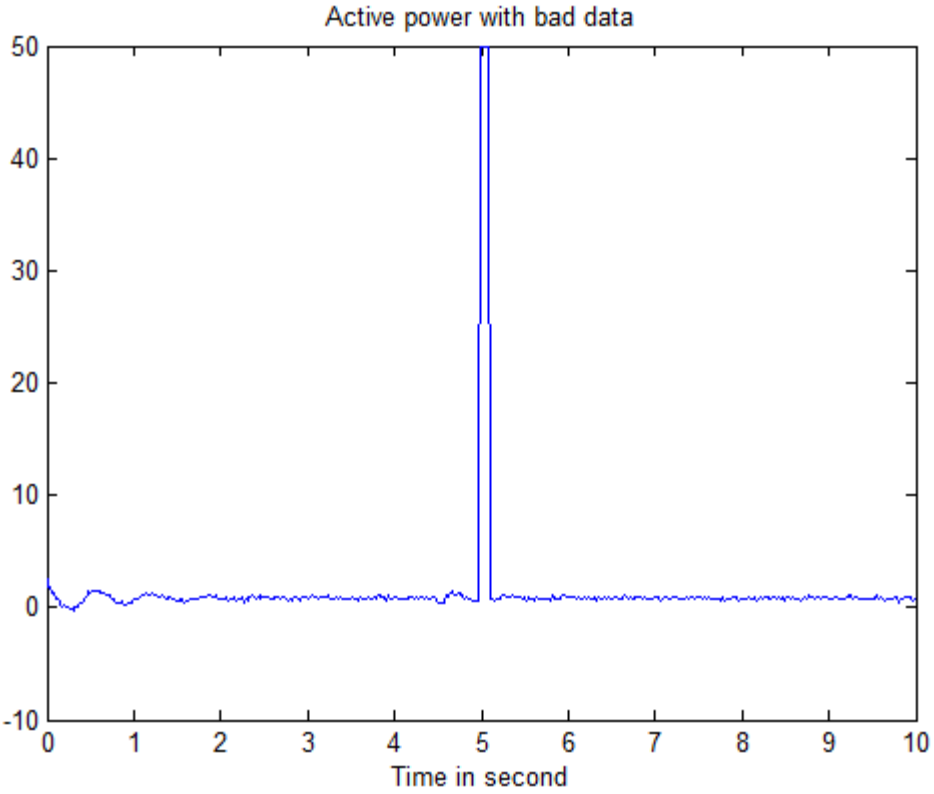

Figure 7.159 Active power with bad data

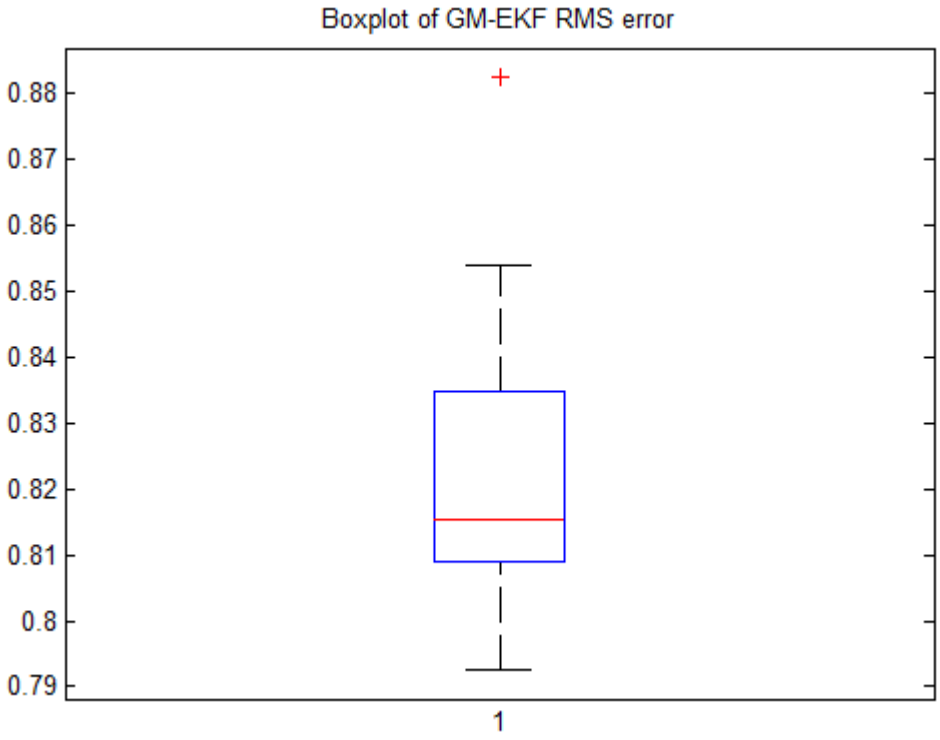

Figure 7.160 GM-EKF RMS error with load loss, bad data at 50 Hz.

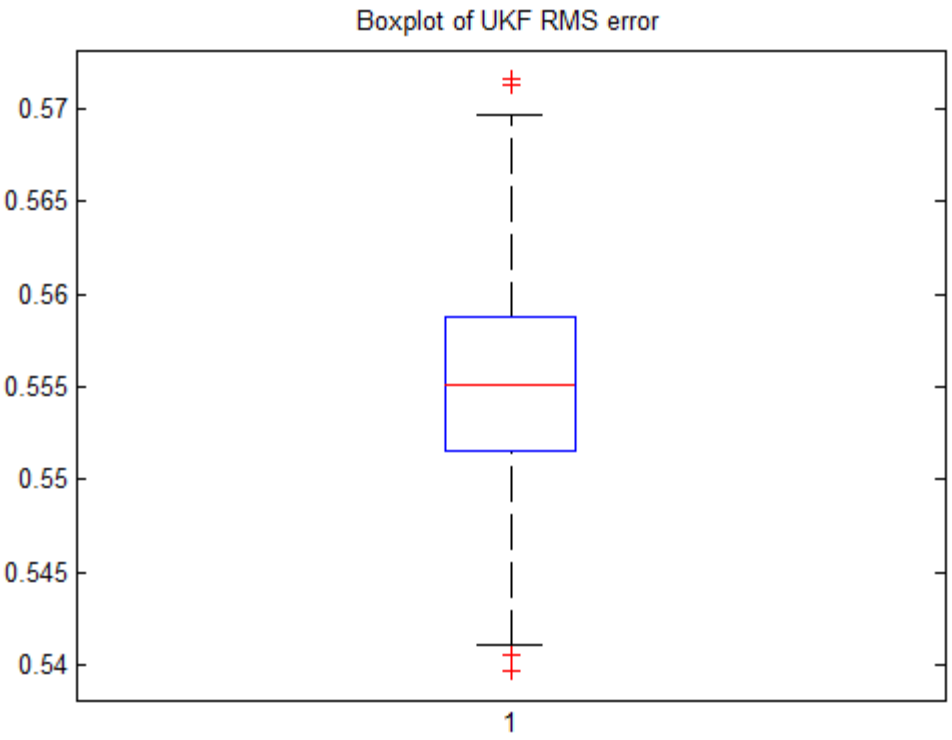

Figure 7.161 UKF RMS error with predicted measurement with load loss, bad data at 50 Hz.

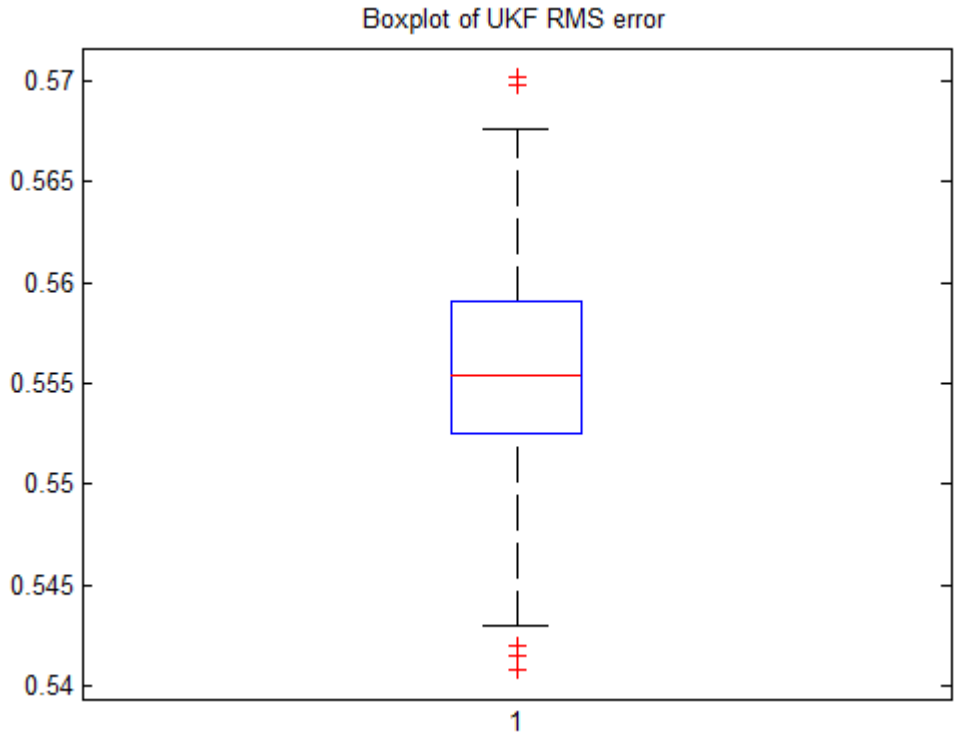

Figure 7.162 UKF RMS error with last uncorrupted measurement with load loss, bad data at 50 Hz.

Table XX Comparison of RMS errors for the KPM, the KLM and the GM-EKF

Filter	RMSE (Max.)	RMSE(Min)	Standard Deviation	RMSE of Rotor Angle (Max)	RMSE of Rotor Angle (Min)	Standard Deviation
KPM	0.5716	0.5397	0.0053	0.1703	0.0025	0.0316
KLM	0.5702	0.5408	0.0050	0.1837	0.0040	0.0329
GM-EKF	0.8825	0.7926	0.0182	0.2056	0.0067	0.0078

7.20 NORMAL MICROGRID, PACKET LOSS AND DELAY, BAD DATA AND PMUMEASUREMENT

In this section, we examine the performance of the robust UKFs and the GM-EKF under normal microgrid and packet loss and delay with bad data at the PMU frequency of 50 Hz. Six outliers are introduced in active power as shown in Figure 7.169. The packet loss and delay distribution are as mentioned in Section 7.5. Simulation results for the robust state estimators subject to packet loss and delay with bad data are presented in Figure 7.163- Figure 7.168. The robust UKFs provide better tracking of the true states than the GM-EKF. This is particularly true for the plots of the rotor angle, the d-axis transient voltage, and d-axis damper flux.

The results of 500 Monte Carlo simulations are provided in the box plots of Figure 7.170- Figure 7.172 and *Table XXI.* The errors for the robust UKFs are significantly smaller than the errors for the GM-EKF. The results show that packet loss and delay with bad data and, at the PMU sampling frequency of 50 Hz, the robust UKFs perform better than the GM-EKF. The Monte Carlo simulation results are similar for the rotor angle.

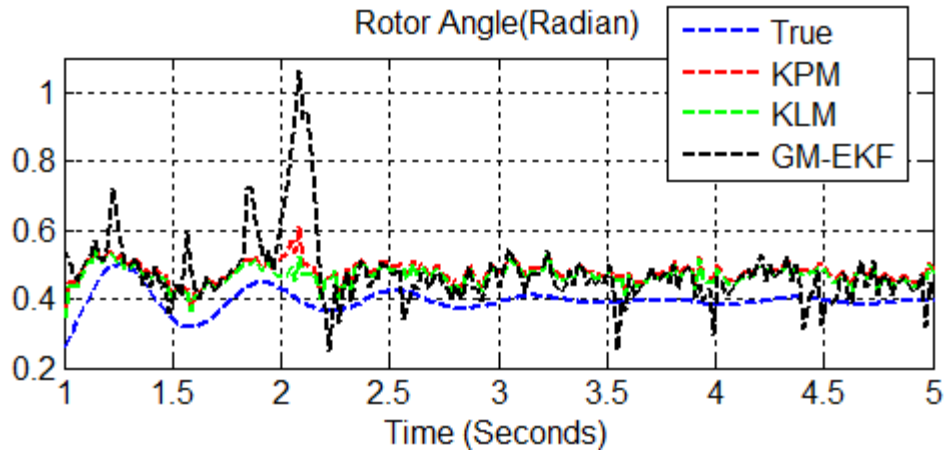

Figure 7.163 Rotor angle and its estimates with packet loss and delay, bad data at 50 Hz.

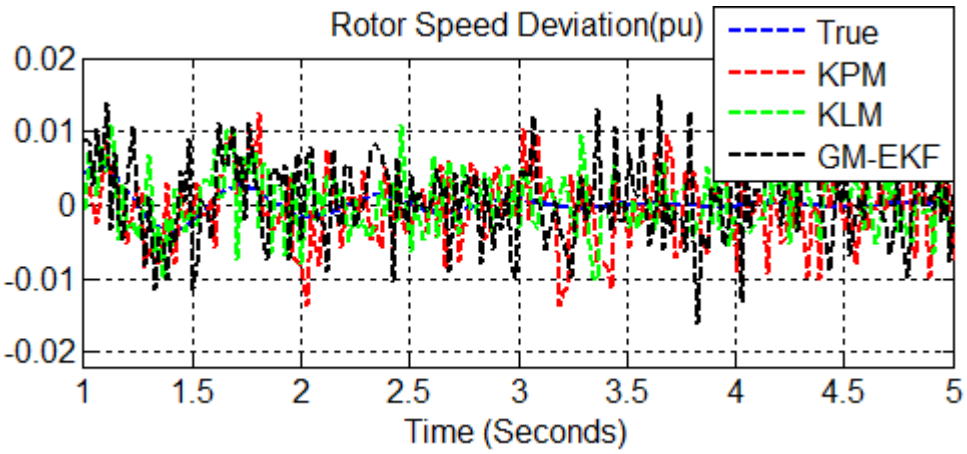

Figure 7.164 Rotor speed deviation and its estimates with packet loss and delay, bad data at 50 Hz.

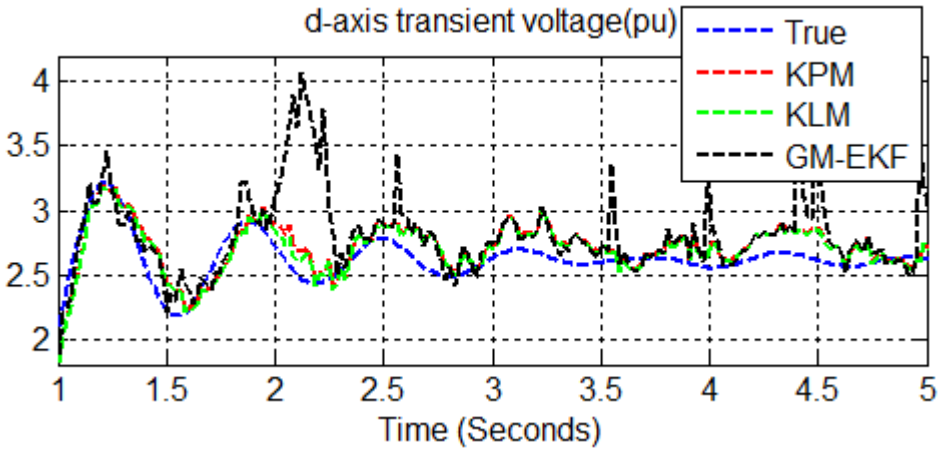

Figure 7.165 d-axis transient voltage and its estimates with packet loss and delay, bad data at 50 Hz.

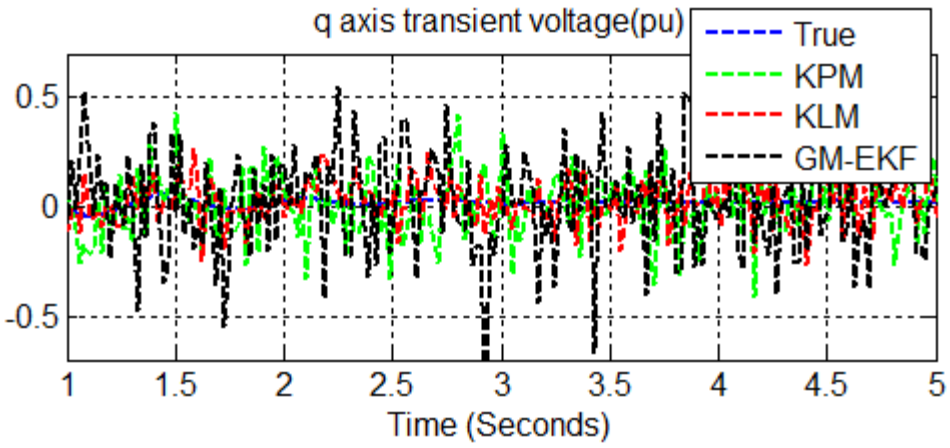

Figure 7.166 q-axis transient voltage and its estimates with packet loss and delay, bad data at 50 Hz.

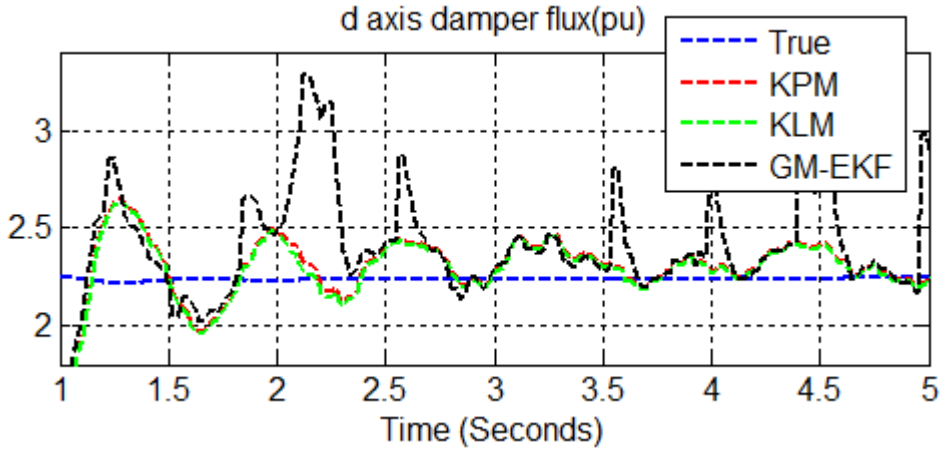

Figure 7.167 d-axis damper flux and its estimates with packet loss and delay, bad data at 50 Hz.

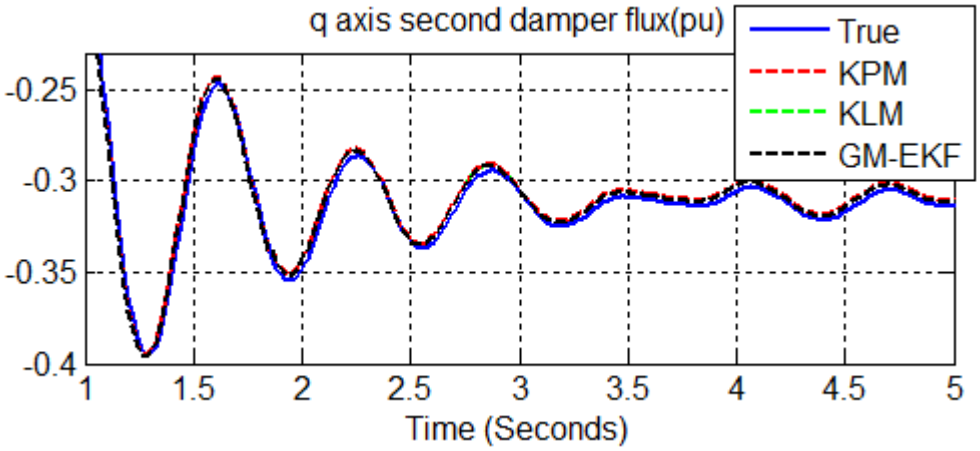

Figure 7.168 q-axis second damper flux and its estimates with packet loss and delay, bad data at 50 Hz.

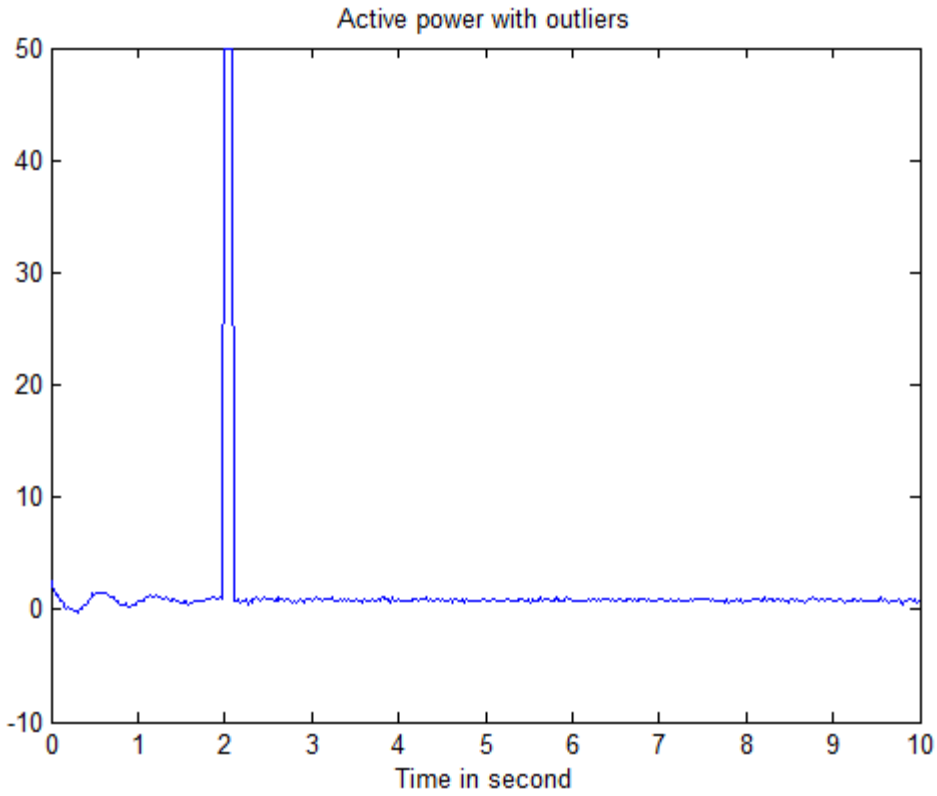

Figure 7.169 Active power with bad data

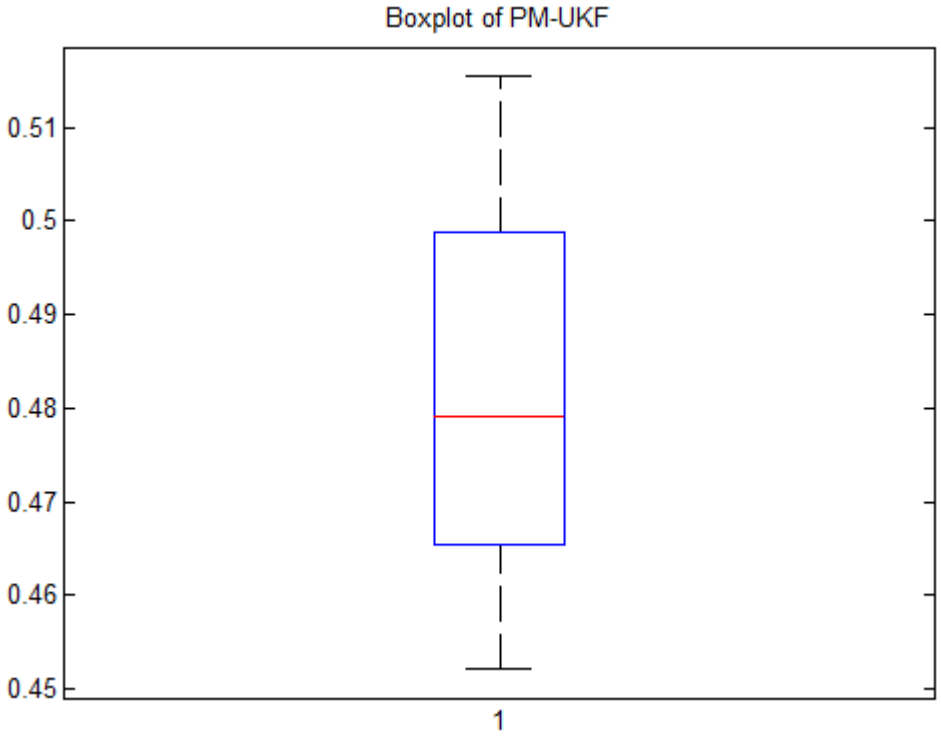

Figure 7.170 Box plot of PM-UKF with packet loss and delay, bad data

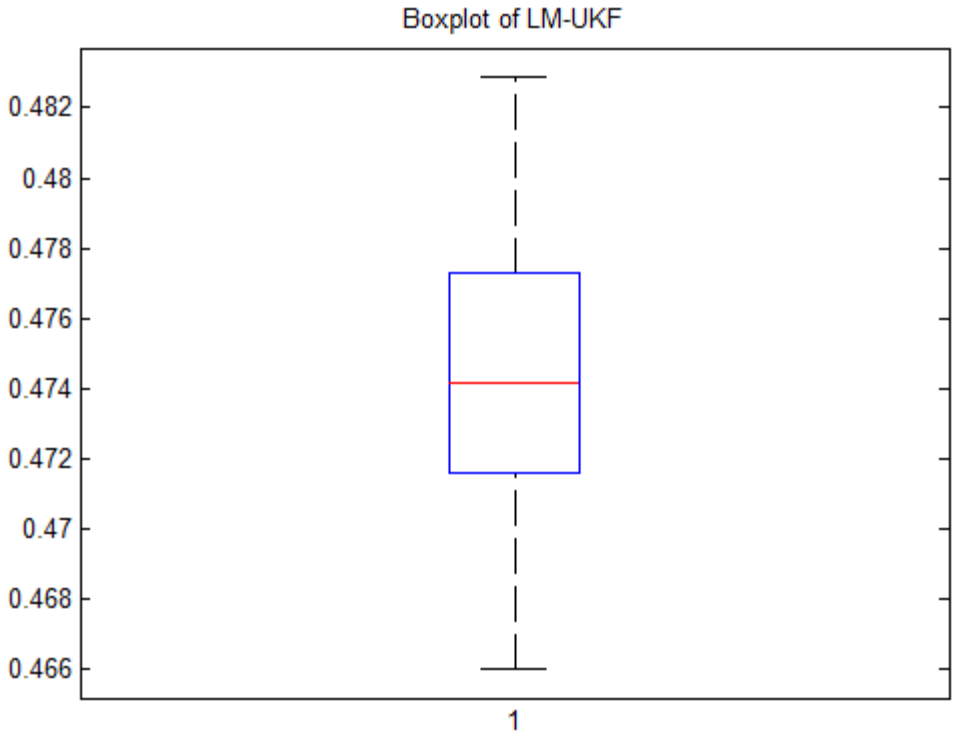

Figure 7.171 Box plot of LM-UKF with packet loss and delay, bad data

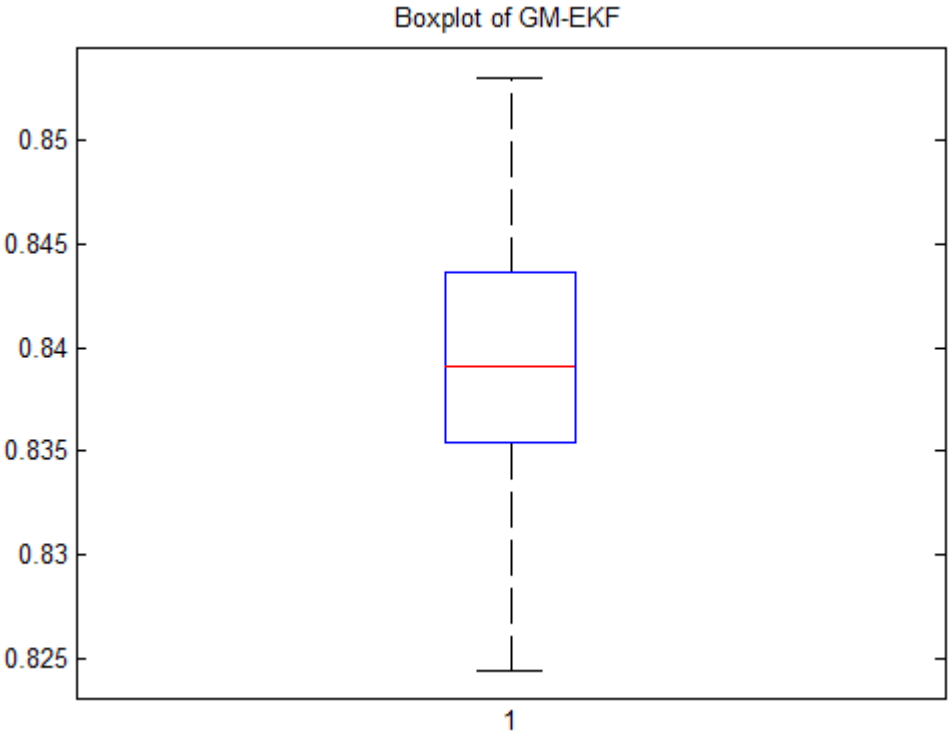

Figure 7.172 Box plot of GM-EKF with packet loss and delay, bad data

Table XXI Comparison of RMS errors for the KPM, KLM and the GM-EKF

Filter	RMSE (Max.)	RMSE(Min)	Standard Deviation	RMSE of Rotor Angle (Max)	RMSE of Rotor Angle (Min)	Standard Deviation
KPM	0.5155	0.4522	0.0057	0.1686	0.0065	0.0343
KLM	0.4829	0.4660	0.0048	0.1748	0.0038	0.0357
GM-EKF	0.8530	0.8244	0.0074	0.1898	0.0049	0.0364

7.21 FAULT AT PCC, PACKET LOSS AND DELAY, BAD DATA AND PMU MEASUREMENT

In this section, we analyze the performance of the robust estimators with fault at PCC, packet loss and delay, and bad data in measurements at the PMU frequency of 50 Hz. A three-phase-to-ground fault is applied at 5 s and cleared at 5.1 s. We also introduced six consecutive outliers in the active power measurements starting at 6 s (Figure 7.179). The packet loss and delay distribution are as mentioned in Section 7.5.The results obtained from the GM-EKF and the robust UKFs are presented in Figure 7.173-Figure 7.178. The results of 500 Monte Carlo simulations are provided in the box plots of Figure 7.180- Figure 7.182 and *Table XXII.* The errors for the robust UKFs are significantly smaller than the errors for the GM-EKF. The results show that for packet loss and delay with bad data and with fault at PCC, the robust UKFs perform better.

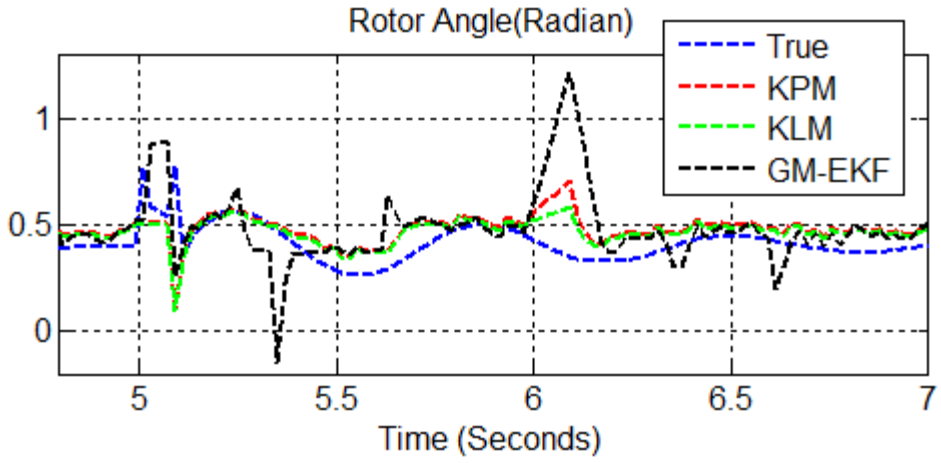

Figure 7.173 Rotor angle and its estimates with fault at PCC, packet loss and delay, bad data at 50 Hz.

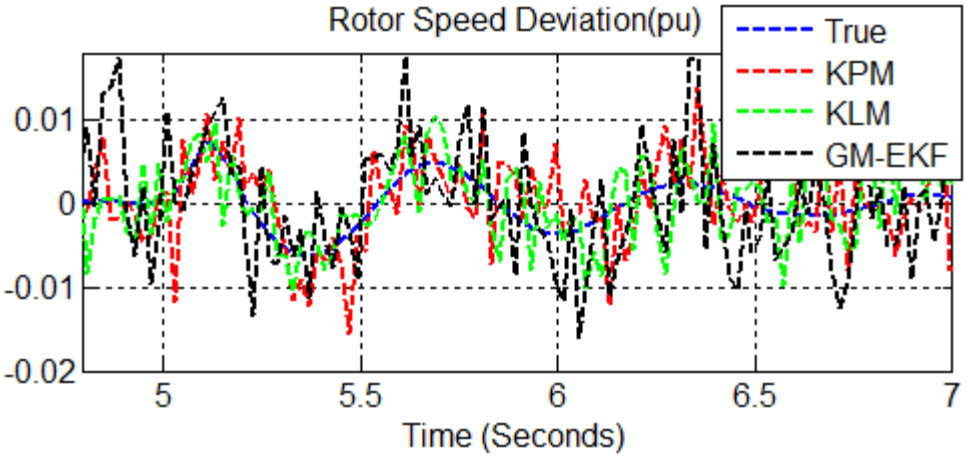

Figure 7.174 Rotor speed deviation and its estimates with fault at PCC, packet loss and delay, bad data at 50 Hz.

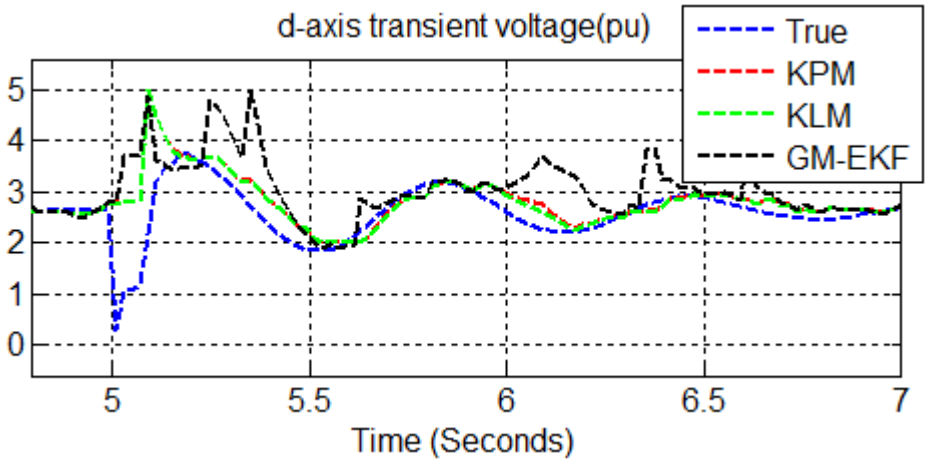

Figure 7.175 d-axis transient voltage and its estimates with fault at PCC, packet loss and delay, bad data at 50 Hz.

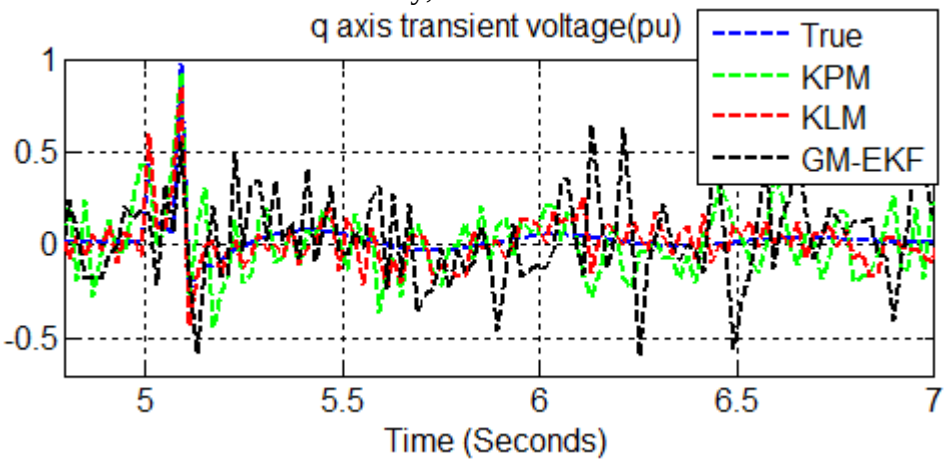

Figure 7.176 q-axis transient voltage and its estimates with fault at PCC, packet loss and delay, bad data at 50 Hz.

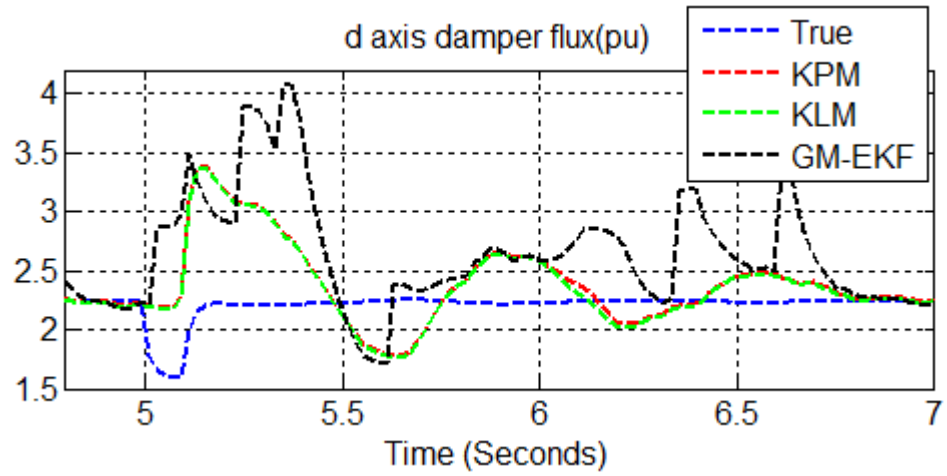

Figure 7.177 d-axis damper flux and its estimates with fault at PCC, packet loss and delay, bad data at 50 Hz.

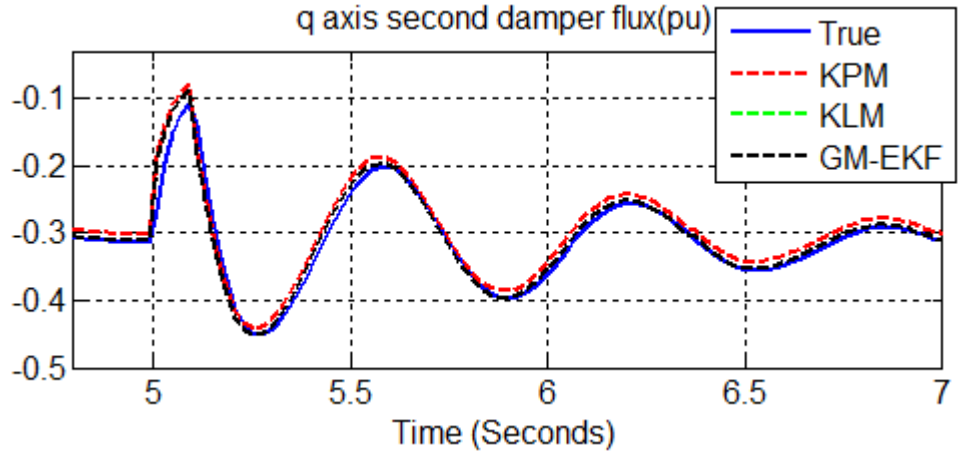

Figure 7.178 q-axis second damper flux and its estimates with fault at PCC, packet loss and delay, bad data at 50 Hz.

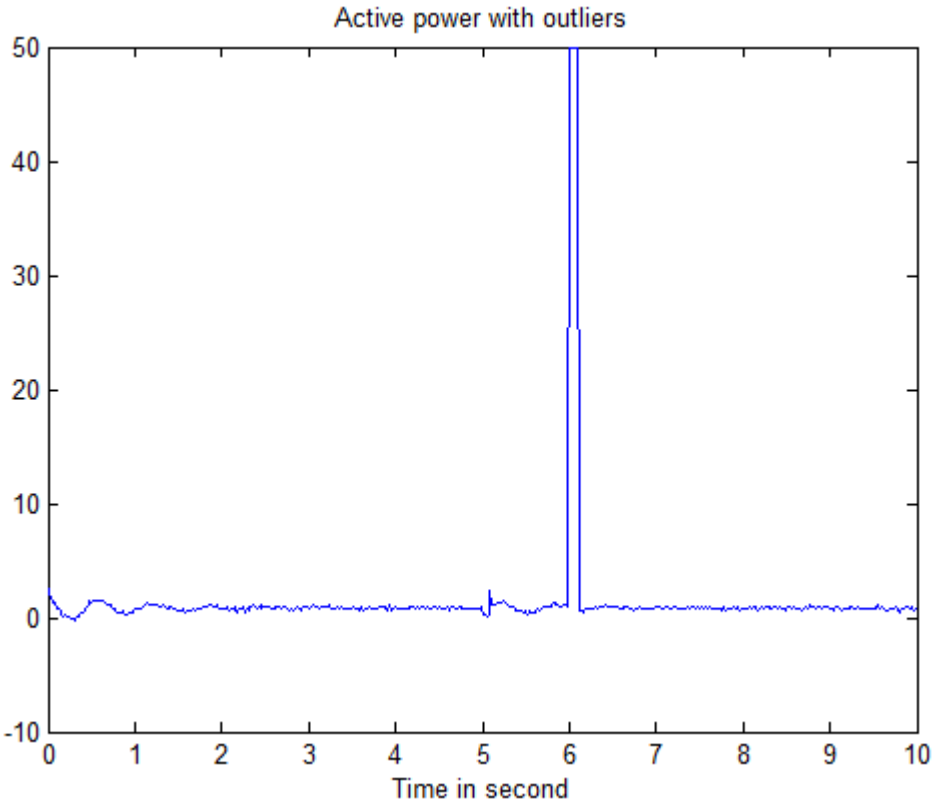

Figure 7.179 Active power with bad data

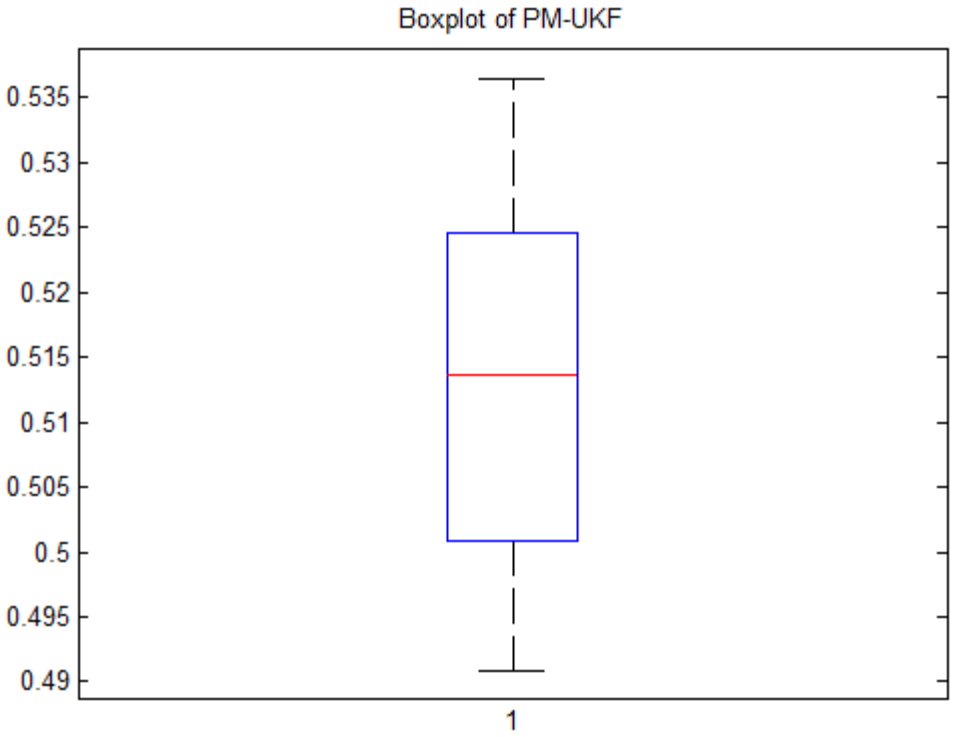

Figure 7.180 Box plot of PM-UKF with fault at PCC, packet loss and delay, bad data

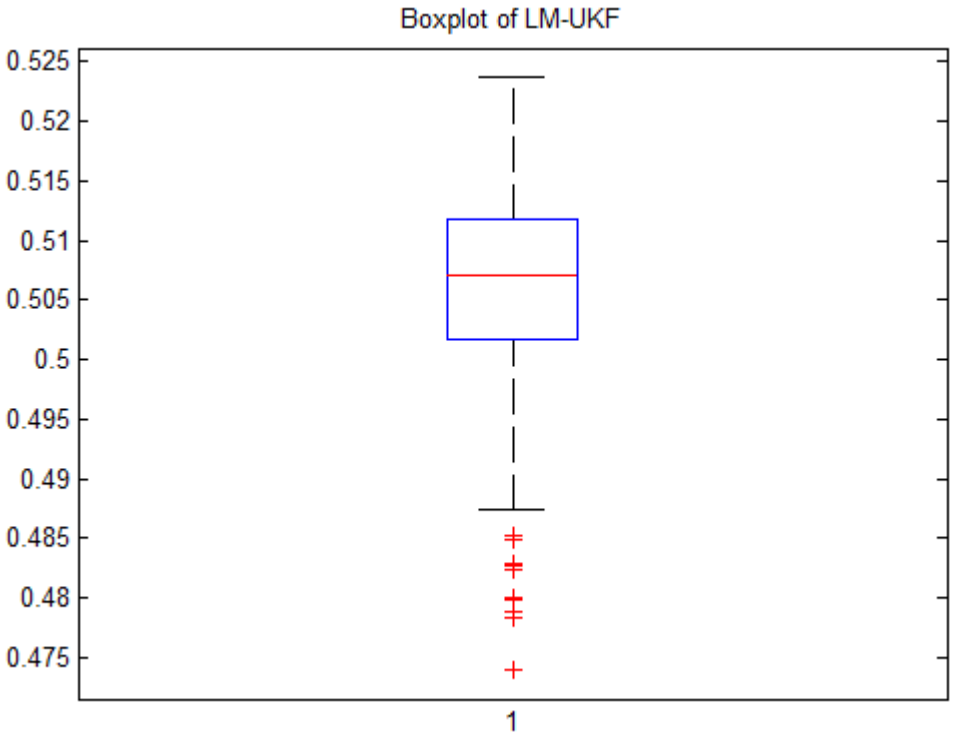

Figure 7.181 Box plot of LM-UKF with fault at PCC, packet loss and delay, bad data

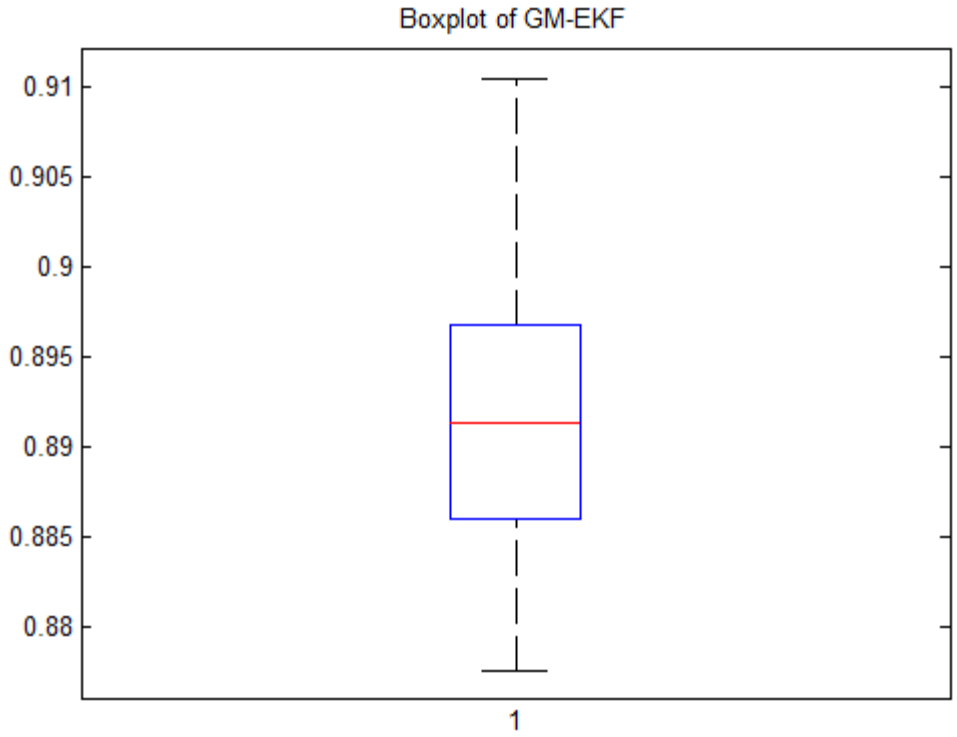

Figure 7.182 Box plot of GM-EKF with fault at PCC, packet loss and delay, bad data

Table XXII Comparison of RMS errors for the KPM, KLM and the GM-EKF

Filter	RMSE (Max.)	RMSE(Min)	Standard Deviation	RMSE of Rotor Angle (Max)	RMSE of Rotor Angle (Min)	Standard Deviation
KPM	0.5364	0.4909	0.0053	0.1119	0.0807	0.0314
KLM	0.5237	0.4740	0.0051	0.1407	0.0043	0.0323
GM-EKF	0.9104	0.8776	0.0087	0.1814	0.0608	0.0407

7.22 GENERATOR LOSS, PACKET LOSS AND DELAY, BAD DATA AND PMUMEASUREMENT

In this section, we examine the performance of the robust UKFs and the GM-EKF under loss of generator with packet loss and delay and with bad data at the PMU frequency of 50 Hz. We simulate the loss of the second generator at 4 s. Six outliers are

introduced in the active power measurements as shown in Figure 7.189. The packet loss and delay distribution are as mentioned in Section 7.5.Simulation results for the robust state estimators subject to packet loss and delay with bad data and loss of generator are presented in Figure 7.183- Figure 7.188. The robust UKFs provide better tracking of the true states than the GM-EKF.

The results of 500 Monte Carlo simulations are provided in the box plots of Figure 7.190- Figure 7.192 and *Table XX*. The errors for the robust UKFs are significantly smaller than the errors for the GM-EKF. The results show that with bad data and load loss, at the PMU sampling frequency of 50 Hz, the robust UKFs perform better than the GM-EKF.

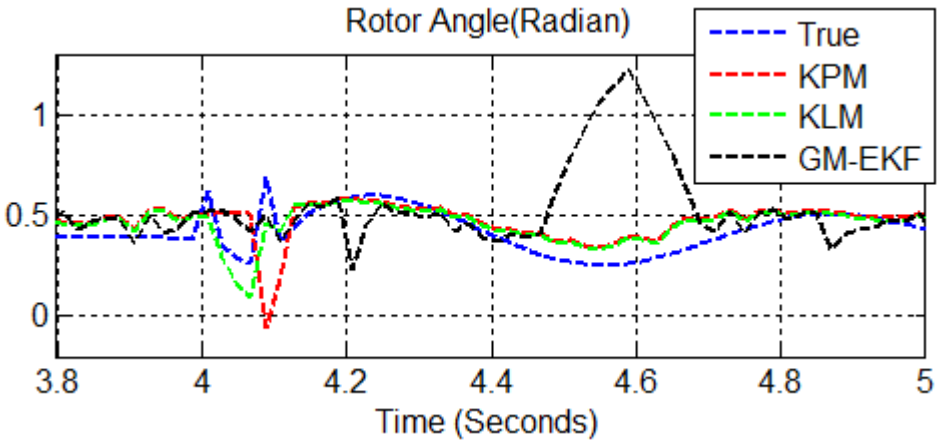

Figure 7.183 Rotor angle and its estimates with generator loss, packet loss and delay, bad data at 50 Hz.

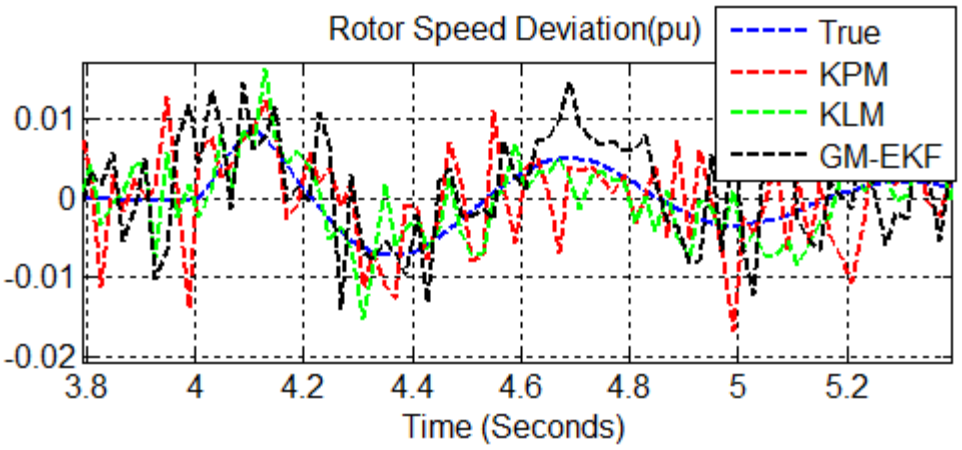

Figure 7.184 Rotor speed deviation and its estimates with generator loss, packet loss and delay, bad data at 50 Hz.

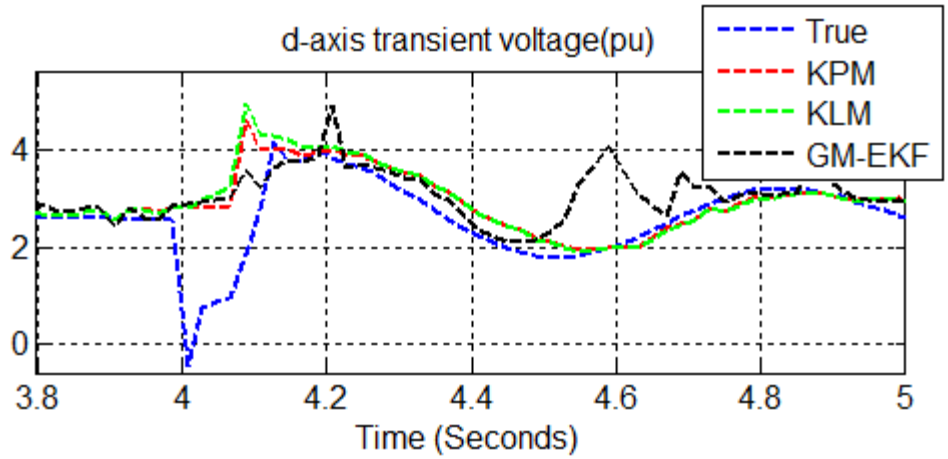

Figure 7.185 d-axis transient voltage and its estimates with generator loss, packet loss and delay, bad data at 50 Hz.

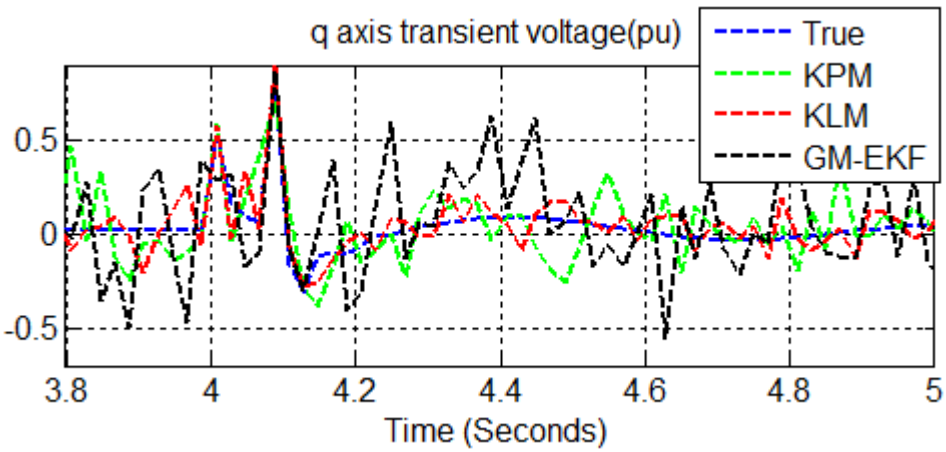

Figure 7.186 q-axis transient voltage and its estimates with generator loss, packet loss and delay, bad data at 50 Hz.

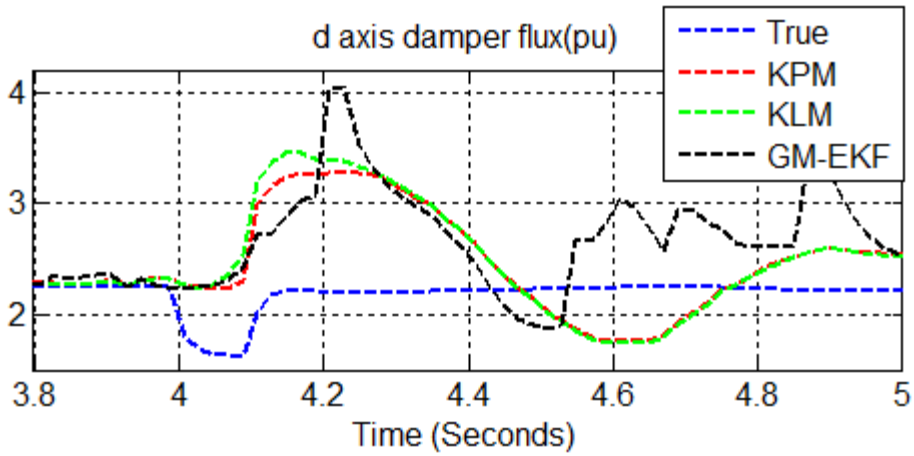

Figure 7.187 d-axis damper flux and its estimates with generator loss, packet loss and delay, bad data at 50 Hz.

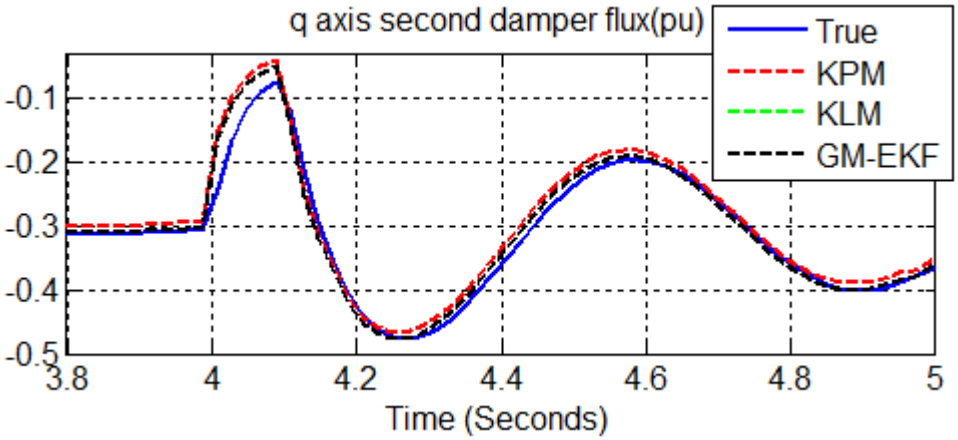

Figure 7.188 q-axis second damper flux and its estimates with generator loss, packet loss and delay, bad data at 50 Hz.

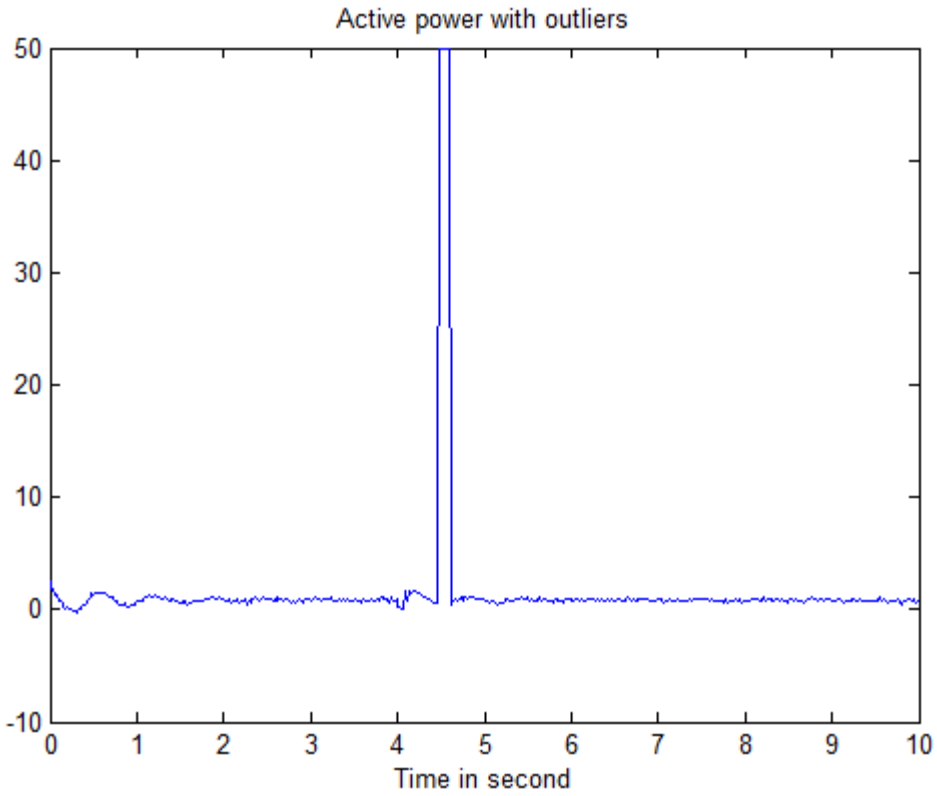

Figure 7.189 Active power with bad data

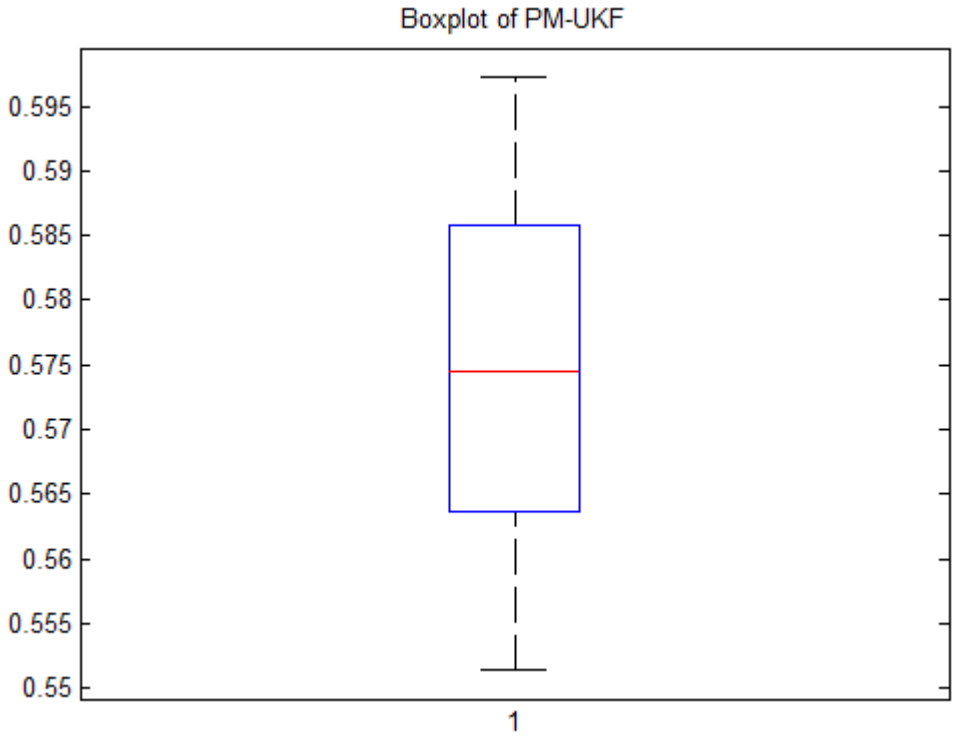

Figure 7.190 Box plot of PM-UKF with generator loss, packet loss and delay, bad data

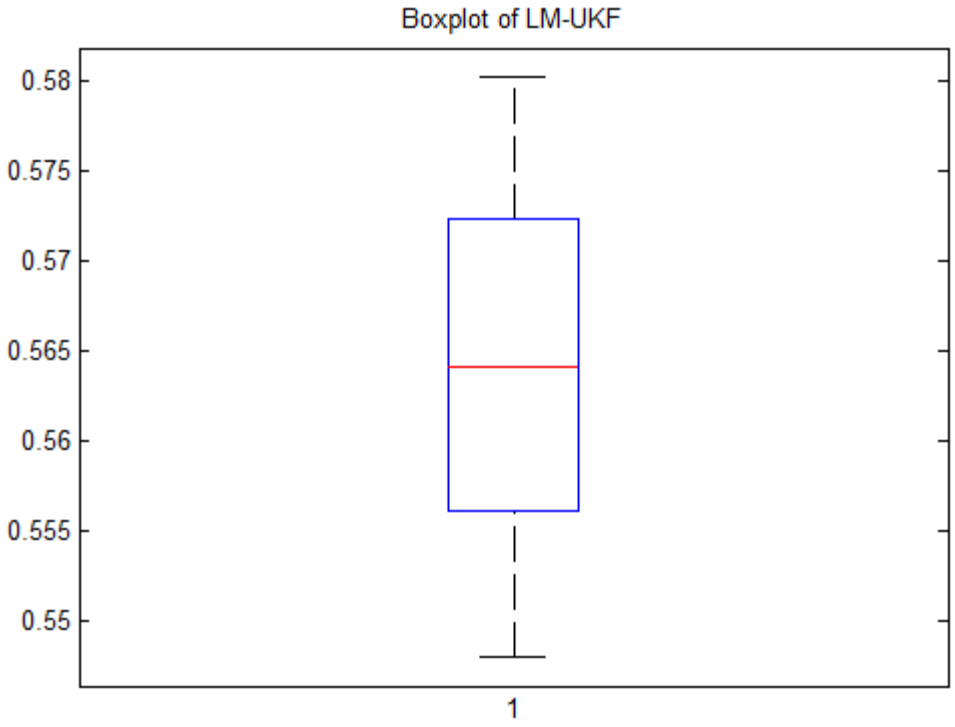

Figure 7.191 Box plot of LM-UKF with generator loss, packet loss and delay, bad data

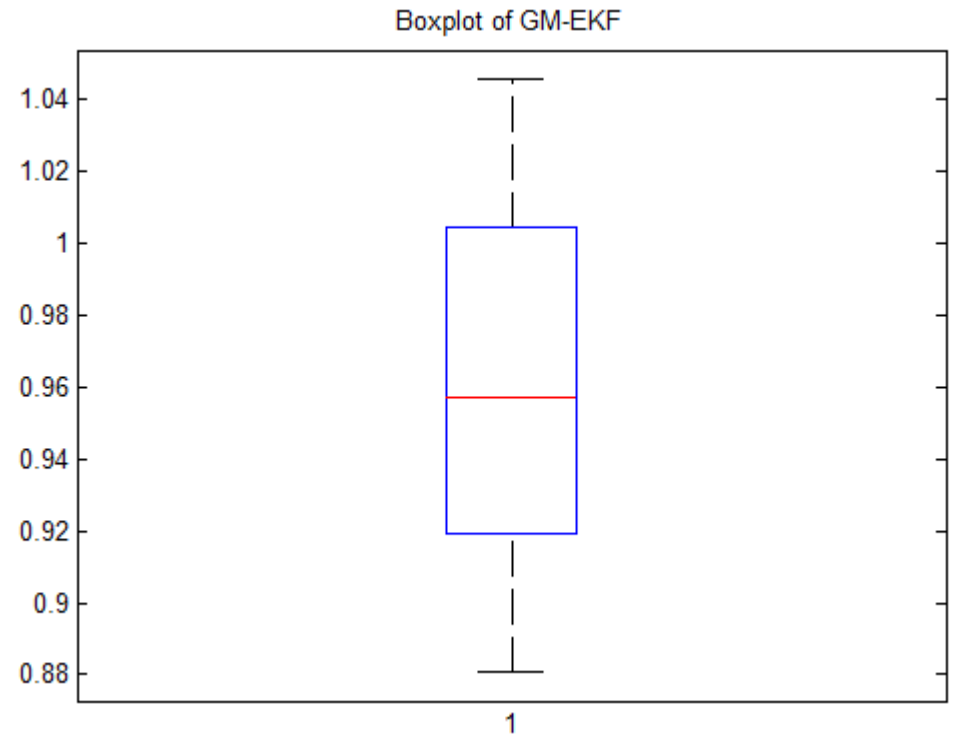

Figure 7.192 Box plot of GM-EKF with generator loss, packet loss and delay, bad data

Table XXIII Comparison of RMS errors for the KPM, KLM and the GM-EKF

Filter	RMSE (Max.)	RMSE(Min)	Standard Deviation	RMSE of Rotor Angle (Max)	RMSE of Rotor Angle (Min)	Standard Deviation
KPM	0.5972	0.5514	0.0071	0.1352	0.0102	0.0341
KLM	0.5802	0.5480	0.0058	0.1684	0.0079	0.0387
GM-EKF	1.0457	0.8810	0.0286	0.2047	0.0143	0.0412

7.23 LOAD LOSS, PACKET LOSS AND DELAY, BAD DATA AND PMUMEASUREMENT

In this section, we investigate the performance of the robust UKFs and the GM-EKF under loss of load, packet loss and delay with bad data at the PMU frequency of 50 Hz. As in Section 7.4, we simulate the loss of the second load at 4.5 s. Six outliers were introduced in the active power measurements as shown in Figure 7.199.The packet loss and delay distribution are as mentioned in Section 7.5.Simulation results for the robust state estimators subject to packet loss and delay with bad data and loss of load are presented in Figure 7.193- Figure 7.198. The robust UKFs provide better tracking of the true states than the GM-EKF. This is particularly true for the plots of the rotor angle, the d-axis transient voltage, and d-axis damper flux.

The results of 500 Monte Carlo simulations are provided in the box plots of Figure 7.200- Figure 7.202 and *Table XX*. The errors for the robust UKFs are significantly smaller than the errors for the GM-EKF. The results show that with bad data and load loss, at the PMU sampling frequency of 50 Hz, the robust UKFs perform better than the GM-EKF.

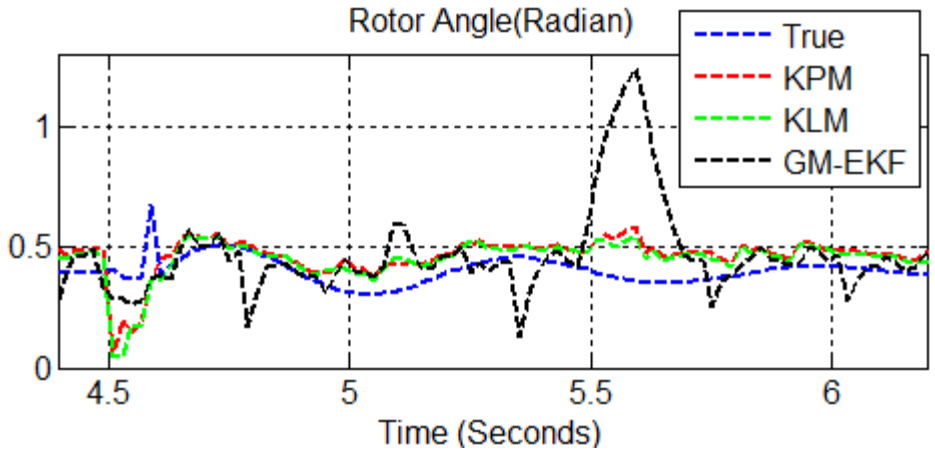

Figure 7.193 Rotor angle and its estimates with load loss, packet loss and delay, bad data at 50 Hz.

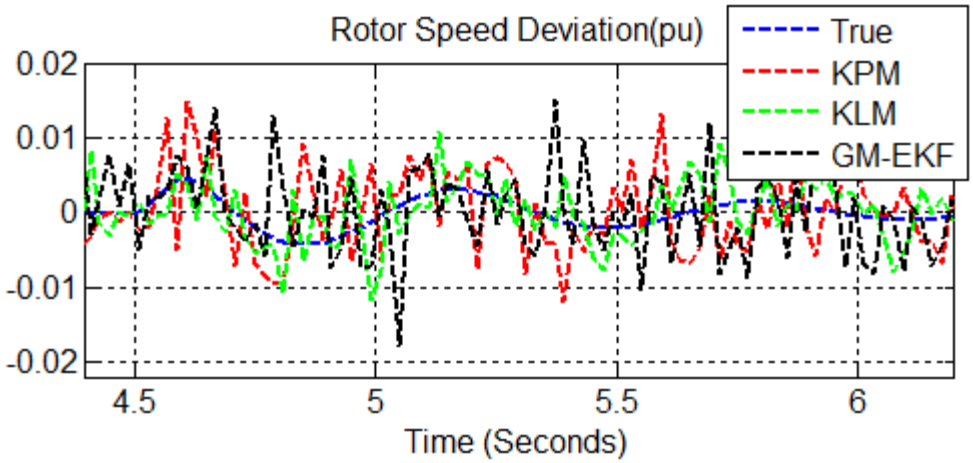

Figure 7.194 Rotor speed deviation and its estimates with load loss, packet loss and delay, bad data at 50 Hz.

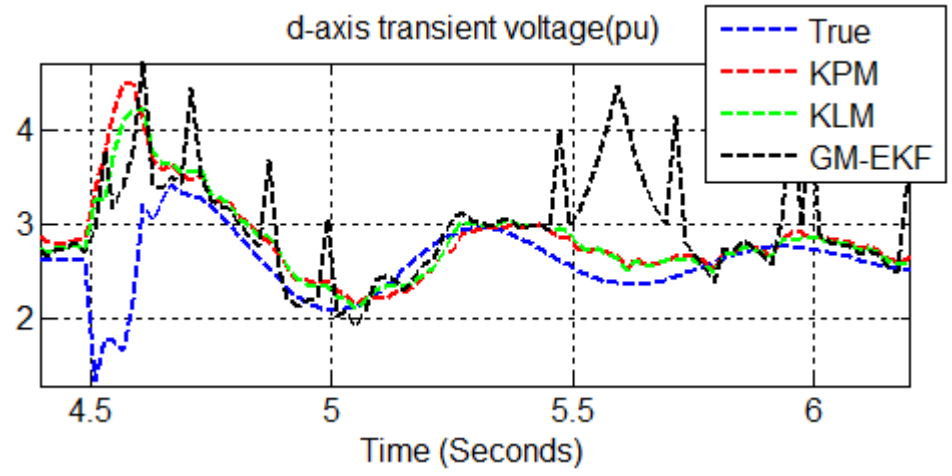

Figure 7.195 d-axis transient voltage and its estimates with load loss, packet loss and delay, bad data at 50 Hz.

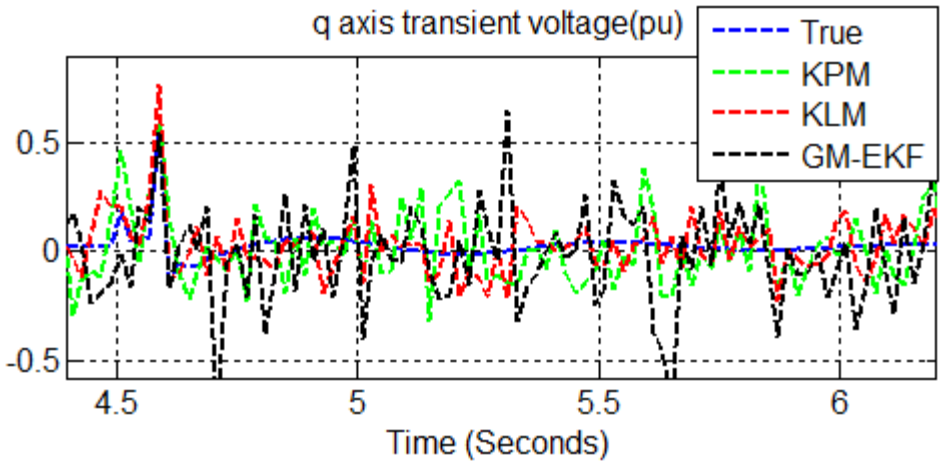

Figure 7.196 q-axis transient voltage and its estimates with load loss, packet loss and delay, bad data at 50 Hz.

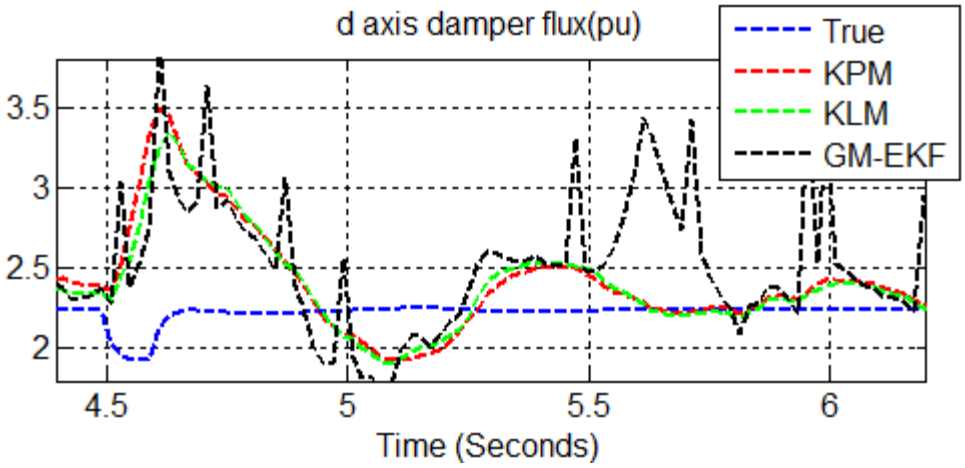

Figure 7.197 d-axis damper flux and its estimates with load loss, packet loss and delay, bad data at 50 Hz.

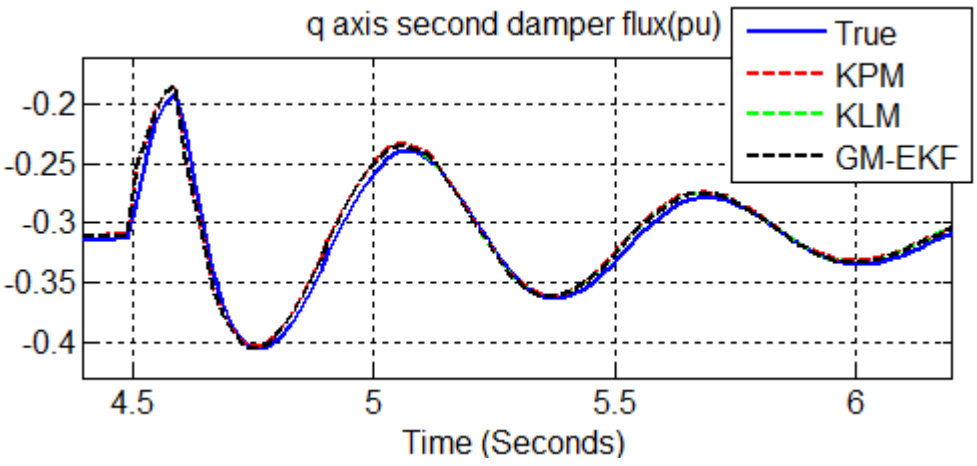

Figure 7.198 q-axis second damper flux and its estimates with load loss, packet loss and delay, bad data at 50 Hz.

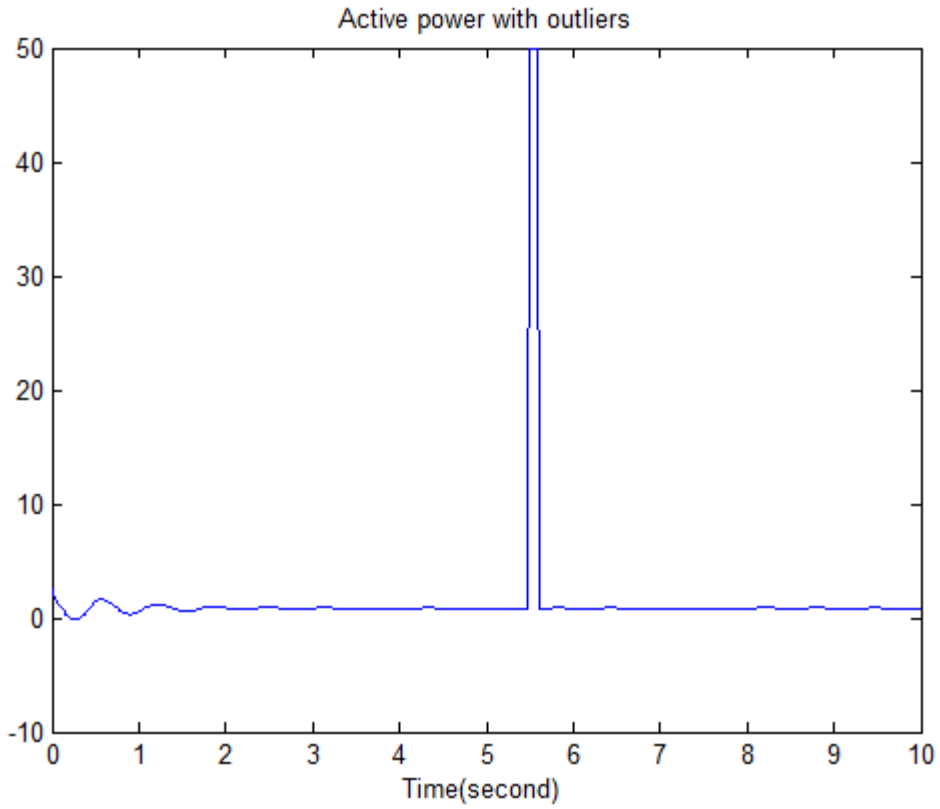

Figure 7.199 Active power with bad data

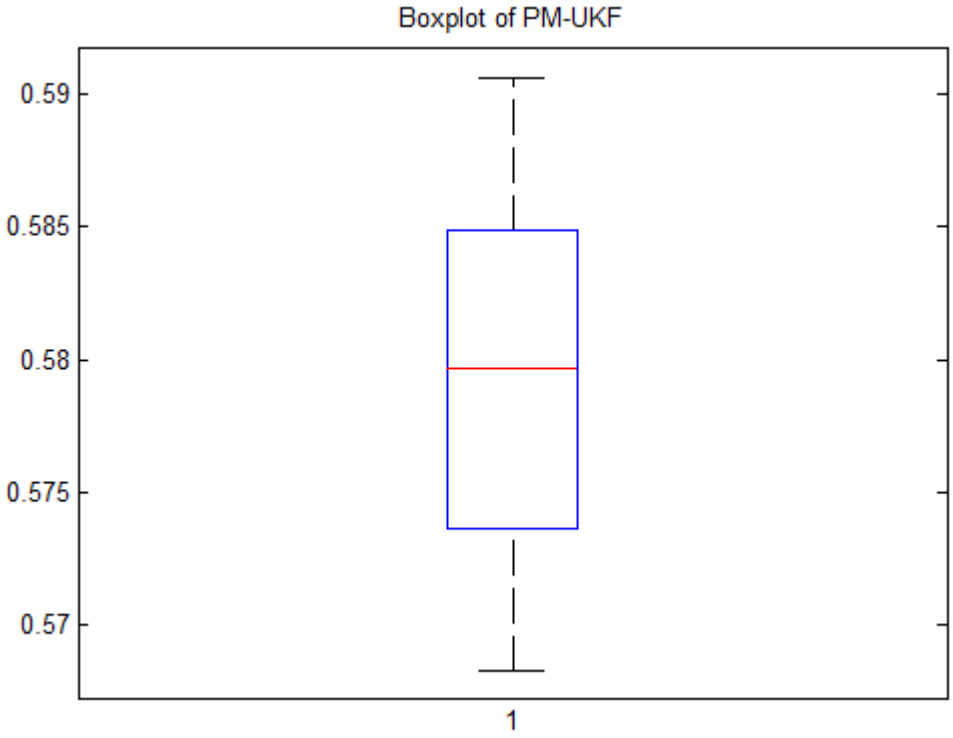

Figure 7.200 Box plot of PM-UKF with load loss, packet loss and delay, bad data

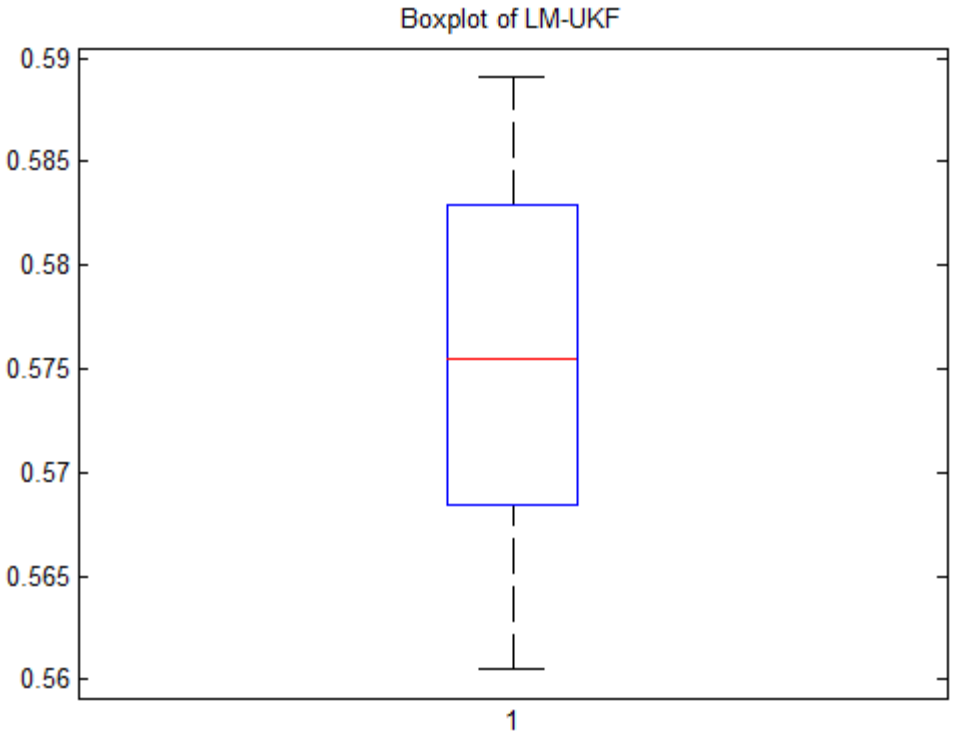

Figure 7.201 Box plot of LM-UKF with load loss, packet loss and delay, bad data

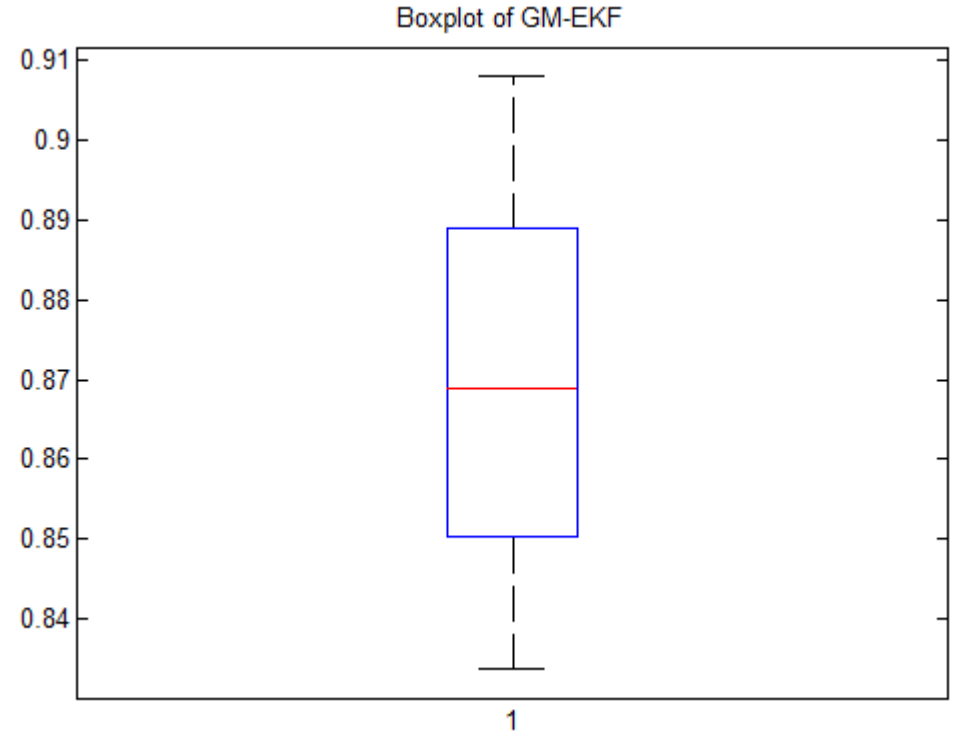

Figure 7.202 Box plot of GM-EKF with load loss, packet loss and delay, bad data

Table XXIV Comparison of RMS errors for the KPM, KLM and the GM-EKF

Filter	RMSE (Max.)	RMSE(Min)	Standard Deviation	RMSE of Rotor Angle (Max)	RMSE of Rotor Angle (Min)	Standard Deviation
KPM	0.5906	0.5683	0.0065	0.1417	0.0085	0.0373
KLM	0.5891	0.5605	0.0056	0.1396	0.0062	0.0341
GM-EKF	0.9079	0.8338	0.0218	0.1752	0.0090	0.0398

CHAPTER 8: CONCLUSION AND FUTURE WORK

8.1 CONCLUSION

The continuous growth in the size of the power grid has resulted in greater complexity for the network, its control, and the analysis required to maintain its safe and economic operation. This has increased interest in and motivated constant development of state estimation techniques in the area of power system operation and control. Static estimators provide the real time running status of a power system. However, dynamic state estimation (DSE) is required to predict the dynamic states of the system. As DSE methods and phasor measurement unit (PMU) measurements develop, the prediction accuracy of filtering for power systems has increased accordingly. In this thesis, the EKF and UKF were implemented to provide dynamic state estimation for a microgrid.

The performance of the EKF and the UKF-based DSE was evaluated under the following scenarios: normal operation of the microgrid, fault at the PCC, loss of generator, and loss of load. In all scenarios, the estimators estimated the dynamic response of the synchronous generator with acceptable accuracy. We obtained simulation results for a high sampling frequency of 1 kHz as well as the phasor measurement unit (PMU) frequency of 50 Hz. Simulation at the high sampling rate allowed us to use the simple Euler approximation to discretize the microgrid model and still obtain good state estimates. At the lower sampling rate, the Euler model is inadequate and a better approximation of the derivative was needed. For simulations with the 50 Hz sampling frequency we used the second order Runge-Kutta approximation, and this was adequate for normal microgrid operation. For abnormal scenarios, the second order Runge-Kutta approximation was inadequate but we were

able to obtain good results by using ten predictor iterations for each sampling period, with no corrector update.

Monitoring and control of a microgrid utilizes a communication network for data transfer. Problems associated with the communication network include rate limits, random delays, quantization errors, data dropping, etc. In this thesis, we assumed the estimator received the measurements through a lossy network and were subject to loss and delay. Packet loss was assumed to be a Bernoulli random process while time delay was assumed to have a binomial distribution. We proposed a method to deal with dropped and/ or delayed measurements based on a modification of the standard Kalman filter. Simulation results of the proposed method show that the method performs with acceptable accuracy.

In addition to data loss or delay, measurement data can be corrupted by outliers in various ways. These outliers can have a great impact on the state estimation results if used with the standard EKF or UKF. In order to make an estimator robust in the presence of outliers, the Generalized Maximum Likelihood Extended Kalman Filter (GM-EKF) can be utilized. We investigated the performance of three robust Kalman filters, the GM-EKF and two robust UKFs that use the normalized residual vector. The first UKF approach replaces the detected bad data with the last uncorrupted measurement and the second replaces the bad data with predicted measurements.

We introduced outliers in the measurements of active power and ran five state estimators, the EKF, the UKF, the GM-EKF, and the two robust UKFs. The results obtained from the EKF and UKF show that they are unable to perform well under these conditions. Simulation results show that they diverge from the true state values. In

contrast, all three robust estimators can deal with the outliers and provide good state estimates. The GM-EKF detects the outliers by the use of projection statistics and suppresses their effects, and the robust EKFs achieve the same result using the normalized residual. The results show that the robust state estimators track the true state values even after they receive bad data.

For comparison of the robust estimators, our simulations show that the robust UKF approaches provide better estimates than those of the GM-EKF. Furthermore, the GM-EKF requires more computation time than robust UKF. However, both robust UKF approaches are susceptible to the masking effects of multiple bad data in the bad data detection process while the GM-EKF is not.

8.1 FUTURE WORK

The results of this thesis can be extended in several research directions. A real-time communication network can be added between the sensor and estimator. This will enable us to investigate the real-time state estimation with the network. In addition, a controller can be implemented to control the frequency of the synchronous generator. This leads to a real time networked control system and can be simulated and studied using a network simulator such as NS3[1].

Several microgrids can be connected to the microgrid considered in this thesis, and the effects of state estimation based on contingencies on other microgrids can be investigated. We can also add renewable energy sources, such as wind, solar and tidal energy, to the microgrid and observe their effects on state estimation.

[1]https://www.nsnam.org/

We considered the packet drop and time delay of sensor data in the communication network between sensor and estimator. The mathematical model can be modified taking into account packet drop and time delay and the stability of the entire system can be analyzed. This will allow us to determine a range of packet drop and time delay beyond which the estimator will diverge from the true states.

REFERENCES

[1] Z. Huang. Peng, K. Schneider, and J. Nieplocha, “Feasibility studies of applying Kalman Filter Techniques to Power System Dynamic State Estimation,” *International Power Engineering Conference, IPEC*, 2007.

[2] J. Qi; K. Sun; J. Wang; H. Liu, "Dynamic State Estimation for Multi-Machine Power System by Unscented Kalman Filter with Enhanced Numerical Stability,"*IEEE Transactions on Smart Grid* , vol.PP, no.99, pp.1-1.

[3] E. Ghahremani, I. Kamwa, “Dynamic State Estimation in Power System by Applying the Extended Kalman Filter With Unknown Inputs to Phasor Measurements ,” *IEEE Transactions on Power Systems*, vol. 26, No. 4, pp. 2556-2566, Nov. 2011.

[4] E. Ghahremani, I. Kamwa, “Online State Estimation of a Synchronous Generator Using Unscented Kalman Filter From Phasor Measurements Units,” *IEEE Transactions on Energy Conversion*, vol. 26, No. 4, pp. 1099-1108, Dec. 2011.

[5] L. Lin, Linawati, L. Jasa, and E. Ambikairajah, "A Hybrid State Estimation Scheme for Power System," *Proc. 2002 IEEE Circuits and Systems Conference (APCCAS’02),*vol.1, pp.555-558.

[6] B. Sinopoli, L. Schenato, M. Franceschetti, K. Poolla, M. I. Jordan and S. S. Sastry, "Kalman filtering with intermittent observations," *IEEE Transactions on Automatic Control*, vol. 49, no. 9, pp. 1453-1464, Sept. 2004.

[7] M. Micheli and M. I. Jordan, "Random Sampling of a continuous time stochastic dynamical system, "*Proc. 15th Intl. Symposium on the Mathematical Theory of Networks and Systems (MTNS),* August 2002.

[8] X. Liu and A. Goldsmith, "Kalman filtering with partial observation losses," *2004 43rd IEEE Conference on Decision and Control (CDC) (IEEE Cat. No.04CH37601)*, 2004, pp. 4180-4186 Vol.4.

[9] L. Shi and L. Qiu, "State estimation over a network: Packet-dropping analysis and design,"*2009 IEEE International Conference on Control and Automation*, Christchurch, 2009, pp. 86-91.

[10] L. Mili, T. Van Cutsem and M. Ribbens-Pavella, "Bad Data Identification Methods in Power System State Estimation - A Comparative Study," *IEEE Power Engineering Review*, vol. PER-5, no. 11, pp. 27-28, Nov. 1985.

[11] E. Handschin, F. C. Schweppe, J. Kohlas and A. Fiechter, "Bad data analysis for power system state estimation," *IEEE Transactions on Power Apparatus and Systems*, vol. 94, no. 2, pp. 329-337, Mar 1975.

[12] M. Netto, J. Zhao and L. Mili, "A robust extended Kalman filter for power system dynamic state estimation using PMU measurements,"*2016 IEEE Power and Energy Society General Meeting (PESGM)*, Boston, MA, 2016, pp. 1-5.

[13] L. Mili, M. G. Cheniae, N. S. Vichare and P. J. Rousseeuw, "Robust state estimation based on projection statistics [of power systems]," *IEEE Transactions on Power Systems*, vol. 11, no. 2, pp. 1118-1127, May 1996.

[14] M. A. Gandhi and L. Mili, "Robust Kalman Filter Based on a Generalized Maximum-Likelihood-Type Estimator," *IEEE Transactions on Signal Processing*, vol. 58, no. 5, pp. 2509-2520, May 2010.

[15] P.J. Rousseeuw and A.M. Leroy, Robust Regression and Outlier Detection. Hoboken, NJ: Wiley, 1987.

[16] P.J. Huber, Robust Statistics, New York: Wiley, 1981.

[17] L. Thomas and L. Mili, "A Robust GM-Estimator for the Automated Detection of External Defects on Barked Hardwood Logs and Stems," *IEEE Transactions on Signal Processing*, vol. 55, no. 7, pp. 3568-3576, July 2007.

[18] F.R. Hampel, E.M. Ronchetti, P.J. Rousseeuw, and W.A. Stahel, Robust Statistics: The Approach Based on Influence Functions. Hoboken, NJ: Wiley 1986.

[19] Junbo Zhao, Gexiang Zhang and M. La Scala, "PMU based Robust Dynamic State Estimation method for power systems," *2015 IEEE Power & Energy Society General Meeting*, Denver, CO, 2015, pp. 1-5.

[20] Kuang-Rong Shih and Shyh-Jier Huang, "Application of a robust algorithm for dynamic state estimation of a power system," *IEEE Transactions on Power Systems*, vol. 17, no. 1, pp. 141-147, Feb 2002.

[21] S. J. Julier and J. K. Uhlmann, "Unscented filtering and nonlinear estimation," *Proceedings of the IEEE*, vol. 92, no. 3, pp. 401-422, Mar 2004.

[22] J. Driesen and F. Katiraei, "Design for distributed energy resources," *IEEE Power and Energy Magazine*, vol. 6, no. 3, pp. 30-40, May-June 2008.

[23] S. Chowdhury, S. P. Chowdhury, P. Crossley, Microgrids and Active Distribution Networks, Institution of Engineering and Technology, 2009.

[24] F. Li, R. Li, F. Zhou, Microgrid Technology and Engineering Application, Academic Press, 2015.

[25] X. Zhou, T. Guo and Y. Ma, "An overview on microgrid technology," *2015 IEEE International Conference on Mechatronics and Automation (ICMA)*, Beijing, 2015, pp. 76-81.

[26] C. A. Gross, Electric Machines, CRC Press, 2006.

[27] J. Rosenblatt, M. H. Friedman, Direct and Alternating Current Machinery, CBS Publishers and Distributors, 2001.

[28] K. H. Padiyar, Power Systems Dynamics: Stability and Control, Anshan Publication, 2004.

[29] S. Crary, "Two-reaction theory of synchronous machines," *Electrical Engineering*, vol. 56, no. 1, pp. 27-31, Jan 1937.

[30] www.mathworks.com/help/physmod/sps/powersys/ref/synchronousmachine.html

[31] P.W. Sauer, M.A. Pai, Power Systems Dynamics and Stability, Stipes Publishing Co., 2007

[32] E. Ghahremani and I. Kamwa, "Simultaneous state and input estimation of a synchronous machine using the Extended Kalman Filter with unknown inputs," *2011 IEEE International Electric Machines & Drives Conference (IEMDC)*, Niagara Falls, ON, 2011, pp. 1468-1473.

[33] G. Welch, G. Bishop, "An Introduction to The Kalman Filter," Published in July 2006.

[34] Ravi Chander Janapati, Ch.Balaswamy, K. Soundararajan," Enhanced Mechanism for Localization in Wireless Sensor Networks using PSO Assisted Extended Kalman Filter Algorithm (PSO-EKF), "*International Conference on Communication, Information & Computing Technology*, Jan, 2015.

[35] Hamed Tebianian, Benjamin Jeyasurya, " Dynamic State Estimation in Power Systems Using Kalman Filters," *IEEE Electrical Power &Energy Conference (EPEC)*, 2013.

[36] D. Simon, Optimal State estimation: Kalman,H_∞, and Nonlinear Approaches. New Jersey: John Wiley & Sons, 2006.

[37] B. Li and M. Q. H. Meng, "Computer-Aided Detection of Bleeding Regions for Capsule Endoscopy Images," *IEEE Transactions on Biomedical Engineering*, vol. 56, no. 4, pp. 1032-1039, April 2009.

[38] D. Zhu, X. Yi, "A mobile sensing system for structural health monitoring: design and validation," *Smart Mater. Struct*., vol. 19 no. 5 pp. 1–11 2010.

[39] C. Wu C. Liao and L. Fu. "Service-oriented smart-home architecture based on OSGi and mobile-agent technology," *IEEE Trans. on Systems Man and Cybernetics Part C: Applications and Reviews*, vol. 37 no. 2 pp. 193–205 2007.

[40] W. Zhang M.S. Branicky and S.M. Phillips "Stability of networked control systems," *IEEE Control Syst. Mag*. vol. 21 no. 1 pp. 84–99 2001.

[41] S. Wang S. X. Meng and T. Chen: "Wide-area control of power systems through delayed network communication," *IEEE Trans. on Control Systems Technology*, vol. 20 no. 2 pp. 495–503 2012.

[42] N. N. P. Mahalik K. K. Kim "A prototype for hardware-in-the-loop simulation of a distributed control architecture," *IEEE Trans. Syst. Man Cybern. C Appl. Rev.*, vol. 38 no. 2 pp. 189-200 Mar. 2008.

[43] M.-Y. Chow Y Tipsuwan "Time sensitive network-based control systems and applications" *IEEE IES Network Based Control Newsletter*, vol. 5 no. 2 pp. 13-18 Jun. 2005.

[44] X. Ye S. Liu and P. X. Liu "Modeling and stabilization of networked control system with packet loss and time-varying delays" *IET Control Theory and Applications*, vol. 4 no. 6 pp. 1094–1100 2010.

[45] M. Yu L. Wang "Stabilization of networked control systems with data packet dropout and network delays via switching system approach*," Proceedings of the 43rd IEEE Conference on Decision and Control*, 2004 pp. 3539–3544.

[46] S. Liu, P. X. Liu and X. Wang, "H∞ control of networked control systems with stochastic measurement losses," *2016 IEEE International Conference on Information and Automation (ICIA)*, Ningbo, China, 2016, pp. 1691-1696.

[47] Hasan, M.S., Harding, C., Yu, "Modeling delay and packet drop in Networked Control Systems using network simulator NS2,*" International Journal of Automat Computing* (2005) 2: 187.

[48] M. B. G. Cloosterman, N. van de Wouw, W. P. M. H. Heemels and H. Nijmeijer, "Stability of Networked Control Systems With Uncertain Time-Varying Delays," *IEEE Transactions on Automatic Control*, vol. 54, no. 7, pp. 1575-1580, July 2009.

[49] P. L. Beaumont, A. Goad, and D. Perira, "Getting Real with Real Time Dispatching in Metrology; an RTD Solution to Metrology's Imperceptible Cycle Time Impact," *2008 IEEESEMI Advanced Semiconductor Manufacturing Conference*, 2008, no. 2, pp. 311–317.

[50] Du Feng, Du Wencai, "Networked control systems based on new Smith estimating compensation [M],"Beijing: Science Press2012.

[51] T. Liu, S. Jiang and F. Pan, "Analysis and design of the time-delay compensation for networked control systems with random communication delay,"*2016 35th Chinese Control Conference (CCC)*, Chengdu, 2016, pp. 7234-7239.

[52] M. Yang and H. Zhang, "Stability analysis of singular networked control system with long time delay and date packet dropout," *2013 Fourth International Conference on Intelligent Control and Information Processing (ICICIP)*, Beijing, 2013, pp. 84-87.

[53] J. P. Hespanha, P. Naghshtabrizi and Y. Xu, "A Survey of Recent Results in Networked Control Systems," *Proceedings of the IEEE*, vol. 95, no. 1, pp. 138-162, Jan. 2007.

[54] A. Abur, A.G.Exposito, Power System State Estimation: Theory and Implementation, CRC Press, 2004.

[55] J. Zhao; M. Netto; L. Mili, "A Robust Iterated Extended Kalman Filter for Power System Dynamic State Estimation," *IEEE Trans. on Power Systems*, vol. PP, no.99, pp.1-1.

[56] C. Croux and P. J. Rousseeuw, *Time-efficient algorithms for two highly robust estimators of scale*. Springer, 1992.

[57] Y. Zhou and L. Xie, "Detection of bad data in multi-area state estimation," *2017 IEEE Texas Power and Energy Conference (TPEC)*, College Station, TX, 2017, pp. 1-6.

[58] A. K. Singh and B. C. Pal, "Decentralized Dynamic State Estimation in Power Systems Using Unscented Transformation," *IEEE Transactions on Power Systems*, vol. 29, no. 2, pp. 794-804, March 2014.

[59] S. Wang, W. Gao and A. P. S. Meliopoulos, "An Alternative Method for Power System Dynamic State Estimation Based on Unscented Transform," *IEEE Transactions on Power Systems*, vol. 27, no. 2, pp. 942-950, May 2012.

[60] G. Valverde and V. Terzija, "Unscented Kalman filter for power system dynamic state estimation," *IET Generation, Transmission & Distribution*, vol. 5, no. 1, pp. 29-37, Jan. 2011

[61] R. Majumder and S. Sadhu, "Robust Extended Kalman filter for ballistic object tracking during re-entry,"*2016 IEEE Annual India Conference (INDICON)*, Bangalore, 2016, pp. 1-6.

[62] F. Katiraei, M. R. Iravani and P. W. Lehn, "Small-signal dynamic model of a micro-grid including conventional and electronically interfaced distributed resources," *IET Generation, Transmission & Distribution*, vol. 1, no. 3, pp. 369-378, May 2007.

APPENDIX

Table XXV Values of Parameters

Parameter	Definitions	Values
D, J	Damping factor and inertia constant per unit	0.05, 3.7
T'_{do} , T'_{qo}	d- and q- transient open circuit time constant	10.0, 1.0
x_d , x_q	d- and q- axis reactance	1.105, 0.474
x'_d , x'_q	d- and q- axis transient reactance	0.402, 0.45
x''_d , x''_q	d- and q- axis sub-transient reactance	0.2022, 0.203
x_l	Leakage reactance	0.10
x_e	Thevenin line reactance	0.94
P_m	Mechanical input per unit	0.85
$x_{td} = x'_d + x_e$	---	1.336
$x_{tq} = x_q + x_e$	---	1.414
δ	1st state, rotor angle	
Δω	2nd state, rotor speed deviation	
e'_q , e'_d	3rd and 4th state	
ω_o	Synchronous speed	377
E_{fd}	Field voltage (pu)	1.02
V_b	Bus voltage	No. = 0.85
i_d , i_q	d- and q-axis stator current	
$I_t = \sqrt{(i_d^2 + i_q^2)}$	Terminal bus current	